

# Roadmap on Sustainable Mixed Ionic-Electronic Conducting Membranes

Guoxing Chen,\* Armin Feldhoff,\* Anke Weidenkaff,\* Claudia Li, Shaomin Liu,\* Xuefeng Zhu,\* Jaka Sunarso,\* Kevin Huang,\* Xiao-Yu Wu,\* Ahmed F. Ghoniem, Weishen Yang, Jian Xue,\* Haihui Wang,\* Zongping Shao,\* Jack H. Duffy, Kyle S. Brinkman,\* Xiaoyao Tan, Yan Zhang, Heqing Jiang,\* Rémi Costa,\* Kaspar Andreas Friedrich, and Ralf Krieger\*

Mixed ionic-electronic conducting (MIEC) membranes have gained growing interest recently for various promising environmental and energy applications, such as H<sub>2</sub> and O<sub>2</sub> production, CO<sub>2</sub> reduction, O<sub>2</sub> and H<sub>2</sub> separation, CO<sub>2</sub> separation, membrane reactors for production of chemicals, cathode development for solid oxide fuel cells, solar-driven evaporation and energy-saving regeneration as well as electrolyzer cells for power-to-X technologies. The purpose of this roadmap, written by international specialists in their fields, is to present a snapshot of the state-of-the-art, and provide opinions on the future challenges and opportunities in this complex multidisciplinary research field. As the fundamentals of using MIEC membranes for various applications become increasingly challenging tasks, particularly in view of the growing interdisciplinary nature of this field, a better understanding of the underlying physical and chemical processes is also crucial to enable the career advancement of the next generation of researchers. As an integrated and combined article, it is hoped that this roadmap, covering all these aspects, will be informative to support further progress in academics as well as in the industry-oriented research toward commercialization of MIEC membranes for different applications.

## 1. Introduction


MIEC membranes have gained considerable interest due to their wide range of potentials related to environmental and energy applications in the past three decades. MIEC membranes simultaneously conducting oxygen ions and electronic charge carriers have been considered as a prominent next-generation technology for chemical and fuel processing and energy storage and conversion. Against the current background of the global energy transition, the societal and scientific needs make a roadmap describing the state-of-the-art, future challenges, and opportunities of MIEC membranes particularly timely. The motivation for this roadmap is a tight connection existing between the domain of membrane- and catalyst-assisted gas conversion and separation and the recent fast development of the sustainable energy sources, as well as

G. Chen, A. Weidenkaff  
Fraunhofer Research Institution for Materials Recycling and Resource  
Strategies IWKS

Brentanostraße 2a, 63755 Alzenau, Germany  
E-mail: guoxing.chen@iwks.fraunhofer.de

A. Feldhoff  
Institute of Physical Chemistry and Electrochemistry  
Leibniz University Hannover  
Callinstr. 3A, 30167 Hannover, Germany  
E-mail: armin.feldhoff@pci.uni-hannover.de

A. Weidenkaff  
Department of Materials and Earth Sciences  
Technical University Darmstadt  
Alarich-Weiss-Str. 2, 64287 Darmstadt, Germany  
E-mail: anke.weidenkaff@iwks.fraunhofer.de

 The ORCID identification number(s) for the author(s) of this article can be found under <https://doi.org/10.1002/adfm.202105702>.

© 2021 The Authors. Advanced Functional Materials published by Wiley-VCH GmbH. This is an open access article under the terms of the Creative Commons Attribution-NonCommercial License, which permits use, distribution and reproduction in any medium, provided the original work is properly cited and is not used for commercial purposes.

DOI: 10.1002/adfm.202105702

C. Li, J. Sunarso  
Research Centre for Sustainable Technologies  
Faculty of Engineering  
Computing and Science  
Swinburne University of Technology  
Jalan Simpang Tiga, Kuching, Sarawak 93350, Malaysia  
E-mail: jsunarso@swinburne.edu.my

S. Liu  
State Key Laboratory of Organic-Inorganic Composites  
College of Chemical Engineering  
Beijing University of Chemical Technology  
Beijing 100029, China  
E-mail: liushaomin@mail.buct.edu.cn

X. Zhu, W. Yang  
State Key Laboratory of Catalysis  
Dalian Institute of Chemical Physics  
Chinese Academy of Sciences  
457 Zhongshan Road, Dalian 116023, China  
E-mail: zhuxf@dicp.ac.cn

X. Zhu, W. Yang  
University of Chinese Academy of Sciences  
Beijing 100049, China

utilization of green energy to which energy storage and environmental issues are directly related.

This roadmap outlines and examines the most important topics as illustrated in **Figure 1** that cut across the recently emerging research fields using MIEC membranes including H<sub>2</sub> production, O<sub>2</sub> production, solar-driven evaporation and energy-saving,

---

K. Huang

Department of Mechanical Engineering  
University of South Carolina  
Columbia, SC 29208, USA  
E-mail: huang46@cec.sc.edu

X.-Y. Wu

Department of Mechanical and Mechatronics Engineering  
University of Waterloo  
200 University Ave W, Waterloo, ON N2L 3G1, Canada  
E-mail: xiaoyu.wu@uwaterloo.ca

A. F. Ghoniem

Department of Mechanical Engineering  
Massachusetts Institute of Technology  
77 Massachusetts Avenue, Cambridge, MA 02139, USA

J. Xue

School of Chemistry and Chemical Engineering  
Guangdong Provincial Key Lab of Green Chemical Product Technology  
South China University of Technology  
Guangzhou 510640, China  
E-mail: xuejian@scut.edu.cn

H. Wang

Department of Chemical Engineering  
Beijing Key Laboratory of Membrane Materials and Engineering  
Tsinghua University  
Beijing 100084, China  
E-mail: cehhwang@tsinghua.edu.cn

Z. Shao

Western Australia School of Mines: Minerals  
Energy and Chemical Engineering  
Curtin University  
Perth, WA 6102, Australia

Z. Shao

College of Chemical Engineering  
Nanjing Tech University  
Nanjing 210009, China  
E-mail: shaozp@njtech.edu.cn

J. H. Duffy, K. S. Brinkman

Department of Materials Science and Engineering  
Clemson University  
Clemson, SC 29634, USA  
E-mail: ksbrink@clemson.edu

X. Tan

State Key Laboratory of Separation Membranes and Membrane Processes  
Department of Chemical Engineering  
Tianjin Polytechnic University  
Tianjin 300387, China

Y. Zhang, H. Jiang

Qingdao Institute of Bioenergy and Bioprocess Technology  
Chinese Academy of Sciences  
Qingdao, Shandong 266101, China  
E-mail: jianghq@qibebt.ac.cn

R. Costa, K. A. Friedrich

German Aerospace Center (DLR)  
Institute of Engineering Thermodynamics  
Pfaffenwaldring 38–40, D-70569 Stuttgart, Germany  
E-mail: remi.costa@dlr.de

R. Krieger

Fraunhofer Institut für Keramische Technologien und Systeme IKTS  
Michael-Faraday-Str. 1, 07629 Hermsdorf, Germany  
E-mail: ralf.krieger@ikts.fraunhofer.de

cathode development for solid oxide fuel cells (SOFCs), modeling of oxygen transport through MIEC membranes, CO<sub>2</sub> reduction, H<sub>2</sub> separation, membrane reactors for production of chemicals, CO<sub>2</sub> separation, electrolyzer cells for power-to-X technologies. The progress on the commercialization of MIEC membrane technology is particularly highlighted. The roadmap involving multi-disciplinary research fields, presented by various global experts in their fields, is intended to give an overview on the status and breakthroughs of this evolving and growing interdisciplinary field and provide insights into the challenges driven by the research needs (such as material and reactor systems development) and opportunities in the diverse and rich field of using MIEC membranes. There is no doubt that MIEC membranes will play a vital role in various energy conversion and storage applications. We hope the roadmap may serve as a bridge for scientists entering the MIEC membranes field. It may also be helpful to those who want to discover the amazing potential of MIEC membranes. The topics presented in this Roadmap have been grouped into 12 sections, ranging from basics and practical applications to commercialization, covering the key interdisciplinary areas.

## 2. MIEC Membranes for Oxygen Separation

### 2.1. Status

As one of the most important chemicals produced globally, oxygen has been utilized in many environmental and industrial processes, such as production of chemicals, waste disposal and medical treatments. With the fast development of oxygen-related applications, O<sub>2</sub> is facing ever-increasing demands. Currently, the cryogenic distillation technology as the commercialized method for O<sub>2</sub> production encounters many challenges because of the high production costs and energy consumption. Against the background of severe environmental pollution issues, searching for alternative approach to reduce the energy consumption for O<sub>2</sub> production and environmental impacts is becoming urgent. Recently, MIEC membranes have attracted increasing attention from industrial and academic communities. Theoretically, these membranes can separate oxygen with 100% permeation selectivity and they offer a cost-effective and simplified way for O<sub>2</sub> production.<sup>[1–3]</sup> The revolutionary method based on MIEC membranes can decrease ≈60% energy consumption and reduce remarkably the production costs by ≈35% in comparison with the current cryogenic technology.<sup>[4]</sup> In addition to the application for O<sub>2</sub> separation, MIEC membranes are becoming increasingly interesting for membrane reactors for the production of chemicals (more details can be found in Section 10).<sup>[5,6]</sup> Oxygen permeable membranes have been intensively investigated in the past decades and can be generally grouped into two types: single-phase and dual-phase (see **Figure 2**).<sup>[1,2,15–24,7,25–34,8,35–38,9–14]</sup> Currently, Ba-, Sr-, or Co-containing single-phase perovskite-type oxygen-transporting membranes (OTMs) with a general formula of ABO<sub>3</sub> show high oxygen permeation and generally have an oxygen permeation flux of more than 1 mL min<sup>-1</sup> cm<sup>-2</sup> at 1173 K for a 1 mm-thick membrane.<sup>[1,2]</sup> However, these OTMs have a poor stability in the presence of CO<sub>2</sub> due to the formation of carbonates. Their practical applications still face many challenges such as poor

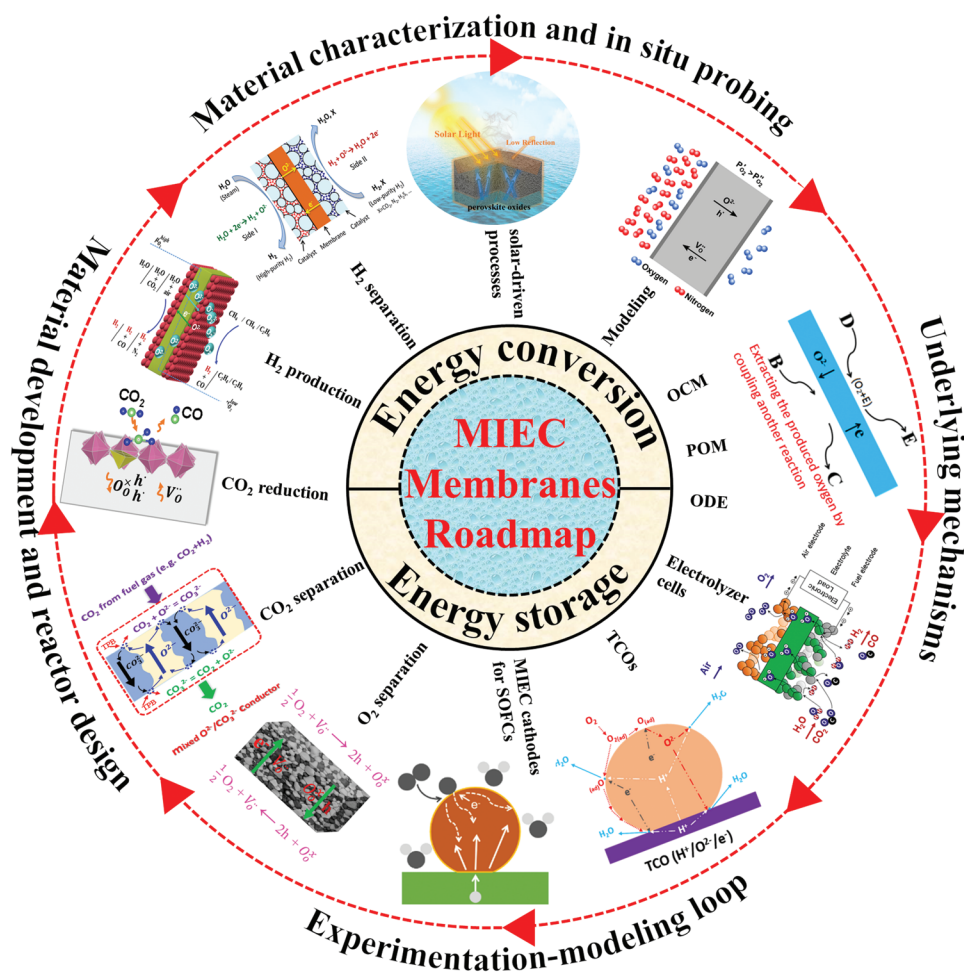


Figure 1. Research topics of MIEC membranes covered in this roadmap.

long-term stability, unsatisfactory mechanical strength and low chemical stability. An attractive alternative to perovskite is single-phase  $K_2NiF_4$ -type (Ruddlesden-Popper phase) membrane, which has shown to be completely  $CO_2$  tolerant during long-term stability tests under  $CO_2$  atmosphere.<sup>[2,7–9,33,34]</sup> Similarly, dual-phase membranes have also displayed high  $CO_2$  resistance after long-term  $CO_2$  exposure. No formation of carbonate or phase change are noticed. Although the  $CO_2$  tolerance is significantly improved for  $K_2NiF_4$ -type and dual-phase membranes, their oxygen permeability is much lower compared to perovskite-type OTMs. The obvious trade-off between oxygen permeation flux and  $CO_2$  tolerance limits the applicability of OTMs for oxygen separation.

## 2.2. Recent Advances and Future Challenges

Designing cost-effective MIEC membranes with good chemical stability and high  $O_2$  permeation flux are still the main goal to be pursued. Intensive scientific research has been devoted to the development of perovskite-type oxygen permeable membranes with selecting suitable A- and B-site cations carefully to address the low chemical stability issue under a harsh gas atmosphere such as  $CO_2$ .<sup>[1,2,10–12]</sup> Development of protective layers on the surface of membranes is currently used as an

effective approach to enhance the  $CO_2$  resistance of the single-phase perovskite-type membranes.<sup>[2,13]</sup> Coating a  $CO_2$ -resistant layer on the membrane surfaces can be achieved by several methods including chemical vapor deposition, spray pyrolysis, spin coating, physical vapor deposition, and plasma spraying.<sup>[2]</sup> Good ionic conductivity, high chemical and mechanical stability in  $CO_2$  atmosphere at high temperature and good compatibility with the protected membrane is requested for an ideal protective layer material.<sup>[2,13]</sup> Complete substitution of alkaline-earth cations Sr or Ba by rare-earth cations and reduction of cobalt content in the single-phase perovskite-type membranes is another strategy to effectively improve the  $CO_2$  resistance. Although many efforts have been devoted to the oxygen permeation performance, deterioration is inevitable under pure  $CO_2$  atmosphere. Recently, focus has been set on the design of dual-phase and  $K_2NiF_4$ -type membranes with inherently excellent phase stability and chemical stability since consistent performance for thousands of hours or more requiring for practical applications. The concept of a dual-phase membrane is an interpenetrating network of an electron conductor (EC) and an ion conductor (IC). Historically, noble metals were chosen as EC in first approaches. Later, oxide phases were chosen as EC. Oxygen incorporation and oxygen release are limited to triple-phase boundaries (gas phase/IC/EC). To overcome this limitation, Fang et al. have combined two MIEC



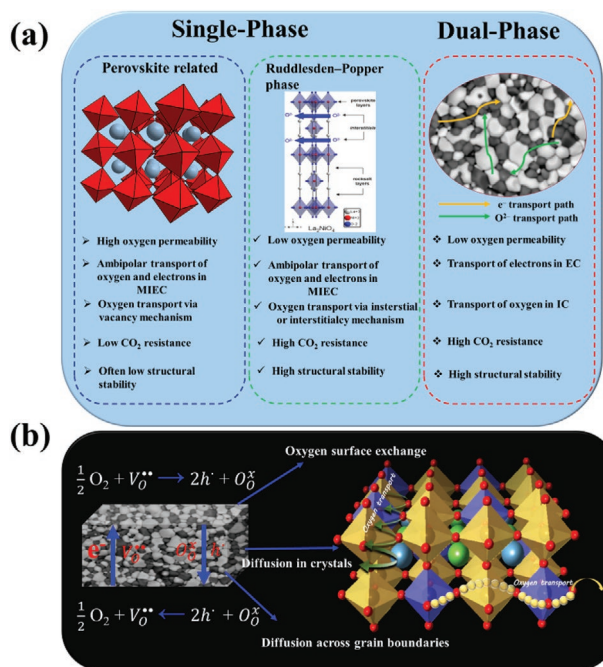


**Figure 2.** a) The Major types of MIEC membranes used for oxygen separation and b) Schematic representation of the oxygen permeation process mechanism. Crystal structure of the La<sub>2</sub>NiO<sub>4+δ</sub> material (Ruddlesden-Popper-phase). Reproduced with permission.<sup>[33]</sup> Copyright 2011, Elsevier.

conductors with different transfer numbers to a dual-phase membrane.<sup>[16]</sup> High performance of the dual-phase membranes consisting mixed ionic electronic conductors and ionic conductors has been obtained in the literature through optimization of the critical factors including phase ratio, grain size, conductivity, phase composition, phase distribution and gas–solid interfaces.<sup>[1,14,36–38,15–18,29–31,35]</sup> Coating a catalyst layer or surface modifications on CO<sub>2</sub> resistant dual-phase and K<sub>2</sub>NiF<sub>4</sub>-type membranes can largely enhance the surface exchange kinetics resulting in the improvement of the oxygen permeability.<sup>[1,2,9]</sup> Still, these membranes have much lower oxygen permeability than perovskite-type oxygen permeable membranes despite having better chemical and phase stability. It is challenging to achieve high oxygen permeation flux and good chemical stability at the same time. The improvement in one property is often on the price of sacrificing the other. Decreasing the membrane thickness or optimizing the membrane configuration can be an alternative way that does not induce such a trade-off. Often, disk- and tube-shaped membrane configurations are explored, but their performance is limited by small surface area and thick wall as well as sealing and connection issues. In contrast, the configuration of hollow-fiber membrane comes with a large surface area and has an asymmetric structure with a thin wall. The hollow-fiber membranes typically have 0.1–0.3 mm wall thicknesses and 1–2 mm outer diameters (with a hollow space inside). This configuration is considered as the most promising and practical one to improve O<sub>2</sub> permeation flux<sup>[2,6,19,20,24–27,32]</sup> and it is also widely used for other applications such as CO<sub>2</sub> conversion and H<sub>2</sub> production (details can be found in the following Sections 4–7 and Section 10). Hollow-fiber membranes, which enable to achieve high oxygen permeability, are getting increasingly interesting and they

have been intensively studied in recent years.<sup>[1,2,34,6,19,20,24–27,32]</sup> Table 1 shows the performance comparison of various MIEC membranes recently reported in literature. The membranes with hollow-fiber configuration exhibited the most excellent oxygen permeability and stability, which should be a promising direction to be pursued in future. Recently, a perovskite-type hollow-fiber membrane with nineteen channels was successfully prepared, which remarkably improved the O<sub>2</sub> permeation due to the creation of different paths for oxygen transport.<sup>[19]</sup> Hollow-fiber perovskite membranes with wrinkled surface were also developed, considered as a promising catalyst carrier.<sup>[20]</sup> The oxygen permeation flux of the wrinkled hollow-fiber membrane is significantly improved by a factor of 3 compared to the oxygen permeation flux of the hollow-fiber membrane without wrinkles.<sup>[20]</sup> All these innovation methods make hollow-fiber membranes possess greater reliability, economic and scaling-up potentials for oxygen production and membrane reactor applications. Toward commercialization of MIEC membranes for oxygen production, Nauels et al. recently make a big step through the design and development of a membrane module for pilot-scale systems.<sup>[22]</sup> A membrane module containing total 596 tubular Ba<sub>0.5</sub>Sr<sub>0.5</sub>Co<sub>0.8</sub>Fe<sub>0.2</sub>O<sub>3–δ</sub> membranes was developed and performed under various conditions. A maximum continuous operational time of 1800 h was obtained.<sup>[22]</sup> It should be pointed out that membrane breakages and leakage occurred during the tests result in a maximum oxygen purity of 98.9%. A huge improvement is highly needed to address these issues in future. Although many advancements have been achieved recently, various challenges remain. Acceptable oxygen permeation flux, good chemical and phase stability, and satisfactory mechanical strength at reduced atmosphere for a long operational period at high temperature are still the goal to be pursued. In real application scenarios for O<sub>2</sub> production, the separation membranes may suffer significant degradation in the permeation flux regarding exposing to very low concentrations of oil vapors from the compressed air.<sup>[12]</sup> However, the studies in the presence of such heavy organics have been overlooked and rarely investigated. In addition, an important factor should be paid attention is that such synthesized membranes should have low material costs and fulfil the current production equipment to realize their commercialization.

### 2.3. Opportunities

Despite many improvements have been obtained, there are still many avenues and opportunities for improvements on using MIEC membranes for O<sub>2</sub> separation. Due to the obvious trade-off between CO<sub>2</sub> tolerance and oxygen permeation observed in numerous studies,<sup>[1,2]</sup> achieving simultaneously high CO<sub>2</sub> resistance and excellent oxygen permeation flux seems a big challenge. Improving the oxygen permeability of CO<sub>2</sub>-tolerant MIEC oxygen-transporting membranes with low permeation flux seems more realistic via engineering approaches and application of the internal (external) electronic short-circuit methods.<sup>[2]</sup> The most promising directions concerning long-term stability, economic feasibility, fundamental understanding and material development are proposed as follows:

**Materials Development:** The development of new dual-phase and K<sub>2</sub>NiF<sub>4</sub>-type membrane materials are highly desirable by

**Table 1.** Summary of the oxygen permeation fluxes of various MIEC membranes recently reported in literature.

Sample	$J(\text{O}_2)^{\text{a}}$ [mL min <sup>-1</sup> cm <sup>-2</sup> ]	$J(\text{O}_2)^{\text{b}}$ [mL min <sup>-1</sup> cm <sup>-2</sup> ]	$d$ [mm]	$T$ [K]	$J(\text{O}_2)^{\text{b}}$ Stability [h]	Type	Configurations	Ref.
Pr <sub>0.5</sub> Sr <sub>0.5</sub> Cu <sub>0.2</sub> Fe <sub>0.8</sub> O <sub>3-δ</sub>	0.4	0.16	1.4	1173	100	Perovskite	Disk	[23]
La <sub>0.6</sub> Sr <sub>0.4</sub> Co <sub>0.2</sub> Fe <sub>0.8</sub> O <sub>3-δ</sub>	1.87	–	0.052	1223	–	Perovskite	6-channel Hollow fiber	[24]
La <sub>0.6</sub> Ca <sub>0.4</sub> Co <sub>0.8</sub> Fe <sub>0.2</sub> O <sub>3-δ</sub>	–	2.28	0.081	1173	–	Perovskite	Hollow fiber	[25]
Ba <sub>0.5</sub> Sr <sub>0.5</sub> Co <sub>0.8</sub> Fe <sub>0.2</sub> O <sub>3-δ</sub>	8.85	–	–	1173	–	Perovskite	19-channel Hollow fiber	[19]
(La <sub>0.9</sub> Ca <sub>0.1</sub> ) <sub>2</sub> (Ni <sub>0.75</sub> Cu <sub>0.25</sub> )O <sub>4+δ</sub>	0.65	0.63	0.65	1173	–	K <sub>2</sub> NiF <sub>4</sub>	Disk	[8]
(Pr <sub>0.9</sub> La <sub>0.1</sub> ) <sub>1.9</sub> Ni <sub>0.74</sub> Cu <sub>0.21</sub> Ga <sub>0.05</sub> O <sub>4+δ</sub> -both side coated La <sub>0.6</sub> Sr <sub>0.4</sub> CoO <sub>3</sub>	0.9	–	0.6	1173	–	K <sub>2</sub> NiF <sub>4</sub>	Disk	[9]
La <sub>2</sub> Ni <sub>0.95</sub> Mo <sub>0.05</sub> O <sub>4+δ</sub>	2.88	2.75	–	1225	185	K <sub>2</sub> NiF <sub>4</sub>	Hollow fiber	[34]
40 wt% Ce <sub>0.9</sub> Gd <sub>0.1</sub> O <sub>2-δ</sub> –60 wt% La <sub>2</sub> NiO <sub>4+δ</sub>	1.55	1.31	0.235	1223	5	Dual-phase	Hollow fiber	[26]
La <sub>0.6</sub> Sr <sub>0.4</sub> Co <sub>0.2</sub> Fe <sub>0.8</sub> O <sub>3-δ</sub> (La <sub>0.5</sub> Sr <sub>0.5</sub> ) <sub>2</sub> CoO <sub>4+δ</sub>	3.2	2.6	–	1173	100	Dual-phase <sup>c)</sup>	Hollow fiber	[27]
75 wt% Ce <sub>0.85</sub> Sm <sub>0.15</sub> O <sub>1.925</sub> – 25 wt%Sm <sub>0.6</sub> Sr <sub>0.4</sub> Al <sub>0.3</sub> Fe <sub>0.7</sub> O <sub>3-δ</sub>	1.03	0.915	≈0.32	1223	56	Dual-phase	Hollow fiber	[32]
75 wt% Ce <sub>0.85</sub> Gd <sub>0.1</sub> Cu <sub>0.05</sub> O <sub>2-δ</sub> – 25 wt% La <sub>0.6</sub> Ca <sub>0.4</sub> FeO <sub>3-δ</sub>	0.87	0.7	0.5	1223	–	Dual-phase	Disk	[16]
60 wt% Ce <sub>0.9</sub> Nd <sub>0.1</sub> O <sub>2-δ</sub> – 40 wt%Nd <sub>0.6</sub> Sr <sub>0.4</sub> CoO <sub>3-δ</sub>	0.65	0.55	0.6	1223	150	Dual-phase	Disk	[17]
60 wt% Ce <sub>0.8</sub> Sm <sub>0.2</sub> O <sub>2-δ</sub> –40 wt% Sm <sub>0.3</sub> Sr <sub>0.7</sub> Cu <sub>0.2</sub> Fe <sub>0.8</sub> O <sub>3-δ</sub>	0.84	0.7	0.6	1223	400	Dual-phase	Disk	[18]
70 vol% Zr <sub>0.79</sub> Sc <sub>0.2</sub> Ce <sub>0.01</sub> O <sub>2-δ</sub> – 30 vol% La <sub>0.7</sub> Sr <sub>0.3</sub> MnO <sub>3-δ</sub> – coated Nd <sub>2</sub> NiO <sub>4+δ</sub>	1.65	≈ 1.4	0.05	1173	–	Dual-phase	Disk	[28]
40 wt% Ce <sub>0.9</sub> Pr <sub>0.1</sub> O <sub>2-δ</sub> –60 wt% Nd <sub>0.5</sub> Sr <sub>0.5</sub> Fe <sub>0.9</sub> Cu <sub>0.1</sub> O <sub>3-δ</sub>	0.97	0.32	0.6	1223	70	Dual-phase	Disk	[29]
30 wt% La <sub>0.15</sub> Sr <sub>0.85</sub> FeO <sub>3-δ</sub> – 70 wt% La <sub>0.15</sub> Ce <sub>0.8</sub> Cu <sub>0.05</sub> O <sub>2-δ</sub>	0.45	0.27	0.6	1173	100	Dual-phase	Disk	[30]
60 wt% Ce <sub>0.8</sub> Sm <sub>0.2</sub> O <sub>2-δ</sub> –40 wt% Sm <sub>0.3</sub> Sr <sub>0.7</sub> Cu <sub>0.2</sub> Fe <sub>0.8</sub> O <sub>3-δ</sub>	1.01	0.7	0.6	1223	50	Dual-phase	Disk	[31]
60 wt% Ce <sub>0.9</sub> Pr <sub>0.1</sub> O <sub>2-δ</sub> –40 wt% Pr <sub>0.6</sub> Ca <sub>0.4</sub> FeO <sub>3-δ</sub>	0.53	0.25	0.6	1273	40	Dual-phase	Disk	[36]

<sup>a)</sup>under air/He or air/Ar gradient; <sup>b)</sup>under air/CO<sub>2</sub> gradient; <sup>c)</sup>Perovskite/Ruddlesden-Popper composite system.

optimizing the preparation approaches and microstructures. Focus should be set on the design and development of oxygen exchange catalysts with high stability, which could largely improve the oxygen permeability of the CO<sub>2</sub>-resistant membranes. Using non-critical earth-abundant materials during the MIEC material development should be considered. Sustainable methods for the material productions are also desired to reduce waste.

**Engineering Approach:** The amount of investigations addressing membrane configurations is relatively limited.<sup>[19,20]</sup> Many improvements associated with the configurations pose many opportunities ahead. The introduction of advanced manufacture techniques (for example, 3D printing) may provide new ways of membrane fabrications. Application and development of the external electronic short-circuit methods for different CO<sub>2</sub> tolerance MIEC membranes should be considered to improve the oxygen permeability. Much more attention should also be paid to the development of current module layout and sealing technology for membranes at high temperature.

**Fundamental Understanding of the Oxygen Permeation Mechanism:** There is a need to improve the understanding of the oxygen transport mechanism via computational simulation and modeling (see Section 3). The mechanisms of oxygen transport

at the gas-solid interfaces and oxygen-ion transport between the ionic conductors and electronic conductors (mixed ionic electronic conductors) especially at the grain boundaries in dual-phase membranes are still not clear. The investigation of this fundamental problems will certainly provide insights into the developments of new MIEC membranes materials and oxygen exchange catalysts (coating materials).

Furthermore, more multidisciplinary research into the combination of MIEC membranes with other novel technologies such as plasma-based technology (plasma spray process for coating, plasma treatment for membrane material modifications and plasma-membrane reactor<sup>[6,39–41]</sup>) is highly desirable to improve the performance of MIEC membranes.

## 2.4. Concluding Remarks

MIEC membranes hold great potential for oxygen production and membrane reactors for production of chemicals. Despite major achieved improvements (more details can be found in Section 13), there are still many research and technological challenges to conquer toward commercialization of

MIEC membranes for oxygen separation. The development of computational simulations and modelling together with developing in situ surface probing techniques will remarkably improve our understanding on oxygen permeation mechanisms and performance degradation mechanisms for facilitating the material design and engineering approaches.

### 3. Modeling of Oxygen Transport through MIEC Membranes

#### 3.1. Status

Modeling represents a powerful complimentary tool to the experimental study, which has been widely used to gain insights on the important oxygen permeation parameters and the transport rate determining steps. Modeling assisted with experimental data validation can be used to simulate the oxygen permeation performance under conditions that are not achievable in normal experimental conditions. Modeling studies thus complement the various experimental breakthroughs to provide further insights on the oxygen transport properties of MIEC membranes and in guiding the development of MIEC membrane module design. This section of the roadmap covers the present status of oxygen permeation modeling, recent advances in the area, future challenges, and opportunities for prospective growth.

Progress in the research of MIEC membranes has seen the development of membrane compositions with high oxygen permeation fluxes such as  $\text{Ba}_{0.5}\text{Sr}_{0.5}\text{Co}_{0.8}\text{Fe}_{0.2}\text{O}_{3-\delta}$  (BSCF) and  $\text{La}_{0.6}\text{Sr}_{0.4}\text{Co}_{0.2}\text{Fe}_{0.8}\text{O}_{3-\delta}$  (LSCF).<sup>[42,43]</sup> Various methods to improve the oxygen permeation fluxes of MIEC membranes include modifying the membrane composition or applying membrane surface decorations.<sup>[44–46]</sup> To obtain further insights on the oxygen permeation mechanism, researchers have developed and utilized various oxygen permeation models to complement the experimental results.<sup>[47]</sup> Based on data obtained from Scopus, these modeling works have traction over the past two decades, producing a steady stream of publications in recent years (Figure 3a).

Oxygen permeates through dense MIEC membranes takes place via the oxygen ionic transfer in one direction and

the simultaneous electronic transfer in the opposite direction (Figure 3b).<sup>[48]</sup> The high temperature oxygen transport in MIEC membranes (above 700 °C) is enabled due to the presence of defects, i.e., oxygen ionic vacancies and/or interstitial oxygen ions, within the membrane crystal lattice.<sup>[49]</sup> The defects facilitate the diffusion of oxygen ions through the membrane, which ultimately contributes to the oxygen ionic conductivity.<sup>[50]</sup> Oxygen vacancies are formed at high temperatures along with the simultaneous reduction of transition metals in the membrane and accordingly, electron transfer.<sup>[51]</sup> Oxygen permeation models through MIEC membranes are generally developed based on the transport of ionic and electronic species through the membrane.<sup>[52]</sup>

Oxygen permeation in MIEC membranes mainly occurs via surface exchange reactions between molecular oxygen and oxygen vacancies on the membrane interfaces and oxygen vacancy diffusion through the membrane bulk. The slowest step limits the oxygen permeation and can be either surface exchange reactions or bulk diffusion. These transport mechanisms form the basis for the initial conceptualization of oxygen permeation models. The Wagner theory (Equation (1)) represents one of the earliest models that was derived based on bulk diffusion as the sole transport mechanism.<sup>[53]</sup> The Wagner theory assumes that a local equilibrium exists between the two charged species of electron and oxygen ion, and a hypothetical neutral species (such as oxygen molecule) in the bulk oxide.

$$J_{\text{O}_2} = \frac{1}{4^2 F^2 L} \int_{\mu_{\text{O}_2(\text{I})}}^{\mu_{\text{O}_2(\text{II})}} t_{\text{ion}} t_e \sigma^{\text{tot}} d\mu_{\text{O}_2} \quad (1)$$

where  $J_{\text{O}_2}$  is oxygen permeation flux ( $\text{mL min}^{-1} \text{cm}^{-2}$ ),  $F$  is Faraday's constant ( $96\,485 \text{ C mol}^{-1}$ ),  $L$  is disk membrane thickness (cm),  $t_{\text{ion}}$  is oxygen ionic transfer number,  $t_e$  is oxygen electronic transfer number,  $\sigma^{\text{tot}}$  is total conductivity ( $\text{S cm}^{-1}$ ), and  $\mu_{\text{O}_2}$  is chemical potential of the hypothetical neutral oxygen in the oxide ( $\text{J mol}^{-1}$ ).

Various authors have developed empirical equations to predict the oxygen permeation fluxes for different limiting cases.<sup>[54–57]</sup> The consideration of surface exchange reactions has led to the introduction of the surface exchange coefficient

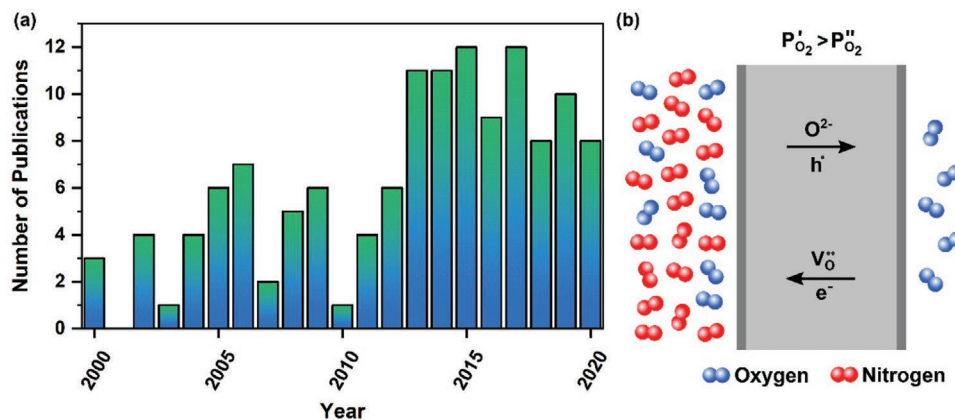
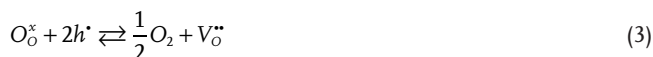


**Figure 3.** a) Trend of oxygen permeation flux modeling-related publications between 2000 and 2020. b) Conceptual figure of oxygen transport through dense MIEC membrane.

or  $k$  to gauge the magnitude of their influence.<sup>[58,59]</sup> The surface exchange reactions on the membrane feed side involve the incorporation of molecular oxygen into the membrane oxygen vacancy to form lattice oxygen along with two electron holes (Equation (2)).<sup>[49]</sup> Lattice oxygen diffuses through the membrane bulk compensated by the flow of electrons in the opposite direction. At the permeate side, the reverse reaction occurs whereby lattice oxygen is converted back to molecular oxygen through recombination with the electron holes and the oxygen vacancy site develops (Equation (3)). In a further effort to differentiate between the surface exchange reactions on the feed and permeate sides, parameters  $k_f$  and  $k_r$  were used to depict the forward and reverse surface exchange reaction rates represented by Equations (2) and (3), respectively. Oxygen permeation flux equations that incorporate  $k_f$  and  $k_r$  are exhibited in Equations (4) and (5) for the membrane feed and permeate sides, respectively.<sup>[49]</sup>



$$J_{O_2} = k_f P_{O_2}^{1/2} C_v' - k_r C_{h_i}'^2 \quad (4)$$

$$J_{O_2} = k_r C_{h_i}''^2 - k_f P_{O_2}^{1/2} C_v'' \quad (5)$$

where  $C$  is the concentration of the species indicated in subscripts and  $P_{O_2}$  is oxygen partial pressure (atm) with superscripts ' indicating the feed side and '' indicating the permeate side of the membrane. The chemical species in Equations (2) to (5) are denoted according to Kröger-Vink notation.

The ratio of the surface exchange kinetics ( $k$ ) to the tracer diffusion coefficient ( $D^*$ ) is defined as the parameter  $h$  in Equation (6). This ratio is considered useful to determine the influence of surface exchange reactions on the oxygen permeation through the membrane. Bouwmeester, Kruidhof, and Burggraaf<sup>[60]</sup> introduced the characteristic thickness,  $L_c$ , which is the inverse of the parameter  $h$  (Equation (6)). If the membrane thickness is significantly larger than the characteristic thickness, the oxygen permeation is mainly limited by bulk diffusion. Likewise, membranes with thicknesses that are significantly lower than the characteristic thickness will have their oxygen permeation limited by surface exchange reactions. It is assumed that the  $L_c$  is only applicable for membranes whereby the surface exchange kinetics are equal on both sides of the membrane, i.e., the oxygen partial pressure difference is small.

$$h = \frac{k}{D^*} = \frac{1}{L_c} \quad (6)$$

The applicability of  $L_c$  is limited in certain experimental situations, i.e., when oxygen exchange kinetics vary on the air and permeate sides (use of argon or methane sweep), and when there is a high drop of oxygen chemical potential on the membrane permeate side. A new criterion inspired by the Biot number,  $B_c$ , was introduced by Geffroy and co-workers<sup>[61,62]</sup> as the ratio of the oxygen chemical potential gradients on the

membrane surface to the bulk volume.  $B_c$  can be evaluated for each membrane surface with Equation (7) and Equation (8) representing the  $B_c$  for the feed and permeate side surfaces, respectively. If  $B_c < 0.5$ , the oxygen transport is mainly bulk diffusion limited, while  $B_c > 1.5$  indicates surface exchange as the main oxygen permeation limiting step. In the case of  $0.5 < B_c < 1.5$ , the oxygen transport is limited by a mixture of bulk diffusion and surface exchange reactions. Other more recent works pertaining to the influence of surface exchange reactions on the oxygen transport mechanism are also highlighted in Geffroy, Blond, Richet, and Chartier.<sup>[3]</sup>

$$B_c' = \frac{\Delta\mu_{O_2}'}{\Delta\mu_{O_2}^{bulk}} \quad (7)$$

$$B_c'' = \frac{\Delta\mu_{O_2}''}{\Delta\mu_{O_2}^{bulk}} \quad (8)$$

where superscript "bulk" indicates the membrane bulk.

### 3.2. Recent Advances and Future Challenges

Progress in the development of oxygen permeation models led to the introduction of more complex models that integrate bulk diffusion and surface exchange reactions, leading to more accurate projection of oxygen permeation fluxes. A notable model is that of Xu and Thomson,<sup>[63]</sup> which was developed based on the surface exchange reactions in Equations (4) and (5) and is illustrated in **Figure 4a**. This model assumes a constant oxygen vacancy diffusion coefficient,  $D_v$  for the steady-state isothermal oxygen bulk diffusion and ideal gas behavior. The oxygen permeation flux equation is derived according to Equation (9).

$$J_{O_2} = \frac{k_r / k_f (P_{O_2}''^{-1/2} - P_{O_2}'^{-1/2})}{(1/k_f P_{O_2}'^{1/2}) + (2L/D_v) + (1/k_r P_{O_2}''^{1/2})} \quad (9)$$

The Xu-Thomson model is applicable for single-phase MIEC disk membranes such as LSCF and  $La_{0.4}Sr_{0.6}CoO_{3-\delta}$ .<sup>[63,65]</sup> A similar model based on surface exchange reactions was developed by Li, Jin, Xu, and Shi,<sup>[66]</sup> with the driving force expressed in terms of the oxygen vacancy concentration difference across the membrane instead of the oxygen partial pressure difference (Equation (10)).

$$J_{O_2} = \frac{C_{v,s}'' - C_{v,s}'}{(1/k_a) + (2L/D_v) + (1/k_d)} \quad (10)$$

where  $C_{v,s}$  is the concentration of oxygen vacancy on the membrane surface.  $k_a$  and  $k_d$  are the adsorption and desorption rate constants, respectively, as reported by Zeng and Lin.<sup>[67]</sup>

Further advancements to the Xu-Thomson model were performed by Tan and Li<sup>[68]</sup> who adapted the Xu-Thomson model simulate the oxygen permeation in hollow fiber membranes (Figure 4b). The Tan-Li model assumes only the radial transport of charged defects takes place in plug flow conditions with negligible axial dispersion axial transport. The adaptation by



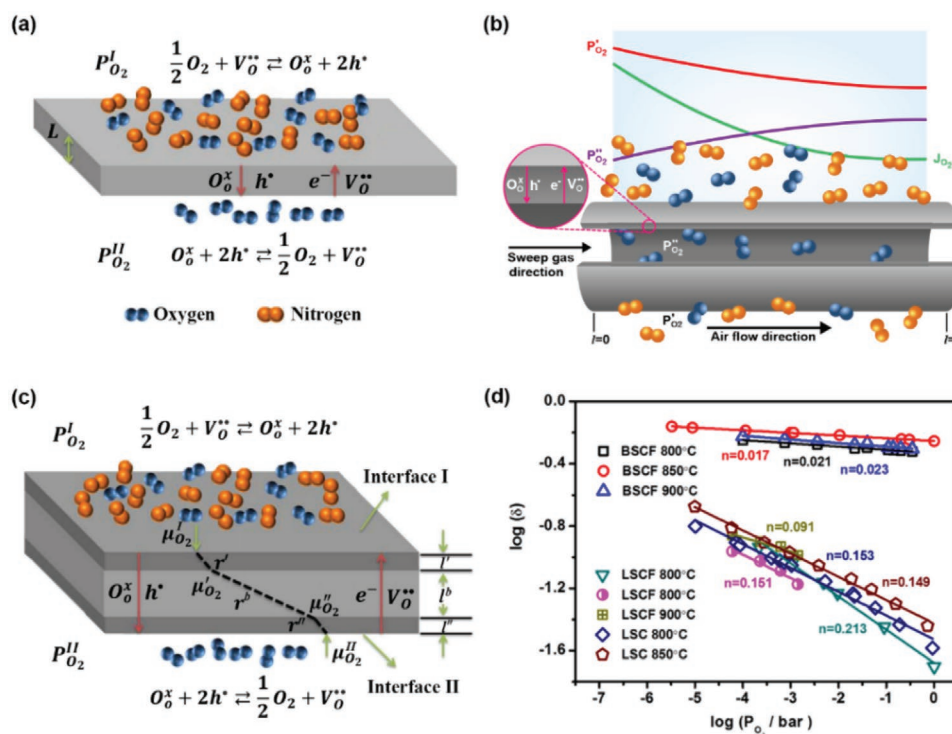


**Figure 4.** Conceptual diagram of a) oxygen transport through disk membrane according to Xu-Thomson model,<sup>[64]</sup> b) oxygen permeation process through hollow fiber membrane according to Tan-Li model in co-current configuration with variation in oxygen partial pressures in feed and permeate sides and oxygen flux along the fiber length, c) oxygen transport according to Zhu model,<sup>[64]</sup> d) Variation in oxygen nonstoichiometry of various disk membrane compositions according to changes in oxygen partial pressure.<sup>[64]</sup> Reproduced with permission.<sup>[64]</sup> Copyright 2017, John Wiley and Sons.

Tan and Li<sup>[68]</sup> is exhibited in Equation (11). In another work, Tan et al.<sup>[69]</sup> specified material balances and boundary conditions to enable the extension of Equation (11) according to different hollow fiber oxygen permeation operating modes that include different feed gas flow positions (directed into the hollow fiber shell or lumen), flow orientations (co-current or counter-current flow) and permeate side conditions (use of inert sweep gas or vacuum operation).

$$dN_{O_2} = \frac{k_r(P'_{O_2}{}^{1/2} - P''_{O_2}{}^{1/2})}{\frac{k_f \ln(R_o / R_{in}) P'_{O_2}{}^{1/2} P''_{O_2}{}^{1/2}}{\pi D_p} + \frac{P'_{O_2}{}^{1/2}}{2\pi R_{in}} + \frac{P''_{O_2}{}^{1/2}}{2\pi R_o}} dl \quad (11)$$

where  $N_{O_2}$  is oxygen molar flow rate ( $\text{mol s}^{-1}$ ),  $R_o$  is outer radius of hollow fiber (cm), and  $R_{in}$  is inner radius of hollow fiber (cm).

Liu, Tan, Shao and Diniz da Costa<sup>[70]</sup> proposed a surface reaction limited version of the Tan-Li model. In this version of the model, it is assumed that the membrane is significantly thin and that the surface exchange reactions are the main oxygen permeation limiting mechanism (Equation (12)). Since the bulk membrane properties are not considered in this model, the model applicability can be extended to materials other than LSCF as listed in Table 2.

$$dN_{O_2} = \frac{k_r(P'_{O_2}{}^{1/2} - P''_{O_2}{}^{1/2})}{\frac{P'_{O_2}{}^{1/2}}{2\pi R_{in}} + \frac{P''_{O_2}{}^{1/2}}{2\pi R_o}} dl \quad (12)$$

Another notable model for disk membranes was conceptualized by Zhu, Liu, Cong and Yang,<sup>[71]</sup> which features the distribution of resistances from the membrane surface reactions and bulk (Figure 4c). Besides assuming elementary reactions and isothermal conditions, other model assumptions include constant transport properties of electrons, oxygen ions, oxygen vacancies and electron holes, and negligible diffusion resistance or concentration polarization resistance on the membrane interfaces. The oxygen permeation flux model (Equation (13)) is expressed as a function of the sum of resistances contributed from the individual membrane “layers” (Equation (14)).

$$J_{O_2} = \frac{RT}{4^2 F^2} \frac{1}{r^{tot}} \ln \frac{P''_{O_2}}{P'_{O_2}} \quad (13)$$

$$r^{tot} = r' + r^b + r'' \quad (14)$$

where  $R$  is gas constant ( $\text{J mol}^{-1} \text{K}^{-1}$ ),  $T$  is temperature (K), and  $r$  is resistance ( $\Omega \text{m}^2$ ). Subscripts “tot” and “b” indicate total and membrane bulk, respectively.

In a comparison of the disk membrane models, Zhu, Li, Liu, Zhu, and Yang<sup>[64]</sup> reported that the Xu-Thomson model is more suited for membranes with oxygen vacancy concentrations that vary widely with changes in oxygen partial pressure. Conversely, the Zhu model is more suited for membranes whose oxygen concentration are independent of changes in oxygen partial pressure. The oxygen nonstoichiometry ( $\delta$ ) or oxygen vacancy concentration of several characteristic membrane compositions such as BSCF, LSCF, and  $\text{La}_{0.7}\text{Sr}_{0.3}\text{CoO}_{3-\delta}$  (LSC) is displayed in Figure 4d along with their dependence on the



**Table 2.** Summary of different membrane compositions and corresponding simulation conditions used in different models.

Membrane composition	Membrane geometry	Membrane thickness <sup>a)</sup>	Oxygen permeation conditions	Ref.
Xu-Thomson model				
La <sub>0.6</sub> Sr <sub>0.4</sub> Co <sub>0.2</sub> Fe <sub>0.8</sub> O <sub>3-δ</sub> (LSCF)	Disk	3.99 mm	T: 750–950 °C; P <sub>O<sub>2</sub></sub> : 0.21–1 atm; P <sub>O<sub>2</sub></sub> '': 4.6 × 10 <sup>-4</sup> –2.3 × 10 <sup>-3</sup> atm;	[63]
La <sub>0.6</sub> Sr <sub>0.4</sub> Co <sub>0.2</sub> Fe <sub>0.8</sub> O <sub>3-δ</sub> (LSCF)	Disk	3.99 mm	T: 750–950 °C; P <sub>O<sub>2</sub></sub> : 0.21–1 atm; P <sub>O<sub>2</sub></sub> '': 4.6 × 10 <sup>-4</sup> –2.3 × 10 <sup>-3</sup> atm;	[80]
BaCo <sub>0.4</sub> Fe <sub>0.4</sub> Zr <sub>0.2</sub> O <sub>3-δ</sub> (BCFZ)	Hollow fiber	0.37 mm; ID: 3.06 mm; OD: 3.80 mm	T: 850–950 °C; P <sub>O<sub>2</sub></sub> : 0.21 atm; Sweep gas flow rate: 75–600 mL min <sup>-1</sup>	[81]
Li model				
La <sub>0.2</sub> Sr <sub>0.8</sub> Co <sub>0.2</sub> Fe <sub>0.8</sub> O <sub>3-δ</sub> (LSCF)	Disk	2 mm	T: 850 °C; P <sub>O<sub>2</sub></sub> : 0.21 atm; P <sub>O<sub>2</sub></sub> '': 2.0 × 10 <sup>-4</sup> –9.0 × 10 <sup>-3</sup> atm;	[66]
La <sub>0.6</sub> Sr <sub>0.4</sub> Co <sub>0.2</sub> Fe <sub>0.8</sub> O <sub>3-δ</sub> (LSCF)	Tubular	1.5 mm; ID: 5 mm; OD: 8 mm	T: 850 °C; P <sub>O<sub>2</sub></sub> : 0.21 atm; P <sub>O<sub>2</sub></sub> '': 2.0 × 10 <sup>-3</sup> –2.5 × 10 <sup>-2</sup> atm;	[82]
Tan-Li model (Surface reaction limited)				
Ba <sub>0.5</sub> Sr <sub>0.5</sub> Co <sub>0.8</sub> Fe <sub>0.2</sub> O <sub>3-δ</sub> (BSCF)	Hollow fiber	0.21 mm; ID: 0.99 mm; OD: 1.41 mm	T: 550–950 °C; Air feed flow rate: 300 mL min <sup>-1</sup> ; Sweep gas flow rate: 0.01–0.111 mmol s <sup>-1</sup>	[70]
La <sub>0.6</sub> Sr <sub>0.4</sub> Co <sub>0.2</sub> Fe <sub>0.8</sub> O <sub>3-δ</sub> (LSCF)	Hollow fiber	0.31 mm; ID: 1.25 mm; OD: 1.87 mm	T: 650–1000 °C; Air feed flow rate: 180 mL min <sup>-1</sup> ; Sweep gas flow rate: 15–52 mL min <sup>-1</sup>	[83]
SrCo <sub>0.9</sub> Sc <sub>0.1</sub> O <sub>3-δ</sub> (SCSc)	Hollow fiber	0.24 mm; ID: 1.24 mm; OD: 1.72 mm	T: 500–800 °C; Air feed flow rate: 200 mL min <sup>-1</sup> ; Sweep gas flow rate: 15–75 mL min <sup>-1</sup>	[84]
Ba <sub>0.5</sub> Sr <sub>0.5</sub> Co <sub>0.75</sub> Zr <sub>0.05</sub> Fe <sub>0.2</sub> O <sub>3-δ</sub> (BSCZ <sub>0.05</sub> F)	Hollow fiber	0.28 mm; ID: 1.01 mm; OD: 1.57 mm	T: 700–950 °C; Air feed flow rate: 0.134 mmol s <sup>-1</sup> ; Sweep gas flow rate: 0.02–0.165 mmol s <sup>-1</sup>	[85]
Ba <sub>0.5</sub> Sr <sub>0.5</sub> Co <sub>0.7</sub> Zr <sub>0.1</sub> Fe <sub>0.2</sub> O <sub>3-δ</sub> (BSCZ <sub>0.1</sub> F)	Hollow fiber	0.28 mm; ID: 1.01 mm; OD: 1.57 mm	T: 700–950 °C; Air feed flow rate: 0.134 mmol s <sup>-1</sup> ; Sweep gas flow rate: 0.02–0.165 mmol s <sup>-1</sup>	[85]
Ba <sub>0.5</sub> Sr <sub>0.5</sub> Co <sub>0.6</sub> Zr <sub>0.2</sub> Fe <sub>0.2</sub> O <sub>3-δ</sub> (BSCZ <sub>0.2</sub> F)	Hollow fiber	0.28 mm; ID: 1.01 mm; OD: 1.57 mm	T: 700–950 °C; Air feed flow rate: 0.134 mmol s <sup>-1</sup> ; Sweep gas flow rate: 0.02–0.165 mmol s <sup>-1</sup>	[85]
BaCo <sub>0.85</sub> Bi <sub>0.05</sub> Zr <sub>0.1</sub> O <sub>3-δ</sub> (BCBZ)	Hollow fiber	0.4 mm; ID: 0.8 mm; OD: 1.6 mm	T: 750–950 °C; Air feed flow rate: 200 cm <sup>3</sup> min <sup>-1</sup> ; Sweep gas flow rate: 30–150 cm <sup>3</sup> min <sup>-1</sup>	[86]
Zhu model				
Ba <sub>0.5</sub> Sr <sub>0.5</sub> Co <sub>0.8</sub> Fe <sub>0.2</sub> O <sub>3-δ</sub> (BSCF)	Disk	0.5, 1.0 mm	T: 680–940 °C; P <sub>O<sub>2</sub></sub> : 0.07–0.40 bar; P <sub>O<sub>2</sub></sub> '': 0.005–0.050 bar;	[71]
Ba <sub>0.5</sub> Sr <sub>0.5</sub> Co <sub>0.8</sub> Fe <sub>0.2</sub> O <sub>3-δ</sub> (BSCF) with ≈20 μm-thick Sm <sub>0.5</sub> Sr <sub>0.5</sub> CoO <sub>3-δ</sub> (SSC) porous layer on both sides	Disk	0.5 mm	T: 600–700 °C; P <sub>O<sub>2</sub></sub> : 0.21 bar; P <sub>O<sub>2</sub></sub> '': 0.01 bar;	[87]
BaCe <sub>0.05</sub> Fe <sub>0.95</sub> O <sub>3-δ</sub> (BCF) with 15–20 μm-thick BaCe <sub>0.05</sub> Fe <sub>0.95</sub> O <sub>3-δ</sub> , Ba <sub>0.5</sub> Sr <sub>0.5</sub> Co <sub>0.8</sub> Fe <sub>0.2</sub> O <sub>3-δ</sub> , or Sm <sub>0.5</sub> Sr <sub>0.5</sub> CoO <sub>3-δ</sub> porous layer on both sides	Disk	0.5 mm	T: 750–950 °C; P <sub>O<sub>2</sub></sub> : 0.1–0.4 bar; P <sub>O<sub>2</sub></sub> '': 0.009–0.060 bar;	[88]
80 wt% Ce <sub>0.9</sub> Gd <sub>0.1</sub> O <sub>2-δ</sub> –20 wt% SrCo <sub>0.8</sub> Fe <sub>0.1</sub> Nb <sub>0.1</sub> O <sub>3-δ</sub> (GDC-SCFN) with ≈10 μm-thick SDC-SCFN porous layer on the permeate side	Disk	0.6, 1.0 mm	T: 800–950 °C; P <sub>O<sub>2</sub></sub> : 0.2–0.9 bar; P <sub>O<sub>2</sub></sub> '': 0.005–0.010 bar;	[89]

**Table 2.** Continued.

Membrane composition	Membrane geometry	Membrane thickness <sup>a)</sup>	Oxygen permeation conditions	Ref.
80 vol% Ce <sub>0.9</sub> Gd <sub>0.1</sub> O <sub>2-δ</sub> -20 vol% La <sub>0.7</sub> Sr <sub>0.3</sub> MnO <sub>3±δ</sub> (GDC-LSM) with ≈30 μm-thick La <sub>0.6</sub> Sr <sub>0.4</sub> CoO <sub>3-δ</sub> (LSC) porous layer on both sides	Disk	0.045 mm	T: 850 °C; P' <sub>O<sub>2</sub></sub> : 0.03–0.13 bar; P'' <sub>O<sub>2</sub></sub> : 0.0017–0.0038 bar;	[90]
60 wt% Ce <sub>0.8</sub> Gd <sub>0.2</sub> O <sub>2-δ</sub> -40 wt% Pr <sub>0.6</sub> Sr <sub>0.4</sub> Co <sub>0.5</sub> Fe <sub>0.5</sub> O <sub>3-δ</sub> (GDC-PSCF)	Disk	0.7, 1.0 mm	T: 750–850 °C; P' <sub>O<sub>2</sub></sub> : 0.1–0.9 bar; P'' <sub>O<sub>2</sub></sub> : 0.002–0.03 bar;	[91,92]
60 wt% Ce <sub>0.8</sub> Gd <sub>0.2</sub> O <sub>2-δ</sub> -40 wt% Pr <sub>0.6</sub> Sr <sub>0.4</sub> Co <sub>0.5</sub> Fe <sub>0.4</sub> Nb <sub>0.1</sub> O <sub>3-δ</sub> (GDC-PSCF <sub>0.4</sub> N <sub>0.1</sub> )	Disk	0.5, 0.7, 1.0 mm	T: 750–850 °C; P' <sub>O<sub>2</sub></sub> : 0.1–0.9 bar; P'' <sub>O<sub>2</sub></sub> : 0.002–0.03 bar;	[91,92]
75 wt% Ce <sub>0.85</sub> Sm <sub>0.15</sub> O <sub>1.925</sub> -25 wt% Sm <sub>0.6</sub> Sr <sub>0.4</sub> Al <sub>0.3</sub> Fe <sub>0.7</sub> O <sub>3-δ</sub> (SDC-SSAF)	Disk	0.5 mm	T: 800–950 °C; P' <sub>O<sub>2</sub></sub> : 0.11–0.30 bar; P'' <sub>O<sub>2</sub></sub> : 0.001–0.012 bar;	[93]
Dimitrakopoulos-Ghoniem model La <sub>0.9</sub> Ca <sub>0.1</sub> FeO <sub>3-δ</sub> (LCF)	Square planar	1 mm	T: 880–1045 °C; Air feed flow rate: 6000 cm <sup>3</sup> min <sup>-1</sup> ; Sweep gas flow rate: 2000 cm <sup>3</sup> min <sup>-1</sup>	[75]

<sup>a)</sup>ID is inner diameter, OD is outer diameter.

oxygen partial pressure. The oxygen nonstoichiometry of LSCF is sensitive to changes in oxygen partial pressure above 800 °C, which indicates that its oxygen permeation flux is suited to be modeled using the Xu-Thomson model. The oxygen permeation fluxes of LSCF simulated using the Zhu model (Figure 5a) and Xu-Thomson model (Figure 5c) appear to produce good correlation with the experimental data. However, the values of the regressed Zhu model resistance parameters cannot

capture completely the experimental trend as indicated by the very small values of permeation resistance constant of interface I (feed side) between 875 and 950 °C. On the other hand, the regression attempts using the Xu-Thomson failed to give a unique set of values of oxygen permeation parameters that are independent of the initial guesses. This is arisen from the intrinsic difficulty to fit simultaneously large number of parameters, i.e., 6 required by this model against the experimental

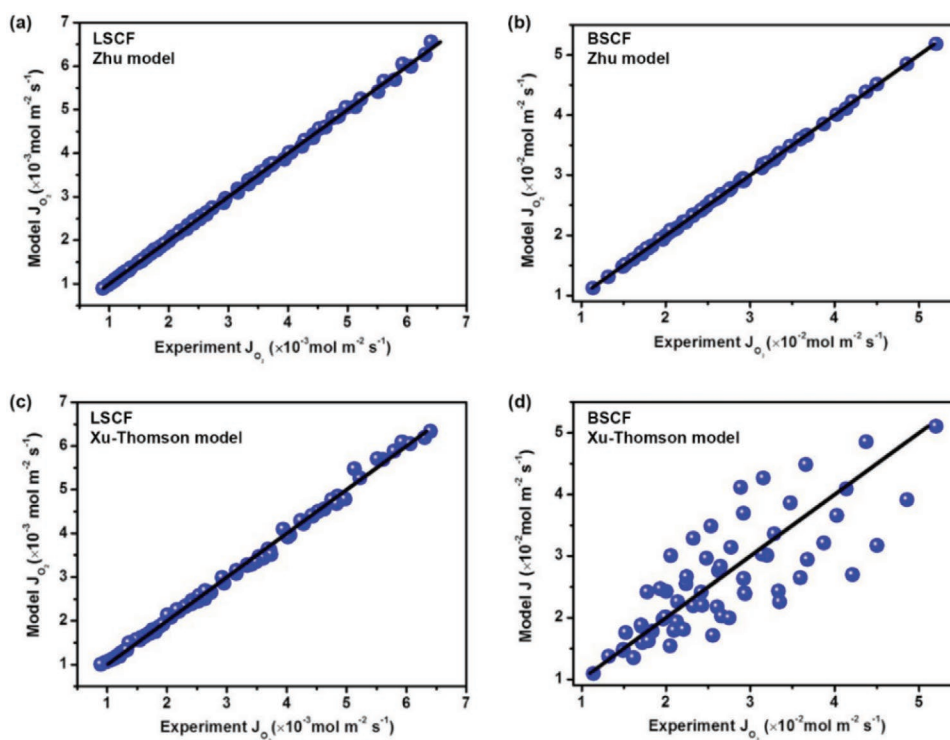
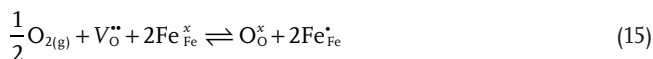


**Figure 5.** Correlation between simulated and experimental oxygen permeation fluxes for a) LSCF and b) BSCF using the Zhu model, and c) LSCF and d) BSCF using the Xu-Thomson model.<sup>[64]</sup> Reproduced with permission.<sup>[64]</sup> Copyright 2017, John Wiley and Sons.

data. As for BSCF, which shows negligible change in oxygen nonstoichiometry with changes in oxygen partial pressure, good correlation is observed between the simulated and experimental oxygen permeation flux when the Zhu model is used (Figure 5b). In contrast, the Xu-Thomson model does not fit well with BSCF (Figure 5d). The difference in model applicability stems from the membrane bulk transport property, i.e., the concentration of oxygen vacancies is greatly influenced by the oxygen partial pressure according to the Xu-Thomson model, while the Zhu model assumes constant transport properties. Also, these models were derived based on different driving forces, i.e., the oxygen vacancy concentration gradient is used in the Xu-Thomson model whereas the chemical potential drop is utilized in the Zhu model. Furthermore, the surface exchange reactions are adopted differently in each model, i.e., the forward and reverse reactions are considered as separate reactions in the Xu-Thomson model while the Zhu model adopts a holistic approach to the surface reactions but considers them to occur on different sides of the membrane.

To counter the discrepancy between the applicability of models to different membrane compositions, Zhu, Li, Cai, Zhu, and Yang<sup>[72]</sup> introduced modifications to the bulk resistance parameter,  $r^b$  to consider the variation in the oxygen partial pressure and translate these changes into the oxygen permeation flux. However, this method requires the concentration of oxygen vacancies in the relevant membrane composition to first be identified before the appropriate  $r^b$  can be selected. More recent works featured the application of the Zhu model to determine the effect of membrane grain size (achieved by sintering BaCe<sub>0.1</sub>Fe<sub>0.9</sub>O<sub>3-δ</sub> membrane at different temperatures and durations) and A-site cation content (Ba/Sr ratio in Ba<sub>x</sub>Sr<sub>1-x</sub>Co<sub>0.8</sub>Fe<sub>0.2</sub>O<sub>3-δ</sub> membrane) toward the oxygen transport kinetics.<sup>[73,74]</sup>

The oxygen permeation model by Dimitrakopoulos and Ghoniem<sup>[75]</sup> was developed based on the two-step surface oxygen incorporation reaction mechanism in La<sub>0.9</sub>Ca<sub>0.1</sub>FeO<sub>3-δ</sub> (Equations (15) and (16)). The diffusion of charged species is modeled using a Planck-Nernst-Poisson (PNP) model, which involves the standard Nernst-Planck conservation equations to consider the species transport and the Poisson equation for the electrostatic potential. The PNP model can simulate the oxygen permeation in MIEC membranes with charged species concentrations that vary with changes in the oxygen partial pressure.<sup>[76]</sup> Thus far, the proposed model has only been applied in the oxygen permeation transport simulation of square planar La<sub>0.9</sub>Ca<sub>0.1</sub>FeO<sub>3-δ</sub> membranes,<sup>[75,77]</sup> besides extended application to methane reforming.<sup>[78,79]</sup>



The present hurdles to the widespread application of oxygen permeation models include a proper in-depth understanding of the model execution and the suitability of different membrane compositions. Table 2 summarizes the various membrane compositions and their respective attributes and oxygen permeation conditions at which the experimental data was obtained and applied in modeling studies. The Xu-Thomson model and

Tan-Li model both appear to be suited for single-phase disk and hollow fiber membranes, respectively. The execution of both these models involve solving ordinary differential equations through numerical means such as the Runge-Kutta method. Several disk membrane compositions that fit well to the Zhu model include single-phase BSCF and dual-phase membranes, all of which possess oxygen nonstoichiometries that do not vary much with changes in oxygen partial pressure. While the Zhu model can be solved through simple linear regression approach, complex experimental dataset is required, i.e., a set of data obtained by varying  $P'_{\text{O}_2}$  while maintaining constant  $P''_{\text{O}_2}$ , and another set at varying  $P''_{\text{O}_2}$  while maintaining constant  $P'_{\text{O}_2}$  at each temperature point of interest. This requires significant time investment and certain expertise in optimizing experimental conditions.

In terms of future challenges, researchers appear to be approaching a bottleneck with regards to the further development of oxygen permeation models. Present modeling works mainly focus on gradual or minor improvements of the available models to emulate closely the oxygen permeation fluxes of membranes in the real scenario. Such improvement can be performed on the Zhu model, which is presently only suited for disk membranes given its assumption of complete mixing at the feed and permeate sides, which cannot be applied to hollow fiber membranes. In hollow fiber membranes case, the oxygen partial pressures in the feed and permeate sides are a function of the fiber length, which translates to the variation in the oxygen flux at different fiber length (Figure 4b). Suitable modifications should thus be made to incorporate such variation to the Zhu model to extend its applicability to hollow fiber membrane geometry. Other than that, entirely novel model conceptualizations may be rare to come by in the coming years. Besides, progress in model advancements is highly dependent on the developments in the experimental aspect, i.e., new membrane geometries, materials, and oxygen permeation flow characteristics. Thus, future development in the modeling aspect can be expected to be tied to advancements in MIEC membrane technology.

### 3.3. Opportunities

Prospects of applying the present oxygen permeation models include their adoption to other applications involving reactions or more extensive modeling studies such as computational fluid dynamics (CFD). Specialized computational studies such as CFD provide more insights through a visualization of the flow conditions according to specified conditions pertaining to the energy and mass flows. One such work by Habib, Ben Mansour and Nemitallah<sup>[94]</sup> that has incorporated oxygen permeation modeling in CFD studied the effect of combustion and oxyfuel combustion in an LSCF disk membrane reactor. Other recent works have featured the CFD modeling of LSCF hollow fiber membrane bundles for oxygen permeation (Figure 6a)<sup>[95]</sup> and LSCF disk membrane reactor for oxidative coupling of methane.<sup>[96]</sup> The latter study provided insight on the selectivity of carbon products for different reactor configurations (forward or reverse flow) and the results from the CFD model were benchmarked against those obtained using a less complex

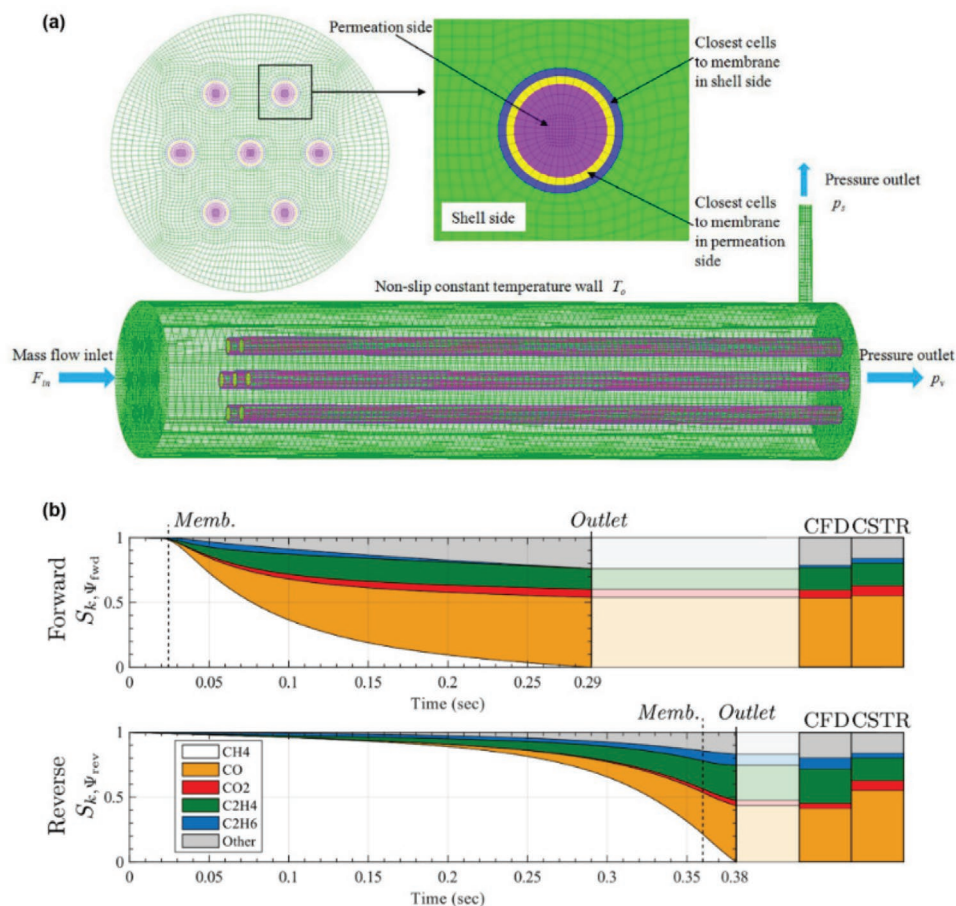


**Figure 6.** a) LSCF hollow fiber membrane module grids used in simulation,<sup>[95]</sup> Reproduced with permission.<sup>[95]</sup> Copyright 2021, Elsevier; b) Local selectivity of carbon products in forward (top) and reverse (bottom) flow button reactor configuration. The outlet selectivity as calculated based on the CFD model is contrasted with the output from a simpler CSTR simulation at the far-right of the graph.<sup>[96]</sup> Reproduced with permission.<sup>[96]</sup> Copyright 2019, Elsevier.

two-chamber continuously stirred tank reactor (CSTR) model (Figure 6b). Nevertheless, this area remains quite niche due to the pre-requisite of computation expertise required.<sup>[97,98]</sup> This concept can be potentially applied using different membrane compositions in other related processes such as partial oxidation of methane, coal gasification, or oxygen production. However, the incorporation of oxygen permeation models in reactive membrane technology requires additional consideration of pressure drop from combustion and the subsequent effects to the oxygen partial pressure driving force or membrane permeability.<sup>[99]</sup> Such in-depth studies on membrane reactors present further perspective and allow comparison against conventional fixed bed reactors in terms of the product selectivity, yield, and overall performance. In general, modeling works based on MIEC membrane applicability are of great interest due to their potential for commercialization.

### 3.4. Concluding Remarks

Modeling studies of MIEC membranes remain an essential component of research to complement experimental studies.

The steady increase in modeling works over the past two decades exhibits the continuous research interest and progressive development in this aspect. Oxygen permeation models were initially developed based on mutually exclusive oxygen transport cases of bulk diffusion or surface exchange reactions, and frequently featured empirical equations. However, recent advances in model conceptualization resulted in models that incorporated bulk diffusion and surface exchange reactions in a single oxygen permeation flux equation, i.e., the Xu-Thomson model and the Zhu model. Further adaptation of these models has seen their implementation in different membrane compositions, geometries, and flow configurations. However, there are hurdles to further innovation in terms of future model development since modeling progress is heavily dependent on experimental progress of MIEC membranes. To counter this barrier, researchers are encouraged to branch into application of oxygen permeation models in more extensive modeling studies such as CFD. Future works that feature in-depth oxygen permeation flux modeling along with membrane applications in value-added processes are expected to provide deep insights for the potential large-scale commercialization of MIEC membranes.



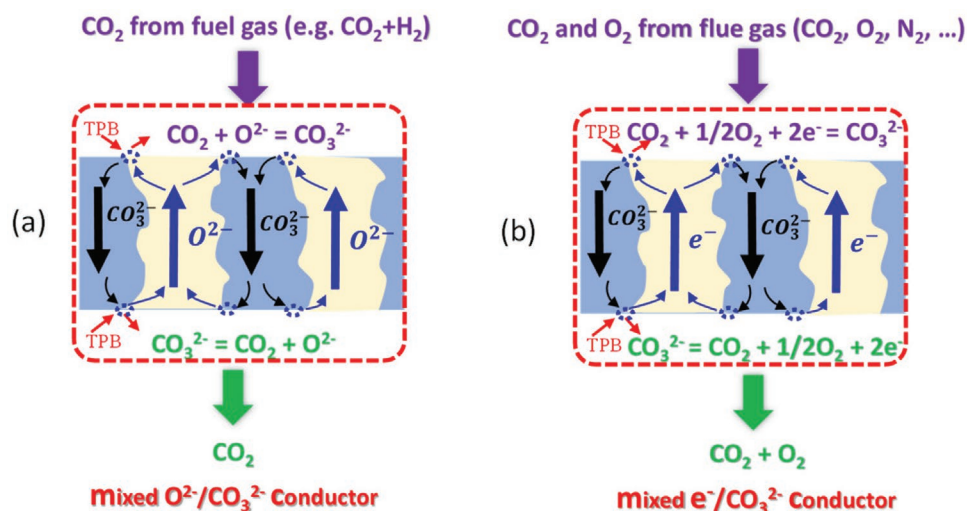


Figure 7. Working principles of a) MOC-based; b) MEC-based CTMs.

## 4. MIEC Membranes for Carbon Dioxide Separation and Conversion

### 4.1. Status

The CO<sub>2</sub> transport membranes (CTMs) based on high-temperature mixed conducting chemistry is an emergent class of promising CO<sub>2</sub> management technology with the ability to capture CO<sub>2</sub> efficiently and selectively from any CO<sub>2</sub>-containing process gases and convert it into valuable products in single reactor. A unique feature of CTMs is their high operating temperatures (500–800 °C), at which catalytic conversion of CO<sub>2</sub> into valuable chemicals can occur in the same reactor with commercially meaningful yield and selectivity. The process heats often embedded in combustion-derived, hot CO<sub>2</sub>-containing streams can also be best utilized by the high-temperature CTM reactors to improve the overall energy efficiency. The core working ion for CTMs is carbonate-ion (CO<sub>3</sub><sup>2-</sup>), which is provided by a molten carbonate (MC) phase. The charge compensating species to CO<sub>3</sub><sup>2-</sup> is either electrons (e<sup>-</sup>) or oxide-ions (O<sup>2-</sup>) or both. The conductors compensating CO<sub>3</sub><sup>2-</sup> are, therefore, a metal or a solid oxide-ion conductor. Another functionality of these solid conductors is to provide a solid porous structure to withhold MC like a sponge with capillary forces. Therefore, CTMs are comprised of at least two phases, one for MC and another for solid conductors.

Figure 7 shows how CTMs with two conducting mechanisms work to transport CO<sub>2</sub>: 1) mixed oxide-ion and carbonate-ion (MOC); 2) mixed electron and carbonate-ion (MEC). The major

charge carrier of CTMs is CO<sub>3</sub><sup>2-</sup> with compensating charge carrier as O<sup>2-</sup> for the MOC-based membranes, see Figure 7a, and e<sup>-</sup> for MEC-based membranes, see Figure 7b. For MOC-based CTMs, CO<sub>2</sub> and O<sup>2-</sup> on the feed side surface (the top) react to form CO<sub>3</sub><sup>2-</sup> that is further migrated across the membrane to the sweep-side surface (the bottom) via the MC phase. Therefore, the MOC-based CTMs are suitable for CO<sub>2</sub> separation from a mixture of CO<sub>2</sub> and H<sub>2</sub> in water-gas-shift-reaction. For the MEC-based CTMs, CO<sub>2</sub> and O<sub>2</sub> in the feed side are reduced into CO<sub>3</sub><sup>2-</sup> via surface reaction CO<sub>2</sub> + 1/2O<sub>2</sub> + 2e<sup>-</sup> = CO<sub>3</sub><sup>2-</sup>, then transported via the MC phase to the sweep side, where CO<sub>2</sub> with O<sub>2</sub> is co-collected via the reverse reaction: CO<sub>3</sub><sup>2-</sup> = CO<sub>2</sub> + 1/2O<sub>2</sub> + 2e<sup>-</sup>. Therefore, MEC-based CTMs are more suitable for CO<sub>2</sub> separation from post combustion flue gas that contains both CO<sub>2</sub> and O<sub>2</sub>. Since CO<sub>2</sub> is transported in the form of CO<sub>3</sub><sup>2-</sup> in both membranes, the theoretical membrane selectivity of CO<sub>2</sub> is infinite.

It is to be noted that the chemical compositions of MC phase used in CTMs have varied from group to group in the literature, but all with eutectic composition. Among the three alkali carbonate systems, i.e., Li-Na, Li-K and Li-Na-K, Li-Na eutectic composition exhibits the highest carbonate-ion conductivity, thus often the MC phase of the choice. Li-Na-K system has the lowest eutectic point (390 °C), which may find applications for lower-temperature CO<sub>2</sub> capture. Table 3 lists the conductivity and eutectic points of the three systems for reference.

The first MOC-based CTMs were studied in the laboratory with Y<sub>2</sub>O<sub>3</sub>-doped ZrO<sub>2</sub> (YSZ) and Sr- and Co-doped LaFeO<sub>3</sub> (LSCF) perovskite.<sup>[105,106]</sup> However, the former has a lower

Table 3. The Carbonate-ion conductivity of different molten carbonates.

Alkali Molten Carbonate Systems	$\sigma_{\text{CO}_3^{2-}}$ @ 923 K [S cm <sup>-1</sup> ]	$\sigma_{\text{CO}_3^{2-}}$ @ 1073 K [S cm <sup>-1</sup> ]	$\sigma_{\text{CO}_3^{2-}}$ @ 1173 K [S cm <sup>-1</sup> ]	Eutectic composition	Ref.
(Li-Na-K) <sub>2</sub> CO <sub>3</sub>	1.434	2.12	2.57	Li <sub>2</sub> CO <sub>3</sub> :Na <sub>2</sub> CO <sub>3</sub> :K <sub>2</sub> CO <sub>3</sub> = 43.5:31.5:25 (mol%)	[100]
(Li-Na) <sub>2</sub> CO <sub>3</sub>	2.06	2.65	3.53	Li <sub>2</sub> CO <sub>3</sub> :Na <sub>2</sub> CO <sub>3</sub> = 52:48 (mol%)	[101]
(Li-K) <sub>2</sub> CO <sub>3</sub>	1.31	1.77	2.46	Li <sub>2</sub> CO <sub>3</sub> :K <sub>2</sub> CO <sub>3</sub> = 62:38 (mol%)	[101,102]
(Na-K) <sub>2</sub> CO <sub>3</sub>	–	–	2.25	Na <sub>2</sub> CO <sub>3</sub> :K <sub>2</sub> CO <sub>3</sub> = 60:40 (mol%)	[101]

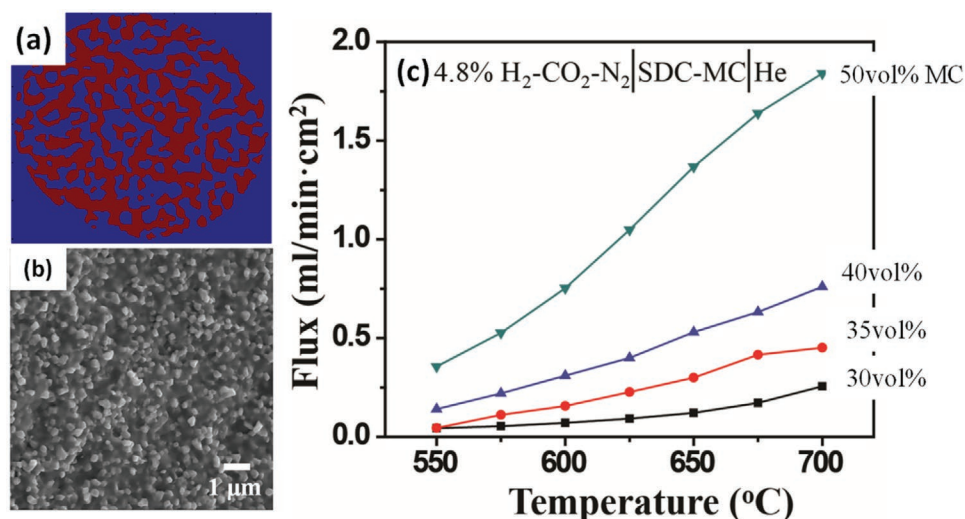


**Figure 8.** a) Porous matrix of SDC (SM-doped CeO<sub>2</sub>) imaged by synchrotron XCT; b) SEM microstructure of SDC-MC; c) flex density versus temperature. Reproduced with permission.<sup>[103,104]</sup> Copyright 2012, Royal Society of Chemistry and Copyright 2012, John Wiley and Sons.

oxide-ion conductivity, thus resulting in a lower CO<sub>2</sub> flux, while the latter vigorously reacts with MC, making their practical applications difficult. Later, Zhang and Huang<sup>[103,104]</sup> show in **Figure 8** that the replacement of YSZ with doped CeO<sub>2</sub> (such as Sm or Gd dopant) can significantly improve the CO<sub>2</sub> flux as well as stability. Since then, doped-CeO<sub>2</sub> matrices filled with MC have become the benchmark MOC-based CTMs for CO<sub>2</sub> capture and conversion. The first MEC-based CTM was demonstrated in laboratory with stainless steel (SS) as the solid porous matrix holding MC phase. However, the serious reactions between SS and MC resulted in fast performance degradation. Later, Huang group<sup>[107,108]</sup> demonstrated that the replacement of SS with silver can not only increase CO<sub>2</sub> flux, but also avoid chemical reactions. The issue with the silver-MC membrane is, however, the gradual sintering of porous silver matrix at elevated temperatures, resulting in loss of MC and flux decay. To solve this issue, Zhang, Tong and Huang<sup>[109–111]</sup> further showed in **Figure 9** that by overcoating silver matrix with a thin layer of refractory ZrO<sub>2</sub> can significantly improve the flux stability and enable the membrane to operate at higher temperatures without appreciable sintering.

#### 4.2. Recent Advances and Future Challenges

There are several new advances in CTMs in recent decade. One is the new CTM created by in situ reaction between NiO and MC,<sup>[112]</sup> by which an electron conducting phase Li<sub>0.4</sub>Ni<sub>0.6</sub>O<sub>2</sub> (LNO) is formed. With an oxide-ion conductor (e.g., SDC) as the porous matrix, the resultant CTM conducts oxide-ions, electrons, and carbonate-ions. Since there are two parallel pathways for CO<sub>2</sub> transport and one pathway for O<sub>2</sub> transport in this type of CTM, the flux ratio of CO<sub>2</sub> to O<sub>2</sub> is increased from 2/1 with MEC-based CTM to 2.3/1,<sup>[113]</sup> see **Figure 10**. The co-transport of CO<sub>2</sub> and O<sub>2</sub> could find unique applications in upgrading natural gas or natural gas liquids (NGLs) into syngas, ethylene, or propylene through oxidative dehydrogenation conversion with high conversion and selectivity without coking. Another advantage of this membrane is the low cost. The early MEC-based CTMs used silver as the electron-conducting phase, which is not only sintering prone, but also at high cost. The new combined MEC- and MOC-based CTM employs relatively low-cost NiO as the starting phase for the electron-conducting phase

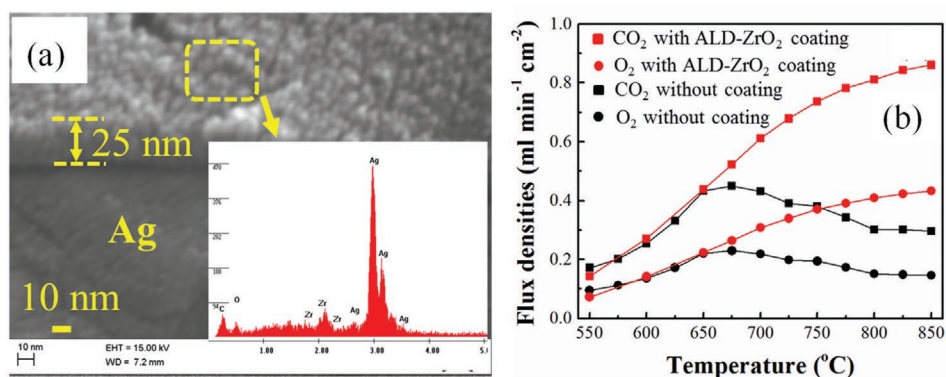


**Figure 9.** a) ALD-ZrO<sub>2</sub> overcoat on Ag matrix; b) flux density comparison at 800 °C. Reproduced with permission.<sup>[111]</sup> Copyright 2016, Royal Society of Chemistry.

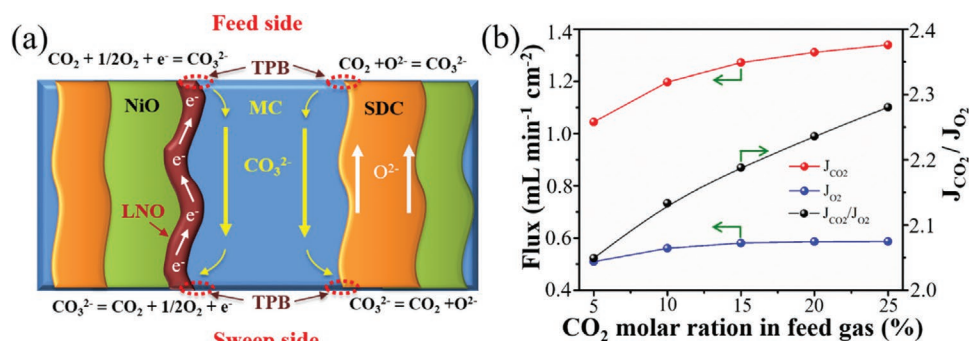


**Figure 10.** a) Schematic representation of  $\text{CO}_2$  and  $\text{O}_2$  transport through the NiO-SDC-MC membrane; b) the corresponding  $\text{CO}_2$  and  $\text{O}_2$  fluxes versus  $\text{CO}_2$  content in the feed gas measured at  $850^\circ\text{C}$ .  $\text{O}_2$  content is kept constant at 10%, and  $\text{N}_2$  is used as the balance gas. Reproduced with permission.<sup>[113]</sup> Copyright 2018, American Chemical Society.

and doped- $\text{CeO}_2$  as the oxide-ion conducting phase, while both phases serve as the solid porous matrix to withhold MC phase.

Another notable advance in CTM is the development of chemical reactors for combined  $\text{CO}_2$  capture and chemical conversions. The basic principle is to use the directly captured (permeated)  $\text{CO}_2$  from a source of  $\text{CO}_2$  (e.g., flue gas) to upgrade methane or ethane into syngas<sup>[114,115]</sup> or ethylene<sup>[116]</sup> in the presence of a specific catalyst. **Figure 11** shows the working principles of two combined  $\text{CO}_2$  capture and conversion reactors. Since  $\text{CO}_2$  is a soft oxidizer, overoxidation of the reactive product is alleviated, thus resulting in high conversion, selectivity and ultimately yield.<sup>[114–116]</sup>

While significant progress toward materials and reactor development has been made since 2005 when the first MEC-based CTM was conceptualized,<sup>[117]</sup> major challenges remain for this technology to be practical. One such a challenge is achieving practically meaningful flux stability because flux stability is the most important factor for practical applications. So far, the longest flux stability demonstrated is  $\approx 1000$  h. There are multiple reasons for the poor stability: the loss of MC caused by the poor solid/MC wettability, and sintering of solid matrix over

time, both which lead to MC-phase discontinuity and decrease in conductivity, ultimately decay in  $\text{CO}_2$  flux. The chemical reactions between sealants (ceramic bond, glass, etc.) and MC could also cause flux degradation.

From a material perspective, CTMs are constructed by filling MC phase into a solid porous matrix. For porous solid matrix in MOC-based membranes, rare-earth doped ceria are so far the best materials due to their good wettability with MC and high  $\text{O}^{2-}$  conductivity. However, their chemical propensity to react with S-containing impurities in flue gas or WGS gas emitted from coal-fired power plants impedes their future applications. Therefore, there is a need to find new S-tolerant solid matrix materials for MOC-based CTMs to capture  $\text{CO}_2$  from flue gas.

For MEC-based CTMs, Ag-based solid matrix has been successfully demonstrated as a high-flux  $\text{CO}_2$  permeation membrane. However, Ag is prone to sinter at high temperatures, presenting a barrier for its practical applications. Efforts to modify surface and microstructure have been devoted to mitigate the sintering issue. However, given the high cost of Ag, more studies are needed to identify new materials to replace Ag. One candidate is NiO. While the initial results are promising, understanding the composition-flux-stability relationship in these new NiO-based MEC-based membranes are still lacking. To address the poor stability issue in reducing atmospheres of the NiO-MC membrane, SDC has been added into NiO-MC membranes with improved stability and enabled better ionic/electronic conduction. However, the phase volume among SDC, NiO and MC need be further optimized to selectively increase either  $\text{CO}_2$  or  $\text{O}_2$  flux for specific applications. On the other hand, increasing electronic conductivity in the SDC phase can reduce the need for high NiO volume.

Thermal stability of MCs at high temperatures is a fundamental problem to MC-based CTMs. Thermodynamics suggests that Li-Na-K carbonates, either binary or ternary, have a tendency to decompose into oxide (e.g.,  $\text{Li}_2\text{O}$ ) at high temperatures by losing  $\text{CO}_2$ . Therefore, CTMs should not be used at too a temperature such as  $>800^\circ\text{C}$ .

From microstructural perspective, microstructural parameters such as pore size/distribution, porosity/tortuosity of the solid porous matrix have a marked impact on flux and stability of CTMs. First, these parameters determine the level of capillary forces that preserve the MC phase. In theory, small and uniformly distributed pores can produce high capillary forces.

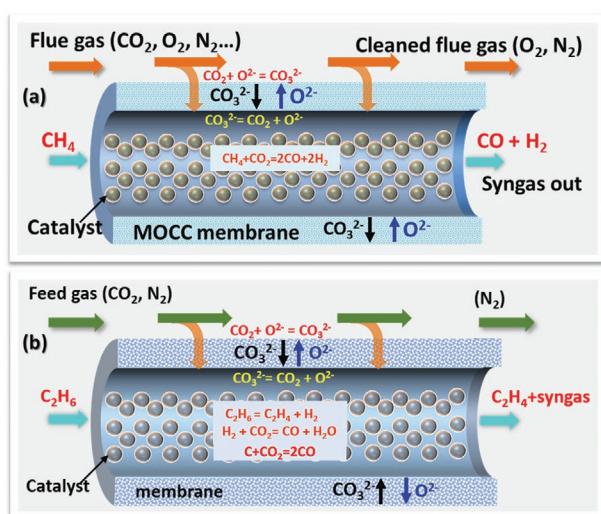


**Figure 11.** Working principles of a) methane reactor; b) ethane reactor. Reproduced with permission.<sup>[114–116]</sup> Copyright 2016, 2017, and 2019, American Chemical Society.



Creating high enough capillary forces are critically important for CTMs in pressurized applications. On the other hand, the ratio of porosity to tortuosity ( $\epsilon/\tau$ ) should be maximized since it is proportional to the CO<sub>2</sub> flux in thick-film CTMs. Research efforts to develop new approaches for fabricating solid porous bodies with large  $\epsilon/\tau$  ratio and fine and evenly distributed pores are appreciated. Last, surface modification of CTMs to achieve a fast rate of CO<sub>2</sub> exchange kinetics also needs to be further explored.

From a chemical reactor perspective, one unique feature of CTM-based reactors is the combined CO<sub>2</sub> capture and conversion into valuable products. So far, all CTMs reactors coupling with DMR (dry methane reforming), ODHE (oxidative dehydrogenation of ethane) and WGS (water gas shift), have been demonstrated in laboratory. One remaining challenge for the CTM reactors to be commercially viable is the demonstration of flux stability at larger scales. Application of conversion catalysts to the CTM's surface versus in a separate bed inside the reactor is another area worth further studying.

From a computational perspective, the flux of a CTM is generally modeled by considering surface reactions and microstructure-related bulk transport properties. The latter is of vital importance to multi-phase CTMs since the phase volume and porosity/tortuosity could significantly impact the flux. Despite the straightforward surface mechanisms of CO<sub>2</sub> ionization in CTMs, the multi-phase charge transport in the bulk of CTMs needs a new set of flux equations to describe their CO<sub>2</sub> flux mathematically. In addition, chemical kinetics of CO<sub>2</sub> conversion reactions with a given feedstock (e.g., CH<sub>4</sub>) should be included in the overall microkinetic model for CTM-based CO<sub>2</sub> capture and conversion reactors.

#### 4.3. Opportunities

The above challenges also offer new opportunities for researchers to further advance the development of multi-phase CTMs toward commercialization. We here suggest few areas of interest for this purpose.

- Design and fabrication of efficient microstructures of solid matrices with highest  $\epsilon/\tau$ , finest pores and most uniform distribution.
- Integrating catalysts with CTMs for combined CO<sub>2</sub> capture and conversion reactors to achieve high conversion efficiency and selectivity.
- Development of mathematical models to calculate CO<sub>2</sub> flux of new multi-phase CTMs (such as three-phase membranes) either in analytical or numerical domain.

#### 4.4. Concluding Remarks

This section briefly summarizes the development of a new class of chemical-potential driven CTMs and the associated reactors suited for combined CO<sub>2</sub> capture and utilization. Specifically, this short review presents various types of high-temperature mixed conducting chemistry based CTMs and reactors. The types of CTMs are multiphase mixed conductors consisting of a mixture of ceramic-ceramic-carbonate, metal-carbonate and ceramic-carbonate.

For membranes to work in a low-temperature range, e.g., 400–500 °C, the eutectic (Li-Na-K)<sub>2</sub>CO<sub>3</sub> system is a better choice for its low eutectic point (396 °C). However, for those operated at higher temperatures such as above 600 °C, eutectic (Li-Na)<sub>2</sub>CO<sub>3</sub> carbonate is a better choice than (Li-K)<sub>2</sub>CO<sub>3</sub> because of its higher CO<sub>3</sub><sup>2-</sup> conductivity. For solid porous matrix materials used in MOC-based membranes, doped ceria (SDC, GDC etc.) are preferred due to their excellent wettability with MC and high oxide-ion conductivity. Their applications in sulfur-containing flue gas might be hindered due to CeO<sub>2</sub> reaction with H<sub>2</sub>S and SO<sub>2</sub> impurities.<sup>[118]</sup> For MEC-based membranes, Ag is a good option from a conductivity and compatibility perspective. However, its scaled-up applications might face sinterability and high-cost issues. A recent noticeable development of using NiO as the solid matrix, which forms conductive Li<sub>0.4</sub>Ni<sub>1.6</sub>O<sub>2</sub> (LNO) phase upon contact with MC above 700 °C, might shed light on developing practically viable MEC-based CTMs for flue-gas CO<sub>2</sub> capture.

Designs and performances of a couple of CTM-based CO<sub>2</sub> reactors have also been reviewed. For instance, the captured CO<sub>2</sub> can catalytically react with CH<sub>4</sub> as a sweep gas and CO<sub>2</sub>-containing flue gas as a feed gas to produce syngas (H<sub>2</sub>+CO) through DMR reaction. For MEC-based membranes, the co-transported CO<sub>2</sub> and O<sub>2</sub> minimize coke formation. Likewise, the CTM reactors have also been demonstrated to convert C<sub>2</sub>H<sub>6</sub> into C<sub>2</sub>H<sub>4</sub> following ODHE reaction with the permeated CO<sub>2</sub> as a soft oxidizer. By combining with the WGS reaction, MOC-based CTMs have been shown to be able to capture CO<sub>2</sub> from the WGS gas, thus shifting the reaction toward H<sub>2</sub> production.

Last, proof-of-concepts of high-temperature CTMs have so far been successfully demonstrated in laboratory. For this new technology to be competitive with commercial “amine washing”, an incumbent benchmark sorption-based technology, more scale-up demonstrations are inevitable. To achieve this ultimate goal, materials advancement reactor designs and system analysis/modeling are needed in the future R&D.

## 5. MIEC Membranes for Carbon Dioxide Reduction

### 5.1. Status

CO<sub>2</sub> is a major greenhouse gas. Its emission must be significantly reduced in order to achieve net-zero carbon economy by 2050; this target is set by many countries including Germany, Canada, UK and France.<sup>[119]</sup> Moreover, its removal from the atmosphere may have to be accelerated.<sup>[120]</sup> Capturing CO<sub>2</sub> from the point source, e.g., flue gases in fossil fuel power plants, hydrogen and ammonia production facilities, steel and cement plants, or from the atmosphere using direct air capture (DAC) are effective means to reach these goals. While captured CO<sub>2</sub> can be used for enhanced oil recovery (EOR), stored in stable geological formations such as porous rocks and salt caverns,<sup>[121]</sup> it is also a carbon source for the production of useful fuels and chemicals such as CO, CH<sub>4</sub>, and methanol.<sup>[122]</sup> Converting captured CO<sub>2</sub> to value-added chemicals reduces the economic penalty of carbon capture, which has been highlighted by many international and regional



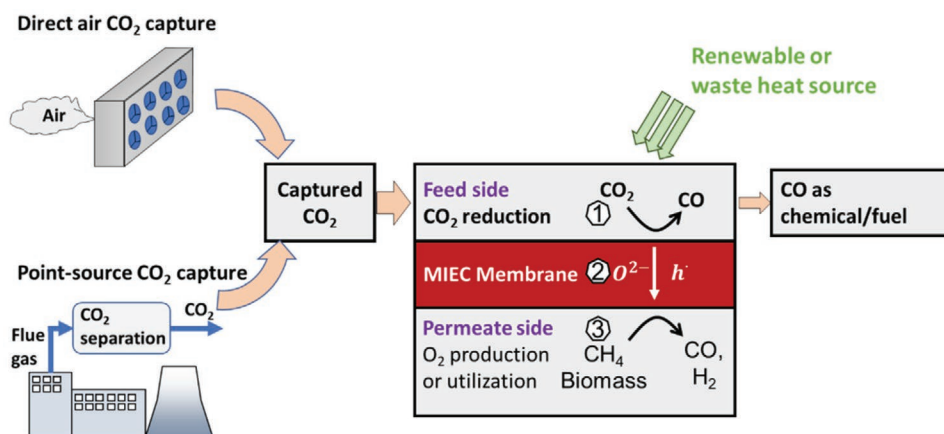


**Figure 12.** Flow diagram of CO<sub>2</sub> capture and utilization supported by the MIEC membrane. There are three steps in the integrated membrane reactor: 1) CO<sub>2</sub> reduction and oxygen incorporation on the feed side, 2) oxygen diffusion across the membrane driven by the chemical potential gradient, and 3) oxygen production/utilization on the permeate side (e.g., partial oxidation of methane or biomass gasification to produce syngas, i.e., a mixture of CO and H<sub>2</sub>).

organizations such as the International Energy Agency<sup>[123]</sup> and the Europe Cluster on Catalysis,<sup>[124]</sup> and is referred to generally as the circular economy.

CO<sub>2</sub> is a thermodynamically stable molecule. Converting CO<sub>2</sub> into higher-value molecules requires energy in the form of electricity, chemical and/or thermal energy (conveniently referred to as intermediate or high temperature heat) to activate the C=O bonds. Several processes have been proposed for CO<sub>2</sub> conversion, such as electrolysis, photocatalysis and thermochemical reduction. Among these, MIEC membrane-supported CO<sub>2</sub> thermochemical reduction provides a flexible and modularized solution, as shown schematically in **Figure 12**. The critical element in this technology is an oxygen permeable membrane, which allows only oxygen produced by CO<sub>2</sub> reduction (CO<sub>2</sub> → CO + ½ O<sub>2</sub>) to diffuse across, from the CO<sub>2</sub> side to the permeate side, thus breaking the thermodynamic equilibrium limit of CO<sub>2</sub> reduction at moderate temperatures. There are three steps involved: 1) CO<sub>2</sub> reduction to CO and oxygen incorporation on the feed side, 2) oxygen diffusion across the membrane (details were discussed in Section 3) and 3) oxygen desorption/utilization on the permeate side. The membrane surface on the feed side can be catalyzed to enhance CO<sub>2</sub> reduction kinetics.<sup>[125]</sup> Because the process operates at elevated temperatures, i.e., 500 – 1000 °C, non-precious metal catalysts can be used. Membrane-supported CO<sub>2</sub> reduction can be further intensified by coupling with other high temperature processes on the permeate side, such as methane partial oxidation<sup>[126]</sup> or biomass or coal gasification<sup>[127,128]</sup> which utilize the separated oxygen, as shown in Figure 12.

Research has focused on understanding the thermodynamics, heat/mass transport phenomena, reaction kinetics and system integration, and material response and stability. Various membranes have been tested and CO<sub>2</sub> reduction rates as high as 3.16 μmol cm<sup>-2</sup> s<sup>-1</sup> were measured.<sup>[129]</sup> Catalysts are often used to improve surface kinetics, which can be the rate-limiting step in oxygen permeation. A resistance-network model for permeation can be used to determine the rate-limiting step.<sup>[130]</sup> In some cases, renewable energy such as solar heat was used as the energy source for CO<sub>2</sub> reduction.<sup>[131,132]</sup>

An extensive literature review on MIEC membrane-supported CO<sub>2</sub> reduction technology has been conducted recently by the authors.<sup>[76]</sup> Here, we highlight the most recent developments, remaining challenges, and needs and requirement for advancing this CO<sub>2</sub> reuse technology to higher technology readiness level (TRL) and industrial adoption.

## 5.2. Recent Advances and Future Challenges

Various membrane materials, both fluorites, e.g., CeO<sub>2-δ</sub> and perovskites, e.g., La<sub>0.9</sub>Ca<sub>0.1</sub>FeO<sub>3-δ</sub> and doped SrCo<sub>0.8</sub>Fe<sub>0.2</sub>O<sub>3-δ</sub> have been tested for CO<sub>2</sub> thermochemical reduction. Material stability in the CO<sub>2</sub> environment is still a concern, as carbonates formed on the membrane surface diminish the oxygen permeation.<sup>[2]</sup> This phenomenon could become more severe at higher CO<sub>2</sub> concentrations. To guide material selection, a common strategy is to use the thermodynamics of carbonate decomposition displayed on the Ellingham diagram.<sup>[33]</sup> Membrane materials prone to form stable carbonates, such as BaCO<sub>3</sub> are undesired, hence some highly permeable MIEC membranes such as Ba<sub>0.5</sub>Sr<sub>0.5</sub>Co<sub>0.8</sub>Fe<sub>0.2</sub>O<sub>3-δ</sub><sup>[133]</sup> cannot be used. Similar approaches have been used to select optimal oxygen carriers for thermochemical redox cycles for CO<sub>2</sub> reduction.<sup>[134]</sup> However, the Ellingham diagram solely cannot explain why the less stable carbonates such as SrCO<sub>3</sub> and CaCO<sub>3</sub> were still observed in some Sr- and Ca- containing membranes, such as SrCo<sub>0.4</sub>Fe<sub>0.5</sub>Zr<sub>0.1</sub>O<sub>3-δ</sub><sup>[135]</sup> and La<sub>0.9</sub>Ca<sub>0.1</sub>FeO<sub>3-δ</sub>.<sup>[130]</sup> Recently, the Lewis acid-base principle was used to explain the persistence of SrCO<sub>3</sub> and CaCO<sub>3</sub> on the membrane surfaces. Lower surface basicity tends to lower CO<sub>2</sub> adsorption. The Lewis acid-base properties of the membrane materials could be changed by the co-existence of the reduction product, i.e., CO. Surface acidity, therefore, is an important descriptor for choosing stable membrane materials for CO<sub>2</sub> reduction. More details regarding the application of Lewis acid-base principle on membrane stability can be found in the two recent reviews.<sup>[2,76]</sup>

Apart from the thermodynamics, advancements in understanding the CO<sub>2</sub> reduction kinetics, and oxygen permeation

pathways guide the development of catalysts and reactor design. A four-step reaction mechanism was proposed for Sm-doped  $\text{CeO}_{2-\delta}$  which includes 1) carbonate formation, 2) carbonate decomposition and oxygen incorporation, 3) electron and 4) lattice oxygen diffusion.<sup>[136]</sup> In most cases, the surface reaction kinetics were found to limit the overall  $\text{CO}_2$  reduction rates, and various catalysts, e.g.,  $\text{NiO}/\text{Al}_2\text{O}_3$ ,<sup>[137]</sup> were used to accelerate the reactions. These catalysts can be distributed over a porous layer on the membrane surface to further improve the reaction rates. In this case, parameters such as the Thiele modulus can be used to optimize the porous layer design by comparing the rates of surface reaction and the gas diffusion in the porous catalytic layers.<sup>[125,138]</sup>

Several advancements have been made in process intensification and system integration for MIEC membrane supported  $\text{CO}_2$  reduction. Direct integration of solar radiation for solar-fuel production has been demonstrated on a coated  $\text{CeO}_{2-\delta}$  membrane ( $\text{La}_{0.5}\text{Sr}_{0.5}\text{Mn}_{0.9}\text{Mg}_{0.1}\text{O}_3$  on the  $\text{CO}_2$  feed side and  $\text{Ca}_{0.5}\text{Sr}_{0.5}\text{MnO}_3$  on the permeate side) at 1450–1550 °C in a vertical-axis medium-size solar reactor; stable continuous CO production was maintained up to 8.5 h, and the maximum CO production rate was  $0.133 \mu\text{mol cm}^{-2} \text{s}^{-1}$  at 1550 °C.<sup>[132]</sup> The MIEC membrane's applications in solar-driven processes are discussed in detail in Section 11. Plasma catalysis was integrated with the membrane supported  $\text{CO}_2$  reduction, leading to a four-fold increase in the oxygen flux across the membrane.<sup>[6]</sup> Co-splitting  $\text{CO}_2$  and  $\text{H}_2\text{O}$  was examined in a 0.5 mm thick  $\text{CeO}_{2-\delta}$  membrane reactor, showing combined CO and  $\text{H}_2$  fuel production rate of  $0.038 \mu\text{mol cm}^{-2} \text{s}^{-1}$  at 1600 °C (feed side:  $\text{CO}_2/\text{H}_2\text{O}$  molar ratio = 2.1, sweep side: Ar).<sup>[139]</sup> While promising, more efforts on these integrated processes are needed to improve the efficiency and economics of the process before industrial deployment can be expected.

Despite notable advancements, several challenges remain in the effort to achieve higher  $\text{CO}_2$  conversion ratios, currently ranging from 0.82%<sup>[131]</sup> to  $\approx 20\%$ <sup>[129]</sup> in lab tests and to integrate the process for downstream utilization. Low conversion ratio means higher separation work to obtain high purity CO and recycle the unconverted  $\text{CO}_2$  back to the reactor. For CO storage as an energy carrier, separation of  $\text{CO}_2$  and CO is necessary. Alternatively, if the goal is to combine CO with hydrogen in a Fischer-Tropsch (FT) process for the production of hydrocarbon or methanol,  $\text{CO}_2$  partial pressure in the mixture can impact the hydrogen requirements, production rates, selectivity, and energy consumption.<sup>[140]</sup>  $\text{CO}_2$  was found to inhibit iron catalysts in FT, even though the effect is not as strong as  $\text{H}_2\text{O}$ .<sup>[141]</sup> Therefore, future studies are needed to evaluate the impacts of  $\text{CO}_2$  conversion on the energy efficiency and techno-economics of the overall  $\text{CO}_2$  utilization process.

An enhancement factor,  $F_E$ , comparing the  $\text{CO}_2$  conversion ratios in the membrane-supported reduction and gas thermolysis,

$$F_E = \frac{X_{\text{CO,membrane}}}{X_{\text{CO,thermolysis}}} \quad (17)$$

can be used to evaluate the enhancement of  $\text{CO}_2$  reduction by the membrane, where  $X_{\text{CO,membrane}}$  and  $X_{\text{CO,thermolysis}}$  are the CO mole fractions in the membrane-supported  $\text{CO}_2$  reduction and  $\text{CO}_2$  thermolysis products, respectively. The  $\text{CO}_2$  conversion ratio

is directly related to oxygen permeability, which strongly depends on the oxygen chemical potential gradient across the membrane, or the difference between feed and permeate side oxygen partial pressures. To maintain a high oxygen permeation flux, needed for higher  $\text{CO}_2$  conversion, a strongly reducing environment is necessary on the sweep side, either by creating a vacuum or using a fuel. For example, the  $F_E$  increased from 3.5 to 277 when the fuel concentrations on the sweep side were raised from 1% to 12% on a 1.3 mm thick  $\text{La}_{0.9}\text{Ca}_{0.1}\text{FeO}_{3-\delta}$  membrane at 990 °C (100%  $\text{CO}_2$  feed and CO+Ar sweep as a model fuel).<sup>[130]</sup> Creating these conditions influences the efficiency, economy, and environmental impacts of  $\text{CO}_2$  reduction, and it is critical to determine these functional relations and their dependency on the membrane materials, catalysts, membrane design and operating conditions through system-level analyses and life-cycle assessments. The discussions on the energy cost using vacuum to maintain low oxygen partial pressures on the permeate side can be found in Section 13.

The economy of  $\text{CO}_2$  reduction technology is key for its adoption. While developing novel low-cost membrane materials is necessary, it is also important to study the overall techno-economics of the integrated process. For example, in solar-fuel production using thermochemical redox cycles, the construction of solar farm accounts for around 70% of the leveled cost of solar-fuels due to the high operating temperature required for the process.<sup>[142]</sup> Similarly, reducing the operating temperatures in MIEC membrane reactors for  $\text{CO}_2$  reduction by improving the kinetics can also reduce the cost to provide the heat.

### 5.3. Opportunities

New membrane materials with good oxygen flux and high stability, especially mixed-phase materials, have been developed recently as summarized in Section 2. Meanwhile, the membrane surface properties are important for reducing carbonate formation and enhancing  $\text{CO}_2$  reduction kinetics, as discussed previously. Here, we highlight two new techniques that could be used to modify the surface to enhance  $\text{CO}_2$  reduction. The first is the infiltration of thin layers of metal oxides on the membrane surface to change the surface acid-base properties and the  $\text{CO}_2$  adsorption kinetics. The acidity of the surface-infiltrated binary oxides were found to impact the surface electronic structure of the bulk materials, and hence, influence the oxygen exchange kinetics (mainly the pre-exponential factors), as shown in **Figure 13a**.<sup>[143]</sup> By changing the infiltrating oxides on the surface of  $\text{Pr}_{0.1}\text{Ce}_{0.9}\text{O}_{2-\delta}$  from strongly acidic  $\text{SiO}_2$  to strongly basic  $\text{Li}_2\text{O}$ , the chemical surface exchange coefficients increased by 6 orders of magnitude; similar phenomenon was also observed on infiltrated  $\text{La}_{0.6}\text{Sr}_{0.4}\text{CoO}_{3-\delta}$  surfaces.<sup>[143]</sup> The second is catalyst exsolution. Dopants can change the reducibility of the host lattice (described by the reduction extent,  $\delta$  in the perovskite unit cell), which control the exsolution phenomenon on the oxide surface (**Figure 13b**). Enhancements in both kinetics and stability by catalyst exsolution have been demonstrated in solid oxide electrochemical cells, thermochemical redox processes, and heterogeneous catalysis.<sup>[144,145]</sup> This novel technique can also be used to decorate the membrane surfaces with exsolved nanoparticles and hence, to facilitate the  $\text{CO}_2$  reduction rates, as demonstrated experimentally in  $\text{La}_{0.85}\text{Ca}_{0.10}\text{Fe}_{0.95}\text{Ni}_{0.05}\text{O}_{3-\delta}$  membranes.<sup>[146]</sup>

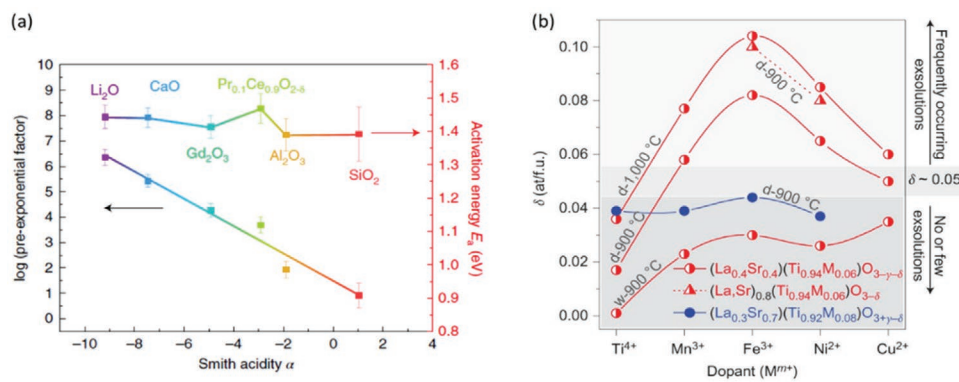


**Figure 13.** a) Pre-exponential factors and activation energies of the oxygen chemical surface exchange coefficient,  $k_{\text{chem}}$  of the infiltrated  $\text{Pr}_{0.1}\text{Ce}_{0.9}\text{O}_{2-\delta}$  samples as a function of the acidity factor of the infiltrating binary oxides. Reproduced with permission.<sup>[143]</sup> Copyright 2020, Springer Nature. b) Impacts of dopants on the reduction extents ( $\delta$ , oxygen atoms per perovskite unit cell) and the observation of exsolution from the native surface under various conditions. Reproduced with permission.<sup>[145]</sup> Copyright 2013, Springer Nature.

Further studies are needed to construct detailed micro-kinetics of  $\text{CO}_2$  reduction on membrane surfaces, to enable the development of high-fidelity reactor model for design optimization. Multi-step  $\text{CO}_2$  reduction mechanisms have been proposed, but the kinetic parameters are not available for many mixed conducting oxides yet. More studies are needed to validate these models on single-phase and examine the characteristics of multi-phase materials. For example, oxygen diffusion channels in the perovskite-ceria interfaces, e.g.,  $\text{La}_{0.65}\text{Sr}_{0.35}\text{MnO}_3\text{-CeO}_2$ ,<sup>[147]</sup> promote oxygen release from the perovskite phase and can lead to new surface reaction and oxygen diffusion pathways. Knowledge gained from  $\text{CO}_2$  electrolysis on solid oxide electrolysis cell and thermochemical redox cycles can be used to help derive the micro-kinetics for  $\text{CO}_2$  reduction on MIEC membranes. The development of in situ surface examination techniques such as in situ Raman spectroscopy<sup>[148]</sup> together with ex situ characterization methods (e.g., X-ray diffraction (XRD) and energy-dispersive X-ray spectroscopy (EDXS)) will also provide new insights in the  $\text{CO}_2$  reduction mechanisms on MIEC membrane surface.

Innovative process intensification with  $\text{CO}_2$  reduction can be enabled by the MIEC membranes. For example, combining  $\text{CO}_2$  reduction with the Sabatier reaction to produce methane has been studied in a solid oxide electrochemical system,<sup>[149]</sup> which is also applicable to a MIEC membrane reactor. As the Sabatier reaction favors higher operating pressures, pressurized  $\text{CO}_2$  reduction on MIEC membranes should be examined both experimentally and theoretically to provide necessary input for developing this technology. In addition, high-fidelity system modeling and techno-economic analysis are needed to define a pathway for industrial adoption, including a high-level sustainability assessment considering the social and environmental impacts. Much can be learned from the commercialization of MIEC membranes for oxygen production (more details can be found in Section 13).

#### 5.4. Concluding Remarks

The MIEC membrane supported  $\text{CO}_2$  reduction technology, integrated with renewable thermal energy sources such as “solar heat” has great potential for carbon dioxide utilization.

Without precious metal catalysts, these membranes exhibit high oxygen permeation fluxes and fast  $\text{CO}_2$  reduction kinetics thanks to the elevated operating temperatures. Fundamental understandings of the transport phenomena and reaction kinetics in MIEC materials will accelerate innovations in the design of membrane reactors and their integration with downstream processes. The development in novel surface modification technologies such as surface infiltration with binary oxides and catalyst exsolution, as well as the creative process integration, will advance the performances and the applications of the MIEC membrane supported  $\text{CO}_2$  reduction in industry.

## 6. MIEC Membranes for Hydrogen Separation

### 6.1. Status

As a clean, efficient and sustainable energy carrier, hydrogen is regarded as one of promising clean energy in future, and is an important development direction of human energy strategy.<sup>[150]</sup> Water is an ideal source for hydrogen production. Hydrogen production via water splitting driven by renewable energy sources (e.g., solar, wind, geothermal and tidal energies) is the most ideal approach. However, these renewable energy technologies themselves are in their initial stages of development at present. Thus, it is not economical using these renewable energy sources to produce hydrogen in large scales in the near future. Currently, the common and effective ways for hydrogen production are based on the steam reforming and water-gas-shift of fossil fuels.<sup>[151]</sup> The gas produced from fossil fuels contains not only  $\text{H}_2$  and  $\text{CO}_2$ , but also a small amount of  $\text{CO}$  and  $\text{H}_2\text{S}$  impurities. However, the impurities are strong poisons for the electro-catalysts of fuel cells, even a few ppm such impurities will cause a serious decline in performance of fuel cells.<sup>[152]</sup> Membrane separation is an important method to improve hydrogen purity. Mixed protonic-electronic conducting membranes, Pd and Pd alloy composite membranes and V-Zr-Nb based alloy membranes<sup>[153–155]</sup> have been widely studied for hydrogen separation. Among the three kinds of dense membranes, Pd and Pd alloy composite membranes are the one most close to practical applications though the difficulty in

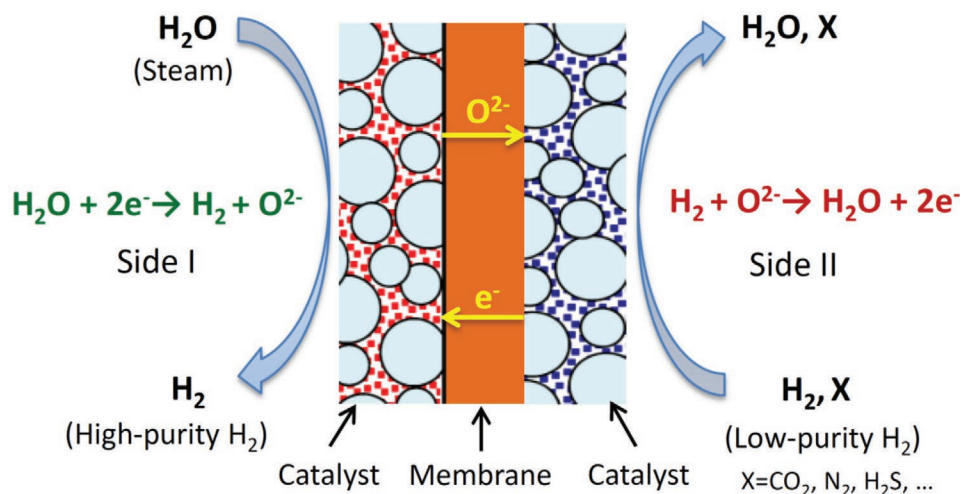


**Figure 14.** Schematic drawing of MIEC membrane reactors for hydrogen separation.

stability still not well solved. Recently, mixed ionic-electronic conducting membrane reactors (MIEC-MRs) were suggested for hydrogen separation via a process coupling water splitting.<sup>[156–159]</sup> The reaction of water to oxygen and hydrogen is simple, but is difficult to achieve in a traditional reactor. The water splitting conversion is only 0.1% even at a high temperature of 1600 °C. In a MIEC-MR, as shown in **Figure 14**, if one side (side I) of the membrane is fed with steam and the other side (side II) is fed with low purity  $\text{H}_2$ , an oxygen chemical potential gradient is established across the membrane; then the water splitting reaction on the side I is significantly improved since the produced oxygen is driven to the side II and consumed by low purity  $\text{H}_2$ . In the above process, the  $\text{H}_2$  separation rate on the side I is equal to the  $\text{H}_2$  consumption rate on the side II. The total reaction including both sides is zero, but pure  $\text{H}_2$  is produced after cooling and drying the effluent of the side I. In a word, high purity  $\text{H}_2$  is obtained by consuming low purity  $\text{H}_2$ . Thus, the whole process can be regarded as a  $\text{H}_2$  separation process by coupling  $\text{H}_2\text{O}$  splitting and  $\text{H}_2$  oxidation reactions in a MIEC-MR.

Early studies have shown that it is possible to decompose water into hydrogen and oxygen at very high temperatures (1400–1800 °C) with the help of MIEC membranes. Naito et al. achieved a  $\text{H}_2$  separation rate of  $0.6 \text{ mL cm}^{-2} \text{ min}^{-1}$  at 1683 °C by regulating the oxygen partial pressure on the other side of the  $\text{ZrO}_2\text{-TiO}_2\text{-Y}_2\text{O}_3$  membrane.<sup>[160]</sup> Later, Balachandran et al. prepared a metal-ceramic dual-phase membrane, 40 vol% Ni – 60 vol% GDC (Gd doped  $\text{CeO}_2$  oxide), and obtained a  $\text{H}_2$  separation rate of  $6.0 \text{ mL cm}^{-2} \text{ min}^{-1}$  by coupling the  $\text{H}_2$  oxidation reaction on the side II.<sup>[161]</sup>

## 6.2. Recent Advances and Future Challenges

Membrane materials and catalysts are the keys to determine the  $\text{H}_2$  separation performance of MIEC-MR. In a MIEC-MR, there are three processes involved, i.e., the water decomposition reaction on the catalyst layer of side I, the oxygen ionic – electronic ambipolar diffusion through the membrane bulk

and the  $\text{H}_2$  oxidation reaction on the catalyst layer of side II. Therefore, the  $\text{H}_2$  separation rate of a MIEC-MR is closely related to the catalytic activities of catalysts on both sides toward the water splitting reaction and  $\text{H}_2$  oxidation reaction, and the ionic – electronic ambipolar diffusion rate. As a MIEC membrane is used for  $\text{H}_2$  separation, both sides of the membrane are exposed in strong reducing atmospheres. Thus, the requirement on structural stability of membrane materials is much higher than those operated for oxygen separation and syngas production, in which air is typically fed to side I. For MIEC materials, their ionic and electronic conductivities change with oxygen partial pressure greatly in the range of  $1\text{--}10^{-21}$  atm at elevated temperatures,<sup>[162]</sup> while the MIEC-MR for  $\text{H}_2$  separation is typically operated in the oxygen partial pressure of  $10^{-10}\text{--}10^{-21}$  atm.<sup>[157–159,163]</sup> Accordingly, the design of membrane materials for  $\text{H}_2$  separation is different from that for oxygen separation. Thus, developing materials with good stability and high oxygen permeability is a challenging task in this field.

According to the phase composition of the material, MIEC membranes can be divided into single phase membranes typically made of perovskite oxides, and dual-phase (DP) membranes made of oxygen ionic conductors and electronic/mixed conductors.<sup>[164]</sup> Researchers have examined the performance of many single-phase membrane materials for  $\text{H}_2$  separation via the water decomposition reaction. MIEC membranes, such as  $\text{SrFeCo}_{0.5}\text{O}_x$ ,<sup>[165]</sup>  $\text{BaZr}_x\text{Co}_y\text{Fe}_z\text{O}_{3-\delta}$  ( $x+y+z=1$ ),<sup>[166]</sup>  $\text{La}_{0.6}\text{Sr}_{0.4}\text{Co}_{0.2}\text{Fe}_{0.8}\text{O}_{3-\delta}$ ,<sup>[167]</sup>  $\text{La}_{0.7}\text{Sr}_{0.3}\text{Cu}_{0.2}\text{Fe}_{0.8}\text{O}_{3-\delta}$ ,<sup>[168]</sup>  $\text{Ba}_{0.98}\text{Ce}_{0.05}\text{Fe}_{0.95}\text{O}_{3-\delta}$ ,<sup>[169]</sup> etc., have been investigated for  $\text{H}_2$  production via water splitting. The  $\text{H}_2$  production rates are high and increase with the reduction of membrane thickness. For example, the  $\text{H}_2$  production rate was  $4.0 \text{ mL cm}^{-2} \text{ min}^{-1}$  for a 1.04-mm-thick  $\text{SrFeCo}_{0.5}\text{O}_x$  membrane at 900 °C, while it increased to  $17.4 \text{ mL cm}^{-2} \text{ min}^{-1}$  when the thickness was reduced to 20  $\mu\text{m}$ .<sup>[165]</sup> However, perovskite phase decomposition and decline of  $\text{H}_2$  separation rate with time were observed on these membranes.<sup>[169]</sup>  $\text{La}_{0.9}\text{Ca}_{0.1}\text{FeO}_{3-\delta}$ <sup>[170]</sup> and  $\text{SrMg}_{0.15}\text{Zr}_{0.05}\text{Ti}_{0.8}\text{O}_{3-\delta}$ <sup>[171]</sup> with higher stability were prepared for water splitting, while their  $\text{H}_2$  separation rates are



one order magnitude lower than those of membranes mentioned above. DP membranes typically contain a fluorite phase oxide, e.g., doped CeO<sub>2</sub> or Y<sub>2</sub>O<sub>3</sub> stabilized ZrO<sub>2</sub>, as the ionic conducting phase, a metal/perovskite oxide as the electronic/mixed conducting phase. These membranes exhibit both higher H<sub>2</sub> separation rate and phase stability under the condition for water splitting.<sup>[157–161,163]</sup> For example, a 0.50-mm-thick Ce<sub>0.85</sub>Sm<sub>0.15</sub>O<sub>1.925</sub>–Sm<sub>0.6</sub>Sr<sub>0.4</sub>Cr<sub>0.3</sub>Fe<sub>0.7</sub>O<sub>3-δ</sub> (SDC-SSCF) DP membrane exhibited a H<sub>2</sub> separation rate of 70 mL cm<sup>-2</sup> min<sup>-1</sup> at 900 °C, and no microstructure and phase changes were observed after more than 500 h on-stream.<sup>[159]</sup>

Except operation conditions, including temperature and oxygen partial pressures, membrane composition, microstructure, thickness, and activity of catalysts on both sides have significant influences on the H<sub>2</sub> separation rate. For ceramic-ceramic DP membranes, one with a higher electronic conductivity in the oxygen partial pressure range of 10<sup>-10</sup>–10<sup>-15</sup> atm exhibits a higher H<sub>2</sub> separation rate. Because the electronic conduction of MIEC perovskite phase changes from p-type to n-type in this oxygen partial pressure range, in which the electronic conductivity is the lowest and electron transfer becomes the limiting step for the ambipolar diffusion in membrane bulk.<sup>[172]</sup> In previous investigation on DP membranes for oxygen separation, the microstructure characteristics, including grain size, grain boundaries, elemental distribution in the two phases, spatial distribution of the two phases, porous structure of the porous support layer etc., have been identified to show significant influences on the oxygen permeation flux.<sup>[1,164]</sup> Similarly, these microstructure characteristics of DP membranes are closely related to the H<sub>2</sub> separation performance.<sup>[173]</sup> According to the Wagner equation and the separation mechanism, the H<sub>2</sub> separation rate is proportional to the reciprocal of membrane thickness. However, most of studies reveal that the increment of H<sub>2</sub> separation rate is much lower than the predicted value when improving the performance by reducing the thickness of the membranes,<sup>[159,161]</sup> indicating the catalytic reaction (i.e., water splitting and H<sub>2</sub> oxidation reaction) rates on both sides dominate the process of H<sub>2</sub> separation. For example, as the thickness of Ni-GDC DP membrane decreased from 1.70 to 0.10 mm, the H<sub>2</sub> separation rate only increases from 1.2 to 4.3 mL cm<sup>-2</sup> min<sup>-1</sup>.<sup>[161]</sup> A simple model was used to study the rate determining step of the H<sub>2</sub> separation process on a SDC-SSCF DP membrane with a Ni/SDC catalyst on both sides.<sup>[159]</sup> Although Ni/SDC, which exhibits the highest activity among the Fe, Co, Ni/SDC catalysts, was used to catalyze both water splitting and H<sub>2</sub> oxidation reactions, for a 0.36-mm-thick membrane, the bulk diffusion resistance is 38.1–50.6% of the total resistance in the temperature range of 800–950 °C, indicating the surface reactions (including both water splitting and H<sub>2</sub> oxidation) dominate the H<sub>2</sub> separation process.<sup>[159]</sup> Ru/SDC showed much higher catalytic activity toward the two reactions. An asymmetric SDC-SSCF DP membrane with 38-μm-thick dense layer showed a H<sub>2</sub> separation rate of > 21 mL cm<sup>-2</sup> min<sup>-1</sup>.<sup>[157]</sup> This value is comparable to Pd-based membranes and 1–3 orders of magnitude higher than mixed protonic-electronic conducting membranes. In addition, MIEC membranes for H<sub>2</sub> separation show high stability even in atmosphere containing high concentrations of CO<sub>2</sub> and H<sub>2</sub>S.<sup>[128,158,163]</sup> For example, the asymmetric SDC-SSCF DP membrane has been

successfully operated for 400 h fed with a syngas containing 500–1000 ppm H<sub>2</sub>S to side II to mimic the mixed gas from a coal gasifier.<sup>[128]</sup>

Similar to Pd-based membrane reactors, natural gas conversion, water-gas-shift and dehydrogenation reactions can be realized in MIEC-MR by feeding side I with steam and side II with natural gas, syngas, etc., respectively. If air and steam with proper ratio is fed to side I and natural gas is fed to side II, two types of syngas, i.e., syngas (H<sub>2</sub>+N<sub>2</sub>) for ammonia synthesis and syngas (H<sub>2</sub>+CO) for liquid fuels synthesis, can be produced in one step in MIEC-MR.<sup>[174]</sup> This MIEC-MR shows high process intensification and significant energy saving (>60%). While, if the side I is fed with steam and side II is fed with syngas coming from a coal gasifier, the MIEC-MR can be used for H<sub>2</sub> production or integrated with the pre-combustion process for power generation and carbon capture. The system efficiency of the MIEC-MR integrated pre-combustion process is 3.6%-point higher than the process using amine-based solvents for carbon capture.<sup>[127]</sup>

### 6.3. Opportunities

Hydrogen will occupy an important position in future energy system, in which its production and separation are the key links. MIEC-MR can couple water decomposition reaction with various oxygen consumption reactions, which provide a new idea for H<sub>2</sub> production and purification. For asymmetric MIEC membranes with thin dense layers, reactions on both sides become the rate limiting steps of the H<sub>2</sub> separation process. A separation rate of 100 mL cm<sup>-2</sup> min<sup>-1</sup> is possible to be achieved on DP membranes if high activity catalysts and optimized membrane microstructure can be developed to minimize the reaction polarization and concentration polarization. The H<sub>2</sub> separation rate of MIEC-MR is comparable to Pd-based composite membranes, indicating the separation rate is not the main constraint for the application of MIEC-MR. Although some MIEC membranes have been reported to be stable in atmosphere containing steam, H<sub>2</sub>, CO, CO<sub>2</sub>, and H<sub>2</sub>S for several hundred hours, much long tests should be done to verify the stability and reliability of MIEC-MR under much complex operation conditions, such as elevated pressures, start and stop cycles, thermal shock, impurities containing halogens, phosphorus, silicon etc. Most of MIEC DP membranes for H<sub>2</sub> production via water splitting are based on doped ceria. However, these materials experience a remarkable chemical expansion under reducing atmospheres at elevated temperatures due to the reduction of Ce<sup>4+</sup> to Ce<sup>3+</sup>,<sup>[175]</sup> which increases the break risk of membranes. Therefore, the development of membrane materials is still on the way. MIEC membranes were operated at high temperatures, typically in the range of 800–1000 °C, for water splitting in the current researches. Degradation of MIEC-MR due to catalysts sintering and elemental segregation of membrane materials would become serious at high temperatures. It is possible to achieve high H<sub>2</sub> separation rates at a low temperature (down to 600 °C) if highly active nano catalysts were applied on asymmetric membranes with thin dense layer. The H<sub>2</sub> oxidation reaction has been well studied in the field of solid oxide fuel cells, and the results are helpful

for understanding the reaction mechanism in MIEC-MR. However, the mechanism of water splitting reaction is still not well addressed because it is a non-spontaneous reaction, that inducing many difficulties in the investigation of the reaction mechanism. In addition, the type of MIEC-MR or geometrical structure is also an important factor affecting the performance of MIEC-MR, while that is still unclear. It is expectable that a flat MIEC-MR with short contact time between reactants and membranes shows limited water splitting conversion, while a tubular MIEC-MR with counter current feeding mode delivers high water splitting conversion since oxygen partial pressure gradient is kept at high values along the tube.

#### 6.4. Concluding Remarks

In summary, MIEC-MR for H<sub>2</sub> separation realized by coupling water splitting and H<sub>2</sub> oxidation reactions is a new method and has shown attractable performance for applications. Membrane materials, membrane structures and catalysts have significant influences on the separation rate and stability of the MIEC-MR. The design of membrane materials is different from those used for oxygen separation since the working oxygen partial pressure is much lower for hydrogen separation. Single phase perovskite membranes and DP membranes have been explored for H<sub>2</sub> separation, while DP membranes display higher separation rate and stability. The MIEC-MR shows outstanding stability in atmosphere containing high concentrated acid gases comparing to other dense inorganic membranes for H<sub>2</sub> separation. Only few researches were focused on the development of catalysts at present, and mechanisms of water splitting and H<sub>2</sub> oxidation reaction need deep understanding to help the design of stable and active catalysts. Water splitting reaction can be coupled with many oxidation reactions in the MIEC-MR for simultaneous producing high purity H<sub>2</sub> and other gases. Therefore, the application of the MIEC-MR is not limited to H<sub>2</sub> separation. Although the research about MIEC-MR is still in the initial stage, it has exhibited many advantages and is promising for H<sub>2</sub> production and separation.

## 7. MIEC Membranes for Hydrogen Production

### 7.1. Status

Hydrogen is not only the cleanest promising energy carrier, but also an important raw material in petrochemical (methanol synthesis etc.), agrochemical (ammonia synthesis etc.) and other industrial applications. Nowadays, most H<sub>2</sub> is produced from fossil resource such as steam reforming of methane (CH<sub>4</sub> + H<sub>2</sub>O = 3H<sub>2</sub> + CO, Δ*H* (25 °C) = 226 kJ mol<sup>-1</sup>).<sup>[176]</sup> This process is highly energy intensive as it is an endothermic reaction. Another method is partial oxidation of methane (POM, CH<sub>4</sub> + 1/2O<sub>2</sub> = 2H<sub>2</sub> + CO, Δ*H* (25 °C) = -36 kJ mol<sup>-1</sup>), which is mildly exothermic and produce H<sub>2</sub> and CO with molar ratio of 2/1 (suitable for methanol synthesis and F-T process), but pure oxygen is required.<sup>[177]</sup> As an ideal oxygen supplier, MIEC membranes can separate oxygen with 100% selectivity, and in situ provide pure oxygen to POM reaction.<sup>[146]</sup> In other words,

the oxygen separation and reaction processes can be simultaneously realized in one MIEC membrane unit, which can significantly simplify the technological scheme and reduce the process energy consumption.<sup>[1]</sup>

In addition, some other developing technologies can also produce H<sub>2</sub>, such as photo/electrochemical water splitting, biomass pyrolysis/fermentation and coal gasification.<sup>[178]</sup> Among them, the water splitting (H<sub>2</sub>O = H<sub>2</sub> + 1/2O<sub>2</sub>) has attracted extensive attention, as water is recommended as the ideal source. However, due to the thermodynamic limitation (equilibrium constant is around 2.1 × 10<sup>-8</sup> at 900 °C), the H<sub>2</sub> generation efficiency is low. It is known that, extracting produced oxygen is a promising strategy to improve the H<sub>2</sub> generation rate, which can shift the equilibrium to hydrogen generation direction. Therefore, the MIEC membranes were applied in hydrogen production by water splitting, through which the generated oxygen can be in situ removed and the H<sub>2</sub> formation rate can be accelerated.<sup>[160]</sup> Moreover, some oxygen-consuming reactions (like POM, etc.) can be coupled with water splitting, which can provide higher oxygen partial pressure gradient across the membrane with faster oxygen extracting rate, resulting in enhanced H<sub>2</sub> production rate.<sup>[166]</sup> It is worth noting that, through the MIEC membrane reactors, not only the thermodynamic equilibrium can be overcome, but also two different valuable products can be obtained simultaneously, such as hydrogen, synthesis gas, ethylene, etc.<sup>[179]</sup>

Therefore, in MIEC membrane reactors, hydrogen can be produced in both feed side (high oxygen chemical potential) from water splitting and sweep side (low oxygen chemical potential) from methane or ethane conversion, as shown in **Figure 15**. In the feed side, hydrogen is generated by water decomposition, which can be enhanced by removing of oxygen through the MIEC membranes. In the sweep side, the permeated oxygen reacts with oxygen consuming reactions (e.g., POM), which can not only establish large oxygen chemical potential gradient to improve the hydrogen generation speed but also produce hydrogen containing chemicals like synthesis gases. In the MIEC membrane reactor, reaction-separation-reaction can be coupled in one unit, realizing a highly intensified and energy saving process for hydrogen production.

### 7.2. Recent Advances and Future Challenges

In the last two decades, MIEC membrane reactors have obtained worldwide attentions as they can integrate reactions with separation in one unit, realizing highly efficient hydrogen production with highly intensified and energy saving process. In early studies, the MIEC membranes were applied to supply oxygen for POM reaction, where the oxygen separation and catalytic oxidation reaction can be simultaneously accomplished.<sup>[180]</sup> The hydrogen-containing syngas (with H<sub>2</sub>:CO = 2:1) was economically produced without N<sub>2</sub>/NO<sub>x</sub>, which can be directly used for liquid-fuel production through F-T processes without further purification. This membrane reactor combined three industrial steps (steam reforming, air separation, and mixed reforming) together, greatly reduced the operation costs and energy consumption. In the fixed bed reactor, the POM reaction is dangerous when directly mixing the methane

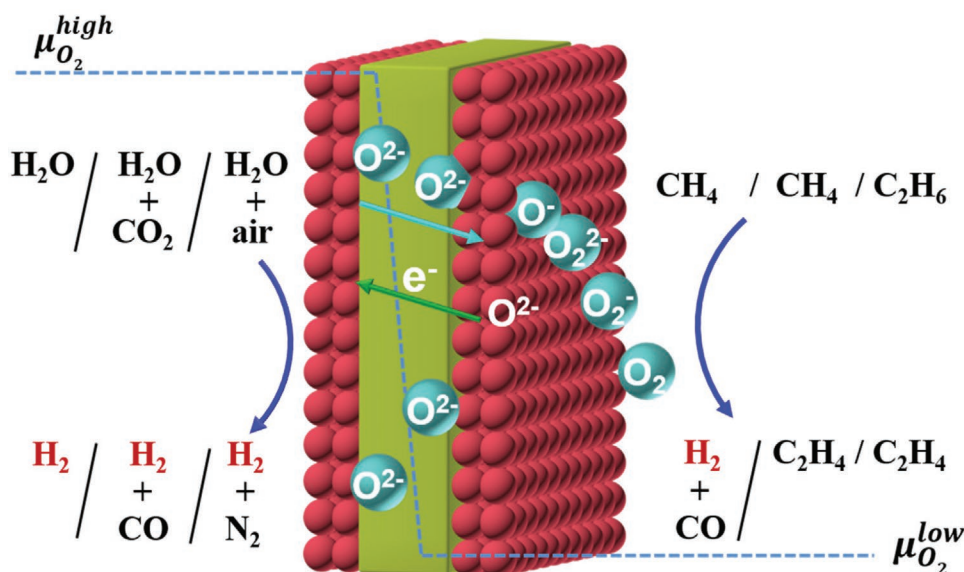


**Figure 15.** Schematic drawing of MIEC membrane reactors for hydrogen production.

with oxygen, due to the probable explosion and temperature runaway. In contrast, in MIEC membrane reactor, the methane and oxygen/air are fed in two different sides, and oxygen species are continuously supplied through the membrane to react with methane, which can avoid the deep oxidation of products and other security issues.<sup>[181]</sup> However, safety problems still exist if leakages or breakages occurring during the operation at high temperature.

Meanwhile,  $H_2$  production from  $H_2O$  splitting in membrane reactors is coming into view, because the membrane can in situ remove generated oxygen and thus intensify the hydrogen production rate. In early studies, the hydrogen production rate was low even the reactors were operated at  $>1400\text{ }^\circ\text{C}$ , due to the limitation of poor permeability of membranes and low oxygen chemical gradient.<sup>[160]</sup> Therefore, Wang et al. applied  $BaCo_xFe_yZr_{1-x-y}O_3$  (BCFZ) hollow-fiber membrane, which possesses thin thickness and high oxygen permeation rate, for extracting the produced oxygen by high-temperature water splitting.<sup>[166]</sup> Moreover, POM reaction was performed in the sweep side to rapidly decrease oxygen concentration and establish large oxygen chemical potential gradient. In this case, a maximum  $H_2$  production rate of  $10\text{ mL min}^{-1}\text{ cm}^{-2}$  was achieved at  $900\text{ }^\circ\text{C}$ .<sup>[166]</sup> This work firstly reported the coupling of water splitting and POM reaction to produce hydrogen and syngas simultaneously in MIEC membrane reactor, which provide an effective strategy for following researches.<sup>[166]</sup> Later, Zhu et al. fed air and water with an appropriate ratio into the high oxygen chemical potential side and methane into the other side.<sup>[174]</sup> As a result, the oxygen from air and water decomposition transport through the membrane and left a mixture of  $H_2$  and  $N_2$  with 3:1 ratio, which is ammonia synthesis gas. Meanwhile, in the low oxygen chemical potential side,  $CH_4$  reacts with the permeated oxygen to  $H_2$  and  $CO$  with 2:1 ratio, which is liquid-fuel synthesis gas. Therefore, this MIEC membrane reactor can simultaneously produce different synthesis gases for different industries with 63% reduction of energy consumption, which integrated nine steps (6 steps for ammonia synthesis

gas production and 3 steps for liquid-fuel synthesis gas production) in one step.<sup>[174]</sup> Recently, Jiang et al. proposed a solar-to-fuel technology in MIEC membrane reactor, which combines catalytic thermolysis, solar energy and oxygen separation membrane together to realize  $CO_2$  and  $H_2O$  into synthesis gas.<sup>[182]</sup> In this reactor, the energy can be supplied by solar and the thermodynamic equilibrium limits of both  $CO_2$  and  $H_2O$  decomposition reactions can be overcome via continuous oxygen removal by membrane. Similar to other reactors, POM reaction was applied to generate low oxygen chemical potential and syngas with  $H_2/CO = 2$ , suitable for F-T processes. In the feed side, the feeding ratio of  $CO_2$  and  $H_2O$  can be adjusted according to practical applications to obtain various synthesis gas with different  $H_2/CO$  ratio.<sup>[182]</sup> Except the POM reaction, other oxygen consuming reactions can be applied to establish large oxygen chemical potential gradient and produce valuable chemicals. For instance, Cao et al. applied oxidative coupling of methane (OCM) to  $C_2$  hydrocarbons reaction to consume oxygen from water decomposition.<sup>[183]</sup> Hence, both the equilibrium limitations of water splitting and OCM reaction are simultaneously overcome by using the MIEC membranes. Instead of synthesis gas, ethylene can be obtained and directly utilized in industry. Beyond that, oxidative dehydrogenation of ethane and oxidative steam reforming of ethanol are also promising in hydrogen production, through the integrated MIEC membrane by reaction-separation-reaction coupling.<sup>[184,185]</sup>

With the developments of membrane materials and the introduction of oxygen consuming reactions, a maximum hydrogen flux of  $174\text{ mL min}^{-1}\text{ cm}^{-2}$  at  $900\text{ }^\circ\text{C}$  was obtained.<sup>[165]</sup> However, there are still several challenges need to be consideration in practical applications. During water splitting process, the generated oxygen should be rapidly removed to shift the equilibrium to hydrogen production, hence, the membrane materials should possess excellent oxygen permeability. To establish large oxygen chemical potential gradient, oxygen consuming reactions are used, forming strong reductive environment in the sweep side. At the same time, the atmosphere in feed side is

also reductive with the hydrogen formation, leading the MIEC membranes are surrounded by reductive atmosphere. Moreover, when hydrocarbons are used to consume oxygen, deep oxidation reaction might happen to  $\text{CO}_2$ .<sup>[180]</sup> Therefore, the membrane materials should possess not only excellent oxygen permeability but also high stability under reducing and  $\text{CO}_2$ -containing atmosphere. However, extensive investigations are focused on the Co-containing and alkaline-earth metals-containing perovskites duo to their high oxygen permeance, whereas their stability are poor due to the reduction of Co and formation of carbonates of alkaline-earth metals.<sup>[167,186]</sup>

In the catalytic MIEC membrane reactors, the thermodynamic limitation can be overcome by the separation membrane, while the kinetic restriction should be solved by catalysts. To obtain fast hydrogen production rates and to improve the dynamic issues and selectivity of target products, high efficient catalysts should be applied. For instance, by the introduction proper catalyst, the water splitting reaction and the POM performance were enhanced.<sup>[157]</sup> It should be noted that, most applied catalysts in MIEC membrane reactors are different from membrane materials, which might react with each other during the long-term high temperature operations, thus destroying the stability of membrane reactors. And in most alkane conversion reactions for oxygen consuming like POM, severe coke was formed on the catalyst, leading the decline of catalytic activity and the decreased performance.<sup>[187]</sup>

### 7.3. Opportunities

Catalytic MIEC membrane reactors are effective technologies for hydrogen production by reaction-separation-reaction coupling in one unit. Through coupling of an endothermic reaction (e.g., water splitting) with an exothermic reaction (e.g., POM), energy self-sufficiency can be achieved in the membrane reactors. Moreover, the thermodynamic limitation of  $\text{H}_2$  production from water splitting can be overcome through removing generated oxygen by MIEC membranes. In the sweep side, oxygen consuming reaction are applied to react with permeated oxygen to establish large oxygen chemical gradient across the membrane, meanwhile producing valuable chemicals. These MIEC membrane reactors are complex, which gather different processes (reaction and separation) and different materials (membrane and catalyst) in one unit. As the core of MIEC membrane reactors, the first priority is developing suitable materials for hydrogen production. To ensure sufficient stability in reducing and  $\text{CO}_2$ -containing atmosphere, the Co-free and alkaline-earth metal-free materials are better choices. The widely applied strategies to tune the separation performance are changing compositions, including doping both anions and cations, as well as introduction of deficiencies.<sup>[188–190]</sup> Besides, dual phase membranes, in which oxygen ions and electrons transporting in different phases, exhibit good stability without sacrificing oxygen permeability.<sup>[174]</sup> Another effective strategy to enhance the separation performance is modification of membrane configurations by using an asymmetric membrane or a hollow fiber membrane to reduce the membrane thickness and then decrease the oxygen ions diffusion resistances.<sup>[191,192]</sup> More than this, the high surface area/volume ratio and porous support can

also promote the reaction performance. Importantly, proper catalysts are indispensable in MIEC membrane reactors, which determine the hydrogen and valuable products yields. Nowadays, most of the catalysts are supported by alumina, silica or zeolites, which might react with membrane materials at high temperature. Therefore, the in situ precipitating of nanoparticle catalysts in membrane materials are more suitable for MIEC membrane reactor, which can not only provide catalytic activities for reactions, but also in situ supply/remove oxygen.<sup>[193]</sup> However, few researches focus on the catalyst's development for MIEC membrane reactors, which need more input to design the catalyst at the atomic level by combining advanced characterization methods and theoretical calculations to speed up the hydrogen production.

### 7.4. Concluding Remarks

In summary, MIEC membrane reactors can realize hydrogen production from both water and fossil fuel, through reaction-separation-reaction coupling. The products can be tuned to pure hydrogen, ammonia synthesis gas ( $\text{H}_2/\text{N}_2 = 3$ ), liquid-fuel synthesis gas ( $\text{H}_2/\text{CO} = 2$ ) and valuable hydrocarbons, which can be directly utilized in further industrial processes. However, more effort should be paid to develop membrane materials with excellent permeability and good stability, appropriate geometrical structure with thinner thickness and enough strength, as well as suitable catalyst with efficient catalytic activity. Although recent studies on MIEC membrane reactors for hydrogen production are in their infancy theoretical and experimental stadium, and no industrial scale application, while these highly intensive reactors are energy-saving, high safety and environmental friendly, which are promising technologies for hydrogen production.

## 8. MIEC Cathode Development for Solid Oxide Fuel Cells

### 8.1. Status

Solid oxide fuel cells (sometimes also known as ceramic fuel cells) are electrochemical energy conversion devices that directly transfer the energy stored in chemical bonds of fuels through catalytic electrochemical reactions into electric power (electricity) with high efficiency and low emission. One significant advantage of SOFC over many other fuel cells is that it can also perform as an electrochemical reactor, realizing value-added chemicals and electric power co-generation from fuels with zero emission.<sup>[194–196]</sup> Based on the conducting mechanism of the electrolytes, SOFCs can be divided into oxygen-ion conducting SOFC ( $\text{O}^{2-}$ -SOFC) and proton-conducting SOFC ( $\text{H}^+$ -SOFC or PCFC).<sup>[197,198]</sup> In a  $\text{O}^{2-}$ -SOFC, during operation (power generation),  $\text{O}_2$  from surrounding air is reduced to oxygen ion over the cathode surface by acquiring electron transported from anode through the external circuit, the oxygen ion then diffuses through the electrolyte to the anode side, where it reacts with  $\text{H}_2$  (fuel) to produce  $\text{H}_2\text{O}$  and electron. Under current polarization, external flow of electron from anode to cathode and



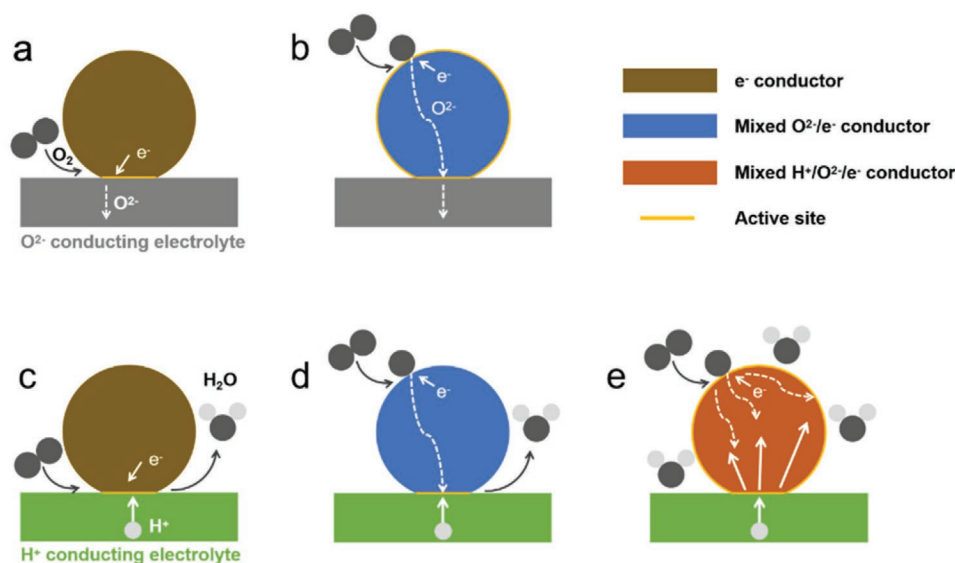


**Figure 16.** Schematic presentation of various electrodes with different electrolytes.  $O^{2-}$ -SOFC based on  $O^{2-}$  conducting electrolyte with a) pure  $e^-$  conducting electrode and b) mixed  $O^{2-}/e^-$  conducting electrode. PCFC based on  $H^+$  conducting electrolyte with c) pure  $e^-$  conducting electrode, d) mixed  $O^{2-}/e^-$  conducting electrode, and e) mixed  $H^+/O^{2-}/e^-$  conducting electrode.

internal diffusion of  $O^{2-}$  from cathode side to anode side happens simultaneously to realize a complete circuit.<sup>[197]</sup> If a PCFC is used, proton ( $H^+$ ) instead of  $O^{2-}$  is transported through the electrolyte and the water is produced at the cathode side instead of anode chamber.<sup>[198]</sup> SOFCs can be operated over a wide range of temperature from as low as 400 °C up to 1000 °C.<sup>[199–201]</sup> However, too high operating temperature (>850 °C) may accelerate the cell performance degradation rate due to promoted electrode sintering and interfacial reactions between different cell components. It is expected, the drop of SOFC operation temperature to the intermediate range (400–650 °C) can effectively reduce system cost, shorten the time for start up and shut down, increase cell efficiency, and prolong cell lifetime.<sup>[202–204]</sup> Therefore, during the past two decades, considerable efforts have been conducted toward decreasing operation temperature of SOFCs to the intermediate range.

The operation temperature of a SOFC is determined by the reaction kinetics at both electrodes and the transport properties of the electrolyte.<sup>[199]</sup> It is believed that PCFC is more preferable for reduced temperature operation because of the high mobility of proton than oxygen ion with lower activation energy for diffusion.<sup>[205,206]</sup> There is an increasing interest in PCFC in recent several years. To reduce the ohmic loss of a SOFC at reduced temperature, thin film electrolyte configuration was widely adopted.<sup>[207–211]</sup> Therefore, the electrode polarization is a more important concern for reducing the operation temperature of a SOFC. As compared to fuel oxidation, the activation of oxygen at cathode is much more difficult, therefore the development of high-performance cathode that demonstrate high activity and durable performance at reduced temperature is key to realize the practical use of intermediate-temperature SOFC.

$La_{0.8}Sr_{0.2}MnO_3$  (LSM) perovskite is a conventional cathode of SOFC with YSZ electrolyte, which shows pure electronic conductivity.<sup>[212]</sup> It is generally believed that the oxygen reduction reaction (ORR) at a SOFC with LSM cathode usually

happens at the cathode-electrolyte-air triple phase boundary (TPB) region.<sup>[213]</sup> Therefore, the active cathodic reaction sites for such SOFC are usually very limited, and operation temperature of higher than 800 °C is needed even for the cell with thin film electrolyte. By applying a cathode with mixed ionic and electronic conductivity, the electrode bulk can also take part in the electrode reactions (for the diffusion of oxygen ion or proton).<sup>[214–216]</sup> **Figure 16** shows the potential pathways for the electrode reactions over the cathode of SOFCs with different conducting properties of the cathodes, i.e., pure electronic conductivity ( $O^{2-}$ -SOFC (Figure 16a) and PCFC (Figure 16c)), mixed oxygen ion and electronic conductivity ( $O^{2-}$ -SOFC (Figure 16b)), mixed proton and electronic conductivity (PCFC (Figure 16d)), and mixed proton-oxygen ion-electronic conductivity (PCFC (Figure 16e)). It shows, that once mixed oxygen ion and electronic conductivity is introduced into cathode of  $O^{2-}$ -SOFC or mixed  $H^+e^-$  conductivity/mixed  $O^{2-}H^+e^-$  conductivity is introduced into cathode of PCFC, the cathodic reactions could extend to the whole exposed electrode surface, and significant cell performance at reduced temperature is expected. A breakthrough was made by Shao and Haile in 2004, they applied the well-known mixed conducting oxygen ion and electronic perovskite  $Ba_{0.5}Sr_{0.5}Co_{0.5}Fe_{0.5}O_{3-\delta}$  (BSCF), which was previously developed as a material for ceramic membrane for oxygen separation, as a cathode for a SOFC with thin film samaria-doped ceria electrolyte ( $\approx 20 \mu\text{m}$ ), a record-breaking maximum power density of  $>1 \text{ W cm}^2$  was reached.<sup>[217]</sup>

## 8.2. Recent Advances and Future Challenges

### 8.2.1. SOFCs Based on $O^{2-}$ Conducting Electrolytes

Mixed oxygen ion and electron conducting perovskite oxides have been extensively exploited for ORR at intermediate

**Table 4.** Ionic conductivity ( $e^-/O^{2-}$ ), TEC values, ASR values of symmetric cells, peak power output and operational stability of  $O^{2-}$ -SOFCs based on some representative reported cathodes.

Cathode	$\sigma, e^-$ [ $S\text{ cm}^{-1}$ ]	$\sigma, O^{2-}$ [ $S\text{ cm}^{-1}$ ]		TEC [ $\times 10^{-6}\text{ K}^{-1}$ ]	ASR [ $\Omega\text{ cm}^2$ ]		SOFC Configuration	Power Density [ $\text{mW cm}^{-2}$ ]		Stability [h]	Ref.
		T	$\sigma, O^{2-}$		600 °C	500 °C		600 °C	500 °C		
$\text{La}_{0.6}\text{Sr}_{0.4}\text{Co}_{0.2}\text{Fe}_{0.8}\text{O}_{3-\delta}$	215–270	800	0.022	13.8	2.63	39.75	Ni-SDC SDC	760		250	[222,238,239]
$\text{Sm}_{0.5}\text{Sr}_{0.5}\text{CoO}_{3-\delta}$	700–1731	800	0.42	25.5	0.42	3.44	Ni-SDC SDC (20 $\mu\text{m}$ )	690	200		[240–242]
		700	0.20								
$\text{Ba}_{0.5}\text{Sr}_{0.5}\text{Co}_{0.8}\text{Fe}_{0.2}\text{O}_{3-\delta}$	27–32	800	0.92	21.0	0.073	0.57	Ni-SDC SDC (20 $\mu\text{m}$ )	1010	402	120	[217,243]
		700	0.50								
$\text{SrCo}_{0.8}\text{Nb}_{0.1}\text{Ta}_{0.1}\text{O}_{3-\delta}$	81–146	600	0.032		0.025	0.16	Ni-GDC GDC (14 $\mu\text{m}$ )		1220		[214]
		500	0.005								
$\text{SrSc}_{0.175}\text{Nb}_{0.025}\text{Co}_{0.8}\text{O}_{3-\delta}$	20–35				0.039	0.31	Ni-SDC SDC (10 $\mu\text{m}$ )		910		[226]
$\text{SrNb}_{0.1}\text{Co}_{0.7}\text{Fe}_{0.2}\text{O}_{3-\delta}$				26.0	0.052	0.301	Ni-SDC SDC (20 $\mu\text{m}$ )	1587	610		[244]
$\text{Sr}_{0.95}\text{Ag}_{0.05}\text{Nb}_{0.1}\text{Co}_{0.9}\text{O}_{3-\delta}$					0.038	0.22	Ni-SDC SDC (12 $\mu\text{m}$ )	1984	1106	140	[227]
$\text{Ba}_2\text{Bi}_{0.1}\text{Sc}_{0.2}\text{Co}_{1.7}\text{O}_{6-\delta}$				17.9	0.22		Ni-YSZ YSZ (10 $\mu\text{m}$ )  SDC (5 $\mu\text{m}$ )	230			[233]
$\text{PrBa}_{0.5}\text{Sr}_{0.5}\text{Co}_{1.5}\text{Fe}_{0.5}\text{O}_{6-\delta}$	428–1170			15.2	0.057	0.33	Ni-GDC GDC (15 $\mu\text{m}$ )	2160	710	150	[245,246]
$\text{GdBa}_{0.5}\text{Sr}_{0.5}\text{CoFeO}_{6-\delta}$	209–401				0.08	0.86	Ni-GDC GDC (14 $\mu\text{m}$ )	1310	410		[232]
$\text{BaCo}_{0.4}\text{Fe}_{0.4}\text{Zr}_{0.1}\text{Y}_{0.1}\text{O}_{3-\delta}$	0.9–1.5			21.6	0.28	1.18	Ni-SDC SDC (10 $\mu\text{m}$ )	970		2500	[197,237]

temperatures, which show obviously improved performance in comparison with that of LSM because the active sites could effectively extend to the whole exposed cathode surface if the cathodes possess sufficiently high oxygen ionic conductivity.<sup>[215,218,219]</sup>

**Table 4** shows the representative mixed conducting perovskite-based materials and the corresponding performance as cathodes of SOFCs at intermediate temperatures, reported up to now. LSCF is a typical mixed conducting perovskite, which is extensively used in SOFCs and exhibits higher ORR activity than LSM at intermediate temperatures (600–800 °C). However, for even lower temperature, the oxygen-ion conductivity because too low, demonstrating insufficient ORR activity.<sup>[220–222]</sup> Thus, new mixed conductors with higher oxygen ionic conductivity are needed to realize the operation of  $O^{2-}$ -SOFCs at lower temperatures than 600 °C. During the past, extensive researches have demonstrated that  $\text{SrCoO}_{3-\delta}$  (SC)-based perovskites have superior ORR activity at intermediate temperature because the low valence of  $\text{Sr}^{2+}$  and good reducibility of Co cations could provide a higher oxygen vacancy concentration and a weaker bonding energy for  $O^{2-}$  mobility.<sup>[202]</sup> Early representative SC-based single perovskites are  $\text{Sm}_{0.5}\text{Sr}_{0.5}\text{CoO}_{3-\delta}$  (SSC) and BSCF.<sup>[217,223–225]</sup> A  $\text{Gd}_{0.1}\text{Ce}_{0.9}\text{O}_{2-\delta}$  supported symmetric cell with a novel structured SSC cathode exhibited an area specific resistance (ASR) of  $0.485\ \Omega\text{ cm}^2$  at 600 °C in air,<sup>[223]</sup> which is much larger than that of the BSCF cathode ( $0.063\ \Omega\text{ cm}^2$ ).<sup>[217]</sup>

Recently, some fixed high valence transition metals co-substituted SC-based single perovskite cathodes, such as  $\text{SrSc}_{0.175}\text{Nb}_{0.025}\text{CoO}_{3-\delta}$  (SSNC)<sup>[226]</sup> and  $\text{SrCo}_{0.8}\text{Nb}_{0.1}\text{Ta}_{0.1}\text{O}_{3-\delta}$  (SCNT),<sup>[214]</sup> were also reported. The high cathodic performance was linked to an optimal balance of surface electron transfer, ionic mobility and oxygen vacancies of the perovskite electrode as promoted by the synergistic effects of the fixed valence transition metals. In addition to cation substitutions in SC-based perovskites, introducing nano-catalysts is also an effective approach to enhance ORR activity at intermediate temperature. Zhu et al. proposed an in situ formed Ag nanoparticles modified  $\text{Sr}_{0.95}\text{Nb}_{0.1}\text{Co}_{0.9}\text{O}_{3-\delta}$  cathode with enhanced oxygen surface exchange kinetics, thus leading to superior ORR activity at intermediate temperature.<sup>[227]</sup> They also explained that decreasing the oxygen vacancy concentrations and increasing the average bonding energy of B-site cations and oxygen in perovskite could enhance the  $\text{CO}_2$  resistance of SC-based cathodes via investigating the serious of  $\text{SrNb}_{0.1}\text{Co}_{1-x}\text{Fe}_x\text{O}_{3-\delta}$  materials.<sup>[228]</sup>

Some  $\text{BaCoO}_{3-\delta}$  (BC)-based perovskites, including both single and double perovskites, also show superior ORR activity at intermediate temperature due to the special properties, i.e., large cation radius of  $\text{Ba}^{2+}$  and good reducibility of Co cations, which could provide more free lattice volume and weak bonding energy of B-O for facilitating oxygen mobility.<sup>[218,229]</sup> It has been

extensively investigated that the most distinguished advantages of BC-based double perovskites over single perovskites are the layered structure and the oxygen vacancies form channels along *a* axis, which is favorable for the oxygen diffusion inside the material.<sup>[218]</sup> It was reported that some cells with representative BC-based double perovskites, such as PrBa<sub>0.5</sub>Sr<sub>0.5</sub>Co<sub>1.5</sub>Fe<sub>0.5</sub>O<sub>5+δ</sub> (PBSCF),<sup>[230]</sup> NdBa<sub>0.5</sub>Sr<sub>0.5</sub>Co<sub>1.5</sub>Fe<sub>0.5</sub>O<sub>5+δ</sub><sup>[231]</sup> and GdBa<sub>0.5</sub>Sr<sub>0.5</sub>Co<sub>1.5</sub>Fe<sub>0.5</sub>O<sub>5+δ</sub>,<sup>[232]</sup> can achieve high power output and excellent operational stability. For example, the Ni-Gd<sub>0.1</sub>Ce<sub>0.9</sub>O<sub>2-δ</sub> anode-supported cell with PBSCF-GDC composite cathode displayed a high peak power density of 0.71 W cm<sup>-2</sup> at 500 °C.<sup>[230]</sup> The high Ba content in Ba<sub>2</sub>Co<sub>2-x</sub>B<sub>x</sub>O<sub>5+δ</sub>, such as Ba<sub>2</sub>Bi<sub>0.1</sub>Sc<sub>0.2</sub>Co<sub>1.7</sub>O<sub>5+δ</sub> and Ba<sub>2</sub>CoMo<sub>0.5</sub>Nb<sub>0.5</sub>O<sub>5+δ</sub>, provides a large lattice spacing due to the larger ion radius of Ba<sup>2+</sup> than Ln<sup>3+</sup>, thus promoting the oxygen-ion diffusion.<sup>[233,234]</sup> For example, Zhou et al. investigated the ORR activity of B-site ordered Ba<sub>2</sub>Bi<sub>0.1</sub>Sc<sub>0.2</sub>Co<sub>1.7</sub>O<sub>6-x</sub> (BBSC) double perovskite cathode with a cubic lattice symmetry. The large oxygen bulk diffusion coefficient, surface exchange coefficient and sufficient electrical conductivity resulted in the high ORR activity of BBSC.<sup>[233]</sup> In addition to the double perovskites, some rationally designed BC-based single perovskites through B-site doping, such as BaCo<sub>0.4</sub>Fe<sub>0.4</sub>Zr<sub>0.2</sub>O<sub>3-δ</sub>,<sup>[235]</sup> BaCo<sub>0.7</sub>Fe<sub>0.22</sub>Y<sub>0.08</sub>O<sub>3-δ</sub>,<sup>[236]</sup> and BaCo<sub>0.4</sub>Fe<sub>0.4</sub>Zr<sub>0.1</sub>Y<sub>0.1</sub>O<sub>3-δ</sub>,<sup>[237]</sup> also achieved high and stable ORR activity at intermediate temperatures. At present, the most promising single perovskite BC-based cathode is BCFZY. As compared to BSCF, BCFZY displays a larger lattice parameter and free cell volume due to the replacement of Co<sup>3+/4+</sup> by larger Zr<sup>4+</sup> and Y<sup>3+</sup> cations. The activation energy of BCFZY is as low as 79.2 kJ mol<sup>-1</sup>, much lower than that of BSCF. As a result, the corresponding O-SOFC displayed a highly attractive PPD of 970 mW cm<sup>-2</sup> at 500 °C in H<sub>2</sub> fuel.<sup>[237]</sup>

### 8.2.2. Protonic Ceramic Fuel Cells

Although a few O<sup>2-</sup>-SOFCs have achieved exceptional performance at the temperature range of 450 to 600 °C, considering the high activation energy (*E*<sub>a</sub>) of oxygen-ion conduction, it is more preferable to adopt protonic conducting electrolyte for reduced temperature operation because of the higher mobility of the proton compared to the oxygen ion. Thus, PCFC can be a durable energy device to convert the chemical energy into electricity with high efficiency at intermediate temperatures.<sup>[206]</sup> Except for the lower *E*<sub>a</sub> of proton diffusion than oxygen ion, the water formation appears at the cathode chamber in PCFC, which can improve the fuel utilization efficiency and lower fuel cycling cost.<sup>[247]</sup> Similar to O<sup>2-</sup>-SOFC, the cathode performance largely determines the power output of PCFCs. Unfortunately, up to now, the performance of most PCFCs still lags far behind that of O<sup>2-</sup>-SOFCs, because of the lack of highly efficient cathodes specifically designed for cells with proton conducting electrolyte.<sup>[206,248]</sup> Anyway during the past five years, considerable improvement in power output of PCFCs at lower than 600 °C have been envisioned. At the early stage of development, conventional mixed oxygen ion-electronic conducting cathodes were usually used in PCFCs with the protonic ceramic electrolytes, such as SSC, La<sub>0.6</sub>Sr<sub>0.4</sub>CoO<sub>3-δ</sub> (LSC), La<sub>0.6</sub>Sr<sub>0.4</sub>Co<sub>1-x</sub>Fe<sub>x</sub>O<sub>3-δ</sub>.

To increase the number of reactive sites, it is key to introduce proton conductivity into the cathode of PCFCs. As mentioned,

if the cathode bulk has sufficient proton conductivity, the whole exposed electrode surface can perform as the active sites for electrode reactions, thus ensuring low electrode polarization resistance. The easiest way to introduce proton conductivity into a cathode is to add another phase with favorable proton conductivity into the conventional mixed oxygen ion and electronic conducting or pure electronic conducting oxide to form a composite electrode. Up to now, many of these types of mixed conductors, such as SSC-BZCY,<sup>[248]</sup> Ag-BSCF,<sup>[249]</sup> LSCF-BaZr<sub>0.7</sub>Y<sub>0.2</sub>Pr<sub>0.1</sub>O<sub>3-δ</sub>,<sup>[250]</sup> Sr<sub>3</sub>Fe<sub>2</sub>O<sub>7-δ</sub>-BaZr<sub>0.3</sub>Ce<sub>0.5</sub>Y<sub>0.2</sub>O<sub>3-δ</sub> (SF-BZCY3),<sup>[247]</sup> PrBaCo<sub>2</sub>O<sub>5+δ</sub>-BaZr<sub>0.7</sub>Y<sub>0.2</sub>Pr<sub>0.1</sub>O<sub>3</sub> (PBC-BZYP)<sup>[251]</sup> and BSCF-BZCY,<sup>[252]</sup> have been reported, which exhibited modestly improved performance as compared to mixed oxygen-ion and electronic conducting cathodes. Unfortunately, the inhomogeneous distribution of the two phases with large grain size in the composite could lead to the limited effective reaction regions.<sup>[253,254]</sup> Also, these simple physical mixing cathode materials usually suffer from poor stability under the operational atmosphere containing large amount of water.<sup>[252]</sup> Recently, we proposed a self-assembly method to develop a composite electrode with superior performance. By applying a material with the nominal composition of BaCo<sub>0.7</sub>(Ce<sub>0.8</sub>Y<sub>0.2</sub>)<sub>0.3</sub>O<sub>3-δ</sub> as a precursor, it was separated into several phases of different conducting behaviors at high temperatures during calcination, thus realizing triple conductivity for the entire electrode. Peak power density of 319 to 985 mW cm<sup>-2</sup> at temperatures between 500 and 650 °C was reached for a cell with such self-assembled composite cathode.<sup>[200]</sup> It thus introduces a new strategy for the development of high-performance mixed conducting composite electrode for PCFCs.

During the past decade, considerable activities have also been devoted to develop the high-performing single-phase cathodes with high triple-conductivity of electrons, oxide ions and protons. By applying such triple-conducting cathodes, the electrochemically active sites can be extended effectively to the entire exposed electrode surface for a significantly improved cathode reaction.<sup>[196,255]</sup> Early efforts to develop single-phase triple-conducting cathodes were mainly focused on partial substituting of the B-site elements (Zr, Y, Ce) in the perovskite-type proton conducting electrolyte materials (such as BaZrO<sub>3</sub>, BaCeO<sub>3</sub>), with multivalent elements (such as Co, Fe) with the development of Fe-doped BaCeO<sub>3</sub> and Co-doped BaZrO<sub>3</sub> perovskite oxides.<sup>[256]</sup> Unfortunately, such past attempts were not so successful. Recently, triple-conducting single-phase cathodes with promising performance data were reported, e.g., 100 to 455 mW cm<sup>-2</sup> at temperatures between 350 and 500 °C for a cell with BaCo<sub>0.4</sub>Fe<sub>0.4</sub>Zr<sub>0.1</sub>Y<sub>0.1</sub>O<sub>3-δ</sub> cathode,<sup>[206]</sup> 690 to 1710 mW cm<sup>-2</sup> at temperatures between 600 and 750 °C for a cell with double perovskite NdBa<sub>0.5</sub>Sr<sub>0.5</sub>Co<sub>1.5</sub>Fe<sub>0.5</sub>O<sub>3-δ</sub> cathode.<sup>[257]</sup>

Table 5 shows the performance comparison of PCFCs at various temperature regimes with different types of cathode materials, as reported in the literature. Different from the traditional oxygen ionic cathodes, triple-conducting cathodes specifically designed for PCFCs exhibited the most excellent power densities in the intermediate to low temperatures. In the future, the triple-conducting cathodes with high proton conductivity are still highly searched after to realize high power output of PCFCs at reduced temperature.

**Table 5.** The peak power output of PCFCs based on some representative reported cathodes.

Cathode	Temperature (°C)	Power Density [mW cm <sup>-2</sup> ]						Ref.
		700	650	600	550	500	450	
Traditional SOFCs cathode	PrBaCo <sub>2</sub> O <sub>5+δ</sub>	545	349	183				[258]
	NdBaCo <sub>2</sub> O <sub>5+δ</sub>	438	250					[259]
	Ba <sub>0.5</sub> Sr <sub>0.5</sub> Co <sub>0.8</sub> Fe <sub>0.2</sub> O <sub>3-δ</sub>	485	436	336	283			[249]
	Sm <sub>0.5</sub> Sr <sub>0.5</sub> CoO <sub>3-δ</sub>	700	560	410				[260]
	PrNi <sub>0.5</sub> Mn <sub>0.5</sub> O <sub>3</sub> -PrO <sub>x</sub>	650	440					[261]
	Ca <sub>3</sub> Co <sub>4</sub> O <sub>9+δ</sub> (2019)	290	220	150				[262]
Mechanical composite cathode	Sm <sub>0.5</sub> Sr <sub>0.5</sub> CoO <sub>3-δ</sub> -BaZr <sub>0.1</sub> Ce <sub>0.7</sub> Y <sub>0.2</sub> O <sub>3-δ</sub>	725	598	445	272			[248]
	Sm <sub>0.5</sub> Sr <sub>0.5</sub> CoO <sub>3-δ</sub> -BaCe <sub>0.5</sub> Zr <sub>0.3</sub> Y <sub>0.1</sub> Zn <sub>0.1</sub> O <sub>3-δ</sub>	528	364	246	143			[253]
	Ba <sub>0.5</sub> Sr <sub>0.5</sub> Fe <sub>0.8</sub> Cu <sub>0.2</sub> O <sub>3-δ</sub> -BaZr <sub>0.1</sub> Ce <sub>0.7</sub> Y <sub>0.2</sub> O <sub>3-δ</sub>	430	301	190				[263]
	La <sub>0.6</sub> Sr <sub>0.4</sub> Co <sub>0.2</sub> Fe <sub>0.8</sub> O <sub>3-δ</sub> -BaZr <sub>0.7</sub> Y <sub>0.2</sub> Pr <sub>0.1</sub> O <sub>3-δ</sub>	172	117	51				[250]
	PrBaCo <sub>2</sub> O <sub>5+δ</sub> -BaZr <sub>0.7</sub> Y <sub>0.2</sub> Pr <sub>0.1</sub> O <sub>3-δ</sub>	254	216	169	133	92		[251]
	Sr <sub>3</sub> Fe <sub>2</sub> O <sub>7-δ</sub> -BaZr <sub>0.3</sub> Ce <sub>0.5</sub> Y <sub>0.2</sub> O <sub>3-δ</sub>	683	530	372	≈250	≈150		[247]
	Ba <sub>0.5</sub> Sr <sub>0.5</sub> Co <sub>0.8</sub> Fe <sub>0.2</sub> O <sub>3-δ</sub> -BaZr <sub>0.1</sub> Ce <sub>0.7</sub> Y <sub>0.1</sub> Yb <sub>0.1</sub> O <sub>3-δ</sub>	634	532	418				[252]
	LaFeO <sub>3</sub> -BaCe <sub>0.51</sub> Zr <sub>0.3</sub> Y <sub>0.15</sub> Zn <sub>0.04</sub> O <sub>3-δ</sub>	420	350	260	100			[264]
	Ca <sub>0.3</sub> Y <sub>0.7</sub> Fe <sub>0.5</sub> Co <sub>0.5</sub> O <sub>3-δ</sub> -BaZr <sub>0.1</sub> Ce <sub>0.7</sub> Y <sub>0.2</sub> O <sub>3-δ</sub>	≈620	≈450	≈300				[265]
	Triple-conducting cathode	Ba <sub>0.5</sub> Sr <sub>0.5</sub> Zn <sub>0.2</sub> Fe <sub>0.8</sub> O <sub>3-δ</sub>	486	415	277	166	61	
BaCe <sub>0.5</sub> Fe <sub>0.5</sub> O <sub>3-δ</sub>		395	276	192	111			[267]
SrFe <sub>0.95</sub> Nb <sub>0.05</sub> O <sub>3-δ</sub>			538	428	341	220	161	[268]
Sr <sub>3</sub> EuFe <sub>2.5</sub> Co <sub>0.5</sub> O <sub>10-δ</sub>		900	720	510	290	190		[269]
Pr <sub>2</sub> NiO <sub>4</sub>			132	96	53			[270]
YBaCo <sub>3</sub> ZnO <sub>7-δ</sub>		307	211	143				[271]
NdBa <sub>0.5</sub> Sr <sub>0.5</sub> Co <sub>1.5</sub> Fe <sub>0.5</sub> O <sub>5+δ</sub>		1370	1050	690				[257]
BaCo <sub>0.4</sub> Fe <sub>0.4</sub> Zr <sub>0.1</sub> Y <sub>0.1</sub> O <sub>3-δ</sub>						455	≈250	[206]
PrBa <sub>0.5</sub> Sr <sub>0.5</sub> Co <sub>1.5</sub> Fe <sub>0.5</sub> O <sub>5+δ</sub>			≈1400	1098	≈780	548	≈380	[205]
BaCo <sub>0.7</sub> (Ce <sub>0.8</sub> Y <sub>0.2</sub> ) <sub>0.3</sub> O <sub>3-δ</sub>			985	743	508	319	187	[198]
Sr <sub>2</sub> Sc <sub>0.1</sub> Nb <sub>0.1</sub> Co <sub>1.5</sub> Fe <sub>0.3</sub> O <sub>6-δ</sub>			840	732	577	405	278	[272]
La <sub>0.7</sub> Sr <sub>0.3</sub> Mn <sub>0.7</sub> Ni <sub>0.3</sub> O <sub>3-δ</sub>	992	≈600	386	≈220	≈140		[273]	

### 8.3. Opportunities

During the past two decades, the major activities in MIEC cathode development are based on experimental studies, which are time consuming, high cost and low efficiency, although recent density functional theory calculations start to show useful assistance in materials screening and design.<sup>[230,274,275]</sup> The development of methodologies for theoretical predication of high performance MIEC cathodes is highly attractive because of low cost and high efficiency. Currently, for low-temperature electrocatalysis, considerable research activities have been conducted to find applicable activity descriptors that can be used to predict new materials, such as A-site ionic electronegativity and  $e_g$  electron occupancy.<sup>[276–278]</sup> However, there are lack of similar works in the field of MIEC cathodes, thus opening a very interesting research area. It should be pointed out that in room temperature electrocatalysis, the catalyst surface is mainly involved, while both the surface and bulk could participate in the ORR for SOFC with MIEC cathode, making it more challengeable to find a reliable activity descriptor. On the other hand, the current advances in machine learning may

provide additional opportunity for the materials screening in MIEC cathode.

Sound match in thermal expansion behavior of the different cell components is important to ensure a long-term thermo-mechanical stability of SOFCs. Unfortunately, the cathode materials that have high ORR activity at intermediate temperature usually are cobalt rich perovskites, which always show high TEC, attributing to the large chemical expansion associated with the oxidation state change and spin state transition of cobalt ions. Although the thermal expansion can be suppressed somewhat through structural tuning, doping or compositing, such cobalt-based perovskites usually still show much larger TEC than the electrolyte. The mismatch in thermal expansion behaviors of the different cell components can cause the easy delamination of cathode layer from electrolyte surface during operation, especially during thermal cycling, consequently quick degradation in cell performance or even the failure of cell is often appeared. Very recent, Shao et al. reported a thermal expansion offset concept by introducing a negative thermal expansion (NTE) material to form composite with cobalt-rich MIEC perovskite, as a result, the TEC of the electrode can be



easily tailored to match the electrolyte.<sup>[279]</sup> The high thermo-mechanical compatibility of such composite electrode with the electrolyte allows a thicker cathode to be used, consequently, further improvement in electrode performance was observed. It thus opens a new way for the development and design of high-performance cathode for IT-SOFCs. Anyway, the potential interfacial reaction between the NTE material with the main active material on a long-term on the performance is still unknown, requiring further clarification.

In most of the current lab-scale researches, the cathodes are directly exposed to the ambient air. For PCFC, however, the water is produced at the cathode side, which dilutes the air near the cathode on the one hand, and the water competitive adsorption over the cathode surface may decrease the adsorption sites of cathode surface on the other hand, and both would have a negative effect on the electrode performance. However, certain amount of water is required to allow the hydration of oxygen vacancies to introduce proton conductivity into the electrode. Thus, the water management of the cathode side is highly important, requiring significant attention in the future. As mentioned, the oxygen ion, electron and proton triple conductor may lead to maximize the cathode performance in PCFC. However, the best ratio for the proton to oxygen ion is still not known. As well, up to now, it is still a big challenge to determine the transfer number of oxygen ion and proton in a triple conductor. Thus, it requires more attention in the future.

#### 8.4. Concluding Remarks

As an ideal cathode of SOFCs, it should possess certain level of electronic conductivity, and high structural stability under real operation conditions (temperature, oxygen partial pressure and polarization). Matchable TEC to other cell components is also a big concern, otherwise delamination of the electrode from electrolyte surface could appear, causing the fast degradation in cell performance. The major concern is to maximize the ionic conductivity inside the electrode bulk and to increase the surface reaction kinetics. To introduce mixed conductivity into a cathode of SOFC, it is need to control the microstructure of the electrode, which however can significantly affect the electrode performance, and the potential phase reactions between the two different phases. Therefore, it is more popular to develop single phase oxides with mixed conductivity. Currently, doping (both cation and anion), cation deficiency manipulation and phase structure tuning have been widely applied in the development of perovskite type MIEC oxides as electrodes for SOFCs. Such strategies could modify not only the conducting behavior of the oxide, but also the structural and chemical stability as well as the TEC.

## 9. Triple Ionic Electronic Conducting Oxides

### 9.1. Status

Triple MIEC conductors, or Triple Ionic Electronic Conducting Oxides (TIECs), are a subset of MIEC materials which concurrently conduct electrons ( $e^-$ ) and multiple ionic species.

Currently, most commonly referenced TIEC's exhibit conduction of protons ( $H^+$ ), oxygen ions ( $O^{2-}$ ), and electrons ( $e^-$ ). Most of the known TIECs are perovskite-type materials with the general  $ABO_3$  unit cell formula. This general formula is often heavily doped with multivalent or aliovalent cations in the A- or B-sites. TIECs are useful in applications where multi-species conduction is needed, but are most commonly used in solid oxide electrochemical cells.

Two main types of solid-state electrochemical cells are the primary focus of oxide-based fuel cell and electrolysis systems under development based on their main species of conduction: oxygen-ion-conducting cells and proton-conducting cells. In fuel cells specifically, these are known as solid oxide fuel cells (SOFCs) and protonic ceramic fuel cells (PCFCs) respectively. Conventional oxygen-ion-conducting ceramics used in SOFCs are effective at a high operation temperature range from 700–1000 °C, but suffer from lengthy start-up and long-term degradation of major components, including gas sealants and interconnect materials.<sup>[280,281]</sup>

Difficulties at high temperature established a growing need for materials able to perform at intermediate temperatures between 400–700 °C. Proton-conducting ceramics used in PCFCs offer a reasonable pathway to improve performance in this intermediate temperature range; protons require a lower activation energy for transport than their oxygen-ion due to their smaller ionic radius, single charge, hydrogen bonding which favors transfer reactions, and absence of an electron cloud.<sup>[282–284]</sup> Reducing the temperature of these electrochemical cells while maintaining comparable performance is beneficial for cost and durability considerations.<sup>[285]</sup> The mechanistic difference between SOFCs and PCFCs (**Figure 17**) highlights the need for triple-conducting cathodes in PCFC applications. Due to water formation at the cathode, it is advantageous for PCFC cathodes to conduct all three species ( $H^+/O^{2-}/e^-$ ) for efficient operation.

One of the first reported examples of triple conducting material systems reported was a composite system consisting of an electronic conductive Ni and a co-ionic conductor  $BaZr_{0.1}Ce_{0.7}Y_{0.1}Yb_{0.1}O_{3-\delta}$  (BZCYYb) which resulted in a fuel-flexible anode that could withstand sulfur impurities and coking.<sup>[208]</sup> The ability to conduct protons allowed for the oxidation of fuels such as propane, while the oxygen ion conduction allowed for impurity reformation with oxygen to reduce carbon and sulfur deposits. More recent work on triple conducting phases has focused on the discovery and use of single-phase TIECs and oxide-oxide triple-phase-conducting composites. Grimaud et al.<sup>[286]</sup> were one of the first to report some MIEC materials such as  $Pr_2NiO_{4+\delta}$  (PNO),  $PrBaCo_2O_{5+\delta}$  (PBC) and  $Ba_{0.5}Sr_{0.5}Co_{0.8}Fe_{0.2}O_{3-\delta}$  (BSCF) having quantifiable proton uptake, thus classifying these materials as TIECs. Subsequent studies were able to classify other previously-discovered MIEC materials as TIECs.<sup>[205,257,287]</sup> Research strategies have historically focused on doping multivalent or aliovalent ions into the A-site and B-site, leading to state-of-the-art single-phase materials such as  $BaCo_{0.4}Fe_{0.4}Zr_{0.1}Y_{0.1}O_{3-\delta}$  (BCFZY0.1)<sup>[206]</sup> and  $Sr_2Sc_{0.1}Nb_{0.1}Co_{1.5}Fe_{0.3}O_{6-\delta}$  (SSNCF).<sup>[272]</sup>

The synthesis of oxide-oxide multi-phase composites as triple phase conductors for cathodes has been achieved via infiltration,<sup>[206,288,289]</sup> mechanical mixing,<sup>[290,291]</sup> or one-pot

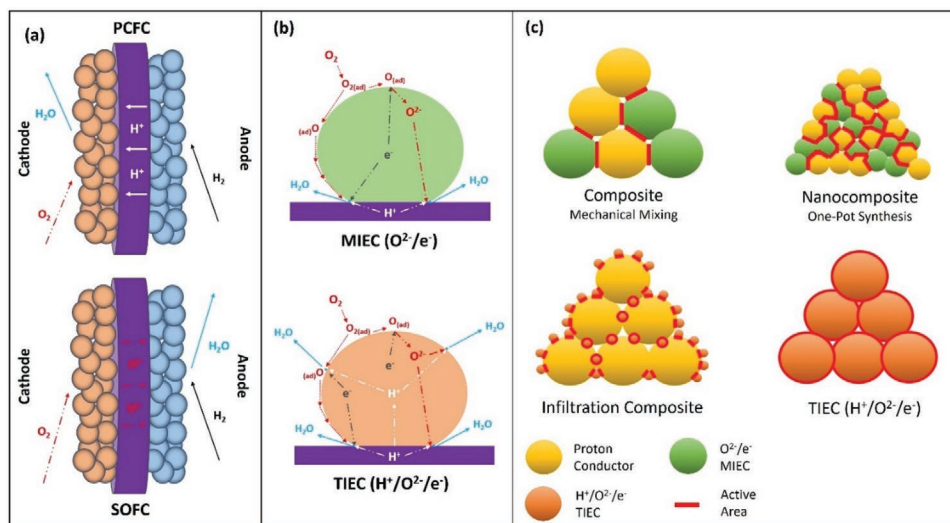


**Figure 17.** a) Schematic of the mechanistic difference where water is formed at the cathode in PCFCs and at the anode in SOFCs. b) Operating in PCFC conditions, a TIEC cathode results in more active sites than a traditional MIEC cathode. c) Comparison of different types of triple-conducting phases, where single-phase TIECs theoretically contain more active area at the surface than composite-type cathodes for PCFCs.

syntheses.<sup>[198,292]</sup> One-pot syntheses result in the self-assembly of two mixed-conducting phases into a nanocomposite, resulting in more active sites than a mechanically mixed composite. One of the highest-performing cathodes to date is an infiltration composite consisting of a TIEC (BCFZY0.1) infiltrated on the surface of a proton-conducting BaCe<sub>0.6</sub>Zr<sub>0.3</sub>Y<sub>0.1</sub>O<sub>3-δ</sub> (BCZY63) scaffold.<sup>[206]</sup> Overall, while a practical advantage exists for single-phase cathodes due to simple synthesis and compatibility, composites have a potential for tuning triple conducting properties over a broader range of partial conductivities.

Efficient operation of TIEC materials in PCFCs relies on the availability of triple phase boundaries (TPBs), where protons, oxygen ions, and electrons recombine to form water at a cathode's surface. TPBs are controlled by a cathode's physical properties (i.e., surface area from microstructure),<sup>[293]</sup> and fundamental material properties, namely the efficiency of surface reactions and the conduction through the bulk phase. At the surface, the two important reactions are the ORR and the formation/dissociation of water. ORR is a multi-step reaction encompassing oxygen surface adsorption, oxygen ionization, lattice incorporation, and bulk diffusion of lattice oxygen.<sup>[294,295]</sup> Bulk diffusion and surface exchange of oxygen often parallel one another in MIEC and TIEC materials.<sup>[296]</sup> Low-ORR activity can be a limiting factor in electrochemical performance,<sup>[297]</sup> especially at low temperatures. Less is known specifically about water formation and dissociation at the surface of TIECs, as most analytical methods focus on uptake rather than formation and dissociation. However, it is essential to consider the relationship between water and TIECs including water causing degradation attributed to the blocking of ORR pathways,<sup>[298]</sup> and surface termination effects on water reactivity.<sup>[299]</sup>

In bulk, the perovskite or perovskite-like structure allows for unique transport properties of H<sup>+</sup>/O<sup>2-</sup>/e<sup>-</sup> species. A small-polaron hopping mechanism is generally accepted for the transfer of electronic charge carriers.<sup>[300–304]</sup> The B-site/oxygen-site (B-O-B) bond in the perovskite structure is also assumed

to be responsible for electronic conduction,<sup>[305]</sup> making multivalent ion doping necessary in the B-site. Heavy doping of these acceptor ions into the bulk creates a predominantly electronic conductor while the original ionic conductivity of the material is maintained.<sup>[306,307]</sup> Oxygen transport in TIECs is dominated by surface exchange and bulk diffusion. Oxygen vacancies in the perovskite allow for bulk diffusion of oxygen ions through the structure.<sup>[308]</sup> When a TIEC is operated in humid, oxidizing atmosphere, as is typical in a PCFC, protons locate near oxygen ions in the structure, forming hydroxyl groups.<sup>[283]</sup> Protons can then transfer across lattice oxygen sites through vibrational and rotational motion, similar to a Grothuss mechanism.<sup>[283]</sup> The transport of all three species is dependent on each other.

Significant interplay and tradeoffs between atmospheric conditions, surface reactions, and bulk conductivity of TIEC materials are evident and must be considered to achieve desired material properties. Indeed, the desired properties are often conflicting with each other, resulting in a limitation to the tunability of TIEC materials.<sup>[287]</sup> These limitations emphasize the importance of understanding properties of TIECs and the prospects of future TIEC composites.

## 9.2. Recent Advances and Future Challenges

TIEC development has remained focused on methods for creating and probing new materials. Recent work has attempted to quantify materials' fundamental properties to understand changes in in the bulk and at the surface. Much of this work has probed systematic, incremental changes to previously known TIECs to probe fundamental changes in material properties, using methods such as A-site and B-site deficiency<sup>[216,309,310]</sup> and simple doping strategies.<sup>[311,312]</sup> These studies build upon the early research which quantified high-performance materials in fuel-cell or electrolysis applications, while providing fundamental benchmarks for future TIECs.

**Table 6.** List of claimed triple ionic-electronic conductors with available bulk material properties. Gaps in literature are highlighted with missing ionic conductivities and surface exchange coefficients. This is especially evident in claimed triple conductors which have no fundamental property data. Where specific values were not given in references, provided data is estimated from graphs embedded in each article. All data listed measured at 600 °C unless specified otherwise. Unless specified otherwise: ECR experiments carried out in dry atmosphere with final  $p_{O_2}$  listed (coefficients are dependent on final  $p_{O_2}$  across constant temperature).<sup>[340]</sup> Unless specified otherwise: Electronic conductivity calculated from four-point probe measurements in dry air. Protonic conductivities calculated from permeation measurements across dense membrane coated in Pd using 10% H<sub>2</sub>/90% N<sub>2</sub> and pure Ar or He sweep. Oxygen ion conductivity calculated from permeation measurements across dense membrane using dry air feed and pure Ar sweep.

Single Phase TIEC	Surface Reactivity			Conductivity [S cm <sup>-1</sup> ] <sup>a</sup>			Ref.
	Final $p_{O_2}$	$D_{chem}$ [cm <sup>2</sup> s <sup>-1</sup> ]	$k_{chem}$ [cm s <sup>-1</sup> ]	e <sup>-</sup>	H <sup>+</sup>	O <sup>2-</sup>	
BCFZY0.1	0.1	2.0E-5	1.9E-4	2	0.11	0.025	[309,310,312]
BCFZY0.95	0.1	5.0E-5	4.0E-4	1.5	0.125	–	[309,310]
BCFZYN	0.1	3.8E-5	3.2E-4	1.5	0.14	0.03	[312]
SSNCF				150	0.078	0.006	[272]
BSCF	0.1	3.0E-5	3.0E-4	40	0.023	0.053	[272,341]
BFSB0.3	1	1.2E-4	1.2E-3	2.5	–	0.0025	[342]
PBCO <sup>b)</sup>	0.21	5.0E-5	9.0E-3	800	–	–	[343]
SFMZ <sup>c)</sup>				17	–	–	[311]
BLFZ				1.4	–	–	[291]
PBSCF				425	–	–	[205,344]
PNO				100	–	–	[345]
PNCO <sup>d)</sup>							[321]
NBSCF							[257]
C-LSMN7373							[273]
LSCN8273							[346]
LNCO							[347]
BSFZ							[348]
Nanocomposite Materials							
BCCY	0.1	2.0E-4	1.8E-3	2.5	0.083	0.02	[198]
BCFC							[292]
Composite Materials							
Co(NO <sub>3</sub> ) <sub>2</sub> – infiltrated BZCY				0.05			[349]
LSCF-BZCY							[350]
GDC infiltrated PBC-BZCY							[351]

<sup>a)</sup>Reported ionic conductivities provide direct comparisons between these materials. It is noted that values from literature are estimates derived from permeation data based on the Wagner Equation, and that conductivities greater than 0.1 S cm<sup>-1</sup> at 600 °C are an order of magnitude greater than previously reported intrinsic bulk proton conductivity in BZY-based perovskites used as electrolytes from EIS and electrochemical measurements<sup>[206]</sup>. <sup>b)</sup>Data for PBCO reported at 500 °C; <sup>c)</sup>Data for SFMZ reported at 700 °C. ECR was performed, but utilized a dry to wet atmosphere transition to find  $D_{O,chem}$ . The coefficient is not reported above due to the different method. Electronic conductivity estimated from ECR graph; <sup>d)</sup>Hydrogen permeation measurements for PNCO are performed across dense membrane coated in Pt using 3% H<sub>2</sub>/1% N<sub>2</sub>/96% He and pure Ar sweep. The Wagner equation cannot be utilized with available data and therefore conductivity is not estimated. BaCo<sub>0.4</sub>Fe<sub>0.4</sub>Zr<sub>0.1</sub>Y<sub>0.1</sub>O<sub>3-δ</sub> (BCFZY0.1); Ba(Co<sub>0.4</sub>Fe<sub>0.4</sub>Zr<sub>0.1</sub>Y<sub>0.1</sub>)<sub>0.95</sub>O<sub>3-δ</sub> (BCFZY0.95); Ba(Co<sub>0.4</sub>Fe<sub>0.4</sub>Zr<sub>0.1</sub>Y<sub>0.1</sub>)<sub>0.95</sub>Ni<sub>0.05</sub>O<sub>3-δ</sub> (BCFZYN); Sr<sub>2</sub>Sc<sub>0.1</sub>Nb<sub>0.1</sub>Co<sub>1.5</sub>Fe<sub>0.3</sub>O<sub>6-δ</sub> (SSNCF); Ba<sub>0.5</sub>Sr<sub>0.5</sub>Co<sub>0.8</sub>Fe<sub>0.2</sub>O<sub>3-δ</sub> (BSCF); LiNi<sub>0.8</sub>Co<sub>0.2</sub>O<sub>2</sub> (LNCO); BaFe<sub>0.5</sub>Sn<sub>0.2</sub>Bi<sub>0.3</sub>O<sub>3-δ</sub> (BFSB0.3); Sr<sub>2</sub>Fe<sub>1.5</sub>Mo<sub>0.4</sub>Zr<sub>0.1</sub>O<sub>6-δ</sub> (SFMZ); La<sub>0.7</sub>Sr<sub>0.3</sub>Mn<sub>0.7</sub>Ni<sub>0.3</sub>O<sub>3-δ</sub> (C-LSMN7373); La<sub>0.8</sub>Sr<sub>0.2</sub>Co<sub>0.7</sub>Ni<sub>0.3</sub>O<sub>3-δ</sub> (LSCN8273); Ba<sub>0.95</sub>La<sub>0.05</sub>Fe<sub>0.8</sub>Zn<sub>0.2</sub>O<sub>3-δ</sub> (BLFZ); Ba<sub>0.5</sub>Sr<sub>0.5</sub>Fe<sub>0.8</sub>Zn<sub>0.2</sub>O<sub>3-δ</sub> (BSFZ); PrBa<sub>0.5</sub>Sr<sub>0.5</sub>Co<sub>1.5</sub>Fe<sub>0.5</sub>O<sub>5+δ</sub> (PBSCF); NdBa<sub>0.5</sub>Sr<sub>0.5</sub>Co<sub>1.5</sub>Fe<sub>0.5</sub>O<sub>5+δ</sub> (NBSCF); PrNi<sub>0.5</sub>Co<sub>0.5</sub>O<sub>3-δ</sub> (PNCO); PrBaCo<sub>2</sub>O<sub>5+δ</sub> (PBCO); Pr<sub>2</sub>NiO<sub>4+δ</sub> (PNO); BaCo<sub>0.7</sub>(Ce<sub>0.8</sub>Y<sub>0.2</sub>)<sub>0.3</sub>O<sub>3-δ</sub> (BCCY); BaCe<sub>0.4</sub>Fe<sub>0.4</sub>Co<sub>0.2</sub>O<sub>3-δ</sub> (BCFC); Ba(Zr<sub>0.4</sub>Ce<sub>0.4</sub>Y<sub>0.2</sub>)<sub>1-x</sub>Co<sub>x</sub>O<sub>3-δ</sub>+Co<sub>3</sub>O<sub>4</sub>+ (Ce, Zr, Y)O<sub>2</sub> (Co(NO<sub>3</sub>)<sub>2</sub> infiltrated BZCY); La<sub>0.6</sub>Sr<sub>0.4</sub>Co<sub>0.2</sub>Fe<sub>0.8</sub>O<sub>3-δ</sub>+BaZr<sub>0.1</sub>Ce<sub>0.7</sub>Y<sub>0.2</sub>O<sub>3-δ</sub> (LSCF-BZCY); Gd<sub>0.1</sub>Ce<sub>0.9</sub>O<sub>2-δ</sub>+PrBaCo<sub>2</sub>O<sub>5+δ</sub>+BaZr<sub>0.1</sub>Ce<sub>0.7</sub>Y<sub>0.2</sub>O<sub>3-δ</sub> (GDC infiltrated PBC-BZCY).

The main challenge associated with TIECs is limited understanding of the complex bulk transport, surface kinetics and stability relationships required for high-performance materials in advanced electrochemical applications. **Table 6** highlights the large gap in the literature for fundamental material properties of many TIEC materials, leaving few materials to understand trends between these factors. In addition, existing materials that are known TIECs are dominant electronic conductors with greater than 90% electronic character. The lack of diversity among TIECs raises questions regarding the best conducting

character for TIEC applications, and how broadly TIECs can be tuned to desired conductivity levels. As such, more systematic studies of doping as it relates to TIEC fundamental properties are necessary for further understanding. In addition, composite studies are further warranted to explore a broad range of partial conductivities from combinations of single-phase materials.

TIEC stability remains a difficult challenge for fuel cell and electrolysis cell applications. TIECs have been shown to remain relatively stable across hundreds of hours under operating conditions,<sup>[206,273,311]</sup> yet fuel cells require lifetimes

of tens-of-thousands of hours to be viable beyond laboratory testing.<sup>[285]</sup> In tandem with the need for long-term testing, the complex doping of these TIECs provides more opportunities for cation segregation and secondary phase formation in operating environments. Some Ba-containing perovskites exhibit decomposition in atmospheres containing water or CO<sub>2</sub>,<sup>[313]</sup> although this is not readily evident in more heavily-doped materials.<sup>[237]</sup> In addition, Sr-containing perovskites can segregate into secondary phases, leading to decreased stability,<sup>[314]</sup> but this may be alleviated with composite approaches.<sup>[315]</sup>

### 9.3. Opportunities

Early research on reported TIECs focused on data from methods such as electrochemical impedance spectroscopy (EIS) and current/voltage/power (I-V-P) testing. These methods can reveal important information such as ORR kinetics,<sup>[294]</sup> but are typically conducted on porous architectures. Porous microstructures make it more difficult to deconvolute resultant data like polarization resistance as effects of microstructure or fundamental properties. Looking at Table 6, a large literature gap is present for fundamental physical properties, specifically bulk ionic conductivity ( $\sigma$ , S cm<sup>-1</sup>) and surface reactivity as defined by surface exchange constants ( $k$ , cm s<sup>-1</sup>).

Methods for direct, bulk comparisons between TIEC materials, especially for charge-carrier contributions, are often difficult and time-consuming. While electronic conductivity is relatively easy to measure because of TIEC's predominantly electronic nature, proton and oxygen-ion transport measurements require more complex methods due to their orders-of-magnitude lower conductivity contribution. The use of blocking electrodes has been employed to extract partial conductivities, but is often difficult to set exact conditions needed for blocking specific ions.<sup>[316,317]</sup> More recently, electromotive force (EMF) measurements<sup>[318,319]</sup> coupled with membrane permeation measurements<sup>[273,320–322]</sup> on a concentration cell setup have been used to provide separate comparison of ionic transport numbers of charge carriers across a multitude of samples and atmospheres. The main impediment to this method is the difficulty to measure permeation in reducing environments, as these TIEC materials are often unstable in these conditions. It is possible to assist in the permeation measurement in reducing environments by depositing a protective layer, while keeping the membrane bulk limiting.

In relation to charge-carrier contributions, the surface phenomena of TIECs require further investigation. Computational modeling has probed both oxygen reduction and water formation/dissociation at the surface of cathode materials to derive their possible mechanisms of action.<sup>[323,324]</sup> Further modeling may predict new materials and conditions for efficient surface reactions before laboratory testing. Experimental methods to probe surface reactions include electrical conductivity relaxation (ECR), which is a well-defined method for oxygen surface exchange characterization to find a material's surface exchange coefficient,  $k_{\text{chem}}$ , and bulk diffusion coefficient,  $D_{\text{chem}}$ , and is historically performed in dry oxidizing environments. PCFCs are operated in humid environments, and ECR performance in wet environments is relatively unknown. The addition of

water results in a more complex relaxation profile, and recently some studies have used wet conditions to predict both oxygen exchange and proton uptake.<sup>[311,325,326]</sup> Despite studies of proton uptake from atmospheric water, few studies<sup>[327]</sup> of water formation or dissociation at the surface of TIECs have been performed, presenting a need for full understanding of this reaction. The use of isotope exchange studies between O<sup>16</sup>/O<sup>18</sup> and H<sub>2</sub>O/D<sub>2</sub>O can provide more insight into the surface reactions of these materials.<sup>[328–330]</sup> Sample requirements including highly dense samples for both ECR and isotope exchange may necessitate nonstandard techniques such as pulsed laser deposition to achieve high densities, especially for materials with high sintering temperature.<sup>[331]</sup>

A combination of ECR with permeation measurements remains as an accessible method to probing the bulk phase properties of TIEC materials. Neither of these methods require highly specialized equipment and have few impediments to implementation. Further modeling of known TIECs may also yield insights toward the atomic level phenomena which account for materials with high reactivity or bulk conductivity, especially when coupled with these laboratory-based experiments. An important opportunity exists to use this methodological combination to discover new TIECs and fill in a large gap of knowledge over a significant portion of known TIEC materials.

Long-term stability of TIECs to date have demonstrated limited stability over hundreds of hours as measured by the change in area specific resistance in ( $\Omega$  cm<sup>2</sup>). However, industry driven performance requirements necessitate significant orders of magnitude greater stability improvements. The issue here is twofold: first, TIECs must remain stable for extended time periods in elevated temperatures and humid air to be viable electrodes, and second, a need exists for accelerated stability tests or stability predictors as opposed to running extremely long-term stability tests. Recently, computational screening techniques using machine learning have yielded promising results for predictive stability on MIEC materials through the correlation of material stability and reactivity with laboratory testing of materials.<sup>[332]</sup> These computational methods could be used to predict similar trends in TIEC materials, connecting stability with bulk and surface properties. Modeling may also help to predict interactions between TIECs and other materials.<sup>[333]</sup>

Thermodynamic data such as formation enthalpies, entropies and interfacial absorption energies as a function of temperature and composition can be provided with a wide range of calorimetry techniques.<sup>[334]</sup> One specific method, high temperature oxide melt solution calorimetry, is a versatile technique to characterize materials in solid-state electrochemistry, including the studying of solid solution mixing, energetics of formation, order/disorder and phase transition in ceramics.<sup>[335,336]</sup> Empirically measured thermodynamic stability, ionic conductivity, and dopant dependent structural features have not been previously reported in TIEC systems. Thermodynamic stability combined with computational methods would be useful to screen for reactions among constituent phases in composites or between functional device layers (i.e., electrolyte-electrode interactions).

Lastly, creation of composite triple conductors using TIECs, MIECs, or pure conductors continues to be a promising strategy to further tune materials for TIEC applications. Combinations



of materials designed to be composite MIECs have revealed chemical complexity resulting in new phases at the grain boundaries between materials, even at nanoscale levels,<sup>[337]</sup> which have improved the fundamental properties of the material system.<sup>[338]</sup> Multi-phase composites, including those with triple ionic-electronic conducting properties, have also been studied for related systems including oxide and carbonate-based CO<sub>2</sub> separation membranes.<sup>[339]</sup> A more complete understanding of fundamental properties of each material used in these composites may allow for interfacial design of tuned materials using both microstructural and bulk properties to achieve desired triple-conducting properties needed for each application, properties that may be conflicting in a single-phase material.

#### 9.4. Concluding Remarks

TIECs as mixed protonic, oxygen-ionic, and electronic conductors present promising applications for proton-conducting electrochemical cells. The perovskite-like structures of TIECs allow for this unique mixture of conduction, with the ability of direct elemental substitution to fundamentally change the properties of TIEC materials. Despite notable improvements in recent work, more comprehensive bulk comparisons of TIECs are required to understand high-performance materials. Specifically, systematic studies of single-phase materials, with incremental changes to composition, are key to understanding the methods needed to create TIECs with desired bulk and electrochemical properties. With present methods for measuring bulk samples, a combination of permeation and ECR provides the most accessible opportunity to understand bulk and surface reactivity without the need for specialized instruments. Computational modeling coupled with these experimental studies for stability, conductivity, and reactivity pose a realistic path toward finely engineered single-phase materials. These single-phase TIEC fundamental properties may yield new insights to form specifically engineered composite phases for a multitude of applications, further improving the prospects of fuel cells and other fields.

## 10. MIEC Membrane Reactors

### 10.1. Status

For petrochemical industry, many chemical oxidation processes occur at temperatures higher than 800 °C. These dense MIEC ceramic membranes can be used as membrane reactors for high temperature oxidations. Depending on the different roles playing, these MIEC membrane reactors can be divided into two major categories: distributor (or supplier) and extractor as shown in Figure S1-I,II (Supporting Information). In Figure S1-I (Supporting Information), oxygen in the feed gas (i.e., air) is permeated into the reaction side along the membrane (distributor) to participate the reactions. Figure S1-II (Supporting Information) describes the second type of reactors where oxygen is produced by the first reaction in one membrane side and subsequently being extracted to the other membrane side. In order to accelerate the oxygen removal rate, another

oxidative reaction is usually applied in the permeate side thus two different reactions can be coupled by such a membrane reactor as shown in Figure S1-II (Supporting Information). There are many application examples for both types of membrane reactors as long as the membrane has a long life under practical reacting conditions of high temperature and reducing atmosphere. The blank membrane material itself cannot provide sufficient catalytic properties for the specified reactions, extra catalysts need to be loaded. The prerequisite condition to choose the catalyst is that the catalyst cannot react with the membrane. In order to achieve a better reaction conversion, the amount of oxygen permeated (or supplied) must match well with the catalytic efficiency; otherwise the over-supplied oxygen may unfavorably oxidize the product thus decreasing the yield. The integration mode of catalyst and the membrane surface has a significant influence on the membrane reactor performance. Depending on the individual reactions, there is an optimum amount of catalyst loading and contact mode with the membrane reactors. For example, if the catalyst is over-deposited on the membrane surface, it may block the oxygen transport thus lowering the performance of the membrane reactor. Several typical reaction examples of both categories of membrane reactors are discussed below to exhibit the advantages or challenges of membrane catalysis.

### 10.2. Recent Advances and Future Challenges

#### 10.2.1. Oxygen Distributor Type MIEC Membrane Reactors

*Oxidative Coupling of Methane (OCM)*: Current commercial technologies for methane conversion via Fischer-Tropsch synthesis to more useful chemicals are expensive and energy-intensive. Thus, direct methane oxidative coupling to higher hydrocarbons C<sub>2</sub> products (C<sub>2</sub>H<sub>4</sub> and C<sub>2</sub>H<sub>6</sub>) is more economically valuable and has inspired intensive research enthusiasm in 1990s from the perspectives of catalyst development. If the catalyst is stable for a long-term operation and a single-pass C<sub>2</sub> yield is higher than 30% (equivalent to methane conversion of 35–37% and selectivity of 85–88%), the OCM technology may be commercially considered. However, it is difficult to obtain C<sub>2</sub> yields more than 25% in a conventional fixed-bed reactor due to the competition between the formation of C<sub>2</sub> and the full combustions as C<sub>2</sub> products are more reactive than methane to be oxidized. Thus, some endeavors are also focusing on the investigation of catalytic membrane reactors for OCM<sup>[352]</sup> as the membrane can provide a better oxygen control along the reactors, offering a possibility to achieve much higher C<sub>2</sub> selectivity and yield. In this sense, tubular membrane is better than disk-shaped configuration to be functioned as the oxygen distributor or supplier. In order to gain a deep understanding of the membrane catalysis for OCM using dense MIEC membranes, the transport and reaction behavior was simulated based on a set of kinetic equations derived from Li/MgO catalyst with several major steps as schematically shown in Figure S2 (Supporting Information).<sup>[353]</sup> With the kinetic data obtained on a Li/MgO catalyst, their theoretical analysis showed that C<sub>2</sub> yield as high as 84% could be achieved when oxygen flux, methane flow rate, and catalytic efficiency have a good match.<sup>[353]</sup> However,

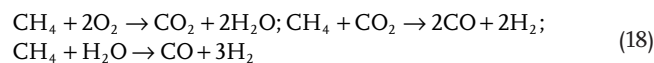
in real experiments, much lower  $C_2$  yields were observed from various groups due to the mismatch of these factors. In 1989, a tubular membrane reactor made of two layers, with one (fluorite structured zirconia, 10% $Y_2O_3$ -89% $ZrO_2$ -1% $TiO_2$  (YSZ)) as the oxygen permeable membrane (thickness: 0.05 mm) and the other porous catalyst layer (LiO/MgO/ $ZrO_2$ ), was designed and tested at 700–750 °C by Hazbun.<sup>[354]</sup> A product yield of 20% to 25%  $C_2$  was reported at 50% to 60% selectivity and 35% to 45% conversion. Thirteen years later, based on another fluorite structured dead-end tubular membrane reactor of  $Bi_{1.5}Y_{0.3}Sm_{0.2}O_3$  (BYS) which is a catalytically active, Akin and Lin reported their results for OCM without extra catalyst.<sup>[355]</sup> They achieved the single-pass  $C_2$  yield of 35% at 900 °C. With the availability of membranes possessing much higher oxygen fluxes (i.e., perovskite  $BaCe_{0.8}Gd_{0.2}O_3$  or  $La_{0.2}Sr_{0.8}Co_{0.2}O_3$ , and  $ZrO_2$ -doped  $SrCo_{0.4}Fe_{0.6}O_3$ ) than fluorite materials, membrane reactor tests for OCM were also reported.<sup>[52,356–359]</sup> Despite of the facts that these perovskite membranes can provide very large oxygen fluxes, one or two orders of magnitude higher than the doped fluorite (YSZ or BYS) materials, the achieved  $C_2$  yield higher than 35% was seldom occurring as shown in Table S1 (Supporting Information). As can be seen, membrane reactor performance in OCM is controlled by the limited catalysis in the reaction side; in particular good catalysts working well in low oxygen partial pressure environment is required. TenElshof et al. employed a perovskite oxide  $La_{0.8}Ba_{0.2}Co_{0.8}Fe_{0.2}O_3$  or  $La_{0.6}Sr_{0.4}Co_{0.8}Fe_{0.2}O_3$  disk-shaped membrane for OCM without extra catalysts.<sup>[52]</sup> Despite that these perovskite oxide catalysts are active for OCM, the yields were less than 3%. One interesting phenomenon was observed that the blank perovskite membrane displayed much higher  $C_2$  selectivity than being used as the catalyst in fixed bed reactor. The low yields obtained by these researchers are mainly due to the insufficient catalytic efficiency or limited membrane area provided by the unfavorable reactor configuration, making the large portion of methane unable to be activated for OCM reactions. To improve the reactor performance, efforts should be placed on membrane configuration change and extra catalyst integration or membrane catalytic surface modification. For example, a comparative study was performed to modify  $Ba_{0.5}Sr_{0.5}Co_{0.8}Fe_{0.2}O_{3-\delta}$  disk-shaped membrane surface with La-Sr/CaO catalyst for OCM, successfully enhancing the  $C_2$  yield up to 18% at 950 °C.<sup>[360]</sup> Using  $La_{0.6}Sr_{0.4}Co_{0.2}Fe_{0.8}O_3$  (LSCF) hollow fiber membrane, the  $C_2$  yields were improved to 14% or 21% for the blank membrane or packed with additional  $SrTi_{0.9}Li_{0.1}O_{3-a}$  catalysts in the fiber lumen.<sup>[359]</sup> In another study using tubular  $Ba_{0.5}Sr_{0.5}Co_{0.8}Fe_{0.2}O_{3-\delta}$  (BSCF) membrane reactor, Wang et al. compared the performances for OCM without or with catalyst.<sup>[361]</sup> They observed that  $C_2$  selectivity with the packed BSCF catalyst was increased by 20%. When loaded with the active OCM catalyst (La-Sr/CaO), the highest  $C_2$  yield (15%) was obtained at 850 °C.

In a more recent work, OCM reaction using a supported tubular  $Ba_{0.5}Ce_{0.4}Gd_{0.1}Co_{0.8}Fe_{0.2}O_{3-\delta}$  membrane with a Na-W-Mn/SiO<sub>2</sub> catalyst on the support was studied by Bhatia et al. Their reactor showed oxygen permeation flux of 1.4 mL  $cm^{-2} min^{-1}$  at 850 °C and  $C_2$  yield up to 34.7% together with methane conversion of 51.6%,  $C_2$  selectivity of 67.4%. Although the oxygen flux of  $Ba_{0.5}Ce_{0.4}Gd_{0.1}Co_{0.8}Fe_{0.2}O_{3-\delta}$  was 10 times

of BYS membrane, both reactors gave much similar  $C_2$  yield around 35% indicating the complex and unique mechanism of heterogeneous-homogeneous OCM reactions.<sup>[355,362]</sup> In 2015, Li's group made an innovative LSCF hollow fiber membrane with micro-channels along the lumen side to increase the inner membrane surface to deposit the BYS catalyst for OCM, achieving a maximum value of  $C_2$  selectivity and yield of 79% and 39%, respectively at 900 °C.<sup>[363]</sup> Compared with the tubular BYS membrane reactor, such a LSCF hollow fiber membrane reactor integrated with BYS nano particles not only improved the  $C_2$  yield but also enhanced the  $C_2$  production rate by a factor of 50 compared with BYS tubular membrane due to the higher oxygen flux provided by a thin LSCF membrane.<sup>[355,363]</sup> This is a perfect example for membrane catalysis to combine large oxygen flux and catalytic efficiency to improve the product yield from the reactions where the product is more active than the reactant. Unfortunately, these perovskite oxide membranes could not last long at high temperatures in reducing gas atmosphere, otherwise commercial interests can be considered.

*Partial Oxidation of Methane (POM) to Syngas*: POM to syngas is another typical example to be widely considered for membrane reactors.  $POM (CH_4 + 0.5O_2 = CO + 2H_2)$  with standard enthalpy of formation of  $-36 kJ mol^{-1}$  is a relatively milder exothermic reaction compared to OCM. The POM product with the  $H_2/CO$  ratio of 2:1 is an ideal feedstock for the methanol synthesis via the Fisher-Tropsch method. The application of dense ceramic membrane reactors can combine air separation, partial oxidation, and methane reforming in a single unit, improving the process efficiency and significantly reducing the capital cost by 30% thus being referred as the possible revolutionary technologies for chemical and petroleum industries.<sup>[364]</sup> Due to the limited catalytic activity from the membrane materials themselves, surface catalytic modification or extra catalyst loading is normally applied to improve  $CH_4$  conversion and CO selectivity. Figure S3 (Supporting Information) displays the pathways of the POM reactions in a typical MIEC membrane reactor packed with POM catalysts. As shown in Figure S3 (Supporting Information), methane and air are entering the two sides of the membrane; oxygen in air is transported from the air side through the membrane to the reaction side to react with  $CH_4$  into syngas.

Compared with OCM, POM to syngas using membrane reactor is much more successful in terms of reaction efficiency than OCM due to the available good catalysts to be integrated with the membranes. The reported membrane reactor for POM could deliver nearly 100% methane conversion and 100% CO selectivity with stability for more than 1000 h as exhibited in Table S1 (Supporting Information).<sup>[365]</sup> Despite the unclear complex reaction system, three major reactions are occurring during the POM in membrane reactors. Initially, a minor portion (around 25%) of methane participates the full combustion with gaseous or lattice oxygen and then the major part of methane would go through the reforming reactions via the produced  $CO_2$  and steam.

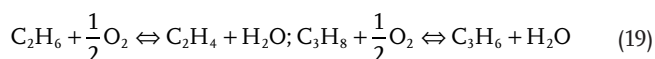


The real reaction pathways are far more complex than the above-mentioned three reactions. For example, the required

CO<sub>2</sub> and H<sub>2</sub>O for methane reforming may be sourced from the oxidations of CO and H<sub>2</sub>. The precise mechanism in the reaction for POM is still not very clear. Due to the huge economic incentives from the commercialization of methane conversion technology, continuous efforts have been devoted in this field in the last two decades, as summarized in Table S1 (Supporting Information).<sup>[365]</sup> The overall performance of MIEC membrane reactors is strongly dependent on the operating conditions and reactor design.<sup>[366]</sup> In most cases the membrane works as an oxygen supplier or distributor, while its catalytic properties of the membrane itself are less important as the loaded catalyst provides sufficiently high activity for reforming reactions. Theoretical studies imply that long tubular or hollow fiber membranes may give better performances to distribute the oxygen to achieve a high conversion or a good hydrogen production,<sup>[367]</sup> much similar to the observation from the methane coupling reactions. In another study, a two-stage membrane reactor was advised with the front part consisting of tubular membrane reactor following by normal packing bed catalyst layer.<sup>[180]</sup> During the membrane stage, oxygen is supplied from air without nitrogen for deep oxidation and heat release; then the produced CO<sub>2</sub> and H<sub>2</sub>O with the released energy to go through the second stage of catalyst bed for the endothermic reforming reactions for syngas production. The amount of catalyst loading and operating conditions (i.e., contact time and temperature) should match with the oxygen permeation rate,<sup>[368,369]</sup> otherwise the over-supplied oxygen will consume the product (H<sub>2</sub> or CO). Due to the available good catalyst to provide sufficient catalytic efficiency, the overall syngas production rate of MIEC membrane reactors is actually limited by the oxygen flux.

Other oxidative applications in membrane reactors can also be found in the literature from liquid hydrocarbons (i.e., gasoline, naphtha, kerosene and diesel oil) which could be applied as the hydrogen sources via in situ reforming reactions. For example, heptane can be converted to the gas mixture of CO<sub>2</sub> and H<sub>2</sub> via a Ba<sub>0.5</sub>Sr<sub>0.5</sub>Co<sub>0.8</sub>Fe<sub>0.2</sub>O<sub>3-δ</sub> disk-shaped membrane reactor packed with LiLaNiO/γ-Al<sub>2</sub>O<sub>3</sub> catalyst.<sup>[370]</sup> At the optimized conditions, the heptane conversion of 100%, a H<sub>2</sub> selectivity of 95–97% and CO selectivity of 91–93% were obtained and the reactor was successfully operated at 850 °C for more than 100 h.<sup>[370]</sup>

*Oxidative Dehydrogenation of Ethane (ODE) and Propane (ODP):* Selective oxidation of alkanes such as ethane and propane to the corresponding olefins is an important catalytic process and currently is completed by the steam cracking method, expensive and energy intensive.



The working principle of the MIEC membrane reactor for oxidative dehydrogenation of ethane and propane (ODE) is much similar to the OCM process where the gaseous oxygen should be avoided as lattice oxygen is more selective. Many studies (Table S1, Supporting Information) were performed on ODE using different membrane materials, configurations, membrane surface modifications and optimizations of the operating conditions. In 2011, Lobera et al. simulated the performance of BSCF membrane reactor for ODE based on

Soft Computing techniques. The predicted C<sub>2</sub>H<sub>4</sub> yield is quite encouraging and exceeded 87%<sup>[371]</sup> far more than the threshold 70% required for commercial consideration to replace the existing technology.<sup>[365]</sup> A disk Ba<sub>0.5</sub>Sr<sub>0.5</sub>Co<sub>0.8</sub>Fe<sub>0.2</sub>O<sub>3-δ</sub> membrane reactor without or with catalytic modification by Pd deposition in the permeate side was reported for ODE.<sup>[372,373]</sup> At 1080 K, an ethylene yield of 66% was observed in the blank membrane; after Pd deposition, the ethylene yield was improved to 76% at 1050 K and long-term stable operation could last 23 days without membrane failure. Caro group studied the performance of ODE in a BaCo<sub>x</sub>Fe<sub>y</sub>Zr<sub>z</sub>O<sub>3-a</sub> (BCFZ) hollow fiber or disk membrane.<sup>[374]</sup> BCFZ itself has a certain catalytic effect on ODE. At 850 °C, the respective C<sub>2</sub>H<sub>6</sub> conversion and C<sub>2</sub>H<sub>4</sub> selectivity were 98% and 24% for ODE test in co-fed packed bed reactor. When BCFZ was prepared into membranes for ODE without extra catalyst, the C<sub>2</sub>H<sub>4</sub> selectivity was improved to 79% (disk membrane) and 40% (hollow fiber membrane) at 850 °C. The lower selectivity observed on hollow fiber membrane was due to the insufficient catalytic efficiency to match the much improved oxygen permeation leading to deep oxidation of C<sub>2</sub>H<sub>4</sub>. Later Caro group further improved the BCFZ hollow fiber membrane reactor design by adopting a multi-zone (dehydrogenation and oxidation zones), which was made by coating gold paste on part of the membrane surface and packed with dehydrogenation catalyst.<sup>[375]</sup> This improved membrane design provided a low oxygen concentration and allowed more precise control of oxygen feeding into the reactor over its axial length thus delivering high C<sub>2</sub>H<sub>6</sub> selectivity by burning off the in situ produced hydrogen from catalytic dehydrogenation. At a lower operation temperature of 725 °C, the C<sub>2</sub>H<sub>6</sub> conversion up to 95–100% with the C<sub>2</sub>H<sub>4</sub> selectivity around 55% was achieved.<sup>[375]</sup> In 2010, the same group applied the multi-zone BCFZ hollow fiber membrane reactor for the ODP.<sup>[376]</sup> Packing with a Pt/Sn/K ODP catalyst, propene formation could be achieved even at temperatures as low as 625 °C with a propane conversion of 26% and propene selectivity of 75%. The reduced operation temperature brings in many engineering benefits like easy sealing and extending membrane life. In another study, Caro and co-workers investigated the mechanistic aspects of ODP with catalytic selective hydrogen combustion in BCFZ membrane reactor packed with a Pt-Sn dehydrogenation catalyst.<sup>[377]</sup> It is again confirmed that for selective oxidation reactions, since the lattice oxygen is more selective, the formation of gas phase O<sub>2</sub> in the permeate side should be avoided to achieve an excellent product selectivity and conversion.

*Oxidation of Ammonia:* Selective oxidation of ammonia (SOA) is another example to use MIEC membrane reactor to simplify the conventional processes to produce nitric oxide (NO), a raw material for nitric acid production.<sup>[378–380]</sup> The conventional technology for SOA is expensive and harmful to the environment as it uses precious metals (Pt-Rh alloy gauzes) as the catalyst and produces N<sub>2</sub>O.<sup>[378,379]</sup> Perovskite oxide membranes can be applied for this reaction to intensify the process by combining oxygen separation from air and ammonia catalytic oxidation. Two groups leading by Pérez-Ramírez and Yang did some pioneering works to demonstrate the membrane reactor concept based on La<sub>1-x</sub>Sr(Ca)<sub>x</sub>FeO<sub>3-a</sub><sup>[378,379]</sup> and Ba<sub>0.5</sub>Sr<sub>0.5</sub>Co<sub>0.8</sub>Fe<sub>0.2</sub>O<sub>3-a</sub><sup>[380]</sup> disk membranes. The results are

promising with high NO selectivity but without N<sub>2</sub>O formation. However, the existing challenges are to enhance the catalytic efficiency to simultaneously achieve the high conversion and selectivity and to improve the membrane stability to withstand the reducing atmosphere containing NH<sub>x</sub>, the unavoidable intermediates produced during the reaction which can etch the membrane surface.

### 10.2.2. Oxygen Extractor (type-II) MIEC Membrane Reactors

As shown in Figure S1-II (Supporting Information), there are two reactions being coupled in each zone of the membrane reactor where the first reaction produces oxygen to be extracted and consumed by the second reaction. Table S2 (Supporting Information) has summarized the applications of membrane reactors where the MIEC membranes work as the oxygen extractor. All the oxidative reactions described in Figure S1-I (Supporting Information) like POM can be applied as the second reaction for extraction purpose. Two typical oxygen-containing molecular decomposition reactions are CO<sub>2</sub> and water splitting to produce useful chemicals of carbon monoxide or hydrogen with the side product of oxygen. These reactions are generally limited by thermodynamic equilibrium, occurring only at high temperatures. For example, due to the low equilibrium constant, H<sub>2</sub> production from water dissociation in conventional reactor is difficult. Using membrane reactor, H<sub>2</sub> generation can be significantly promoted due to the equilibrium shift caused by the removal of one of the products (oxygen). Using membrane reactors for water splitting to produce hydrogen and CO<sub>2</sub> thermal decomposition for CO generation are already discussed in other sections of this roadmap (more details can be found in Sections 4–7), thus being treated in less attention. Noteworthy is that when the reacting conditions for the coupled reactions are well optimized, useful products can be provided from each zone of the catalytic membrane (type-II) reactors. For example, when water splitting is coupled by POM, hydrogen and syngas can be separately produced from each side of the membrane reactor. The prerequisite to ensure such a success is the requirement of high membrane material stability to withstand both reactions at high temperatures.

### 10.3. Opportunities

In spite of the progress made as discussed above, how to integrate the catalyst inside the membrane reactor is still not clear. A more in-depth discussion is made here to explore the influence of different catalyst loading methods on the membrane reactor performance. As displayed in Figure 18, there are four modes of catalysts being arranged inside the membrane reactors. In mode-I (most left in Figure 18), the catalysts are loosely attached inside the membrane and there is a certain distance between catalyst particles and the membrane surface. Due to the insufficient catalytic efficiency, the accumulated lattice oxygen diffused from the air side cannot be consumed by the activated methane and thus part of the lattice oxygen and electron holes will be recombined to form molecular oxygen. Gaseous oxygen will then diffuse in the gas phase to reach the surface of the catalyst to participate the reactions.

As mentioned earlier for COM, in order to enhance the C<sub>2</sub> selectivity, the gaseous oxygen should be avoided. Thus, the catalyst contact in mode-I would not lead to high C<sub>2</sub> yield, which is the reason for the undesirable performance in Table S1 (Supporting Information) for MIEC membrane reactors for OCM. Comparatively, the intimate contact in mode-II is a better design than mode-I for OCM as the catalyst particles are on the membrane surface with more interface. The most active sites for OCM are located in the triple-phase-boundary (TPB) (lattice oxygen, catalyst and methane) area as marked in Figure 18-II. In mode-II, the activated methane will also spill over along the particle surface to the TPB area, where more activated methane will react with lattice oxygen to form C<sub>2</sub> product. To prepare the membrane reactor with catalyst contact of mode-II usually requires much a higher temperature than mode-I as catalyst agglomerates would experience particle coalescence. At such circumstances, the amount of catalyst should be carefully controlled as the catalyst particles are easily sintered into a large agglomerate to cover the membrane area, unfavorably blocking the gas transport through the membrane. Mode-III is the best situation where the intimately contacted OCM catalysts also possess ion conducting properties. As marked in Figure 18-III, TPB area has been largely expanded to the whole exposed particle surface, therefore giving the best performance. The best C<sub>2</sub> yield of 39% achieved by Li's group using the LSCF hollow

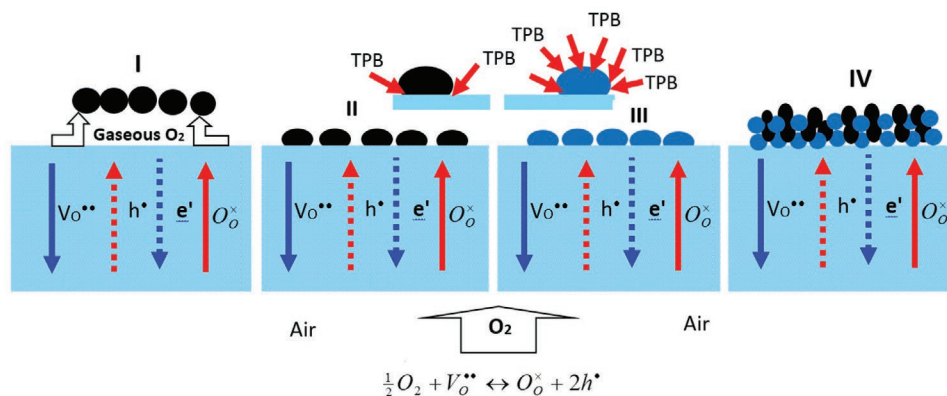


Figure 18. Oxygen permeation and reaction pathways for oxidative reactions by MIEC membranes with different catalyst contact modes.



fiber membrane integrated with OCM BSY catalyst was just the case described in Figure 18-III.<sup>[363]</sup> For some oxidations, such catalysts of mode-III are not available; then a better design is mode-IV, which is the combination of mode-II and mode-III where normal catalyst and membrane material particles are integrated together to expand the TPB area to promote the reaction.<sup>[187,381]</sup> The volume ratio of the membrane material in the composite catalyst in mode-IV should be at least 35% to ensure that there is a continuous material phase for oxygen evolution from membrane bulk to the composite catalyst.

With regards to the partial oxidation of methane, this reaction does not require the lattice oxygen to improve the selectivity as shown in Figure S2 (Supporting Information). Both catalyst contacts of mode-I and mode-II in Figure 18 can be applied for catalyst arrangement but each of them has its unique features. By comparing the two modes (I and II) in Figure 18 for POM, less oxygen would be consumed in mode-I as the oxygen partial pressure in the membrane interface facing the catalyst is higher than mode-II decreasing the driving force for oxygen transport. However, the presence of oxygen partial pressure in mode-I can help to protect the membrane from the strong reducing atmosphere of CO and H<sub>2</sub>. On the other hand, for catalyst contact in mode-II, the oxygen permeation will be accelerated due to the lattice oxygen is more active than gaseous oxygen to fully oxidize methane, CO or H<sub>2</sub>, leading to a higher oxygen permeation and syngas production rates. The big disadvantage of mode-II (Figure 18) is the requirement of high membrane stability as the reactors have to be chemically and mechanically stable at elevated temperatures not only in oxidative atmosphere (air side) but also in strongly reducing atmosphere containing CO and H<sub>2</sub> (methane side). Despite considerable efforts to develop various materials, membranes that can withstand such asymmetric atmospheres for long term operation for POM are rarely reported.

The working principles described in Figure 18 for various catalyst contact modes can provide a general guideline for membrane reactor design for other oxidative reactions. This is dependent on their individual reaction mechanism requiring the controlled gaseous oxygen or lattice oxygen. Fundamental understanding of catalyst contact mode will help to improve the membrane reactor performance.

#### 10.4. Concluding Remarks

In comparison with the intensive studies for air separation solely, MIEC membrane reactors are less investigated despite they represent a more advanced application of the membranes. The reason for this phenomenon is the lack of sufficiently robust membrane materials to withstand the reacting conditions containing acidic or reducing gases at high temperatures for a long-term operation. In particular, compared to the type-I membrane reactors, coupling two reactions to simultaneously maximize the reaction efficiency on both sides by membrane extractor reactor (type-II) is more challenging and more robust membranes are required to withstand the respective reacting conditions on each membrane side. It seems still a long way to go for the successful applications of these catalytic MIEC membrane reactors in a large industrial scale; but the hope is also there as more and more joint efforts from multidisciplinary teams are established to tackle the problems.

## 11. MIEC Membranes for Solar-Driven Processes

### 11.1. Status

MIEC membranes, mainly based on perovskites and/or fluorites, which offer advantages of high electrical and ionic conductivity, broadband optical absorption and excellent electrochemical properties, superior thermal stability and robustness have gained a huge interest in the applications of catalysis,<sup>[382,383]</sup> air separation,<sup>[46,384,385]</sup> and photothermal process,<sup>[386]</sup> etc. With the rapid development of solar capture and storage technologies in recent years,<sup>[387,388]</sup> solar-driven process utilizes MIEC membrane provides a promising way to convert solar energy to various kinds of energy forms, including thermal energy and chemical fuels through electrochemical, photochemical, thermochemical and their combinations, reaching a critical stage because of its important role in alleviating energy and environmental problems. Of the current methods proposed for solar energy conversion, photochemical process has the highest achievable conversion efficiency and the photothermal effect can be obtained by photoexcitation leading to partial or complete thermal energy (heat) production, including high-temperature solar-to-fuel production and low-temperature solar-driven water evaporation, etc.

During the last few decades, thermochemical H<sub>2</sub>O/CO<sub>2</sub> splitting process driven by concentrated solar energy (exceeding 2000 suns, 1 sun = 1 kW m<sup>-2</sup>) has been especially promising because it utilizes the entire solar spectrum and operates under high temperatures. So that it offers the potential to obtain high solar-to-fuel energy conversion efficiencies ( $\eta_{\text{solar-to-fuel}}$ ) and consequently, producing solar fuels (H<sub>2</sub>/CO) at competitive costs and at large scale industrialization.<sup>[389]</sup> Two-step thermochemical cycling with metal oxides, such as ceria and perovskites, being reaction intermediates has been put forward and widely investigated. The H<sub>2</sub>O/CO<sub>2</sub>-splitting thermochemical cycle<sup>[390,391]</sup> can be represented by:

1<sup>st</sup> step: reduction



2<sup>nd</sup> step: oxidation



In the first step, the metal oxide is heated under low O<sub>2</sub> pressure by concentrated sunlight ( $q_{\text{solar}}$ ) and reduced at elevated temperatures ( $T_{\text{red}} > 1473$  K) to generate O<sub>2</sub> (Equation (17)). In the second step, the reduced oxide is reoxidized with H<sub>2</sub>O and/or CO<sub>2</sub> at temperatures ( $T_{\text{ox}}$ ) at least 500 °C lower than  $T_{\text{red}}$  to produce H<sub>2</sub>(g) and/or CO(g), which in turn, can be further catalytically processed to liquid hydrocarbon fuels (gasoline, diesel, etc.) for the transportation sector. In these cases, the solar process efficiency is directly related to the oxygen storage capacity of materials ( $\delta$ ). In contrast to direct thermolysis ( $T > 2500$  K), two-step thermochemical cycles occur at relatively moderate upper temperatures, and bypass the high-temperature fuel/O<sub>2</sub> separation problem. In recent years, advances have

been made both in thermodynamic, kinetic, and mechanical properties of the materials, and various irreversibility reductions in the system-level optimization.<sup>[392]</sup> However, one of the greatest challenges against the efficiency improvement of two-step thermochemical cycles is the “anisothermal” operation because of the high thermal stresses on the reactor due to cooling and reheating and the increasing need for solid-solid heat recuperation.<sup>[387,393]</sup>

Specially, a thermochemical membrane reactor provides a way to isothermal and continuously splitting of H<sub>2</sub>O and CO<sub>2</sub>, by removing the oxygen generated from thermolysis in situ with a selective MIEC membrane. The idea to apply this concept to solar-driven processes was first proposed about 40 years ago by Fletcher et al.,<sup>[394]</sup> Browall et al.<sup>[395]</sup> and Noring et al.,<sup>[396]</sup> and the vast majority of previous work has focused on MIEC membranes.<sup>[131,139,167,397,398]</sup> In recent years, decisive progress in MIEC membranes focused primarily on oxygen permeation membrane based on doped ceria and perovskites.<sup>[217,399,400]</sup> Such membrane reactors can separate oxygen or produce hydrogen and syngas from water and alkanes. Compared with the discontinuous conventional thermochemistry with alternating-direction oxygen transport due to redox cycles, the combination of thermolysis, membrane reactor and solar energy could thereby simplify the solar fuel production system and offer an alternative and a new perspective way for solar-driven processes. Here we focus specially on reviewing state of art MIEC materials utilized in solar thermochemical reactors and survey recent developments of solar-driven processes with MIEC membranes.

## 11.2. Recent Advances and Future Challenges

### 11.2.1. MIEC Materials for Solar Thermochemical Processes

To date, various materials have been explored for solar-driven processes. MIEC materials, such as doped ceria and perovskite oxides, exhibit more active properties than stoichiometric oxides and remain crystallographically stable during the redox cycle. Moreover, the accommodation ability with different chemical elements allows innumerable combinations of elements in metal oxides and leaving many space for improving their thermodynamic and kinetic properties, thus opening a new direction for the development of solar thermochemical materials.

**Ceria-Based Oxide:** Ceria-based oxide is considered as one of the most promising candidates, as it possesses good oxygen diffusivity and electronic conductivity originating in the Ce<sup>4+</sup>↔Ce<sup>3+</sup> redox couple, and abundance in the earth's crust. Since the originally proposed reduction cycle of CeO<sub>2</sub> to Ce<sub>2</sub>O<sub>3</sub> in solar thermochemical water splitting by Abanades et al.,<sup>[401]</sup> the use of ceria has attracted substantial interest; however, the required reduction temperature of above 2000 °C led to sintering and substantial extensive sublimation of Ce. Based on the non-stoichiometric CeO<sub>2</sub>/CeO<sub>2-δ</sub> cycle, Steinfeld et al.<sup>[392]</sup> developed the first ceria-based solar reactor (Figure 19), and successfully demonstrated the feasibility of the cycle with porous ceria under realistic solar concentrating conditions. The simultaneous H<sub>2</sub>O/CO<sub>2</sub> splitting was experimentally shown in consecutive splitting cycles, obtaining syngas with H<sub>2</sub>:CO molar ratios (0.25–2.34)

which can be tuned by adjusting the molar co-feeding ratio of H<sub>2</sub>O:CO<sub>2</sub> (0.8–7.7).<sup>[402]</sup> Ionic and electronic conductivities of ceria directly dictate the ambipolar oxygen diffusion rates, rendering larger length scales suitable for driving redox reaction. This was demonstrated by Steinfeld et al.,<sup>[403]</sup> optimizing solar cavity-receiver configuration with a scalable reticulated ceria with dual-scale porosity via temperature/pressure-swing operation. With enhanced mass and heat transport properties for rapid redox reaction kinetics, they experimentally demonstrated 5.25% solar-to-fuel energy efficiency, with 83% molar conversion of CO<sub>2</sub> and 100% selectivity, which was comparable to the highest value reported to date. The kinetic and thermodynamic properties of ceria can be altered by doping rare earth metal and transition metal oxides in its fluorite structure. Dopants for ceria-based cycles are considered to be included with +2 (Ca, Sr, Li),<sup>[404–406]</sup> +3 (Sm, Gd, Y, Pr, La, Sc)<sup>[404,405,407,408]</sup> and +4 (Zr, Hf)<sup>[404,407,409]</sup> cations. Considering that the diffusion of oxygen occurs through ambipolar diffusion of both ions and electrons in ceria, higher oxygen diffusion coefficients and electronic mobilities can be achieved by the introduction of +2 and +3 cations due to stable intrinsic oxygen vacancies within the ceria lattice.<sup>[410,411]</sup> However, +2 and +3 dopants are not expected to have a thermodynamic benefit compared to pure ceria. Tetravalent dopants in cerium oxide have been shown to have positive effect on lowering the temperature of reduction and increasing yields under conditions relevant to thermochemical cycles. Abanades et al.<sup>[412]</sup> showed that the zirconium addition significantly improved the reduction of ceria (up to 70%) at < 1500 °C. For example, maximum H<sub>2</sub> production from Ce<sub>0.75</sub>Zr<sub>0.25</sub>O<sub>2-δ</sub> was 0.24 mmol g<sup>-1</sup> at 1045 °C, and it could be further optimized by adjusting the Zr content. Gal et al. reported that the reduction rate in ceria/zirconia solid solutions increased with Zr content, and the ≈27.9% maximum value was obtained with 50% Zr content at 1400 °C.<sup>[407]</sup> Moreover, the reduction yield was increased with lowering the reaction pressure, which provided a new prospect for the operation of solar thermochemical reactors.

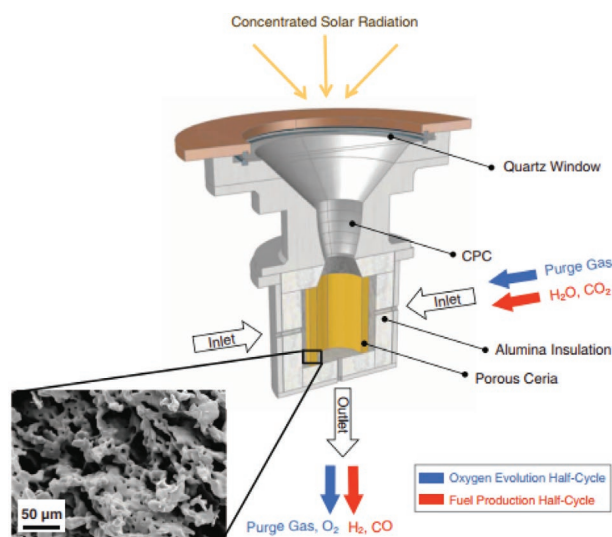


**Figure 19.** Ceria-based solar reactor for two-step cyclic H<sub>2</sub>O/CO<sub>2</sub> splitting. Reproduced with permission.<sup>[392]</sup> Copyright 2010, The American Association for the Advancement of Science.

**Perovskite Oxide:** Perovskite oxides are another type of promising redox materials capable of solar thermochemical H<sub>2</sub>O and/or CO<sub>2</sub> splitting. Perovskites with the general form of ABO<sub>3-δ</sub> are very versatile materials and are highly amenable to structurally doping on the A and B cation sites.<sup>[413]</sup> The advantages of perovskites are lower reactor temperatures for reduction, and the larger possible change of nonstoichiometry compared to ceria. Till date, investigations on solar-to-fuel production using perovskites were firstly performed on manganese-based perovskite compositions.<sup>[414–418]</sup> Scheffe et al. performed a thermodynamic analysis based on extraction of partial enthalpies and entropies and evaluation of oxygen nonstoichiometry data, and shown that La<sub>1-x</sub>Sr<sub>x</sub>MnO<sub>3-δ</sub> possessed higher oxygen exchange capacity than pure ceria.<sup>[419]</sup> Experimental investigation in two-step thermochemical cycles for CO<sub>2</sub> splitting indicated that total CO yield is greater than ceria, based on the greater reduction extent (about 2 times by mass at 1773 K) although less favorable oxidation thermodynamics resulting in incomplete oxidation. McDaniel et al. explored an even more promising perovskites by doping LaAlO<sub>3-δ</sub> with Sr<sup>2+</sup> on A sites and Mn<sup>2+/3+/4+</sup> on B sites.<sup>[414]</sup> When applied in the solar thermochemical H<sub>2</sub>O/CO<sub>2</sub> splitting cycles, the H<sub>2</sub> and CO yields are 9 and 6 times higher than those of the current state-of-the-art ceria materials, respectively, when reduced at 1350 °C and re-oxidized at 1000 °C. However, also other compositions show promising results with different transition metals and combinations, such as perovskites with general ABO<sub>3-δ</sub> structure including Fe/Co<sup>[420,421]</sup> and Co/Cr<sup>[422]</sup> on the B sites. These results demonstrate the potential promise of perovskite based solar-driven systems, however, the major drawback is their relatively high heat capacity. Therefore, to reduce the heat losses associated with large temperature swings, isothermal or near-isothermal operation is required for perovskite cycles.

### 11.2.2. MIEC Membranes for Solar Fuel Production

Thermochemical redox cycles for H<sub>2</sub>O/CO<sub>2</sub> splitting facilitate storage of solar energy in the form of chemical fuels, such as H<sub>2</sub> and/or CO. Firstly, concentrated solar energy supplied high temperature for endothermic reduction of oxygen carrier materials, such as ceria and perovskite, liberating O<sub>2</sub>. Secondly, in the re-oxidation process at lower temperatures, reduced metal oxides split H<sub>2</sub>O/CO<sub>2</sub>. Alternatively, isothermal redox

cycles driven by pressure swing process were demonstrated recently.<sup>[393,397,423]</sup> To advance this concept, researchers proposed isothermal redox membrane reactor. In membrane-assisted thermolysis, the oxidation and reduction processes are separated spatially, and one of products transports across a selective membrane to prevent recombination and boost reaction conversion. The solar thermal membrane reactors were first theoretically studied by Fletcher et al.<sup>[394]</sup> and Browall et al.,<sup>[395]</sup> for which the process was driven by the difference of chemical potential across the barrier. Since then, vast majority of the advanced previous works focused on oxygen permeation membranes with mixed ionic and electronic conductivity.

**Conceptual MIEC Membrane Reactor for Solar Fuel Production:** In the case of hydrolysis based on solar thermal membrane reactors, the energy conversion efficiency is a vital metric especially when concentrated solar heat is part of the system. Many researches evaluated the thermodynamic efficiency of H<sub>2</sub>O/CO<sub>2</sub> dissociation with an MIEC reactor operated under isothermal conditions. A conceptual oxygen transport membrane reactor for solar thermochemical fuel production was first proposed by Wang et al.<sup>[398]</sup> Compared with traditional reactors, reduction and oxidation occur simultaneously on different sides of the membrane, which serves as a barrier for gases and pressures but a channel for oxygen ions. The continuous production of solar fuels can be achieved without technical challenges because of high-temperature moving and mechanical consumption resulting from metal oxide transportation, and solid heat loss can be eliminated because of the isothermal reaction mode. A theoretical framework is established with MIEC membrane reactor for understanding of solar-driven isothermal H<sub>2</sub>O splitting and the solar-to-fuel efficiency are compared for the case of pump and methane-assisted scenarios. Thermodynamic analysis implies that the pump-assisted case achieves solar-to-fuel efficiency (e.g., 2.9% at 1500 °C) as low as isothermal solar thermochemical cycles, attributing to the low conversion of water, much elevated temperature range, and short effective length. This is also consistent with thermodynamic analysis of the isothermal ceria-based membrane reactor system by Li et al.,<sup>[424]</sup> and the results show that maximum efficiencies of 1.3% and 3.2% are attainable for H<sub>2</sub>O and CO<sub>2</sub> splitting, respectively, at about 1700 °C with inert sweep gas on the reduction side of the membrane. Actually, Zhu et al. established a thermodynamic model of the ceria membrane reactor system with heat recovery (Figure 20a),<sup>[425]</sup> and indicated that a pump-assisted membrane

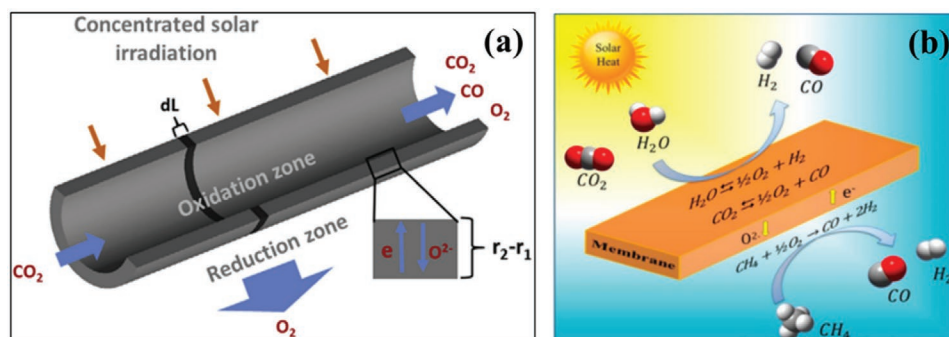
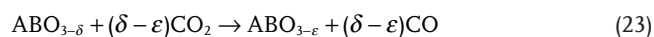


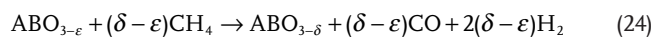
**Figure 20.** a) Scheme of CO<sub>2</sub> converting process (Reproduced with permission.<sup>[425]</sup> Copyright 2016, Elsevier) and b) simultaneous thermal decomposition of H<sub>2</sub>O and CO<sub>2</sub> (Reproduced with permission.<sup>[182]</sup> Copyright 2017, American Chemical Society) (b) in the membrane reactor.

reactor can maintain a low oxygen pressure in the reduction side and simplify steady state model for the system. The solar-to-fuel efficiency was calculated to be above 40% assuming good heat recovery, and further demonstrate by Tou et al. in a ceria redox membrane reactor for solar-driven CO<sub>2</sub> splitting.<sup>[131]</sup> In contrast to both the inert gas and pump-assisted modes, the methane-assisted case attains much higher efficiency (net solar-to-fuel efficiency ≈63%) at much lower temperatures (850–900 °C), owing to the improved thermodynamic driving force by partial oxidation of CH<sub>4</sub>.<sup>[398]</sup> This higher efficiency might indicate a new trend in solar-driven thermochemistry.

Seinfeld et al. demonstrated the feasibility of methane dry reforming using an isothermal redox La<sub>0.6</sub>Sr<sub>0.4</sub>Co<sub>0.2</sub>Fe<sub>0.8</sub>O<sub>3-δ</sub> membrane, that combines the benefits of thermochemical methane dry reforming and continuous isothermal solar fuel production.<sup>[126]</sup> The reactor technology realizes the continuous reduction of CO<sub>2</sub> by the oxygen vacancies of La<sub>0.6</sub>Sr<sub>0.4</sub>Co<sub>0.2</sub>Fe<sub>0.8</sub>O<sub>3-δ</sub> into CO on the inner side of the tubular membrane:



where  $\delta$  is the oxygen non-stoichiometry. The oxygen adsorbed on inner side of the membrane travels along oxygen gradient to the outer side, and is abstracted from lattice oxygen from the solid by CH<sub>4</sub> dry reforming:



CO<sub>2</sub> and CH<sub>4</sub> are reformed into solar syngas, the energy value of which was solar-upgraded by a factor of 3 than that of methane feedstock. La<sub>0.6</sub>Sr<sub>0.4</sub>Co<sub>0.2</sub>Fe<sub>0.8</sub>O<sub>3-δ</sub> membranes yielded up to 1.27 μmol<sub>CO</sub> g<sup>-1</sup> s<sup>-1</sup> from CO<sub>2</sub> splitting, and 3.77 μmol<sub>CO</sub> g<sup>-1</sup> s<sup>-1</sup> from CH<sub>4</sub> dry reforming at 840–1030 °C.

Different from the previous studies either on the individual H<sub>2</sub>O or CO<sub>2</sub> as feed gas in an oxygen transport membrane reactor, Jiang et al. further proposed a simultaneous solar-thermal decomposition of CO<sub>2</sub> and H<sub>2</sub>O to produce syngas with a H<sub>2</sub>/CO ratio of 2/1, using a dual-phase Ce<sub>0.9</sub>Pr<sub>0.1</sub>O<sub>2-δ</sub>Pr<sub>0.6</sub>Sr<sub>0.4</sub>FeO<sub>3-δ</sub> membrane with mixed oxygen ion and electron conductivity (Figure 20b).<sup>[182]</sup> In this case, high-temperature furnace was utilized as a substitution of solar oven. Benefiting from the in situ oxygen removal by the membrane, effective CO<sub>2</sub> and H<sub>2</sub>O splitting were achieved at relatively lower temperatures (<1000 °C). For example, at 930 °C, a syngas production rate of 1.3 mL min<sup>-1</sup> cm<sup>-2</sup> was obtained with H<sub>2</sub>O conversion

of > 1.7% and CO<sub>2</sub> conversion of > 4.2% for a H<sub>2</sub>O/CO<sub>2</sub> feed ratio of 5/1. This combination of catalytic thermolysis, oxygen transport membrane, and solar energy offers a new perspective route to convert CO<sub>2</sub> and H<sub>2</sub>O to solar syngas. The membrane concept used in all these works in situ removes one of the reaction products and drives the reactions to dissociation and avoids downstream recombination. Analyses show that thermodynamic driving force is crucial for both conversion rate and effective length of reactor. Maintaining low partial oxygen pressure requires additional energy for vacuum pumping or inert gas assistant separation. Methane assisted membrane reactors, on the other hand, improve thermodynamic driving force because of partial oxidation of methane, and appear to be a better choice when considering energy efficiencies. This isothermal operation and high efficiency might indicate a promising trend in solar thermochemistry.

*Experimental MIEC Membrane Reactor for Solar Fuel Production:* To demonstrate the proof-of-concept application of solar-driven membrane reactor, Tou et al. experimentally displayed for the first time the continuous CO<sub>2</sub> splitting under steady-state isothermal/isobaric conditions driven by concentrated radiation, applying a solar-driven ceria membrane reactor conducting electrons (Ce<sup>3+</sup>/Ce<sup>4+</sup> change), oxygen ions, and vacancies induced by different oxygen chemical potential gradient across membrane (Figure 21).<sup>[131]</sup> The solar reactor was operated at 1450–1600 °C and 3000–3500 suns radiation, yielding total selectivity of CO<sub>2</sub> to CO and O<sub>2</sub> with 0.024 μmol s<sup>-1</sup> cm<sup>-2</sup> at 3 × 10<sup>-6</sup> bar P<sub>O<sub>2</sub></sub>. In this case, the theoretical limit exceeds 40% at 1600 °C, which is in good agreement with a comparable thermodynamic study by Zhu et al.<sup>[425]</sup> The authors went further and also demonstrated the feasibility of co-feeding both CO<sub>2</sub> and H<sub>2</sub>O into separate streams of syngas (H<sub>2</sub>/CO) and O<sub>2</sub>, using a tubular ceria membrane (CeO<sub>2-δ</sub>) reactor heated by simulated concentrated solar radiation of up to 4200 suns, and assessed the relative favorability between these two thermolysis reactions occurred simultaneously.<sup>[139]</sup> Combined CO and H<sub>2</sub> fuel production rates were measured in the range of 1500–1600 °C and 0.2–1.7 Pa O<sub>2</sub>. A maximum rate of 2.3 μmol cm<sup>-2</sup> min<sup>-1</sup> at 1600 °C and 0.2 Pa of O<sub>2</sub> was yielded at steady state, corresponding to a 0.7% conversion of reactants. This solar membrane reactor technology under realistic high-flux conditions is simple and compact, and the scalability of tubular design demonstrate its viability for splitting and co-splitting CO<sub>2</sub> and/or H<sub>2</sub>O to fuels. However, the reaction rates were limited by heat and mass transfer, the extent of CO<sub>2</sub> and H<sub>2</sub>O thermolysis, even enhanced by an MIEC membrane,

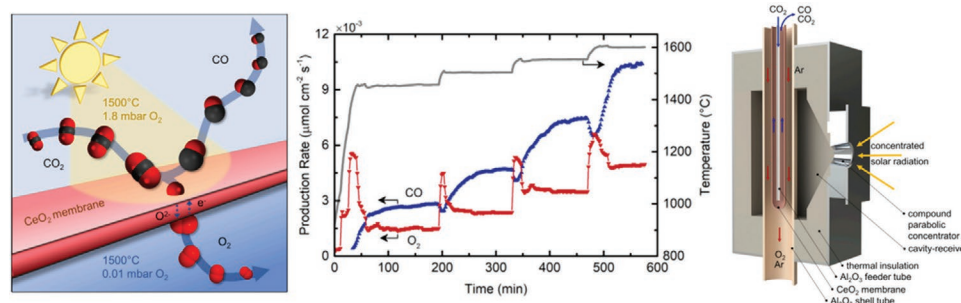


Figure 21. Solar-driven thermochemical CO<sub>2</sub> splitting across a membrane reactor. Reproduced with permission.<sup>[131]</sup> Copyright 2017 Elsevier.



is impractically low under the required operating temperatures typically in the range of 1250–1750 °C. The solar-to-fuel efficiency was limited by the lack of heat recovery and the available membrane surface. Therefore, alternative membrane materials, such as perovskite oxides, with higher oxygen ion diffusivity and structural and thermochemical stability should be developed. In addition, alternative membrane configurations, such as dual-membrane reactors<sup>[426]</sup> for in situ removal of both the separate productions by thermolysis should be explored to control the purity of the fuel produced and boost mass conversions, and consequently obtain favorable solar-to-fuel energy efficiencies.

### 11.2.3. MIEC Membrane for Solar-Driven Evaporation

Photothermal technology (Figure 22) is a direct method to harvest solar energy into thermal energy, thus improving localized surface temperature. In the midst of the photothermal technology implementation, solar-driven evaporation, different from solar-to-fuel membrane reactor requiring high optical concentrations, can utilize the illumination with low optical concentrations even like the solar irradiation in the natural environment for generating vapor at the temperatures lower than the boiling temperature. Photothermal materials are the key factor in solar-driven evaporation for fresh water generation in desalination. As the semiconducting materials, perovskite oxides endowed with the suitable bandgap can generate electron-hole pairs, when exposed to solar illumination, and then part of such excited electrons eventually return to the low-level states with non-radiative relaxation in the form of phonons (heat), resulting in the photothermal effect.<sup>[386]</sup> Various perovskite oxides with photothermal performance have been reported as solar absorbers in solar-driven evaporation process. Yang et al. introduced double perovskites  $\text{Sm}_{0.7}\text{Sr}_{0.3}\text{BaCo}_2\text{O}_{5+\delta}$  into solar-driven water evaporation system, achieving evaporation efficiency of

86% under two-sun illumination.<sup>[427]</sup> Such photothermal membrane provide a new insight for applying perovskites as photothermal materials into solar-driven evaporation. However, the relatively low evaporation efficiency and complicated preparation process may obstruct its large-scale application. Besides, Zeng et al. demonstrated that OV-enriched  $\text{MoO}_{3-x}$  exhibited a water evaporation rate of  $1.51 \text{ kg m}^{-2} \text{ h}^{-1}$  and the energy conversion efficiency of 95% under one-sun irradiation, with adsorbing charged organic dyes for wastewater purification.<sup>[428]</sup> The above  $\text{MoO}_{3-x}$  material combined with its photothermal performance and photocatalytic activity represents a new avenue for wastewater purification, while the actual application in natural scenarios is still limited. In the practical application, performance degradation or even invalidation of photothermal materials occurs because of the biological or organic contaminants. Pyrolysis can decompose the contaminants but still suffers high energy consumption. Jiang et al. developed a multi-functional  $\text{La}_{0.7}\text{Sr}_{0.3}\text{CoO}_3$  perovskite for high-efficiency solar-driven evaporation and energy-saving regeneration, in view of its high photothermal performance, desirable catalytic activity in combustion, and excellent thermostability.<sup>[429]</sup> Under one-sun irradiation, such hierarchically porous  $\text{La}_{0.7}\text{Sr}_{0.3}\text{CoO}_3$  accelerates the evaporation up to  $1.67 \text{ kg m}^{-2} \text{ h}^{-1}$ , about 420% of the nature water evaporation rate. Moreover, the  $\text{La}_{0.7}\text{Sr}_{0.3}\text{CoO}_3$  catalyze thermal decomposition of biological and organic contaminants at a relatively lower temperature, which means a lower energy consumption. This work provides an ideal kind of photothermal material for practical application in the fields of wastewater treatment and desalination, which is an extension of the utilization of MIEC membranes for solar-driven processes. Compared to traditional solar distillation systems, MIEC membrane assisted photothermal evaporation is a promising solution and a green technology for clean water production because of its largely improved efficiency. In the future, more efforts are needed to explore available photothermal materials with excellent chemical and thermal stability and compatibility with different environments and compact installations.

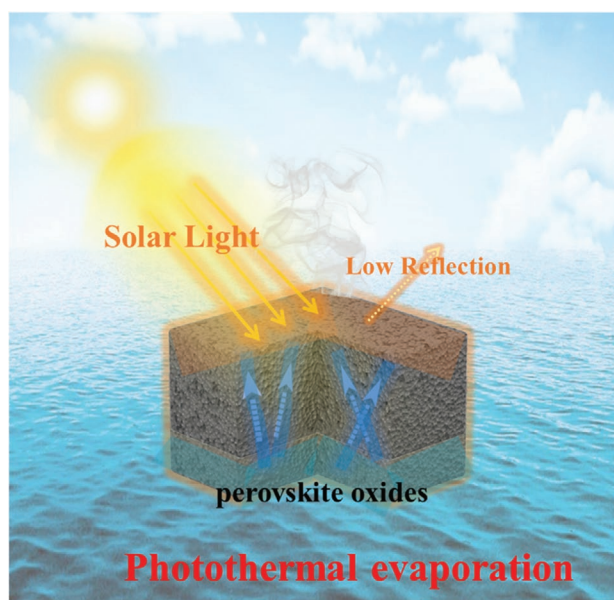


**Figure 22.** Scheme for photothermal water vaporization process.

## 11.3. Opportunities

The remarkable development of solar-driven processes in recent years greatly motivates intense efforts in this field, however, there are still crucial challenges to be confronted. Firstly, although the theoretical solar-to-fuel energy efficiency can be achieved as high as 40%, the ideal energy efficiency is related with solar concentration ratio and operating temperature. The optimum temperature for maximum energy efficiency varies between 800 °C and 1500 °C. However, the solar energy cannot be completely used, and loss occurs in the transfer of energy. In this regard, to improve the solar-to-fuel energy conversion efficiency, the operation of the solar furnace should be optimized and unwanted radiation and nighttime heat loss be minimized. Since most of the actual operating efficiency is rather low, it is thus necessary to develop reactors and investigate economic operating modes, including the synthesis of advanced catalysts, improvement of reactor performances and operating modes, etc. Moreover, thermodynamic properties of MIEC materials are one of the most important considerations. Further progress

is expected to predict promising new materials compositions with both computational techniques and materials screening studies. Other factors, such as reaction kinetics, chemical reactivity, and thermal and mechanical stability are also required favorable characteristics. Therefore, more efforts are highly needed to explore MIEC materials with excellent stability and compatibility with the design of efficient installations in terms of thermal loss minimization and heat recovery, to significantly improve the overall efficiency and yield.

#### 11.4. Concluding Remarks

Solar-driven process utilizes MIEC membrane provides a promising way to convert solar energy to various kinds of energy forms, reaching a critical stage because of its important role in alleviating energy and environmental problems. Optimal MIEC membrane materials are still to be developed. Doped ceria and perovskite oxides with exceptional features are encouraged to be researched and developed toward solar-to-fuel conversion. Here we focus specially on reviewing state of art MIEC materials including doped ceria and perovskites utilized in solar thermochemical reactors, and survey recent developments of solar-driven processes with MIEC materials for solar fuels production and for solar-driven evaporation. Despite many improvements have been achieved, there are still many challenges to conquer for commercialization. Further progress can be expected in future with both computational techniques and solar reactor studies to predict promising new materials.

## 12. MIEC in Electrolyzer Cells for Power-to-X Technologies

### 12.1. Status

The direct conversion of electrical energy into a chemical product is particularly advantageous with solid oxide electrochemical devices. The high operating temperature around 800 °C of such reactors, makes the process particularly efficient compared to low temperature devices, as a significant part of the energy required for the splitting of the oxygen is supplied in a form of heat.<sup>[430]</sup> The reaction kinetics are fast and such devices have been proven to operate reversibly either in fuel cell mode, to generate power, or in electrolysis mode to store electricity, for instance in the form of green hydrogen from steam. Among all electrolysis technologies, solid oxide cells (SOC) requires the lowest amount of electricity to produce hydrogen, with a specific energy consumption below 3.5 kWh Nm<sup>-3</sup>. Moreover, they are versatile with respect of the molecules to electrolyze and allow simultaneous reduction of CO<sub>2</sub> and H<sub>2</sub>O into a valuable synthetic gas, consisting in a mixture CO and H<sub>2</sub> whose precise ratio can be fine-tuned depending on the client process and the final product to be synthesized. This is particularly attractive for the production of e-fuels and green bulk chemicals.

For long the development of such electrochemical devices has been driven by the fuel cell application. Nonetheless in the current context of the energy transition with decarbonation of the industrial processes and the use of hydrogen as energy

carrier, the perspective of producing green hydrogen and bulk chemical with incomparable efficiency out of renewables represent an incomparable incentive for the development of electrolyzers based on SOC.

The key elements determining the performance and the lifetime of the electrochemical devices are the two electrodes and their interface with the electrolyte.<sup>[431]</sup> Since the two electrode reactions implies gaseous species, electrons and oxygen ions, the nature of the selected materials, determines the nature of the electrochemical interface. If a porous electrode made of a mixture of a pure ionic conductor, that is typically the same material as for the electrolyte, and an electronic conductor presents a convenient approach especially with respect of the thermo-chemical compatibility of the cell components, it has the disadvantage to confine the charge transfer reaction at TPBs, i.e., where the three species involved in the electrode reaction may be in contact. As a result, the electroactive regions are usually characterized as a length per unit volume of electrode, i.e., μm/μm<sup>3</sup>. With this respect, MIEC offers a change in the paradigm of performance optimization. In a MIEC electrode, the entire surface of the materials that is exposed to the reactive gases is in principle active. Rated to the electrode volume, this solid-gas interface, characterized as a double phase boundary (DPB) is quantified as a surface by unit volume, i.e., μm<sup>2</sup>/μm<sup>3</sup>. Therefore, electrodes with DPBs are game changers compared to traditional electrodes relying on TPBs (**Figure 23**).

As MIEC materials, perovskite oxides ABO<sub>3</sub> and related structures such as the double perovskite AA'B<sub>2</sub>O<sub>5+δ</sub> and Ruddlesden-Popper A<sub>n+1</sub>B<sub>n</sub>O<sub>3n+1</sub> are of particular relevance,<sup>[431]</sup> as they offer a board range of functionalities either as oxygen electrode or as fuel electrode because of the vast compositional array.

#### 12.1.1. Oxygen Electrode

State-of-the-art oxygen electrodes usually rely on materials with ABO<sub>3</sub> perovskite structure. For MIEC oxygen-electrode materials the 2PB pathway dominates. The performance of such a MIEC oxygen electrode is dominated by the oxygen surface exchange reaction which is rate limiting.<sup>[60,431]</sup> This involves the contribution from both oxygen vacancies and molecular oxygen.<sup>[432,433]</sup> An indication of the extension of the active region is the characteristic length  $L_c = D_{\text{chem}}/k_{\text{chem}}$ , with  $D_{\text{chem}}$ : oxygen chemical diffusion coefficient, and  $k_{\text{chem}}$ : the oxygen chemical exchange coefficient.<sup>[300]</sup> The value ranges from 8 nm for La<sub>0.5</sub>Sr<sub>0.5</sub>MnO<sub>3-δ</sub> to 500 μm for La<sub>0.6</sub>Sr<sub>0.4</sub>Co<sub>0.8</sub>Ni<sub>0.2</sub>O<sub>3-δ</sub> at 800 °C with  $p_{\text{O}_2} = 70$  kPa.<sup>[60]</sup> Besides the intrinsic properties of the materials, the actual extension of the electrochemically active area in the volume of the electrode strongly depends on the microstructural parameters such as particle size, porosity and tortuosity.<sup>[434]</sup> For practical application, it is sometimes advantageous to consider composite materials, in which the MIEC material is mixed with a fluorite phase, typically a doped cerium oxide, either to enable a better thermo-mechanical match of the electrode with the electrolyte, by reducing the mismatch in thermal expansion coefficient or to boost the oxygen ion conductivity if the selected MIEC materials present limited ionic transport properties.<sup>[434]</sup> Nowadays, materials from the solid solution La<sub>1-x</sub>Sr<sub>x</sub>CoO<sub>3-α</sub> (LSC) – La<sub>1-x</sub>Sr<sub>x</sub>FeO<sub>3-α</sub> (LSF) identified

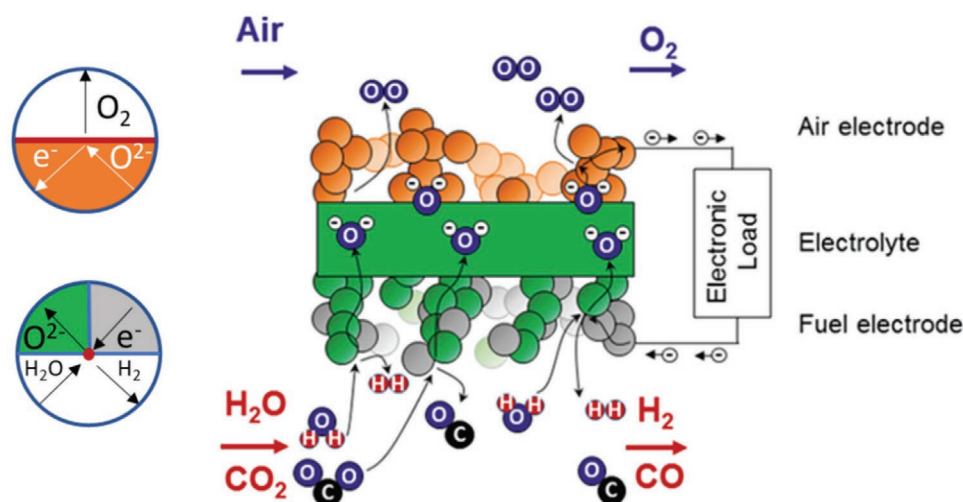


**Figure 23.** Co-electrolysis process with SOC regardless of the cell architecture for the production of syngas. The two inserts offer a schematic representation of the electrochemical reaction at TPB (fuel electrode) and at double phase boundary (oxygen electrode). Interfaces are marked in red (adapted with permission<sup>[430]</sup>).

as LSCF are widely used as oxygen electrode for SOC. LSC is preferred for operation at 600–700 °C because of the high  $k_{\text{chem}}$  even at moderate temperature. This makes it material of choice for SOC with a fuel electrode supported architecture,<sup>[435]</sup> while for the electrolyte supported cells, that operate at a temperature of  $\approx 800$  °C and above, LSCF are still preferred.<sup>[436]</sup>

If the integration of LSCF oxygen electrode enabled to significantly improve the performance of SOC devices over the oxygen electrode materials from the family SrO-LaMnO<sub>3</sub>, this showed severe chemical compatibility issues with the various stabilized zirconia that are used as electrolyte materials. This has implied the intercalation of an intermediate layer, also called diffusion barrier layer, whose purpose is to block the interdiffusion of cations between zirconia and LSCF and avoid the formation of a highly resistive zirconate layer.

### 12.1.2. Ceria-Based Barrier Layer

To this end, a doped ceria layer of few microns in thickness and with mixed ionic and electronic transport properties<sup>[411,437,438]</sup> is usually added between the dense electrolyte and the porous LSCF electrode. Preferred processing route for this interlayer is screen printing followed by a sintering step. There is usually a trade-off between the densification of the ceria layer that is preferable for the functionality and the durability of the device and the interdiffusion with the zirconia electrolyte which is detrimental for the performance. As a result, screen printed barrier layers are usually sintered at mild conditions yielding a porous microstructure.

### 12.1.3. Fuel Electrode

Typical SOC fuel electrodes consists in a porous composite made of nickel and stabilized zirconia which confines the electrochemical reaction near the TPBs.<sup>[439]</sup> Nonetheless, in

electrolysis application such ceramic-metal composites, i.e., cermets, have shown microstructural instabilities at high overpotential and  $p\text{H}_2\text{O}$ .<sup>[440]</sup> This is particularly exacerbated in fuel electrode supported cell architecture, with which, a current density of 1.5 A cm<sup>2</sup> is typically reached at 1.29 V in steam electrolysis.<sup>[441]</sup> Moreover, in presence of carbon species, as in co-electrolysis, because of the nickel phase, those cermet electrodes have shown a propensity to favor carbon deposition that may lead in fine to the destruction of the electrode.<sup>[442]</sup>

Nickel cermet with ceria materials have emerged, in which the electrochemical reactions is delocalize over the DBP ceria – gas because of the MIEC properties of the material.<sup>[443,444]</sup> They exhibit a superior tolerance against carbon deposition and show excellent performance for electrolysis and co-electrolysis application.<sup>[430]</sup> Nonetheless, the poor mechanical properties of such a porous cermet do not enable them to ensure the structural function in fuel electrode supported cell architecture which restrict their use to electrolyte supported cell architectures<sup>[430]</sup> for which they are state of the art<sup>[436]</sup> or metal supported cell architectures.<sup>[445]</sup>

Recently, MIEC fuel electrodes based on materials with the ABO<sub>3</sub> perovskite structure have emerged and have been investigated. It was historically based on LaCrO<sub>3</sub> that was considered as interconnect material due to its outstanding stability in dual atmosphere and good electronic conductivity.<sup>[431]</sup> Investigations focused on the partial substitution on A site with Sr and Ca, while elements such as Ti, Mn, Fe, Ni were investigated as B-site cations. The results have yielded two main families of fuel electrode materials, i.e., the chromites which are p-type conductors and titanates which are n-type conductors. Both have shown their ability to host transition metals on their B-site that can be then exsolved operando, either chemically or electrochemically, at the surface of the material in the form of metallic nanoparticles that boost the electrochemical activity of the electrode.<sup>[145,446]</sup> Nonetheless, for electrolysis application, performance reports with perovskite electrode though very promising with respect of the performance of traditional cermet, are limited to samples size below 20 cm<sup>2</sup>.<sup>[447]</sup>

## 12.2. Recent Advances and Future Challenges

If adequate performance has been achieved with current MIEC oxygen electrode, current challenges focuses on the processing of the ceria interlayer and the fuel electrode. In SOC, it is desirable to integrate thin film ceria intercalation layer with higher density compared to traditional screen printed and sintered layer and with clean interface, i.e., without formation of the zirconia – ceria interdiffusion layer. Physical vapor deposition (PVD) methods, such as pulsed laser deposition (PLD),<sup>[448,449]</sup> magnetron sputtering,<sup>[450,451]</sup> or electron beam (EB) – PVD<sup>[452]</sup> have demonstrated layers with appropriate properties but the cost effectiveness of such processes for up-scaling and mass production is questionable especially for PLD processes. Focus should be on the development of processing methods that enable the processing of thin and dense layers of MIEC materials with improved interfacial properties with zirconia electrolytes and electrode materials.

Currently other challenges remain on the integration of nickel – ceria cermet electrode in a fuel electrode supported cell architecture. Because in SOC electrolyzer H<sub>2</sub>O or CO<sub>2</sub> flows on the fuel electrode, metal supported cell architecture, in which a porous ferritic stainless steel is used as a substrate for the fuel electrode, may face critical challenges due to corrosion issues at high steam content or risks of metal dusting when exposed to mixtures with high carbon activity. Integration of functional nickel ceria layer onto a mechanically stable and highly conductive porous substrate may be of interest<sup>[453]</sup> to exploit the properties of the ceria materials against the carbon deposition risk in co-electrolysis but also to enhance the tolerance to sulfur containing impurities that may be present in the feed gas.<sup>[442]</sup>

If very promising performances have been achieved with perovskite fuel electrode at the button cell level, i.e., ≈1 cm<sup>2</sup> of active area, it is challenging to develop high performance fuel electrode based on perovskite at a stack scale which requires working area of about ≈100 cm<sup>2</sup>.<sup>[454]</sup> As electronic conductivity level in perovskite fuel electrode is typically in the range 1 – 10 S cm<sup>-1</sup> it becomes crucial to engineer the electrode to ensure sufficient current collection to compete with nickel cermets that shows conductivity values above 100 – 500 S cm<sup>-1</sup>. At the stack level the development of highly conducting backbone and contact elements between the fuel electrode and the bi-polar plate with sufficient lateral conductivity is crucial to enable integration of perovskite fuel electrode material into stack.<sup>[455]</sup> If the recent development work primarily aimed at integration in stacks for fuel cell application, the challenge remains for stacks in electrolysis application.

One should emphasize that most of the studies and reports on SOC electrolyzers for *Power-to-X* are based on investigations at lab scale, meaning the use of H<sub>2</sub>O and CO<sub>2</sub> feed streams of high quality. Nonetheless considering a technological deployment of SOC electrolyzer for *Power-to-X* and sector coupling application, would imply systems operating with feed streams of CO<sub>2</sub> and H<sub>2</sub>O that are of uncertain quality. Since the nature and the amount of impurities are determining for the lifetime of electrodes in SOC devices,<sup>[431]</sup> and that may jeopardize the cost effectiveness of the hydrogen or syngas production, it appears that the design of fuel electrodes with a superior tolerance to impurities would represent a key asset for the

technologies. Common impurities that affect the durability of SOC electrolyzers are SiO<sub>2</sub><sup>[430]</sup> or sulphur compounds.<sup>[442]</sup> This issue may be extended to the oxygen electrode that is also exposed to the impurities that are present in air, if it is used as sweep gas. The optimization of the acid-base properties of electrode materials surface by fine tuning of the composition of the electrode material could be an approach.<sup>[431]</sup>

In situ regeneration of the fuel electrode would also contribute to enhance the lifetime of electrolyzers. The application of a redox cycle to perovskite MIEC fuel electrode materials with exsolution of nanoparticles have been shown to restore the performance when operated under anodic bias after exposure to sulphur species<sup>[455]</sup> and should be investigated when operated under cathodic bias. The reincorporation of the ex-solved nanoparticles into the lattice upon oxidation and their regeneration upon subsequent reduction represents an attractive opportunity to restore the electro-catalytic properties of the materials after a certain operating time. Dimensional stability of the electrode in dual atmosphere, i.e., in both reducing and oxidative conditions, and its capacity in operating in pure steam or CO<sub>2</sub> atmosphere is therefore essential and is a key advantage for most of the MIEC materials over traditional nickel-based cermet electrodes.

Finally, the deployment of SOC technologies with MIEC materials at the GW scale which would represent a mass market will imply a large use of Rare Earth elements and strategic materials such as Co. This necessarily raises the question of the sustainability of the resources and the treatment of these materials at end of life. Therefore, the development of efficient recycling processes for reuse of the elements that make the ceramic materials used in SOC represent an inevitable challenge on the path of the deployment of these materials in electrolyzers.

## 12.3. Opportunities

MIEC electrode materials with large surface exchange coefficient  $k_{\text{chem}}$  are crucial to achieve high performance especially at moderate temperature. In oxygen electrode, three order of magnitudes higher  $k_{\text{chem}}$  have been reported upon surface modification by infiltration of alkaline oxide.<sup>[143]</sup> If the infiltration method to enhance surface chemistry is still challenging for up-scaling and technological deployment, the large flexibility of the perovskite structure in hosting different cations may facilitate the development of MIEC electrode materials by fine tuning their composition.

The co-doping on B-site with reducible cations can enable exsolution of nanoparticles in a form of metallic alloys which gives an additional option to develop fuel electrode that are less prone to poisoning or carbon deposition issues. Fe, Co, Ni, Pd, and Ru were shown to exsolve from perovskite chromites or titanates perovskites<sup>[456–459]</sup> and can create alloys. The exsolution of Mn, Cr and/or NiO represent an attractive route to develop electrodes that are tolerant to carbon deposition for dry CO<sub>2</sub> electrolysis.<sup>[460,461]</sup>

Interfacial strain engineering represents an additional approach for optimizing the oxygen exchange and the ionic transport in MIEC electrode.<sup>[431]</sup> An increase by a factor 1000 of the oxygen surface exchange coefficient was reported in



heterostructures (La,Sr)CoO<sub>3-δ</sub>/(La,Sr)<sub>2</sub>CoO<sub>4-δ</sub>.<sup>[462]</sup> Similarly, in perovskite based fuel electrodes, a strained perovskite lattice may create upon exsolution of nanoparticles when remaining trapped in the bulk.<sup>[463]</sup> Thus, nanocomposites represent a large potential to develop high performance electrode for SOC electrolyzers.

#### 12.4. Concluding Remarks

Development of MIEC oxygen electrode have played a crucial role in the development of SOC and their implementation for fuel cell applications. Operating under reverse potential as electrolyzer raises new challenges especially at the fuel electrode to cope with electrolysis of H<sub>2</sub>O and/or CO<sub>2</sub>. If additional developments to fine tune both electrodes properties are required in order to mitigate poisoning or fast degradation issues and unlock high performance at intermediate temperature, the further development of MIEC fuel electrode, eventually in the form of nanocomposites with regenerating capabilities have the potential to solve the critical issue of nickel migration that traditional cermet materials suffer. As such performant and durable MIEC fuel electrode represent an important milestone in the development of viable high temperature electrolyzer for *power-to-X* applications. Beyond the materials, their cost-effective processing to implement them into stacks and their efficient recycling at end of life are also determining challenges to address to envision their deployments at large scale.

### 13. Progress on the Commercialization of MIEC Membrane Technology

#### 13.1. Status

##### 13.1.1. Industrial Applications for Mixed Conductors

The commercialization of MIEC materials is already happening for distinct applications, e.g., as conductive coatings for SOFC and SOEC (Solid Oxide Electrolyzer Cell), as electrocatalysts for water electrolysis, for metal-air batteries and et cetera. They are used as a core component in membrane separation processes to produce O<sub>2</sub> or H<sub>2</sub>.

A first commercialization of MIEC membranes should focus on a simple process scheme and plant design, but also on low interdependencies with other industrial processes. Since the introduction of a new technology is expensive and risky, the economic benefit must be large enough and very clear. Applications requiring a low number of MIEC membranes and a low O<sub>2</sub> throughput should be preferred, due to the high manufacturing costs for the membranes without a pre-established mass production line. Otherwise, very high investments would be necessary, resulting in a very high risk.

Therefore, it makes sense to take another look at the possible process routes for O<sub>2</sub> MIEC membranes. If a chemical reaction is combined with a separation process by a membrane, it is typically called a membrane reactor (MR).<sup>[464]</sup> If a catalytic effect is incorporated, it is referred to as a catalytic membrane reactor (CMR).<sup>[465]</sup> In contrast to that, simple separation of O<sub>2</sub>

represents a membrane separator. The latter one always needs energy for the separation, but a membrane reactor is driven by the chemical reaction itself. For that reason alone, a membrane reactor has a higher efficiency and a larger economical benefit. However, it is typically focused on and designed for one specific chemical reaction and not really versatile.

The most famous application for a MIEC membrane reactor is the partial oxidation of natural gas<sup>[466–469]</sup> to produce synthesis gas, the swiss pocket knife for the synthesis chemistry. Another dream reaction is the oxidative coupling of methane,<sup>[353,470]</sup> but the oxidative dehydrogenation of saturated hydrocarbons to alkenes<sup>[377]</sup> is also promising. A lot of other chemical reactions are possible,<sup>[471]</sup> e.g., the production of H<sub>2</sub> by water splitting using fuels,<sup>[472]</sup> selective oxidation of ammonia to NO<sup>[380]</sup> for production of nitric acid,<sup>[473]</sup> the total oxidation of hydrocarbons to produce heat for industrial processes resulting in a highly efficient capture of carbon dioxide.<sup>[474,475]</sup> Recently, even the generation of useful work or mechanical power was proposed.<sup>[476]</sup> The approach is comparable to an SOFC with an inner short-circuit, but the energy is converted by gas expansion work. An EU project utilizes this approach to provide NH<sub>3</sub> as a C-free, sustainable fuel.<sup>[477]</sup>

MIEC membranes are able to operate with and without a sweep gas, sometimes called 4 end and 3 end operation. The latter case represents a membrane separator, the former one a membrane reactor. The gas management is more challenging for a membrane reactor and the material demands are typically higher.<sup>[478]</sup> A well-defined gas distribution at high temperatures, e.g., a counter flow of gases, is difficult to realize and expensive regarding the construction details. Besides, membrane reactors typically need gas-tight joinings or sealings of the ceramic membranes to special steel alloys suited for high temperatures.<sup>[479]</sup> Such joinings are always a weak point and a safety risk, as well as the brittle membranes themselves separating a highly flammable gas from glowing air. Moreover, technical plants often need high gas pressures<sup>[468]</sup> to fulfill the requirements for following process steps. If high pressure differences occur, tubular MIEC membranes should be used instead of planar ones.<sup>[480]</sup>

The different oxygen partial pressures at both surfaces of a working MIEC membrane generates always a different chemical expansion of the crystal lattice resulting in so-called chemically induced mechanical stress. It dominates the whole stress situation of a working MIEC membrane.<sup>[480–483]</sup> Its tensile component should be kept as low as possible by a smart combination with the outer loads generated by the total pressure differences.<sup>[480,482]</sup> Besides, MIEC materials are frequently not stable against reducing conditions or distinct gases used in membrane reactors like steam,<sup>[44]</sup> CO<sub>2</sub><sup>[484,485]</sup> or even SO<sub>2</sub>.<sup>[486]</sup>

Obviously, the production of cheap gaseous O<sub>2</sub> by a membrane separator is much simpler. Already the use of a condensable sweep gas like steam is more ambitious, although the combined thermal compression of O<sub>2</sub> generates an additional benefit.<sup>[487]</sup>

##### 13.1.2. Oxygen Production Technologies

The market for pure O<sub>2</sub> is vast and well established. Accordingly, a detailed comparison to mature O<sub>2</sub> production technologies and a market analysis are inevitable.

**Table 7.** O<sub>2</sub> production technologies and their energy demand to produce 1 m<sup>3</sup> O<sub>2</sub> and entailed energy costs and CO<sub>2</sub> emissions.

Oxygen manufacturing technology	Purity vol%	Energy demand		Energy costs			Total CO <sub>2</sub> emissions <sup>a, b)</sup> g m <sup>-3</sup> O <sub>2</sub>	
		Electr.	Heat	Electr. <sup>a)</sup>	Therm. <sup>b)</sup>	Total		
		[kWh]		[€-Ct.]		[€/t]		
cryo ASU <sup>[489]c)</sup>	>99.6	>0.46		4.60		4.60	32.2	215.3
LOx delivery <sup>[492]c)</sup>	>99.6	>0.86		8.60		8.60	60.3	402.5
PSA <sup>[488]</sup>	<95	>0.90		9.00		9.00	63.1	421.2
VPSA <sup>[494]</sup>		>0.34		3.40		3.40	23.8	159.1
polymer membr. <sup>[495]</sup>	<35	>0.35		3.50		3.50	24.5	163.8
MIEC-V. el./el. <sup>e[496]</sup>	>99.6	>0.72		7.20		7.20	50.5	337.0
MIEC-V. gas/el. <sup>e)</sup>		>0.20	0.25	2.00	0.63	2.63	18.4	144.1
MIEC-V. wh/el. <sup>f)</sup>		>0.20	0.25	2.00		2.00	14.0	93.6

<sup>a)</sup>electricity: 0.10 € kWh<sup>-1</sup>, 468 g CO<sub>2</sub> kWh<sup>[497]</sup>; <sup>b)</sup>natural gas: 0.025 € kWh<sup>-1</sup>, 202 g CO<sub>2</sub> kWh<sup>[498]</sup>; <sup>c)</sup>without costs and emissions for transport; <sup>d)</sup>MIEC membrane plant, heated by electricity and with an electrical vacuum pump, experimental values from<sup>[496,499,500]</sup>; <sup>e)</sup>as before<sup>(d)</sup>, but thermally optimized and heated by natural gas combustion; <sup>f)</sup>as before<sup>(e)</sup>, but heated by waste heat.

**Table 7** compares the known technologies for O<sub>2</sub> production. O<sub>2</sub> is mainly produced by cryo ASU (cryogenic Air Separation Unit). A cryo ASU produces at least 25 000 m<sup>3</sup> O<sub>2</sub> h<sup>-1</sup> but usually significantly more. The Capex (capital expenditures) and the energy demand normalized to production capacity decrease with plant size.<sup>[488]</sup> The real energy demand amounts to at least 0.46 kWh m<sup>-3</sup>,<sup>[489]</sup> although a theoretical limit between 0.21 and 0.28 kWh m<sup>-3</sup> was proposed.<sup>[490,491]</sup> It could be further decreased if a lower O<sub>2</sub> purity is accepted.<sup>[492]</sup> Customers with a large O<sub>2</sub> demand like steel plants are supplied by short pipelines. Smaller customers with less than ≈1000 m<sup>3</sup> O<sub>2</sub> h<sup>-1</sup> were provided by tank trucks with LOx (Liquid Oxygen). Its energy content amounts to ≈0.86 to 1.14 kWh m<sup>-3</sup> O<sub>2</sub>.<sup>[492]</sup> Linde plc assumes 1 kWh m<sup>-3</sup> O<sub>2</sub> for LOx,<sup>[493]</sup> but its transport to the customer and the emissions entailed are not included.

An alternative for on-site O<sub>2</sub> production is the PSA (Pressure Swing Adsorption) technique. The purity of the product gas is limited to 93 – 95 vol% O<sub>2</sub>, the energy demand amounts to at least 0.9 kWh m<sup>-3</sup> O<sub>2</sub>.<sup>[488]</sup> VPSA plants (Vacuum PSA or VSA) need at least 0.34 kWh m<sup>-3</sup> O<sub>2</sub> above 1500 m<sup>3</sup> h<sup>-1</sup>.<sup>[494]</sup> Polymer membranes are characterized by a very low separation selectivity. They are only competitive for an O<sub>2</sub> enrichment up to ≈35 vol% O<sub>2</sub>.<sup>[495]</sup> Within Table 7, three kinds of MIEC membrane plants are listed. All three plants and their properties are based on a pilot plant built and tested at Fraunhofer IKTS in 2017.<sup>[496,499–501]</sup> The MIEC plant labeled with “el./el” is driven by electricity only and the real electricity demand of a tested pilot plant with 9.6 m<sup>3</sup> O<sub>2</sub> h<sup>-1</sup> is used.

The energy demand of the vacuum pump for O<sub>2</sub> extraction amounted to 0.2 kWh m<sup>-3</sup> O<sub>2</sub>, the heat demand amounted to ≈0.5 kWh m<sup>-3</sup> O<sub>2</sub>. It must be noted that the thermal insulation of the plant was rather poor as discussed later. A minimal heat demand of 0.25 kWh m<sup>-3</sup> O<sub>2</sub> shall be possible for larger plants. Accordingly, the second MIEC plant in Table 7 represents a prospective plant heated by natural gas combustion. Presently, such a device is realized within a publicly funded project dealing with the oxy-fuel operation of an internal combustion engine and CO<sub>2</sub> capture.<sup>[502]</sup> The third MIEC device is

heated by waste heat of a thermal process. It will be realized by another running project dealing with oxy-fuel fired furnaces, and is aiming at saving primary fuel.<sup>[503]</sup>

The comparison of energy costs clearly indicates large advantages for MIEC plants, especially if cheap thermal energy can be used for heating. Obviously, the energy costs of the highly optimized cryo ASU could be nearly halved. Since the specific CO<sub>2</sub> emissions for conventional electricity production are higher than for gas combustion, much lower CO<sub>2</sub> emissions would be possible.

### 13.1.3. Basics of MIEC Membrane Plants for O<sub>2</sub> Production

The Fraunhofer IKTS has been developing MIEC membranes since 1998. We are mainly focused on tubular MIEC membranes to enable large pressure differences. Besides, a manufacturing of membrane tubes by extrusion is one of the cheapest manufacturing techniques well established for mass production in the ceramic industry. The simplest gas management for O<sub>2</sub> production corresponds to a cross flow 3-end arrangement. This approach was already used by Air Products and Chemicals (APC, Allentown, USA),<sup>[466,504]</sup> the process is mainly driven by feed overpressure. Since highly efficient turbo-components comparable to a gas turbine are necessary but not available for small gas throughputs, small plants are not possible, at least not with a competitive efficiency. The pressure vessel is always heavy and large.<sup>[22,505]</sup> Therefore, a market entry at a small O<sub>2</sub> production capacity is not possible. Nevertheless, the APC plant concept was the dominating one for several years.<sup>[22,505,506]</sup> Although APC proposed a decrease of Capex, Opex (operational expenditures) and footprint compared to cryo ASU,<sup>[504]</sup> the whole development was cancelled in 2015.

Few people were dealing with a vacuum driven separation of O<sub>2</sub>. The use of ambient air at the feed side results in a simple furnace structure equipped with one-side closed MIEC membrane tubes connected to the vacuum piping system at the open end of the tubes. No pressure vessel is needed, expensive turbo

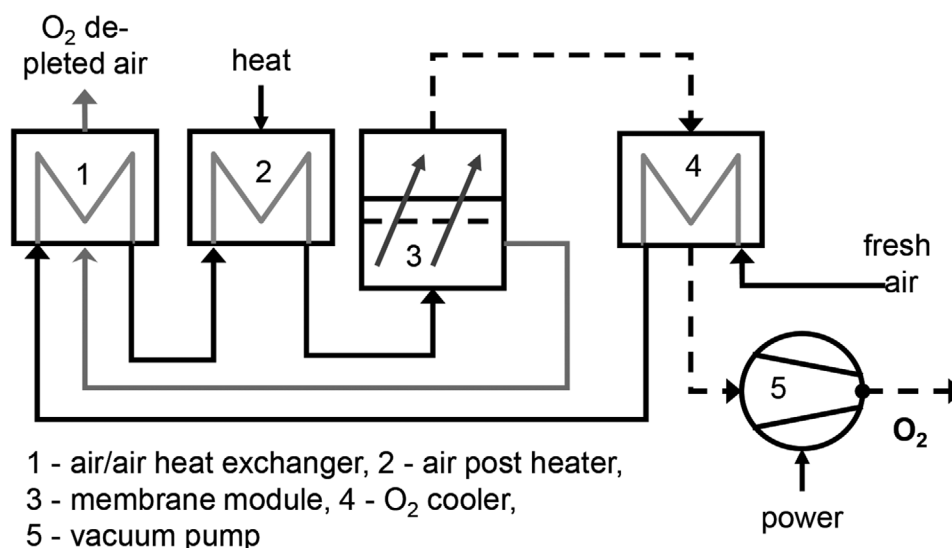


**Figure 24.** Process scheme of the vacuum driven MIEC membrane separation process for O<sub>2</sub> production.

components are spared. The O<sub>2</sub> throughput is freely scalable from very small to large. Altogether, this approach is easy to realize.<sup>[507,508]</sup>

Overpressure or vacuum driven 3-end O<sub>2</sub> separation needs a comparable amount of heat for balancing of the thermal losses. Regarding to the gas compression, we can assume that the compression energy depends on mainly on the pressure ratio. Therefore, the extraction of 1 m<sup>3</sup> gas at 0.1 bar to environmental pressure (1 bar) is comparable to a compression from 1 bar to 10 bar. The O<sub>2</sub> flux should be also comparable. However, we have to compress ≈10 m<sup>3</sup> of air to produce 1 m<sup>3</sup> O<sub>2</sub>. The recovery of compression energy is restricted to ≈80%, if the gas turbine reaches a very high isentropic efficiency of 90% for air compression as well as for hot gas expansion. The remaining 20% losses correspond to the energy required for a compression of 2 m<sup>3</sup> gas. The vacuum process has to compress 1 m<sup>3</sup> O<sub>2</sub> only. Accordingly, the losses for gas compression for the overpressure process are roughly twice as much.<sup>[509]</sup>

Vacuum extraction also results in much lower chemically induced tensile stress for the MIEC membranes compared to feed overpressure.<sup>[480]</sup> Therefore, life span predictions for overpressure separation are much more critical.<sup>[510]</sup> Besides, we had already measured higher O<sub>2</sub> permeation rates for vacuum extraction of BSCF (Ba<sub>0.5</sub>Sr<sub>0.5</sub>Co<sub>0.8</sub>Fe<sub>0.2</sub>O<sub>3.δ</sub>) tubes compared to a sweeping with N<sub>2</sub> or Ar.<sup>[509,511]</sup> Therefore, Fraunhofer IKTS had primarily focused on the vacuum process schematically depicted in **Figure 24**.

## 13.2. Recent Advances and Future Challenges

### 13.2.1. MIEC Pilot Plants for O<sub>2</sub> Production

Since 2009, different pilot plants have been developed in Fraunhofer IKTS, which typically characterized by a growing oxygen production rate and a decreasing energy demand.<sup>[496,512,513]</sup>

Elaborated data and results for six different pilot plants described hereafter are summarized in the supplementary information. Up to now, all pilot plants were powered by electricity only, although heating by gas combustion or waste heat would be much cheaper.

The first plant was erected in 2009.<sup>[512]</sup> The feed air is used to cool down the hot O<sub>2</sub> and flows into the hot zone in a counter flow to the outgoing O<sub>2</sub> depleted air. The membranes tubes are sealed by a cold sealing. The device was used during 1700 h at different exhibitions and fairs.

The second device was constructed for experiments with different membranes geometries and for long-term tests. In 2011, it was equipped with 31 BSCF tubes hanging down freely. A stable production of 2.4 L O<sub>2</sub> min<sup>-1</sup> was proven for 9500 h. The device was reconstructed in 2014. A long-term measurement using 93 capillaries was carried out for ≈18 000 h. The O<sub>2</sub> permeation dropped down by app. 6% during the last 14 000 h at constant conditions.

The third device was assigned by an external client. The energy demand for gas compression was found to be 0.43 kWh m<sup>-3</sup> O<sub>2</sub>, very close to the engineered value.<sup>[513,514]</sup> However, the total energy demand was higher than expected because of an inadequate efficiency of the recuperative heat exchanger. Therefore, we were looking for alternative heat exchangers. We found the old and well-known principle of regenerative heat storage using ceramic balls or combs. It is easy to realize, cheap and usable for very high temperatures. A heat recovery of up to 98% is possible as proven for large RTO (Regenerative thermal oxidizer) plants.<sup>[515,516]</sup>

The fourth and fifth devices were equipped with capillaries together with regenerative heat exchangers. The calculated O<sub>2</sub> flux of the fifth device was 1.0 m<sup>3</sup> O<sub>2</sub> h<sup>-1</sup>, the experimental one amounts to 0.94 m<sup>3</sup> O<sub>2</sub> h<sup>-1</sup>. Obviously, a distinct pressure drop inside the thin capillaries slightly lowered the flux, as was already observed for single capillaries.<sup>[134]</sup> Also the heat demand was higher than calculated, probably because of a very complicated air and heat management.

The sixth device was realized within a publicly funded project.<sup>[499]</sup> It was intended to reach a low specific energy demand of  $0.5 \text{ kWh m}^{-3} \text{ O}_2$  comparable to an optimized large cryo ASU. The average total energy demand was determined to be  $0.716 \text{ kWh m}^{-3} \text{ O}_2$ . After subtracting  $0.03 \text{ kWh m}^{-3} \text{ O}_2$  for peripheral electrical devices and  $0.2 \text{ kWh m}^{-3} \text{ O}_2$  for the vacuum pump, the remaining heat demand was determined to be  $0.49 \text{ kWh m}^{-3} \text{ O}_2$ ,  $\approx 0.2 \text{ kWh m}^{-3} \text{ O}_2$  higher than calculated. An infrared camera system was used for a thermal inspection. Several hot spots with up to  $80 \text{ }^\circ\text{C}$  on the outside of the metallic casing were found, e.g., near some feedthroughs for thermocouples and the wirings to the electrical heaters. We assume that such weak points can be avoided for further plants and the low engineered heat demand is realistic.

Obviously, MIEC membrane plants driven by vacuum are able to reach a very low energy demand for gas compression. Besides, the experimental values for compression energy demand and  $\text{O}_2$  throughput agree very well with the calculated values. This highlights the benefits of a reliable modeling of the gas separation and compression, and also for the  $\text{O}_2$  permeation model used for BSCF. In contrast to that, the real heat demand is difficult to estimate due to the deviations between calculated and observed values. Nevertheless, thermal losses should decrease for larger plants since the ratio of surface to volume will be better.

Presently, the MIEC plant design is constantly developed further. It deals especially with the development of a membrane module that enables membrane plants on a common frame system but with a freely scalable  $\text{O}_2$  throughput (see supplementary information).

### 13.2.2. Prospective Energy Demand of Vacuum Driven MIEC Plants

Our development of MIEC membrane pilot plants was accompanied by an iterative improvement of its basic engineering. The comparison of the models with experimental values results in some insights about interactions of gas throughputs with the variation of  $\text{O}_2$  partial pressures and driving forces depending on gas flows along the membrane contact zone. These insights and findings were claimed in a patent along with special arrangements and components necessary to realize an efficient but simple and cheap MIEC membrane plant.<sup>[501]</sup>

The detailed energetic model is not a part of this roadmap, but the main contributions will be explained as briefly as possible. A first prerequisite for operating the membranes is the typical operation temperature. The thermal losses are determined by the heat recovery of the heat exchangers and the losses across the casing. The same amount of "heat" has to be added as already mentioned in Figure 24. That is the first important part of the total energy demand.

The  $\text{O}_2$  separation always requires an  $\text{O}_2$  partial pressure gradient across the membrane. Its maintenance requires power corresponding to the label "power" inside Figure 24. That is the second important contribution to the total energy demand. The energy demand of small fans used to shift the air through the plant is very low. The electricity consumption of the control unit is typically negligible.

Within a technical  $\text{O}_2$  membrane plant, only a part of the  $\text{O}_2$  is separated from the feed air. The amount of  $\text{O}_2$  separated is quantified by the so-called  $\text{O}_2$  recovery. Assuming a constant production of  $1 \text{ m}^3 \text{ O}_2 \text{ h}^{-1}$ , a decreasing  $\text{O}_2$  recovery from the feed air results in a higher air throughput entailed by growing thermal losses of the heat exchangers. Therefore, the  $\text{O}_2$  recovery enables a calculation of the heat recovery. The thermal losses via the casing can be estimated using its surface temperature times its total surface area.

The vacuum pressure at the permeate side of the membrane results from the interaction of the  $\text{O}_2$  delivered by the membranes as a source and the suction speed of the vacuum pump as a drain. A lower vacuum pressure increases the  $\text{O}_2$  flux but is always accompanied by a higher energy demand for vacuum generation. Since a higher  $\text{O}_2$  recovery decreases the  $\text{O}_2$  partial pressure at the feed side, it is entailed by a higher specific energy demand for the vacuum pump.

The interaction of the individual gas throughputs can be described using the  $\text{O}_2$  recovery  $f_{\text{ORec}}$ .

$$f_{\text{ORec}} = \frac{F_{\text{O}_2}}{F_{\text{Fin}} p_{\text{OFin}}}; f_{\text{ORec}} = \frac{J_{\text{O}_2}}{j_{\text{Fin}} p_{\text{OFin}}} \quad (25)$$

$F$  – total fluxes ( $\text{O}_2$  – oxygen through the membrane,  $F_{\text{in}}$  – Feed air in),  $j$  – membrane area normalized fluxes,  $p_{\text{OFin}}$  –  $\text{O}_2$  partial pressure at feed inlet.

Therefore, the  $\text{O}_2$  recovery is usable as a central independent variable to describe the interactions and enables the calculation of the contributions of heat and power.

Selected results are shown in Figure 25. Obviously, the specific total energy demand is characterized by a minimum between 40% and 70%  $\text{O}_2$  recovery. The precise position depends especially on the heat recovery of the heat exchangers represented by the different curves, but also on the energy demand of the vacuum pump. Vacuum pump systems with an

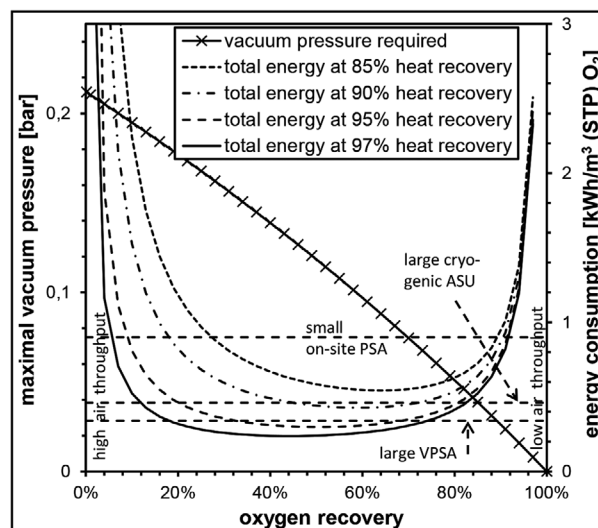


**Figure 25.** Total energy demand and vacuum pressure of a vacuum driven MIEC membrane plant depending on oxygen recovery; energy consumption of the vacuum pump was fixed to  $0.018 \text{ kWh/Sm}^3$ , without thermal losses via the casing.



energy consumption down to 0.13 kWh/Sm<sup>3</sup> are available but typically not relevant because of higher costs. Obviously, at a moderate heat recovery of the heat exchangers of 90%, the total specific energy demand falls below a large cryo ASU. The more efficient large VPSA is undercut at a heat recovery of at least 95%, which seems to be realistic for larger MIEC plants.

### 13.3. Opportunities

#### 13.3.1. Energy Costs of Vacuum Driven MIEC Plants

The comparison of O<sub>2</sub> production technologies in Table 7 indicates a very low electricity demand for MIEC membrane plants heated by gas combustion or waste heat. Gas is typically 3 to 4 times cheaper per kWh than electricity, resulting in much lower running costs. Actually, if the low heat demand cannot be realized for the next MIEC plants, there is a remaining advantage regarding the running costs compared to all other O<sub>2</sub> production technologies. Besides, this advantage is combined with lower CO<sub>2</sub> emissions.

If necessary, energy costs could be decreased further, e.g., by the use of mechanical power to propel the vacuum pump using a gas piston engine. The whole plant would need nearly no electricity but more cheap gas. Moreover, several very cheap lean gases are available to drive the whole process, e.g., sewage gas, landfill, mine, and coal gas or blast furnace gas from iron foundries. Accordingly, the cost-cutting potential for running expenses is high.

#### 13.3.2. Economic Comparison of Technologies

Regarding to the economic competitiveness, the critical part of MIEC plants is the Capex. The Capex of VPSA plants normalized to the O<sub>2</sub> production capacity amounts to ≈3000 €/m<sup>3</sup> O<sub>2</sub> h<sup>-1</sup>) as confirmed by market studies. The last MIEC membrane device was more than 8 times as expensive. In other words, a VPSA plant producing 10 m<sup>3</sup> O<sub>2</sub> h<sup>-1</sup> is available for app. 30 000 € resulting in a depreciation of 3000 € per year. The MIEC plant needs an annual depreciation of 25 000 €! If we use electricity with 0.1 € kWh<sup>-1</sup> and gas with a price a fourth of electricity, the energy costs amount to 2980 €/a for the VPSA and 2.400 € for the MIEC plant. The MIEC plant could never win because of its high depreciation dominating the whole Opex.

Nevertheless, it must be considered that some O<sub>2</sub> applications need pure O<sub>2</sub> instead of 95 vol% only. That is an advantage, but typically it does not compensate for an 8-fold investment for a typical customer. Besides, real O<sub>2</sub> price increases steeply with decreasing O<sub>2</sub> demand,<sup>[517]</sup> because of the large effort to distribute small amounts of O<sub>2</sub> as LOx or compressed gas to individual customers. For that reason, an on-site O<sub>2</sub> production is often competitive compared to an O<sub>2</sub> delivery. Its economic benefit usually increases with a decreasing O<sub>2</sub> demand rate, especially if the annual use efficiency is very high. Accordingly, there are distinct O<sub>2</sub> applications with low but continuous O<sub>2</sub> demand well suited for a market entry.

Presently, some employees at Fraunhofer IKTS already dealing with MIEC membranes are trying to establish a

spin-off company. However, some special tasks have to be done beforehand. The most important one is to decrease the Capex for the MIEC membrane plants to lower the barrier for the market entry. Since the membranes themselves are presently the most expensive part, the cost reduction was primarily focused on that.

The first step was a detailed analysis of the membrane manufacturing process, which was already done. As expected, personnel costs dominate the overall costs, but can be reduced significantly through the substitution of time-consuming work steps. Nevertheless, raw powder costs for BSCF powder were also identified as a critical part, especially if a distinct decrease of the personnel costs were realized and the membrane cost were already decreased. The powder costs would be constant and would hinder a further cost decrease. For that reason, an in-house powder synthesis was developed together with a powder conditioning route. For the same reason, a recycling route for process waste was also developed and successfully tested.

Besides, the extrusion of capillaries is permanently improved<sup>[518,519]</sup> to decrease the effort of manufacturing. A significant step is the use of special extrusion tools enabling a multi-line extrusion of capillaries combined with semi-automated closing, handling and drying. This is not yet fully realized, but we expect a distinct cost reduction for the BSCF capillaries.

Another task is the construction and successful testing of a pilot plant suitable as the base for the serial production of membrane plants. It is necessary for a market entry for some of the applications mentioned, e.g., waste water treatment, gasification or oxy-fuel furnaces. The constant improvement of the MIEC plant design is accompanied by the substitution of expensive parts by cheaper ones, as has already been done for the heat exchangers. Moreover, the modular approach successfully realized for the membrane modules (see supplementary information) will be repeated regarding to the whole membrane plant design. The modular concept regarding the plant frame should enable lower prices for components because of a higher number of identical parts.

Based on the use of cheaper membranes, the membrane modules developed, and a modular plant concept, we have developed a cost model for the membrane plants. Naturally, an adequate profit was included to ensure a sustainable development of the new company. **Figure 26** compares the O<sub>2</sub> production costs for a small and a large MIEC membrane plant with a small PSA, a large VPSA and a cryo ASU. The minimal possible energy demands for the mature technologies were assumed according to Table 7. The energy costs of the MIEC plants were calculated according to the basic engineering of these plants. They could reach lower energy costs as the horizontal line illustrates, but this is presently not competitive because of the increasing Capex. The maintenance costs were assumed to be 3% of the Capex. The depreciation for 10 years is directly proportional to the Capex and seems to be comparable for the mature technologies. The small MIEC plant has a higher depreciation because of relatively high costs of the basic furnace structure needed for the MIEC plant. Nevertheless, the depreciation will decrease below that of the mature technologies for larger devices as the depreciation of the large MIEC plant indicates.

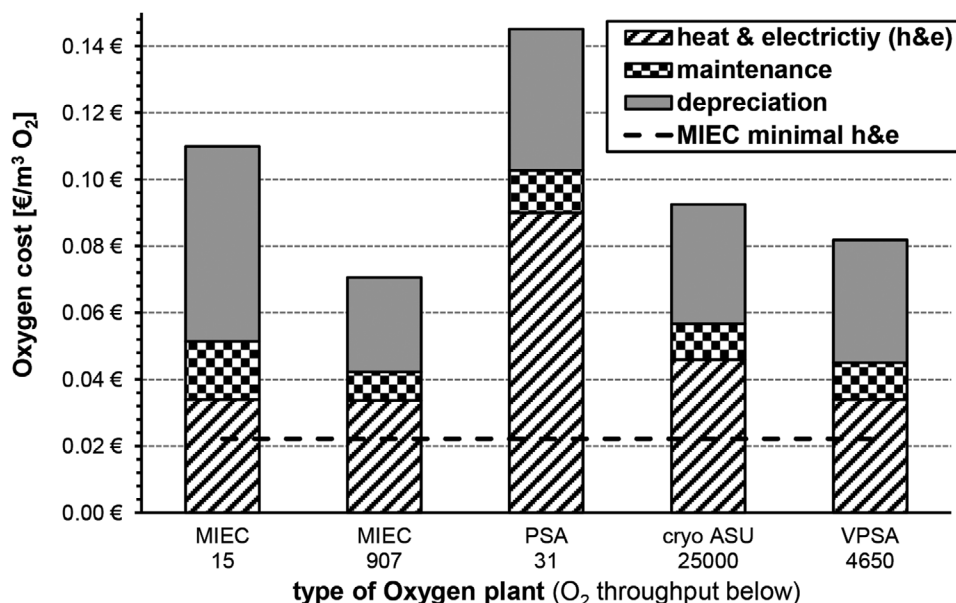


**Figure 26.** Comparison of O<sub>2</sub> production costs for different kinds of O<sub>2</sub> production plants; a minimal energy consumption was assumed for mature technologies; assumed energy costs: 0.10 € kWh<sup>-1</sup> for electricity, 0.025 € kWh<sup>-1</sup> for natural gas, 3% of Capex as maintenance, depreciation of Capex for 10 years, annual efficiency 100%, 8760 h/a.

### 13.4. Concluding Remarks

The highest TRL for devices using MIEC membranes was presently reached for membrane separators producing pure O<sub>2</sub> by a vacuum driven process. The process is much simpler than the overpressure process and reaches much lower energy costs and CO<sub>2</sub> emissions compared to mature technologies. If a decrease of the Capex close to the level of VPSA plants can be realized, a successful introduction into the industrial application has to be expected within the next few years. This would enable an easy and energy-efficient carbon dioxide capture (CCS)<sup>[520]</sup> from industrial combustion processes causing fuel saving and a decrease of the CO<sub>2</sub> amounts generated.<sup>[521–527]</sup> Advanced CCS power plants like Allam-Fetveld<sup>[528]</sup> and Graz Cycle<sup>[529]</sup> with net efficiencies above 52%<sup>[530]</sup> could increase their efficiencies by ≈5%-points,<sup>[476]</sup> if a commercialization of MIEC membrane plants enables a mass production of MIEC membranes and high O<sub>2</sub> throughputs.

The very low energy costs of MIEC membrane plants enhances the economic benefit for all O<sub>2</sub> applications. Especially small-scale industrial applications will profit because of the higher O<sub>2</sub> price at low O<sub>2</sub> demand<sup>[517]</sup> and a larger financial benefit. This will enlarge the existing markets for O<sub>2</sub> applications but probably opens new markets as well. Altogether, a lot of industrial branches with different O<sub>2</sub> demand rates would benefit from the very low energy demand and minimal CO<sub>2</sub> emissions of the novel MIEC membrane devices.

### Supporting Information

Supporting Information is available from the Wiley Online Library or from the author.

### Acknowledgements

G.C. and A.W. acknowledges funding by the German Federal Ministry of Education and Research in the framework of the “Kopernikus projects for the Energiewende”. A.F. acknowledges funding by the Deutsche Forschungsgemeinschaft (DFG; German Research Foundation) – 435833397. X.Y.W. was supported by the Start-up Grant of University of Waterloo. X.Z. and Y.W. appreciate the financial supports from the National Natural Science Foundation of China (21776267), Dalian National Laboratory for Clean Energy (DICP&QIBEBT UN201708), and Liaoning Revitalization Talents Program (XLYC1801004). J.X. and H.W. gratefully acknowledge the funding from the Natural Science Foundation of China (22075086), the Guangdong Basic and Applied Basic Research Foundation (2020A1515011157) and the PetroChina Innovation Foundation (2019D-5007-0406). Z.S. would like to thank the Australia Research Council for supporting the project under contract DP150104365 and DP160104835. K.S.B. and J.D. acknowledge financial supported by the National Energy Technology Laboratory (NETL) and Oak Ridge Institute for Science and Education (ORISE). K.S.B. was supported in part by an appointment to the NETL Research Participation Program, sponsored by the U.S. Department of Energy and administered by the Oak Ridge Institute for Science and Education. Y.Z. and H.J. gratefully acknowledge the funding from the Natural Science Foundation of China (21676284, 22175193). S.L. thanks the Fundamental Research Fund for the Central University (Buctrc202115). X.T. acknowledges the financial support provided by the National Natural Science Foundation of China (91745116). R.K. thanks Dr. Robert Kircheisen for the evaluation of pilot plant test data and Dr. Robert Hoffmann for the membrane manufacturing as well as analyzing and optimizing the membrane manufacturing costs.

Open access funding enabled and organized by Projekt DEAL.

### Conflict of Interest

The authors declare no conflict of interest.

## Author Contributions

**Organizers:** G.C., A.F., A.W. Introduction and Section 2: G.C., A.F., A.W.; Section 3: C.L., S.L., X.Z., J.S.; Section 4: K.H.; Section 5: X.-Y.W., A.F.G.; Section 6: X.Z., W.Y.; Section 7: J.X., H.W.; Section 8: Z.S.; Section 9: J.H.D., K.S.B.; Section 10: S.L., X.T.; Section 11: Y.Z., H.J.; Section 12: R.C., K.A.F.; Section 13: R.K.

## Keywords

energy conversion, energy storage, gas separation, MIEC membranes, production of chemicals and fuels

Received: July 13, 2021

Revised: September 12, 2021

Published online:

- 
- [1] X. Zhu, W. Yang, *Adv. Mater.* **2019**, *31*, 1902547.
- [2] C. Zhang, J. Sunarso, S. Liu, *Chem. Soc. Rev.* **2017**, *46*, 2941.
- [3] P. M. Geffroy, E. Blond, N. Richet, T. Chartier, *Chem. Eng. Sci.* **2017**, *162*, 245.
- [4] P. A. Armstrong, D. L. Bennett, E. P. T. Foster, E. E. Stein, *ITM Oxygen for Gasification, Proceedings of Gasification Technologies Conference*, Washington, DC, USA **2004**.
- [5] A. Arratibel Plazaola, A. Cruellas Labella, Y. Liu, N. Badiola Porras, D. Pacheco Tanaka, M. Sint Annaland, F. Gallucci, *Processes* **2019**, *7*, 128.
- [6] G. Chen, F. Buck, I. Kistner, M. Widenmeyer, T. Schiestel, A. Schulz, M. Walker, A. Weidenkaff, *Chem. Eng. J.* **2020**, *392*, 123699.
- [7] J. Li, S. Lei, B. Deng, J. Xue, Y. Wang, H. Wang, *J. Membr. Sci.* **2021**, *618*, 118628.
- [8] G. Chen, M. Widenmeyer, B. Tang, L. Kaeswurm, L. Wang, A. Feldhoff, A. Weidenkaff, *Front. Chem. Sci. Eng.* **2020**, *14*, 405.
- [9] J. Xue, G. Weng, L. Chen, Y. Suo, Y. Wei, A. Feldhoff, H. Wang, *J. Membr. Sci.* **2019**, *573*, 588.
- [10] J. Zhu, G. Liu, Z. Liu, Z. Chu, W. Jin, N. Xu, *Adv. Mater.* **2016**, *28*, 3511.
- [11] G. Chen, W. Liu, M. Widenmeyer, P. Ying, M. Dou, W. Xie, C. Bubeck, L. Wang, M. Fyta, A. Feldhoff, A. Weidenkaff, *J. Membr. Sci.* **2019**, *590*, 117082.
- [12] N. F. Himma, A. K. Wardani, N. Prasetya, P. T. P. Aryanti, I. G. Wenten, *Rev. Chem. Eng.* **2019**, *35*, 591.
- [13] C. Solís, M. Balaguer, J. García-Fayos, E. Palafox, J. M. Serra, *Sustainable Energy Fuels* **2020**, *4*, 3747.
- [14] G. Chen, B. Tang, M. Widenmeyer, L. Wang, A. Feldhoff, A. Weidenkaff, *J. Membr. Sci.* **2020**, *595*, 117530.
- [15] J. García-Fayos, R. Ruhl, L. Navarrete, H. J. M. Bouwmeester, J. M. Serra, *J. Mater. Chem. A* **2018**, *6*, 1201.
- [16] W. Fang, F. Liang, Z. Cao, F. Steinbach, A. Feldhoff, *Angew. Chem., Int. Ed.* **2015**, *54*, 4847.
- [17] Y. He, L. Shi, F. Wu, W. Xie, S. Wang, D. Yan, P. Liu, M. R. Li, J. Caro, H. Luo, *J. Mater. Chem. A* **2017**, *6*, 84.
- [18] F. Liang, H. Luo, K. Partovi, O. Ravkina, Z. Cao, Y. Liu, J. Caro, *Chem. Commun.* **2014**, *50*, 2451.
- [19] T. Wang, Z. Liu, X. Xu, J. Zhu, G. Zhang, W. Jin, *J. Membr. Sci.* **2020**, *595*, 117600.
- [20] N. Han, W. Zhang, W. Guo, S. Xie, C. Zhang, X. Zhang, J. Fransær, S. Liu, *Sep. Purif. Technol.* **2021**, *261*, 118295.
- [21] M. Widenmeyer, K. S. Wieggers, G. Chen, S. Yoon, A. Feldhoff, A. Weidenkaff, *J. Membr. Sci.* **2020**, *595*, 117558.
- [22] N. Nauels, S. Herzog, M. Modigell, C. Broeckmann, *J. Membr. Sci.* **2019**, *574*, 252.
- [23] Z. Wang, W. Liu, Y. Wu, W. Sun, C. Wang, *J. Membr. Sci.* **2019**, *573*, 504.
- [24] T. Li, T. Kamhangdatepon, B. Wang, U. W. Hartley, K. Li, *J. Membr. Sci.* **2019**, *578*, 203.
- [25] F. Buck, A. Feldhoff, J. Caro, T. Schiestel, *Sep. Purif. Technol.* **2021**, *259*, 118023.
- [26] N. Han, Q. Wei, H. Tian, S. Zhang, Z. Zhu, J. Liu, S. Liu, *Energy Technol.* **2019**, *7*, 1800701.
- [27] N. Han, R. Chen, T. Chang, L. Li, H. Wang, L. Zeng, *Ceram. Int.* **2019**, *45*, 18924.
- [28] Y. Il Kwon, J. H. Park, S. M. Kang, G. D. Nam, J. W. Lee, J. H. Kim, D. Kim, S. M. Jeong, J. H. Yu, J. H. Joo, *Energy Environ. Sci.* **2019**, *12*, 1358.
- [29] G. Chen, Z. Zhao, M. Widenmeyer, R. Yan, L. Wang, A. Feldhoff, A. Weidenkaff, *Membranes (Basel)* **2020**, *10*, 183.
- [30] Z. Du, Y. Ma, H. Zhao, K. Li, Y. Lu, *J. Membr. Sci.* **2019**, *574*, 243.
- [31] K. Partovi, C. H. Rüscher, F. Steinbach, J. Caro, *J. Membr. Sci.* **2016**, *503*, 158.
- [32] S. Zhang, C. Li, X. Meng, X. Tan, Z. Zhu, J. Sunarso, S. Liu, *Asia-Pac. J. Chem. Eng.* **2020**, *15*, 2528.
- [33] T. Klande, K. Efimov, S. Cusenza, K. D. Becker, A. Feldhoff, *J. Solid State Chem.* **2011**, *184*, 3310.
- [34] N. Han, Q. Wei, S. Zhang, N. Yang, S. Liu, *J. Alloys Compd.* **2019**, *806*, 153.
- [35] W. Fang, F. Steinbach, C. Chen, A. Feldhoff, *Chem. Mater.* **2015**, *27*, 7820.
- [36] S. Wang, L. Shi, M. Boubeche, X. Wang, L. Zeng, H. Wang, Z. Xie, W. Tan, H. Luo, *Sep. Purif. Technol.* **2020**, *251*, 117361.
- [37] G. Chen, Z. Zhao, M. Widenmeyer, T. Frömling, T. Hellmann, R. Yan, F. Qu, G. Himm, J. P. Hofmann, A. Feldhoff, A. Weidenkaff, *J. Membr. Sci.* **2021**, *639*, 119783.
- [38] C. Li, J. Song, S. Zhang, X. Tan, X. Meng, J. Sunarso, S. Liu, *J. Am. Ceram. Soc.* **2021**, *104*, 2268.
- [39] D. Tejero-Martin, M. Rezvani Rad, A. McDonald, T. Hussain, *J. Therm. Spray Technol.* **2019**, *28*, 598.
- [40] G. Chen, T. Godfroid, N. Britun, V. Georgieva, M. P. Delplancke-Ogletree, R. Snyders, *Appl. Catal., B* **2017**, *214*, 114.
- [41] G. Chen, R. Snyders, N. Britun, *J. CO<sub>2</sub> Util.* **2021**, *49*, 101557.
- [42] L. W. Tai, M. M. Nasrallah, H. U. Anderson, D. M. Sparlin, S. R. Sehlin, *Solid State Ionics* **1995**, *76*, 259.
- [43] S. Shao, G. Xiong, J. Tong, H. Dong, W. Yang, *Sep. Purif. Technol.* **2001**, *25*, 419.
- [44] A. Leo, S. Liu, J. C. Diniz Da Costa, *Sep. Purif. Technol.* **2011**, *78*, 220.
- [45] X. Tan, Z. Wang, H. Liu, S. Liu, *J. Membr. Sci.* **2008**, *324*, 128.
- [46] J. Sunarso, S. Baumann, J. M. Serra, W. A. Meulenber, S. Liu, Y. S. Lin, J. C. Diniz da Costa, *J. Membr. Sci.* **2008**, *320*, 13.
- [47] C. Li, J. J. Chew, A. Mahmoud, S. Liu, J. Sunarso, *J. Membr. Sci.* **2018**, *567*, 228.
- [48] W. D. Kingery, J. Pappis, M. E. Doty, D. C. Hill, *J. Am. Ceram. Soc.* **1959**, *42*, 393.
- [49] Y.-S. Lin, W. Wang, J. Han, *AICHE J.* **1994**, *40*, 786.
- [50] A. Feldhoff, J. Martynczuk, M. Arnold, M. Myndyk, I. Bergmann, V. Šepelák, W. Gruner, U. Vogt, A. Hähnel, J. Woltersdorf, *J. Solid State Chem.* **2009**, *182*, 2961.
- [51] M. Arnold, Q. Xu, F. D. Tichelaar, A. Feldhoff, *Chem. Mater.* **2009**, *21*, 635.
- [52] J. E. ten Elshof, H. J. M. Bouwmeester, H. Verweij, *Appl. Catal., A* **1995**, *130*, 195.
- [53] P. J. Gellings, H. J. M. Bouwmeester, *Catal. Today* **1992**, *12*, 1.
- [54] S. Dou, C. R. Masson, P. D. Pacey, *J. Electrochem. Soc.* **1985**, *132*, 1843.
- [55] J. Han, Y. Zeng, Y. S. Lin, *J. Membr. Sci.* **1997**, *132*, 235.
- [56] P. Zeng, Z. Chen, W. Zhou, H. Gu, Z. Shao, S. Liu, *J. Membr. Sci.* **2007**, *291*, 148.

- [57] X. Qi, Y. S. Lin, S. L. Swartz, *Ind. Eng. Chem. Res.* **2000**, *39*, 646.
- [58] C. Ftikos, S. Carter, B. C. H. Steele, *J. Eur. Ceram. Soc.* **1993**, *12*, 79.
- [59] B. C. H. Steele, *Mater. Sci. Eng., B* **1992**, *13*, 79.
- [60] H. J. M. Bouwmeester, H. Kruidhof, A. J. Burggraaf, *Solid State Ionics* **1994**, *72*, 185.
- [61] P. M. Geffroy, A. Vivet, J. Fouletier, C. Steil, E. Blond, N. Richet, P. Del Gallo, T. Chartier, *J. Electrochem. Soc.* **2013**, *160*, F60.
- [62] M. Reichmann, P. M. Geffroy, J. Fouletier, N. Richet, T. Chartier, *J. Power Sources* **2014**, *261*, 175.
- [63] S. J. Xu, W. J. Thomson, *Chem. Eng. Sci.* **1999**, *54*, 3839.
- [64] Y. Zhu, W. Li, Y. Liu, X. Zhu, W. Yang, *AIChE J.* **2017**, *63*, 4043.
- [65] L. Ge, Z. Shao, K. Zhang, R. Ran, J. C. Diniz da Costa, S. Liu, *AIChE J.* **2009**, *55*, 2603.
- [66] S. Li, W. Jin, N. Xu, J. Shi, *Solid State Ionics* **1999**, *124*, 161.
- [67] Y. Zeng, Y. S. Lin, *Solid State Ionics* **1998**, *110*, 209.
- [68] X. Tan, K. Li, *AIChE J.* **2002**, *48*, 1469.
- [69] X. Tan, Y. Liu, K. Li, *AIChE J.* **2005**, *51*, 1991.
- [70] S. Liu, X. Tan, Z. Shao, J. C. Diniz da Costa, *AIChE J.* **2006**, *52*, 3452.
- [71] X. Zhu, H. Liu, Y. Cong, W. Yang, *AIChE J.* **2012**, *58*, 1744.
- [72] Y. Zhu, W. Li, L. Cai, X. Zhu, W. Yang, *Chem. Eng. Sci.* **2020**, *215*, 115455.
- [73] Y. Zhu, J. Wang, A. I. Rykov, X. Zhu, W. Yang, *J. Membr. Sci.* **2020**, *603*, 118038.
- [74] Y. Zhu, L. Cai, W. Li, Z. Cao, H. Li, H. Jiang, X. Zhu, W. Yang, *AIChE J.* **2020**, *66*, 16291.
- [75] G. Dimitrakopoulos, A. F. Ghoniem, *J. Membr. Sci.* **2016**, *510*, 209.
- [76] X. Y. Wu, A. F. Ghoniem, *Prog. Energy Combust. Sci.* **2019**, *74*, 1.
- [77] C. Berger, E. Bucher, W. Sitte, *Solid State Ionics* **2017**, *299*, 46.
- [78] G. Dimitrakopoulos, A. F. Ghoniem, *J. Membr. Sci.* **2017**, *529*, 114.
- [79] G. Dimitrakopoulos, A. F. Ghoniem, *Proc. Combust. Inst.* **2017**, *36*, 4347.
- [80] J. Hong, P. Kirchen, A. F. Ghoniem, *J. Membr. Sci.* **2012**, *407–408*, 71.
- [81] N. Lu, F. Gallucci, T. Melchiorri, D. Xie, M. Van Sint Annaland, *Chem. Eng. Process.* **2018**, *124*, 308.
- [82] N. Xu, S. Li, W. Jin, J. Shi, Y. S. Lin, *AIChE J.* **1999**, *45*, 2519.
- [83] Z. Wang, N. Yang, B. Meng, X. Tan, K. Li, *Ind. Eng. Chem. Res.* **2009**, *48*, 510.
- [84] B. Meng, Z. Wang, X. Tan, S. Liu, *J. Eur. Ceram. Soc.* **2009**, *29*, 2815.
- [85] X. Meng, N. Yang, B. Meng, X. Tan, Z. F. Ma, S. Liu, *Ceram. Int.* **2011**, *37*, 2701.
- [86] Z. Qiu, Y. Hu, X. Tan, S. S. Hashim, J. Sunarso, S. Liu, *Chem. Eng. Sci.* **2018**, *177*, 18.
- [87] Y. Liu, X. Zhu, W. Yang, *AIChE J.* **2015**, *61*, 3879.
- [88] Y. Liu, Y. Zhu, M. Li, X. Zhu, W. Yang, *AIChE J.* **2016**, *62*, 2803.
- [89] J. Zhou, X. Tang, D. He, C. Wu, Y. Zhang, W. Ding, Y. Jin, C. Sun, *J. Alloys Compd.* **2015**, *646*, 204.
- [90] B. T. Na, J. H. Park, J. H. Park, J. H. Yu, J. H. Joo, *ACS Appl. Mater. Interfaces* **2017**, *9*, 19917.
- [91] H. Cheng, P. Wang, H. Zhao, K. Li, X. Lu, Q. Xu, *Ceram. Int.* **2017**, *43*, 6477.
- [92] C. Liu, H. Cheng, G. Yan, H. Zhao, X. Lu, P. Wang, *J. Mater. Sci.* **2018**, *53*, 11962.
- [93] C. Li, W. Li, J. J. Chew, S. Liu, X. Zhu, J. Sunarso, *J. Membr. Sci.* **2019**, *573*, 628.
- [94] M. A. Habib, R. Ben Mansour, M. A. Nemitallah, *Comput. Fluids* **2013**, *76*, <https://doi.org/10.1016/j.compfluid.2013.01.007>.
- [95] B. Feng, J. Song, Z. Wang, N. Dewangan, S. Kawi, X. Tan, *Chem. Eng. Sci.* **2021**, *230*, 116214.
- [96] D. E. Sommer, P. Kirchen, *Chem. Eng. Sci.* **2019**, *195*, 11.
- [97] M. A. Nemitallah, *J. Nat. Gas Sci. Eng.* **2016**, *28*, 61.
- [98] M. A. Nemitallah, M. A. Habib, K. Mezghani, *Energy* **2015**, *84*, 600.
- [99] N. D. Mancini, S. Gunasekaran, A. Mitsos, *Ind. Eng. Chem. Res.* **2012**, *51*, 7988.
- [100] T. Kojima, Y. Miyazaki, K. Nomura, K. Tanimoto, *J. Electrochem. Soc.* **2008**, *155*, F150.
- [101] T. Kojima, Y. Miyazaki, K. Nomura, K. Tanimoto, *J. Electrochem. Soc.* **2007**, *154*, F222.
- [102] V. Lair, V. Albin, A. Ringuedé, M. Cassir, *Int. J. Hydrogen Energy* **2012**, *37*, 19357.
- [103] L. Zhang, N. Xu, X. Li, S. Wang, K. Huang, W. H. Harris, W. K. S. Chiu, *Energy Environ. Sci.* **2012**, *5*, 8310.
- [104] L. Zhang, Z. Mao, J. D. Thomason, S. Wang, K. Huang, *J. Am. Ceram. Soc.* **2012**, *95*, 1832.
- [105] H. Ahn, D. Kim, V. M. A. Melgar, J. Kim, M. R. Othman, H. V. P. Nguyen, J. Han, S. P. Yoon, *J. Ind. Eng. Chem.* **2014**, *20*, 3703.
- [106] Z. Rui, M. Anderson, Y. S. Lin, Y. Li, *J. Membr. Sci.* **2009**, *345*, 110.
- [107] N. Xu, X. Li, M. A. Franks, H. Zhao, K. Huang, *J. Membr. Sci.* **2012**, *401–402*, 190.
- [108] J. Fang, J. Tong, K. Huang, *J. Membr. Sci.* **2016**, *505*, 225.
- [109] J. Tong, X. Lei, J. Fang, M. Han, K. Huang, *J. Mater. Chem. A* **2016**, *4*, 1828.
- [110] J. Tong, F. Si, L. Zhang, J. Fang, M. Han, K. Huang, *Chem. Commun.* **2015**, *51*, 2936.
- [111] P. Zhang, J. Tong, Y. Jee, K. Huang, *Chem. Commun.* **2016**, *52*, 9817.
- [112] P. Zhang, J. Tong, K. Huang, *J. Mater. Chem. A* **2017**, *5*, 12769.
- [113] P. Zhang, J. Tong, K. Huang, *ACS Sustainable Chem. Eng.* **2018**, *6*, 14162.
- [114] P. Zhang, J. Tong, K. Huang, *ACS Sustainable Chem. Eng.* **2016**, *4*, 7056.
- [115] P. Zhang, J. Tong, K. Huang, *ACS Sustainable Chem. Eng.* **2017**, *5*, 5432.
- [116] P. Zhang, J. Tong, K. Huang, *ACS Sustainable Chem. Eng.* **2019**, *7*, 6889.
- [117] S. J. Chung, J. H. Park, D. Li, J. I. Ida, I. Kumakiri, J. Y. S. Lin, *Ind. Eng. Chem. Res.* **2005**, *44*, 7999.
- [118] T. Chen, H. C. Wu, Y. Li, Y. S. Lin, *Ind. Eng. Chem. Res.* **2017**, *56*, 14662.
- [119] The International Energy Agency, *Achieving Net-Zero Emissions by 2050, World Energy Outlook 2020*, **2020**.
- [120] United Nations Environment Programme (UNEP), “The Emissions Gap Report 2017,” **2017**.
- [121] M. E. Boot-Handford, J. C. Abanades, E. J. Anthony, M. J. Blunt, S. Brandani, N. Mac Dowell, J. R. Fernández, M.-C. Ferrari, R. Gross, J. P. Hallett, R. S. Haszeldine, P. Heptonstall, A. Lyngfelt, Z. Makuch, E. Mangano, R. T. J. Porter, M. Pourkashanian, G. T. Rochelle, N. Shah, J. G. Yao, P. S. Fennell, *Energy Environ. Sci.* **2014**, *7*, 130.
- [122] E. V. Kondratenko, G. Mul, J. Baltrusaitis, G. O. Larrazabal, J. Perez-Ramirez, *Energy Environ. Sci.* **2013**, *6*, 3112.
- [123] The International Energy Agency, *CCUS in Clean Energy Transitions*, **2020**.
- [124] The European Cluster on Catalysis, *Science and Technology Roadmap on Catalysis for Europe*, **2016**.
- [125] X. Wu, A. F. Ghoniem, *Proc. Combust. Inst.* **2019**, *37*, 5517.
- [126] R. Michalsky, D. Neuhaus, A. Steinfeld, *Energy Technol.* **2015**, *3*, 784.
- [127] X.-Y. Wu, L. Cai, X. Zhu, A. F. Ghoniem, W. Yang, *J. Adv. Manuf. Process.* **2020**, *2*, 10059.
- [128] L. Cai, X. Y. Wu, X. Zhu, A. F. Ghoniem, W. Yang, *AIChE J.* **2020**, *66*, 16247.
- [129] K. Zhang, G. Zhang, Z. Liu, J. Zhu, N. Zhu, W. Jin, *J. Membr. Sci.* **2014**, *471*, 9.
- [130] X. Wu, A. F. Ghoniem, *ChemSusChem* **2018**, *11*, 483.
- [131] M. Tou, R. Michalsky, A. Steinfeld, *Joule* **2017**, *1*, 146.
- [132] A. Haeussler, S. Abanades, J. Jouannaux, A. Julbe, *J. Membr. Sci.* **2021**, *634*, 119387.
- [133] M. Schulz, U. Pippardt, L. Kiesel, K. Ritter, R. Kriegel, *AIChE J.* **2012**, *58*, 3195.
- [134] T. Cooper, J. R. Scheffe, M. E. Galvez, R. Jacot, G. Patzke, A. Steinfeld, *Energy Technol.* **2015**, *3*, 1130.



- [135] W. Jin, C. Zhang, X. Chang, Y. Fan, W. Xing, N. Xu, *Environ. Sci. Technol.* **2008**, *42*, 3064.
- [136] Z. A. Feng, M. L. Machala, W. C. Chueh, *Phys. Chem. Chem. Phys.* **2015**, *17*, 12273.
- [137] W. Jin, C. Zhang, P. Zhang, Y. Fan, N. Xu, *AIChE J.* **2006**, *52*, 2545.
- [138] F. Schulze-Küppers, S. Baumann, W. A. Meulenber, H. J. M. Bouwmeester, *J. Membr. Sci.* **2020**, *596*, 117704.
- [139] M. Tou, J. Jin, Y. Hao, A. Steinfeld, R. Michalsky, *React. Chem. Eng.* **2019**, *4*, 1431.
- [140] G. P. Van der Laan, A. A. C. M. Beenackers, *Catal. Rev.* **1999**, *41*, 255.
- [141] W. H. Zimmerman, D. B. Bukur, *Can. J. Chem. Eng.* **1990**, *68*, 292.
- [142] M. Moser, M. Pecchi, T. Fend, *Energies* **2019**, *12*, 352.
- [143] C. Nicollet, C. Toparli, G. F. Harrington, T. Defferriere, B. Yildiz, H. L. Tuller, *Nat. Catal.* **2020**, *3*, 913.
- [144] J. H. Kim, J. K. Kim, J. Liu, A. Curcio, J.-S. Jang, I.-D. Kim, F. Ciucci, W. Jung, *ACS Nano* **2021**, *15*, 81.
- [145] D. Neagu, G. Tsekouras, D. N. Miller, H. Ménard, J. T. S. Irvine, *Nat. Chem.* **2013**, *5*, 916.
- [146] G. Dimitrakopoulos, A. F. Ghoniem, B. Yildiz, *Sustainable Energy Fuels* **2019**, *3*, 2347.
- [147] A. H. Bork, A. J. Carrillo, Z. D. Hood, B. Yildiz, J. L. M. Rupp, *ACS Appl. Mater. Interfaces* **2020**, *12*, 32622.
- [148] X. Li, J.-P. Lee, K. S. Blinn, D. Chen, S. Yoo, B. Kang, L. A. Bottomley, M. A. El-Sayed, S. Park, M. Liu, *Energy Environ. Sci.* **2014**, *7*, 306.
- [149] Y. Luo, X. Y. Wu, Y. Shi, A. F. Ghoniem, N. Cai, *Appl. Energy* **2018**, *215*, 371.
- [150] N. L. Panwar, S. C. Kaushik, S. Kothari, *Renewable Sustainable Energy Rev.* **2011**, *15*, 1513.
- [151] M. Balat, *Int. J. Hydrogen Energy* **2008**, *33*, 4013.
- [152] X. Cheng, Z. Shi, N. Glass, L. Zhang, J. Zhang, D. Song, Z. S. Liu, H. Wang, J. Shen, *J. Power Sources* **2007**, *165*, 739.
- [153] F. Gallucci, E. Fernandez, P. Corengia, M. van Sint Annaland, *Chem. Eng. Sci.* **2013**, *92*, 40.
- [154] N. A. Al-Mufachi, N. V. Rees, R. Steinberger-Wilkens, *Renewable Sustainable Energy Rev.* **2015**, *47*, 540.
- [155] E. Yan, Y. Chen, K. Zhang, Y. Zou, H. Chu, L. Sun, *Sep. Purif. Technol.* **2021**, *257*, 117945.
- [156] W. Li, X. Zhu, Z. Cao, W. Wang, W. Yang, *Int. J. Hydrogen Energy* **2015**, *40*, 3452.
- [157] L. Cai, W. Liu, Z. Cao, H. Li, Y. Cong, X. Zhu, W. Yang, *J. Membr. Sci.* **2020**, *599*, 117702.
- [158] W. Li, Z. Cao, L. Cai, L. Zhang, X. Zhu, W. Yang, *Energy Environ. Sci.* **2017**, *10*, 101.
- [159] L. Cai, Y. Zhu, Z. Cao, W. Li, H. Li, X. Zhu, W. Yang, *J. Membr. Sci.* **2020**, *594*, 117463.
- [160] H. Naito, H. Arashi, *Solid State Ionics* **1995**, *79*, 366.
- [161] U. Balachandran, T. H. Lee, S. Wang, S. E. Dorris, *Int. J. Hydrogen Energy* **2004**, *29*, 291.
- [162] M. V. Patrakeev, J. A. Bahteeva, E. B. Mitberg, I. A. Leonidov, V. L. Kozhevnikov, K. R. Poepplmeier, *J. Solid State Chem.* **2003**, *172*, 219.
- [163] L. Cai, S. Hu, Z. Cao, H. Li, X. Zhu, W. Yang, *AIChE J.* **2019**, *65*, 1088.
- [164] X. Zhu, W. Yang, *Mixed Conducting Ceramic Membranes, Fundamentals, Materials and Applications*, Springer-Verlag, Berlin Heidelberg **2017**.
- [165] T. H. Lee, C. Y. Park, S. E. Dorris, U. (Balu) Balachandran, *ECS Trans.* **2019**, *13*, 379.
- [166] H. Jiang, H. Wang, S. Werth, T. Schiestel, J. Caro, *Angew. Chem., Int. Ed.* **2008**, *47*, 9341.
- [167] R. V. Franca, A. Thursfield, I. S. Metcalfe, *J. Membr. Sci.* **2012**, *389*, 173.
- [168] C. Y. Park, T. H. Lee, S. E. Dorris, U. (Balu) Balachandran, *ECS Trans.* **2019**, *13*, 393.
- [169] W. Li, Z. Cao, X. Zhu, W. Yang, *AIChE J.* **2017**, *63*, 1278.
- [170] X.-Y. Wu, A. F. Ghoniem, M. Uddi, *AIChE J.* **2016**, *62*, 4427.
- [171] G. He, W. Liang, C. L. Tsai, X. Xia, S. Baumann, H. Jiang, W. A. Meulenber, *iScience* **2019**, *19*, 955.
- [172] L. Cai, W. Li, Z. Cao, X. Zhu, W. Yang, *J. Membr. Sci.* **2016**, *520*, 607.
- [173] L. Cai, Z. Cao, X. Zhu, W. Yang, *Green Chem. Eng.* **2020**, *2*, 96.
- [174] W. Li, X. Zhu, S. Chen, W. Yang, *Angew. Chem., Int. Ed.* **2016**, *55*, 8566.
- [175] H. Hayashi, M. Kanoh, C. J. Quan, H. Inaba, S. Wang, M. Dokiya, H. Tagawa, *Solid State Ionics* **2000**, *132*, 227.
- [176] H. Malerød-Fjeld, D. Clark, I. Yuste-Tirados, R. Zanón, D. Catalán-Martinez, D. Beeaff, S. H. Morejudo, P. K. Vestre, T. Norby, R. Haugsrud, J. M. Serra, C. Kjølsseth, *Nat. Energy* **2017**, *2*, 923.
- [177] J. Xue, L. Chen, Y. Wei, H. Wang, *Chem. Eng. J.* **2017**, *327*, 202.
- [178] M. Rhandi, M. Trégaro, F. Druart, J. Deseure, M. Chatenet, *Chin. J. Catal.* **2020**, *41*, 756.
- [179] Y. Wei, W. Yang, J. Caro, H. Wang, *Chem. Eng. J.* **2013**, *220*, 185.
- [180] C. Chen, S. Feng, S. Ran, D. Zhu, W. Liu, H. J. M. Bouwmeester, *Angew. Chem.* **2003**, *115*, 5354.
- [181] E. Shelepova, A. Vedyagin, V. Sadykov, N. Mezentseva, Y. Fedorova, O. Smorygo, O. Klenov, I. Mishakov, *Catal. Today* **2016**, *268*, 103.
- [182] W. Liang, Z. Cao, G. He, J. Caro, H. Jiang, *ACS Sustainable Chem. Eng.* **2017**, *5*, 8657.
- [183] Z. Cao, H. Jiang, H. Luo, S. Baumann, W. A. Meulenber, H. Voss, J. Caro, *Catal. Today* **2012**, *193*, 2.
- [184] H. Jiang, Z. Cao, S. Schirmermeister, T. Schiestel, J. Caro, *Angew. Chem., Int. Ed.* **2010**, *49*, 5656.
- [185] N. Zhu, X. Dong, Z. Liu, G. Zhang, W. Jin, N. Xu, *Chem. Commun.* **2012**, *48*, 7137.
- [186] M. Arnold, H. Wang, A. Feldhoff, *J. Membr. Sci.* **2007**, *293*, 44.
- [187] W. Fang, F. Steinbach, Z. Cao, X. Zhu, A. Feldhoff, *Angew. Chem., Int. Ed.* **2016**, *55*, 8648.
- [188] J. Tang, Y. Wei, L. Zhou, Z. Li, H. Wang, *AIChE J.* **2012**, *58*, 2473.
- [189] J. Xue, Q. Liao, W. Chen, H. J. M. Bouwmeester, H. Wang, A. Feldhoff, *J. Mater. Chem. A* **2015**, *3*, 19107.
- [190] J. Xue, J. Li, L. Zhuang, L. Chen, A. Feldhoff, H. Wang, *Chem. Eng. J.* **2018**, *347*, 84.
- [191] Q. Liao, L. Zhuang, Y. Wei, J. Xue, H. Wang, *Ceram. Int.* **2018**, *44*, 10852.
- [192] L. Chen, L. Liu, J. Xue, L. Zhuang, H. Wang, *Sep. Purif. Technol.* **2018**, *207*, 363.
- [193] C. Zhu, S. Hou, X. Hu, J. Lu, F. Chen, K. Xie, *Nat. Commun.* **2019**, *10*, 1173.
- [194] C. Duan, R. J. Kee, H. Zhu, C. Karakaya, Y. Chen, S. Ricote, A. Jarry, E. J. Crumlin, D. Hook, R. Braun, N. P. Sullivan, R. O'Hayre, *Nature* **2018**, *557*, 217.
- [195] G. Yang, C. Su, H. Shi, Y. Zhu, Y. Song, W. Zhou, Z. Shao, *Energy Fuels* **2020**, *34*, 15169.
- [196] M. Papac, V. Stevanović, A. Zakutayev, R. O'Hayre, *Nat. Mater.* **2020**, *20*, 301.
- [197] Y. Song, Y. Chen, M. Xu, W. Wang, Y. Zhang, G. Yang, R. Ran, W. Zhou, Z. Shao, *Adv. Mater.* **2020**, *32*, 1906979.
- [198] Y. Song, Y. Chen, W. Wang, C. Zhou, Y. Zhong, G. Yang, W. Zhou, M. Liu, Z. Shao, *Joule* **2019**, *3*, 2842.
- [199] Y. Zhang, R. Knibbe, J. Sunarso, Y. Zhong, W. Zhou, Z. Shao, Z. Zhu, *Adv. Mater.* **2017**, *29*, 1700132.
- [200] Z. Shao, S. M. Haile, J. Ahn, P. D. Ronney, Z. Zhan, S. A. Barnett, *Nature* **2005**, *435*, 795.
- [201] Y. Chen, W. Zhou, D. Ding, M. Liu, F. Ciucci, M. Tade, Z. Shao, *Adv. Energy Mater.* **2015**, *5*, 1500537.
- [202] M. Li, W. Zhou, Z. Zhu, *Asia-Pac. J. Chem. Eng.* **2016**, *11*, 370.
- [203] C. Su, Y. Wu, W. Wang, Y. Zheng, R. Ran, Z. Shao, *J. Power Sources* **2010**, *195*, 1333.
- [204] J. F. Shin, W. Xu, M. Zanella, K. Dawson, S. N. Savvin, J. B. Claridge, M. J. Rosseinsky, *Nat. Energy* **2017**, *2*, 16214.
- [205] S. Choi, C. J. Kucharczyk, Y. Liang, X. Zhang, I. Takeuchi, H. Il Ji, S. M. Haile, *Nat. Energy* **2018**, *3*, 202.
- [206] C. Duan, J. Tong, M. Shang, S. Nikodemski, M. Sanders, S. Ricote, A. Almansoori, R. O'Hayre, *Science* **2015**, *349*, 1321.
- [207] M. Liu, L. Yang, S. Wang, K. Blinn, M. Liu, Z. Liu, Z. Cheng, *Science* **2009**, *326*, 1250.

- [208] M. Liu, D. Ding, Y. Bai, T. He, M. Liu, *J. Electrochem. Soc.* **2012**, *159*, B661.
- [209] J. Yan, H. Matsumoto, M. Enoki, T. Ishihara, *Electrochem. Solid-State Lett.* **2005**, *8*, A389.
- [210] S. Hong, H. Yang, Y. Lim, Y. B. Kim, *Thin Solid Films* **2016**, *618*, 207.
- [211] D. Konwar, H. H. Yoon, *J. Mater. Chem. A* **2016**, *4*, 5102.
- [212] Y. Chen, Y. Fan, S. Lee, G. Hackett, H. Abernathy, K. Gerdes, X. Song, *J. Power Sources* **2019**, *438*, 227043.
- [213] Y. Zhu, W. Zhou, Y. Chen, Z. Shao, *Angew. Chem., Int. Ed.* **2016**, *55*, 8988.
- [214] M. Li, M. Zhao, F. Li, W. Zhou, V. K. Peterson, X. Xu, Z. Shao, I. Gentle, Z. Zhu, *Nat. Commun.* **2017**, *8*, 13990.
- [215] A. Jun, J. Kim, J. Shin, G. Kim, *ChemElectroChem* **2016**, *3*, 511.
- [216] R. Ren, Z. Wang, C. Xu, W. Sun, J. Qiao, D. W. Rooney, K. Sun, *J. Mater. Chem. A* **2019**, *7*, 18365.
- [217] Z. Shao, S. M. Halle, *Nature* **2004**, *431*, 170.
- [218] R. Pelosato, G. Cordaro, D. Stucchi, C. Cristiani, G. Dotelli, *J. Power Sources* **2015**, *298*, 46.
- [219] W. Zhou, R. Ran, Z. Shao, *J. Power Sources* **2009**, *192*, 231.
- [220] H. Wang, K. J. Yakal-Kremiski, T. Yeh, G. M. Rupp, A. Limbeck, J. Fleig, S. A. Barnett, *J. Electrochem. Soc.* **2016**, *163*, F581.
- [221] J. W. Lee, Z. Liu, L. Yang, H. Abernathy, S. H. Choi, H. E. Kim, M. Liu, *J. Power Sources* **2009**, *190*, 307.
- [222] Y. Chen, Y. M. Choi, S. Yoo, Y. Ding, R. Yan, K. Pei, C. Qu, L. Zhang, I. Chang, B. Zhao, Y. Zhang, H. Chen, Y. Chen, C. Yang, B. deGlee, R. Murphy, J. Liu, M. Liu, *Joule* **2018**, *2*, 938.
- [223] L. M. Acuña, J. Peña-Martínez, D. Marrero-López, R. O. Fuentes, P. Nuñez, D. G. Lamas, *J. Power Sources* **2011**, *196*, 9276.
- [224] C. Xia, W. Rauch, F. Chen, M. Liu, *Solid State Ionics* **2002**, *149*, 11.
- [225] R. Scurtu, S. Somacescu, J. M. Calderon-Moreno, D. Culita, I. Bulimestru, N. Popa, A. Gulea, P. Osiceanu, *J. Solid State Chem.* **2014**, *210*, 53.
- [226] W. Zhou, J. Sunarso, M. Zhao, F. Liang, T. Klandt, A. Feldhoff, *Angew. Chem., Int. Ed.* **2013**, *52*, 14036.
- [227] Y. Zhu, W. Zhou, R. Ran, Y. Chen, Z. Shao, M. Liu, *Nano Lett.* **2016**, *16*, 512.
- [228] Y. Zhu, J. Sunarso, W. Zhou, Z. Shao, *Appl. Catal., B* **2015**, *172–173*, 52.
- [229] J. Sunarso, S. S. Hashim, N. Zhu, W. Zhou, *Prog. Energy Combust. Sci.* **2017**, *61*, 57.
- [230] S. Choi, S. Yoo, J. Kim, S. Park, A. Jun, S. Sengodan, J. Kim, J. Shin, H. Y. Jeong, Y. Choi, G. Kim, M. Liu, *Sci. Rep.* **2013**, *3*, 2426.
- [231] T. H. Lee, K. Y. Park, N. I. Kim, S. J. Song, K. H. Hong, D. Ahn, A. K. Azad, J. Hwang, S. Bhattacharjee, S. C. Lee, H. T. Lim, J. Y. Park, *J. Power Sources* **2016**, *331*, 495.
- [232] J. Kim, A. Jun, J. Shin, G. Kim, *J. Am. Ceram. Soc.* **2014**, *97*, 651.
- [233] W. Zhou, J. Sunarso, Z. G. Chen, L. Ge, J. Motuzas, J. Zou, G. Wang, A. Julbe, Z. Zhu, *Energy Environ. Sci.* **2011**, *4*, 872.
- [234] Z. Q. Deng, J. P. Smit, H. J. Niu, G. Evans, M. R. Li, Z. L. Xu, J. B. Claridge, M. J. Rosseinsky, *Chem. Mater.* **2009**, *21*, 5154.
- [235] L. Zhang, J. Shan, Q. Wang, *J. Alloys Compd.* **2019**, *771*, 221.
- [236] W. He, X. Wu, G. Yang, H. Shi, F. Dong, M. Ni, *ACS Energy Lett.* **2017**, *2*, 301.
- [237] C. Duan, D. Hook, Y. Chen, J. Tong, R. O'Hayre, *Energy Environ. Sci.* **2017**, *10*, 176.
- [238] P. Zeng, R. Ran, Z. Chen, H. Gu, Z. Shao, J. C. D. da Costa, S. Liu, *J. Membr. Sci.* **2007**, *302*, 171.
- [239] H. Ullmann, N. Trofimenko, F. Tietz, D. Stöver, A. Ahmad-Khanlou, *Solid State Ionics* **2000**, *138*, 79.
- [240] Y. Guo, D. Chen, H. Shi, R. Ran, Z. Shao, *Electrochim. Acta* **2011**, *56*, 2870.
- [241] F. Dong, D. Chen, R. Ran, H. Park, C. Kwak, Z. Shao, *Int. J. Hydrogen Energy* **2012**, *37*, 4377.
- [242] Y. Guo, H. Shi, R. Ran, Z. Shao, *Int. J. Hydrogen Energy* **2009**, *34*, 9496.
- [243] Z. Chen, Z. Shao, R. Ran, W. Zhou, P. Zeng, S. Liu, *J. Membr. Sci.* **2007**, *300*, 182.
- [244] Y. Zhu, J. Sunarso, W. Zhou, S. Jiang, Z. Shao, *J. Mater. Chem. A* **2014**, *2*, 15454.
- [245] S. Choi, S. Yoo, J. Kim, S. Park, A. Jun, S. Sengodan, J. Kim, J. Shin, H. Y. Jeong, Y. Choi, G. Kim, M. Liu, *Sci. Rep.* **2013**, *3*, 2426.
- [246] M. Li, K. Chen, B. Hua, J. Li Luo, W. D. A. Rickard, J. Li, J. T. S. Irvine, S. P. Jiang, *J. Mater. Chem. A* **2016**, *4*, 19019.
- [247] Z. Wang, W. Yang, S. P. Shafi, L. Bi, Z. Wang, R. Peng, C. Xia, W. Liu, Y. Lu, *J. Mater. Chem. A* **2015**, *3*, 8405.
- [248] L. Yang, C. Zuo, S. Wang, Z. Cheng, M. Liu, *Adv. Mater.* **2008**, *20*, 3280.
- [249] Y. Lin, R. Ran, Z. Shao, *Int. J. Hydrogen Energy* **2010**, *35*, 8281.
- [250] L. Bi, E. Fabbri, Z. Sun, E. Traversa, *Energy Environ. Sci.* **2011**, *4*, 1352.
- [251] L. Bi, E. Fabbri, Z. Sun, E. Traversa, *Energy Environ. Sci.* **2011**, *4*, 409.
- [252] G. Taillades, P. Pers, V. Mao, M. Taillades, *Int. J. Hydrogen Energy* **2016**, *41*, 12330.
- [253] S. H. Kim, K. B. Shim, C. S. Kim, J. T. Chou, T. Oshima, Y. Shiratori, K. Ito, K. Sasaki, *J. Fuel Cell Sci. Technol.* **2010**, *7*, 0210111.
- [254] R. R. Liu, S. H. Kim, S. Taniguchi, T. Oshima, Y. Shiratori, K. Ito, K. Sasaki, *J. Power Sources* **2011**, *196*, 7090.
- [255] H. An, H. W. Lee, B. K. Kim, J. W. Son, K. J. Yoon, H. Kim, D. Shin, H. Il Ji, J. H. Lee, *Nat. Energy* **2018**, *3*, 870.
- [256] Y. Rao, S. Zhong, F. He, Z. Wang, R. Peng, Y. Lu, *Int. J. Hydrogen Energy* **2012**, *37*, 12522.
- [257] J. Kim, S. Sengodan, G. Kwon, D. Ding, J. Shin, M. Liu, G. Kim, *ChemSusChem* **2014**, *7*, 2811.
- [258] L. Zhao, B. He, B. Lin, H. Ding, S. Wang, Y. Ling, R. Peng, G. Meng, X. Liu, *J. Power Sources* **2009**, *194*, 835.
- [259] L. Zhao, B. He, Z. Xun, H. Wang, R. Peng, G. Meng, X. Liu, *Int. J. Hydrogen Energy* **2010**, *35*, 753.
- [260] L. Zhao, G. Li, K. Chen, Y. Ling, Y. Cui, L. Gui, B. He, *J. Power Sources* **2016**, *333*, 24.
- [261] Y. Chen, S. Yoo, K. Pei, D. Chen, L. Zhang, B. deGlee, R. Murphy, B. Zhao, Y. Zhang, Y. Chen, M. Liu, *Adv. Funct. Mater.* **2018**, *28*, 1704907.
- [262] E. Pikalova, A. Kolchugin, M. Koroleva, G. Vdovin, A. Farlenkov, D. Medvedev, *J. Power Sources* **2019**, *438*, 226996.
- [263] L. Zhao, B. He, Y. Ling, Z. Xun, R. Peng, G. Meng, X. Liu, *Int. J. Hydrogen Energy* **2010**, *35*, 3769.
- [264] J. Choi, B. Kim, S. H. Song, J. S. Park, *Int. J. Hydrogen Energy* **2016**, *41*, 9619.
- [265] J. Cui, J. Wang, X. Zhang, G. Li, K. Wu, Y. Cheng, J. Zhou, *J. Power Sources* **2019**, *413*, 148.
- [266] H. Ding, B. Lin, X. Liu, G. Meng, *Electrochem. Commun.* **2008**, *10*, 1388.
- [267] Z. Tao, L. Bi, Z. Zhu, W. Liu, *J. Power Sources* **2009**, *194*, 801.
- [268] R. hua Yuan, W. He, C. Zhang, M. Ni, *Mater. Lett.* **2017**, *200*, 75.
- [269] D. Huan, L. Zhang, X. Li, Y. Xie, N. Shi, S. Xue, C. Xia, R. Peng, Y. Lu, *ChemSusChem* **2020**, *13*, 4994.
- [270] G. Taillades, J. Dailly, M. Taillades-Jacquín, F. Mauvy, A. Essouhmi, M. Marrony, C. Lalanne, S. Fourcade, D. J. Jones, J.-C. Grenier, J. Rozière, *Fuel Cells* **2009**, *10*, 166.
- [271] H. Wang, Z. Tao, W. Liu, *Ceram. Int.* **2012**, *38*, 1737.
- [272] C. Zhou, J. Sunarso, Y. Song, J. Dai, J. Zhang, B. Gu, W. Zhou, Z. Shao, *J. Mater. Chem. A* **2019**, *7*, 13265.
- [273] N. Wang, S. Hinokuma, T. Ina, C. Zhu, H. Habazaki, Y. Aoki, *J. Mater. Chem. A* **2020**, *8*, 11043.
- [274] E. Olsson, J. Cottom, X. Aparicio-Anglès, N. H. De Leeuw, *Phys. Chem. Chem. Phys.* **2020**, *22*, 692.
- [275] H. Kwon, J. Park, B. K. Kim, J. W. Han, *J. Korean Ceram. Soc.* **2015**, *52*, 331.
- [276] D. Guan, J. Zhou, Y. C. Huang, C. L. Dong, J. Q. Wang, W. Zhou, Z. Shao, *Nat. Commun.* **2019**, *10*, 3755.

- [277] J. Suntivich, H. A. Gasteiger, N. Yabuuchi, H. Nakanishi, J. B. Goodenough, Y. Shao-Horn, *Nat. Chem.* **2011**, 3, 546.
- [278] J. Suntivich, K. J. May, H. A. Gasteiger, J. B. Goodenough, Y. Shao-Horn, *Science* **2011**, 334, 1383.
- [279] Y. Zhang, B. Chen, D. Guan, M. Xu, R. Ran, M. Ni, W. Zhou, *Nature* **2021**, 591, 246.
- [280] S. P. S. Badwal, *Solid State Ionics* **2001**, 143, 39.
- [281] I. Sreedhar, B. Agarwal, P. Goyal, A. Agarwal, *J. Solid State Electrochem.* **2020**, 24, 1239.
- [282] E. Fabbri, D. Pergolesi, E. Traversa, *Chem. Soc. Rev.* **2010**, 39, 4355.
- [283] K. D. Kreuer, *Annu. Rev. Mater. Res.* **2003**, 33, 333.
- [284] K. Kreuer, *Solid State Ionics* **2000**, 136–137, 149.
- [285] A. Dubois, S. Ricote, R. J. Braun, *J. Power Sources* **2017**, 369, 65.
- [286] A. Grimaud, F. Mauvy, J. M. Bassat, S. Fourcade, L. Rocheron, M. Marrony, J. C. Grenier, *J. Electrochem. Soc.* **2012**, 159, B683.
- [287] R. Zohourian, R. Merkle, G. Raimondi, J. Maier, *Adv. Funct. Mater.* **2018**, 28, 1801241.
- [288] R. Strandbakke, E. Vøllestad, S. A. Robinson, M.-L. Fontaine, T. Norby, *J. Electrochem. Soc.* **2017**, 164, F196.
- [289] G. Li, H. Jin, Y. Cui, L. Gui, B. He, L. Zhao, *J. Power Sources* **2017**, 341, 192.
- [290] Y. Bu, S. Joo, Y. Zhang, Y. Wang, D. Meng, X. Ge, G. Kim, *J. Power Sources* **2020**, 451, 227812.
- [291] Z. Wang, P. Lv, L. Yang, R. Guan, J. Jiang, F. Jin, T. He, *Ceram. Int.* **2020**, 46, 18216.
- [292] Z. Zhao, J. Cui, M. Zou, S. Mu, H. Huang, Y. Meng, K. He, K. S. Brinkman, J. Tong, *J. Power Sources* **2020**, 450, 227609.
- [293] A. Seong, J. Kim, J. Kim, S. Kim, S. Sengodan, J. Shin, G. Kim, *J. Electrochem. Soc.* **2018**, 165, F1098.
- [294] C. Endler-Schuck, J. Joos, C. Niedrig, A. Weber, E. Ivers-Tiffée, *Solid State Ionics* **2015**, 269, 67.
- [295] S. B. Adler, J. A. Lane, B. C. H. Steele, *J. Electrochem. Soc.* **1996**, 143, 3554.
- [296] L. Wang, R. Merkle, J. Maier, *J. Electrochem. Soc.* **2010**, 157, B1802.
- [297] E. Fabbri, L. Bi, D. Pergolesi, E. Traversa, *Adv. Mater.* **2012**, 24, 195.
- [298] Y. L. Huang, C. Pellegrinelli, E. D. Wachsman, *J. Electrochem. Soc.* **2016**, 163, F171.
- [299] K. A. Stoerzinger, R. Comes, S. R. Spurgeon, S. Thevuthasan, K. Ihm, E. J. Crumlin, S. A. Chambers, *J. Phys. Chem. Lett.* **2017**, 8, 1038.
- [300] S. Pal, A. Banerjee, E. Rozenberg, B. K. Chaudhuri, *J. Appl. Phys.* **2001**, 89, 4955.
- [301] W. Khan, A. H. Naqvi, M. Gupta, S. Husain, R. Kumar, *J. Chem. Phys.* **2011**, 135, 054501.
- [302] F. R. van Buren, J. H. W. de Wit, *J. Electrochem. Soc.* **1979**, 126, 1817.
- [303] J. Mizusaki, *Solid State Ionics* **1992**, 52, 79.
- [304] K. Huang, H. Y. Lee, J. B. Goodenough, *J. Electrochem. Soc.* **1998**, 145, 3220.
- [305] A. V. Nikonov, K. A. Kuterbekov, K. Z. Bekmyrza, N. B. Pavzderin, *Eurasian J. Phys. Funct. Mater.* **2018**, 2, 274.
- [306] D. Y. Kim, S. Miyoshi, T. Takashi, S. Yamaguchi, *ECS Trans.* **2012**, 45, 161.
- [307] L. R. Tarutina, G. K. Vdovin, J. G. Lyagaeva, D. A. Medvedev, *J. Alloys Compd.* **2020**, 831, 154895.
- [308] M. Cherry, M. S. Islam, C. R. A. Catlow, *J. Solid State Chem.* **1995**, 118, 125.
- [309] X. Kuai, G. Yang, Y. Chen, H. Sun, J. Dai, Y. Song, R. Ran, W. Wang, W. Zhou, Z. Shao, *Adv. Energy Mater.* **2019**, 9, 1902384.
- [310] F. He, M. Liang, W. Wang, R. Ran, G. Yang, W. Zhou, Z. Shao, *Energy Fuels* **2020**, 34, 11464.
- [311] R. Ren, Z. Wang, X. Meng, X. Wang, C. Xu, J. Qiao, W. Sun, K. Sun, *ACS Appl. Energy Mater.* **2020**, 3, 4914.
- [312] M. Liang, F. He, C. Zhou, Y. Chen, R. Ran, G. Yang, W. Zhou, Z. Shao, *Chem. Eng. J.* **2021**, 420, 127717.
- [313] S. V. Bhide, A. V. Virkar, *J. Electrochem. Soc.* **1999**, 146, 2038.
- [314] B. Koo, K. Kim, J. K. Kim, H. Kwon, J. W. Han, W. C. Jung, *Joule* **2018**, 2, 1476.
- [315] N. Tsvetkov, Q. Lu, L. Sun, E. J. Crumlin, B. Yildiz, *Nat. Mater.* **2016**, 15, 1010.
- [316] T. Inoue, J. I. Kamimae, M. Ueda, K. Eguchi, H. Arai, *J. Mater. Chem.* **1993**, 3, 751.
- [317] I. Riess, *Solid State Ionics* **1996**, 91, 221.
- [318] D. P. Sutija, T. Norby, P. Bjornbom, *Solid State Ionics* **1995**, 2738, 167.
- [319] H. K. Bentzer, N. Bonanos, J. W. Phair, *Solid State Ionics* **2010**, 181, 249.
- [320] K. Brinkman, T. Iijima, H. Takamura, *Solid State Ionics* **2010**, 181, 53.
- [321] H. Ding, W. Wu, C. Jiang, Y. Ding, W. Bian, B. Hu, P. Singh, C. J. Orme, L. Wang, Y. Zhang, D. Ding, *Nat. Commun.* **2020**, 11, 1907.
- [322] J. Guan, *Solid State Ionics* **1997**, 100, 45.
- [323] Z. Wang, W. Yang, Z. Zhu, R. Peng, X. Wu, C. Xia, Y. Lu, *J. Mater. Chem. A* **2014**, 2, 16707.
- [324] W. Tan, D. Huan, W. Yang, N. Shi, W. Wang, R. Peng, X. Wu, Y. Lu, *RSC Adv.* **2018**, 8, 26448.
- [325] T. Hong, W. Lu, K. Ren, T. Liu, *Ionics (Kiel)* **2020**, 26, 5293.
- [326] Y. Chen, T. Hong, P. Wang, K. Brinkman, J. Tong, J. Cheng, *J. Power Sources* **2019**, 440, 227122.
- [327] A. Nenning, E. Navickas, H. Hutter, J. Fleig, *J. Phys. Chem. Lett.* **2016**, 7, 2826.
- [328] Y. Tomura, T. Tazawa, I. Oikawa, H. Takamura, *J. Mater. Chem. A* **2020**, 8, 21634.
- [329] H. H. Shin, S. McIntosh, *J. Mater. Chem. A* **2013**, 1, 7639.
- [330] A. Seong, J. Kim, D. Jeong, S. Sengodan, M. Liu, S. Choi, G. Kim, *Adv. Sci.* **2021**, 8, 2004099.
- [331] L. Wang, R. Merkle, J. Maier, T. Acartürk, U. Starke, *Appl. Phys. Lett.* **2009**, 94, 071908.
- [332] R. Jacobs, T. Mayeshiba, J. Booske, D. Morgan, *Adv. Energy Mater.* **2018**, 8, 1702708.
- [333] H. Zhu, R. J. Kee, *J. Electrochem. Soc.* **2017**, 164, F1400.
- [334] S. V. Ushakov, A. Navrotsky, *J. Am. Ceram. Soc.* **2012**, 95, 1463.
- [335] A. Navrotsky, *AIP Conf. Proc.* **2000**, 535, 288.
- [336] N. Birkner, C. Li, S. L. Estes, K. S. Brinkman, *ChemSusChem* **2021**, 14, 2621.
- [337] H. Yan, N. Bouet, J. Zhou, X. Huang, E. Nazaretski, W. Xu, A. P. Cocco, W. K. S. Chiu, K. S. Brinkman, Y. S. Chu, *Nano Futures* **2018**, 2, 011001.
- [338] Y. Lin, S. Fang, D. Su, K. S. Brinkman, F. Chen, *Nat. Commun.* **2015**, 6, 6824.
- [339] X. Li, K. Huang, X. Jin, *J. Electrochem. Soc.* **2020**, 167, 164512.
- [340] Y. Li, K. Gerdes, T. Horita, X. Liu, *J. Electrochem. Soc.* **2013**, 160, F343.
- [341] D. Chen, Z. Shao, *Int. J. Hydrogen Energy* **2011**, 36, 6948.
- [342] Y. Xia, Z. Jin, H. Wang, Z. Gong, H. Lv, R. Peng, W. Liu, L. Bi, *J. Mater. Chem. A* **2019**, 7, 16136.
- [343] G. Kim, S. Wang, A. J. Jacobson, L. Reimus, P. Brodersen, C. A. Mims, *J. Mater. Chem.* **2007**, 17, 2500.
- [344] L. Jiang, T. Wei, R. Zeng, W. X. Zhang, Y. H. Huang, *J. Power Sources* **2013**, 232, 279.
- [345] V. A. Sadykov, E. Y. Pikalova, A. A. Kolchugin, E. A. Filonova, E. M. Sadovskaya, N. F. Ereemeev, A. V. Ishchenko, A. V. Fetisov, S. M. Pikalov, *Solid State Ionics* **2018**, 317, 234.
- [346] N. Wang, H. Toriumi, Y. Sato, C. Tang, T. Nakamura, K. Amezawa, S. Kitano, H. Habazaki, Y. Aoki, *ACS Appl. Energy Mater.* **2021**, 4, 554.
- [347] L. Fan, P. C. Su, *J. Power Sources* **2016**, 306, 369.
- [348] D. Poetzsch, R. Merkle, J. Maier, *Faraday Discuss.* **2015**, 182, 129.
- [349] Z. Zhang, J. Wang, Y. Chen, S. Tan, Z. Shao, D. Chen, *J. Power Sources* **2018**, 385, 76.

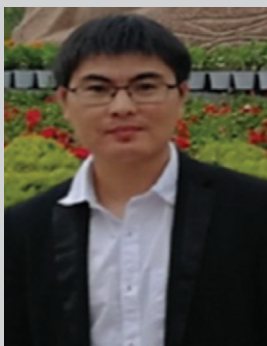


- [350] L. Yang, Z. Liu, S. Wang, Y. M. Choi, C. Zuo, M. Liu, *J. Power Sources* **2010**, 195, 471.
- [351] G. Li, Y. Zhang, Y. Ling, B. He, J. Xu, L. Zhao, *Int. J. Hydrogen Energy* **2016**, 41, 5074.
- [352] S. Liu, X. Tan, K. Li, R. Hughes, *Catal. Rev.* **2001**, 43, 147.
- [353] W. Wang, Y. S. Lin, *J. Membr. Sci.* **1995**, 103, 219.
- [354] E. A. Hazbun, US4827071, **1989**.
- [355] F. T. Akin, Y. S. Lin, *AIChE J.* **2002**, 48, 2298.
- [356] Y. Lu, A. G. Dixon, W. R. Moser, Y. H. Ma, U. Balachandran, *J. Membr. Sci.* **2000**, 170, 27.
- [357] S. J. Xu, W. J. Thomson, *AIChE J.* **1997**, 43, 2731.
- [358] Y. Zeng, Y. S. Lin, S. L. Swartz, *J. Membr. Sci.* **1998**, 150, 87.
- [359] X. Tan, Z. Pang, Z. Gu, S. Liu, *J. Membr. Sci.* **2007**, 302, 109.
- [360] L. Olivier, S. Haag, C. Mirodatos, A. C. van Veen, *Catal. Today* **2009**, 142, 34.
- [361] H. Wang, Y. Cong, W. Yang, *Catal. Today* **2005**, 104, 160.
- [362] S. Bhatia, C. Y. Thien, A. R. Mohamed, *Chem. Eng. J.* **2009**, 148, 525.
- [363] N. H. Othman, Z. Wu, K. Li, *J. Membr. Sci.* **2015**, 488, 182.
- [364] T. Ishihara, Y. Takita, *Catal. Surv. Jpn.* **2001**, 4, 125.
- [365] X. Tan, K. Li, in *Handbook of Membrane Reactors*, (Ed: A. Basile), Woodhead Publishing, Sawston, UK **2013**, pp. 347–383.
- [366] C. Delbos, G. Lebain, N. Richet, C. Bertail, *Catal. Today* **2010**, 156, 146.
- [367] D. L. Hoang, S. H. Chan, *Int. J. Hydrogen Energy* **2006**, 31, <https://doi.org/10.1016/j.ijhydene.2005.03.012>.
- [368] X. Tan, K. Li, *AIChE J.* **2009**, 55, 2675.
- [369] P. Zhang, X. Chang, Z. Wu, W. Jin, N. Xu, *Ind. Eng. Chem. Res.* **2005**, 44, 1954.
- [370] W. Zhu, W. Han, G. Xiong, W. Yang, *Catal. Today* **2005**, 104, 149.
- [371] M. P. Lobera, S. Valero, J. M. Serra, S. Escolástico, E. Argente, V. Botti, *Chem. Eng. Sci.* **2011**, 66, 6308.
- [372] M. Rebeilleau-Dassonneville, A. C. Van Veen, D. Farrusseng, J. Rousset, C. Mirodatos, Z. Shao, G. Xiong, *Stud. Surf. Sci. Catal.* **2004**, 147, 655.
- [373] M. Rebeilleau-Dassonneville, S. Rosini, A. C. Van Veen, D. Farrusseng, C. Mirodatos, *Catal. Today* **2005**, 104, 131.
- [374] H. Wang, C. Tablet, T. Schiestel, J. Caro, *Catal. Today* **2006**, 118, 98.
- [375] O. Czuprat, S. Werth, S. Schirrmeyer, T. Schiestel, J. Caro, *Chem-CatChem* **2009**, 1, 401.
- [376] O. Czuprat, S. Werth, J. Caro, T. Schiestel, *AIChE J.* **2010**, 56, 2390.
- [377] O. Czuprat, J. Caro, V. A. Kondratenko, E. V. Kondratenko, *Catal. Commun.* **2010**, 11, 1211.
- [378] J. Pérez-Ramírez, B. Vigeland, *Catal. Today* **2005**, 105, 436.
- [379] J. Pérez-Ramírez, B. Vigeland, *Angew. Chem., Int. Ed.* **2005**, 44, 1112.
- [380] S. Sun, M. Rebeilleau-Dassonneville, X. Zhu, W. Chu, W. Yang, *Catal. Today* **2010**, 149, 167.
- [381] C. Zhang, X. Meng, J. Sunarso, L. Liu, R. Xu, Z. Shao, S. Liu, *J. Mater. Chem. A* **2015**, 3, 19033.
- [382] G. Rothenberg, E. A. (Bart) de Graaf, A. Blik, *Angew. Chem., Int. Ed.* **2003**, 42, 3366.
- [383] F. He, F. Li, *Energy Environ. Sci.* **2015**, 8, 535.
- [384] P. M. Geffroy, J. Fouletier, N. Richet, T. Chartier, *Chem. Eng. Sci.* **2013**, 87, 408.
- [385] G. He, Q. Lan, Y. J. Sohn, S. Baumann, R. Dunin-Borkowski, W. A. Meulenber, H. Jiang, *Chem. Mater.* **2019**, 31, 7487.
- [386] M. Gao, L. Zhu, C. K. Peh, G. W. Ho, *Energy Environ. Sci.* **2019**, 12, 841.
- [387] C. L. Muhich, B. D. Ehrhart, I. Al-Shankiti, B. J. Ward, C. B. Musgrave, A. W. Weimer, *Wiley Interdiscip. Rev.: Energy Environ.* **2016**, 5, 261.
- [388] Y. Mao, Y. Gao, W. Dong, H. Wu, Z. Song, X. Zhao, J. Sun, W. Wang, *Appl. Energy* **2020**, 267, 114860.
- [389] S. Abanades, P. Charvin, G. Flamant, P. Neveu, *Energy* **2006**, 31, 2805.
- [390] A. Steinfeld, *Sol. Energy* **2005**, 78, 603.
- [391] G. P. Smestad, A. Steinfeld, *Ind. Eng. Chem. Res.* **2012**, 51, 11828.
- [392] W. C. Chueh, C. Falter, M. Abbott, D. Scipio, P. Furler, S. M. Haile, A. Steinfeld, *Science*. **2010**, 330, 1797.
- [393] Y. Hao, C. K. Yang, S. M. Haile, *Phys. Chem. Chem. Phys.* **2013**, 15, 17084.
- [394] E. A. Fletcher, R. L. Moen, *Science*. **1977**, 197, 1050.
- [395] K. W. Browall, R. H. Doremus, *J. Am. Ceram. Soc.* **1977**, 60, 262.
- [396] J. E. Noring, R. B. Diver, E. A. Fletcher, *Energy* **1981**, 6, 109.
- [397] C. L. Muhich, B. W. Evanko, K. C. Weston, P. Lichty, X. Liang, J. Martinek, C. B. Musgrave, A. W. Weimer, *Science* **2013**, 341, 540.
- [398] H. Wang, Y. Hao, H. Kong, *Int. J. Energy Res.* **2015**, 39, 1790.
- [399] K. Zhang, L. Liu, Z. Shao, R. Xu, J. C. Diniz Da Costa, S. Wang, S. Liu, *J. Mater. Chem. A* **2013**, 1, 9150.
- [400] L. Jia, G. He, Y. Zhang, J. Caro, H. Jiang, *Angew. Chem., Int. Ed.* **2021**, 60, 5204.
- [401] S. Abanades, G. Flamant, *Sol. Energy* **2006**, 80, 1611.
- [402] P. Furler, J. R. Scheffe, A. Steinfeld, *Energy Environ. Sci.* **2012**, 5, 6098.
- [403] D. Marxer, P. Furler, M. Takacs, A. Steinfeld, *Energy Environ. Sci.* **2017**, 10, 1142.
- [404] Q. L. Meng, C. Il Lee, T. Ishihara, H. Kaneko, Y. Tamaura, *Int. J. Hydrogen Energy* **2011**, 36, 13435.
- [405] J. R. Scheffe, A. Steinfeld, *Energy Fuels* **2012**, 26, 1928.
- [406] Q. L. Meng, C. Il Lee, S. Shigeta, H. Kaneko, Y. Tamaura, *J. Solid State Chem.* **2012**, 194, 343.
- [407] A. Le Gal, S. Abanades, N. Bion, T. Le Mercier, V. Harlé, *Energy Fuels* **2013**, 27, 6068.
- [408] J. R. Scheffe, R. Jacot, G. R. Patzke, A. Steinfeld, *J. Phys. Chem. C* **2013**, 117, 24104.
- [409] M. Takacs, J. R. Scheffe, A. Steinfeld, *Phys. Chem. Chem. Phys.* **2015**, 17, 7813.
- [410] T. Kobayashi, S. Wang, M. Dokiya, H. Tagawa, T. Hashimoto, *Solid State Ionics* **1999**, 126, 349.
- [411] S. Wang, T. Kobayashi, M. Dokiya, T. Hashimoto, *J. Electrochem. Soc.* **2000**, 147, 3606.
- [412] S. Abanades, A. Legal, A. Cordier, G. Peraudeau, G. Flamant, A. Julbe, *J. Mater. Sci.* **2010**, 45, 4163.
- [413] J. R. Scheffe, A. Steinfeld, *Mater. Today* **2014**, 17, 341.
- [414] A. H. McDaniel, E. C. Miller, D. Arifin, A. Ambrosini, E. N. Coker, R. O'Hayre, W. C. Chueh, J. Tong, *Energy Environ. Sci.* **2013**, 6, 2424.
- [415] A. M. Deml, V. Stevanović, A. M. Holder, M. Sanders, R. Ohayre, C. B. Musgrave, *Chem. Mater.* **2014**, 26, 6595.
- [416] C. K. Yang, Y. Yamazaki, A. Aydin, S. M. Haile, *J. Mater. Chem. A* **2014**, 2, 13612.
- [417] S. Dey, B. S. Naidu, A. Govindaraj, C. N. R. Rao, *Phys. Chem. Chem. Phys.* **2015**, 17, 122.
- [418] S. Dey, B. S. Naidu, C. N. R. Rao, *Chem. Eur. J.* **2015**, 21, 7077.
- [419] J. R. Scheffe, D. Weibel, A. Steinfeld, *Energy Fuels* **2013**, 27, 4250.
- [420] A. Evdou, V. Zaspalis, L. Nalbandian, *Fuel* **2010**, 89, 1265.
- [421] A. Demont, S. Abanades, E. Beche, *J. Phys. Chem. C* **2014**, 118, 12682.
- [422] A. H. Bork, M. Kubicek, M. Struzik, J. L. M. Rupp, *J. Mater. Chem. A* **2015**, 3, 15546.
- [423] R. Bader, L. J. Venstrom, J. H. Davidson, W. Lipiński, *Energy Fuels* **2013**, 27, 5533.
- [424] S. Li, P. B. Kreider, V. M. Wheeler, W. Lipinski, *J. Sol. Energy Eng.* **2019**, 141, 021012.
- [425] L. Zhu, Y. Lu, S. Shen, *Energy* **2016**, 104, 53.
- [426] M. Tou, A. Grylka, A. Schuller, B. Bulfin, A. Steinfeld, R. Michalsky, *Front. Energy Res.* **2020**, 8, 570884.
- [427] Y. Lu, T. Dai, C. Lu, C. Cao, W. Zhang, W. Xu, H. Min, X. Yang, *Ceram. Int.* **2019**, 45, 24903.
- [428] S. Huang, Y. Long, H. Yi, Z. Yang, L. Pang, Z. Jin, Q. Liao, L. Zhang, Y. Zhang, Y. Chen, H. Cui, J. Lu, X. Peng, H. Liang, S. Ruan, Y. J. Zeng, *Appl. Surf. Sci.* **2019**, 491, 328.



- [429] Y. Wang, C. Wang, W. Liang, X. Song, Y. Zhang, M. Huang, H. Jiang, *Nano Energy* **2020**, *70*, 104538.
- [430] D. M. A. Dueñas, M. Riedel, M. Riegraf, R. Costa, K. A. Friedrich, *Chem. Ing. Tech.* **2020**, *92*, 45.
- [431] J. T. S. Irvine, D. Neagu, M. C. Verbraeken, C. Chatzichristodoulou, C. Graves, M. B. Mogensen, *Nat. Energy* **2016**, *1*, 15014.
- [432] F. S. Baumann, J. Fleig, H. U. Habermeier, J. Maier, *Solid State Ionics* **2006**, *177*, 1071.
- [433] M. M. Kuklja, E. A. Kotomin, R. Merkle, Y. A. Mastrikov, J. Maier, *Phys. Chem. Chem. Phys.* **2013**, *15*, 5443.
- [434] J. Nielsen, T. Jacobsen, M. Wandel, *Electrochim. Acta* **2011**, *56*, 7963.
- [435] "Solid Oxide Fuel Cells | Products | Elcogen," can be found under <https://elcogen.com/products/solid-oxide-fuel-cells/>.
- [436] "Elektrolytgetragene Zellen (ESC), LSM, LSCF, Elektrolyse, Elektrolyt – KERAFOFOL – KERAFOFOL," can be found under <https://www.kerafol.com/sofc/komponenten-fuer-brennstoffzellentechnologie/elektrolytgetragene-zellen-esc> (accessed: October 2021).
- [437] H. L. Tuller, A. S. Nowick, *J. Phys. Chem. Solids* **1977**, *38*, 859.
- [438] M. Mogensen, N. M. Sammes, G. A. Tompsett, *Solid State Ionics* **2000**, *129*, 63.
- [439] A. Atkinson, S. Barnett, R. J. Gorte, J. T. S. Irvine, A. J. McEvoy, M. Mogensen, S. C. Singhal, J. Vohs, *Nat. Mater.* **2004**, *3*, 17.
- [440] M. P. Hoerlein, M. Riegraf, R. Costa, G. Schiller, K. A. Friedrich, *Electrochim. Acta* **2018**, *276*, 162.
- [441] A. Hauch, R. Küngas, P. Blennow, A. B. Hansen, J. B. Hansen, B. V. Mathiesen, M. B. Mogensen, *Science* **2020**, *370*, eaba6118.
- [442] T. L. Skafte, P. Blennow, J. Hjelm, C. Graves, *J. Power Sources* **2018**, *373*, 54.
- [443] W. C. Chueh, Y. Hao, W. Jung, S. M. Haile, *Nat. Mater.* **2012**, *11*, 155.
- [444] M. Riegraf, R. Costa, G. Schiller, K. A. Friedrich, S. Dierickx, A. Weber, *J. Electrochem. Soc.* **2019**, *166*, F865.
- [445] D. Udomsilp, J. Rechberger, R. Neubauer, C. Bischof, F. Thaler, W. Schafbauer, N. H. Menzler, L. G. J. de Haart, A. Nanning, A. K. Opitz, O. Guillon, M. Bram, *Cell Rep. Phys. Sci.* **2020**, *1*, 100072.
- [446] J. H. Myung, D. Neagu, D. N. Miller, J. T. S. Irvine, *Nature* **2016**, *537*, 528.
- [447] D.-M. Amaya-Dueñas, G. Chen, A. Weidenkaff, N. Sata, F. Han, I. Biswas, R. Costa, K. A. Friedrich, *J. Mater. Chem. A* **2021**, *9*, 5685.
- [448] R. Knibbe, J. Hjelm, M. Menon, N. Pryds, M. Søgaard, H. J. Wang, K. Neufeld, *J. Am. Ceram. Soc.* **2010**, *93*, 2877.
- [449] M. Morales, A. Pesce, A. Slodczyk, M. Torrell, P. Piccardo, D. Montinaro, A. Tarancón, A. Morata, *ACS Appl. Energy Mater.* **2018**, *1*, 1955.
- [450] N. Coppola, P. Polverino, G. Carapella, C. Sacco, A. Galdi, A. Ubaldini, V. Vaiano, D. Montinaro, L. Maritato, C. Pianese, *Catalysts* **2018**, *8*, 571.
- [451] L. Bouleau, N. Coton, P. Coquoz, R. Ihringer, A. Billard, P. Briois, *Crystals* **2020**, *10*, 759.
- [452] M. Riegraf, F. Han, N. Sata, R. Costa, *ACS Appl. Mater. Interfaces* **2021**, *13*, 37239.
- [453] C. Lenser, H. Jeong, Y. J. Sohn, N. Russner, O. Guillon, N. H. Menzler, *J. Am. Ceram. Soc.* **2018**, *101*, 739.
- [454] R. Price, M. Cassidy, J. G. Grolig, G. Longo, U. Weissen, A. Mai, J. T. S. Irvine, *Adv. Energy Mater.* **2021**, *11*, 2003951.
- [455] M. Riegraf, D. M. Amaya-Dueñas, N. Sata, K. A. Friedrich, R. Costa, *ChemSusChem* **2021**, *14*, 2401.
- [456] T. Zhu, H. E. Troiani, L. V. Mogni, M. Han, S. A. Barnett, *Joule* **2018**, *2*, 478.
- [457] C. Yang, Z. Yang, C. Jin, G. Xiao, F. Chen, M. Han, *Adv. Mater.* **2012**, *24*, 1439.
- [458] Y. F. Sun, J. H. Li, L. Cui, B. Hua, S. H. Cui, J. Li, J. L. Luo, *Nanoscale* **2015**, *7*, 11173.
- [459] Z. Yang, Y. Chen, N. Xu, Y. Niu, M. Han, F. Chen, *J. Electrochem. Soc.* **2015**, *162*, F718.
- [460] L. Ye, M. Zhang, P. Huang, G. Guo, M. Hong, C. Li, J. T. S. Irvine, K. Xie, *Nat. Commun.* **2017**, *8*, 14785.
- [461] W. Wang, L. Gan, J. P. Lemmon, F. Chen, J. T. S. Irvine, K. Xie, *Nat. Commun.* **2019**, *10*, 1550.
- [462] M. Sase, K. Yashiro, K. Sato, J. Mizusaki, T. Kawada, N. Sakai, K. Yamaji, T. Horita, H. Yokokawa, *Solid State Ionics* **2008**, *178*, 1843.
- [463] K. Kousi, D. Neagu, L. Bekris, E. I. Papaioannou, I. S. Metcalfe, *Angew. Chem., Int. Ed.* **2020**, *59*, 2510.
- [464] J. Caro, *Chem. Ing. Tech.* **2014**, *86*, 1901.
- [465] J. Caro, *Chin. J. Catal.* **2008**, *29*, 1169.
- [466] L. L. Anderson, P. A. Armstrong, R. R. Broekhuis, M. F. Carolan, J. Chen, M. D. Hutcheon, C. A. Lewinsohn, C. F. Miller, J. M. Repasky, D. M. Taylor, C. M. Woods, *Solid State Ionics* **2016**, *288*, 331.
- [467] S. A. Diethelm, J. Sfeir, F. Clemens, J van Herle, D. Favrat, *J. Solid State Electrochem.* **2004**, *8*, 611.
- [468] H. Lu, J. Tong, Y. Cong, W. Yang, *Catal. Today* **2005**, *104*, 154.
- [469] S. W. Carolan, M. F. Chen, C. M. Rynders, *Fuel Chem. Div. Prepr.* **2003**, *48*, 343.
- [470] J. E. ten Elshof, B. A. van Hassel, H. J. M. Bouwmeester, *Catal. Today* **1995**, *25*, 397.
- [471] A. Thursfield, I. S. Metcalfe, *J. Mater. Chem.* **2004**, *14*, 2475.
- [472] U. (Balu) Balachandran, T. H. Lee, S. E. Dorris, *Int. J. Hydrogen Energy* **2007**, *32*, 451.
- [473] Z. Cao, H. Jiang, H. Luo, S. Baumann, W. A. Meulenber, H. Voss, J. Caro, *ChemCatChem* **2014**, *6*, 1190.
- [474] K. Mezghani, A. Hamza, *J. Membr. Sci.* **2016**, *518*, 254.
- [475] R. Ben-Mansour, P. Ahmed, M. A. Habib, A. Jamal, *Int. J. Energy Environ. Eng.* **2018**, *9*, 21.
- [476] R. Kriegel, *15th Int. Conf. Inorgan. Membranes ICIM, Dresden 2018*.
- [477] "Highly efficient Power Production by green Ammonia total Oxidation in a Membrane Reactor | HiPowAR Project | H2020 | CORDIS | European Commission," can be found under <https://cordis.europa.eu/project/id/951880> (accessed: October 2021).
- [478] R. Kriegel, I. Voigt, W. Burckhardt, in *Proc. 10th ECerS Conf.*, (Eds: J. G. Heinrich, C. Aneziris), Göller Verlag, Baden-Baden, Berlin **2007**, pp. 2161–2168, ISBN: 3-87264-022-4.
- [479] R. Kiebach, K. Engelbrecht, K. Kwok, S. Molin, M. Søgaard, P. Niehoff, F. Schulze-Küppers, R. Kriegel, J. Kluge, P. V. Hendriksen, *J. Membr. Sci.* **2016**, *506*, 11.
- [480] I. Kriegel, R. Schulz, M. Ritter, K. Kiesel, L. Pippardt, U. Stahn, M. Voigt, in *Efficient Carbon Capture for Coal Power Plants, Book of Extended Abstracts*, Dechema, Frankfurt a.M **2011**, p. 114.
- [481] M. Schulz, R. Kriegel, in *A Global Roadmap for Ceramics, 1st Intern. Conf. on Ceramics, CD-ROM File*, Wiley-American Ceramic Society, New York **2006**.
- [482] M. Schulz, R. Kriegel, R. Burckhardt, *Proc. 10th Intern. Conf. Inorgan. Membranes ICIM, Tokyo, Japan 2008*.
- [483] A. A. Yaremchenko, S. M. Mikhalev, E. S. Kravchenko, J. R. Frade, *J. Eur. Ceram. Soc.* **2014**, *34*, 703.
- [484] M. Schulz, R. Kriegel, A. Kämpfer, *J. Membr. Sci.* **2011**, *378*, 10.
- [485] J. Yi, M. Schroeder, *J. Membr. Sci.* **2011**, *378*, 163.
- [486] S. Engels, T. Markus, M. Modigell, L. Singheiser, *J. Membr. Sci.* **2011**, *370*, 58.
- [487] M. Kriegel, R. Kircheisen, R. Sonnenberg, C. Schulz, *Method and Arrangement for the Production and Thermal Compression of Oxygen. EP 3212569B1, Granted 04. 04. 2018*.
- [488] P. Rao, M. Muller, *ACEEE Summer Study on Energy Efficiency*, **2007**, *6*, 124.
- [489] Y. A. Alsultanny, N. N. Al-Shammari, *Eng. J.* **2014**, *18*, 67.
- [490] W. F. Castle, *Int. J. Refrig.* **2002**, *25*, 158.
- [491] C. Fu, T. Gundersen, *Energy* **2012**, *44*, 60.

- [492] M. Chorowski, W. Gizicki, *Arch. Thermodyn.* **2015**, 36, 157.
- [493] M. Redenz, *ECOVAR Concept Eigenerzeugung von Sauerstoff Für Kupolöfen. Oral Presentation, Session of the BDG Working Circle Cupol Furnaces (Online)*, 27. 01. 2021.
- [494] H. Haruna, K. Miyake, M. Sasano, Development of PSA Gas Separation Technology to Reduce Greenhouse Effect. translated R&D Report, "SUMITOMO KAGAKU", vol. 2005-II; [https://www.sumitomo-chem.co.jp/english/rd/report/theses/docs/20050206\\_ki0.pdf](https://www.sumitomo-chem.co.jp/english/rd/report/theses/docs/20050206_ki0.pdf).
- [495] A. Meriläinen, A. Seppälä, P. Kauranen, *Appl. Energy* **2012**, 94, 285.
- [496] R. Kircheisen, R. Bernhardt, M. Kriegel, *15th Int. Conf. Inorganic Membranes ICIM*, Dresden, Germany **2018**.
- [497] "Entwicklung der spezifischen Kohlendioxid-Emissionen des deutschen Strommix in den Jahren 1990 –2019 | Umweltbundesamt," can be found under <https://www.umweltbundesamt.de/publikationen/entwicklung-der-spezifischen-kohlendioxid-6> (accessed: October 2021).
- [498] AGFW FW 309-1 A 2016 Part 6 – Energetical Assessment of District Heating – CO<sub>2</sub> Emissions of Heat Delivery. AGFW Der Energieeffizienzverband Für Wärme, Kälte und KWK e.V. (German Only).
- [499] A. Kriegel, R. Burgstedt, F. Kaiser, S. Müller, Final Report to the Joint Project MedPROmM. BMBF – Federal Ministry for Education and Research, FKZ 01LY1413A+C+E), <https://www.Tib.Eu/de/Suchen/Id/TIBKAT%3A103867591X/Abschlussbericht-Zum-Verbundprojekt-Machbarkeitsnachweis/> (accession: February 2021).
- [500] I. Kühnert, J.-Th. Kriegel, R. Voigt, *Inorganic Membranes for Sophisticated Separation Processes. Filtrieren Und Separieren, Global Guide 2020–2022*, 172.
- [501] R. Kriegel, Membrane separation process and membrane plant for energy-efficient production of oxygen. EP 3022152B1, priority 23.12.2013, granted 30. 09. 2020.
- [502] OGiS – Oxyfuel Gas Engine with Integrated Oxygen Generation for CO<sub>2</sub> Capture. BMWI – Federal Ministry for Economy and Research, FKZ: 0324315A-C (German Only).
- [503] *DeSa – Decentral Oxygen Generation. AiF Research Project, FKZ 20252 BG/2 (German Only)*, [https://www.ikts.fraunhofer.de/en/press\\_media/news/archive/12\\_12\\_2018\\_bmwi\\_funds\\_oxyfuel\\_combined\\_heat\\_an\\_power\\_plant.html](https://www.ikts.fraunhofer.de/en/press_media/news/archive/12_12_2018_bmwi_funds_oxyfuel_combined_heat_an_power_plant.html) (accessed: October 2021).
- [504] E. E. Armstrong, P. A. Benett, D. L. Foster, E. P. van Stein, *ITM Oxygen: The New Oxygen Supply for the New IGCC Market. Oral Presentation, Gasification Technologies 2005, San Fransisco, USA*, <https://vdocuments.net/itm-oxygen-the-new-oxygen-supply-for-the-new-igcc-libraryresearchcoalenergy.html> (accessed: October 2021).
- [505] E. M. Pfaff, A. Kaletsch, C. Broeckmann, *Chem. Eng. Technol.* **2012**, 35, 455.
- [506] J. F. Vente, W. G. Haije, R. Ijpelaan, F. T. Rusting, *J. Membr. Sci.* **2006**, 278, 66.
- [507] X. Tan, K. Li, *AIChE J.* **2007**, 53, 838.
- [508] X. Tan, Z. Wang, B. Meng, X. Meng, K. Li, *J. Membr. Sci.* **2010**, 352, 189.
- [509] E. Kriegel, R. Burckhardt, W. Voigt, I. Schulz, M. Sommer, *Proc. 10<sup>th</sup> Int. Conf. Inorganic Membranes ICIM*, Tokyo, Japan **2008**, Poster Session I P8.Pdf, ISBN 978-4904353-01-1.
- [510] G. Pećanac, S. Baumann, J. Malzbender, *J. Membr. Sci.* **2011**, 385–386, 263.
- [511] F. Liang, H. Jiang, H. Luo, R. Kriegel, J. Caro, *Catal. Today* **2012**, 193, 95.
- [512] R. Kriegel, in *DKG Handbuch Technische Keramische Werkstoffe*, (Ed: J. Kriegesmann), HvB-Verlag, Ellerau **2010**, p. 119. Delivery complement, 11/2010, Chapter 8.10.1.1, 1 (german only).
- [513] R. Voigt, I. Kiesel, L. Kircheisen, R. Kriegel, *14th Intn. Conf. on Inorganic Membranes ICIM*, Atlanta, USA **2016**.
- [514] I. Richter, H. Kriegel, R. Klefenz, H. Voigt, *13th Intn. Conf. on Inorganic Membranes ICIM*, Brisbane, Australia **2014**.
- [515] M. Amelio, G. Florio, P. Morrone, S. Senatore, *Int. J. Energy Res.* **2008**, 32, 24.
- [516] M. Amelio, P. Morrone, *Appl. Therm. Eng.* **2007**, 27, 762.
- [517] A. Ostrikow, *Assessment of Competitiveness of Oxygen Production by Ceramic Membranes in Comparison to Conventional Technologies*, University for Appl. Sc, Jena, **2014**.
- [518] R. Hoffmann, U. Pippardt, R. Kriegel, *J. Membr. Sci.* **2019**, 570–571, 61.
- [519] R. Hoffmann, U. Pippardt, R. Kriegel, *J. Membr. Sci.* **2019**, 581, 270.
- [520] T. Kuramochi, A. Ramírez, W. Turkenburg, A. Faaij, *Prog. Energy Combust. Sci.* **2012**, 38, 87.
- [521] S. J. O'connor, *Regenerative Firing vs. Oxy Fuel Firing: An Applications Approach. AISTech Proc.* **2013**, 2265.
- [522] H. Kobayashi, *Proc. XX. Int. Congr. on Glass (ICG)*, Kyoto, Japan **2004**.
- [523] P. Bělohradský, P. Skryja, I. Hudák, *Energy* **2014**, 75, 116.
- [524] K. K. Wu, Y. C. Chang, C. H. Chen, Y. Da Chen, *Fuel* **2010**, 89, 2455.
- [525] R. Prieler, M. Demuth, D. Spoljaric, C. Hochenauer, *Fuel* **2015**, 140, 731.
- [526] M. Bernhardt, R. Kircheisen, R. Kriegel, *15th Int. Conf. Inorganic Membranes ICIM*, Dresden, Germany **2018**.
- [527] R. Kriegel, *gaswärme Int.* **2017**, 4, 43.
- [528] R. J. Allam, M. R. Palmer, G. W. Brown, J. Fetvedt, D. Freed, H. Nomoto, M. Itoh, N. Okita, C. Jones, *Energy Procedia* **2013**, 37, 1135.
- [529] H. Jericha, W. Sanz, J. Woisetschläger, M. Fesharaki, CIMAC Conf. Paper, Interlaken, Switzerland **1995**, [https://www.google.com/url?sa=t&rct=j&q=&esrc=s&source=web&cd=&ved=2ahUKEwj125jvtrzAhXeSvEDHSACAgQFnoECAQQAQ&url=http%3A%2F%2Fttm-old.tugraz.at%2Ffw%2Fdown%2F1995\\_cimac.pdf&usg=AOvVaw3SKL1XEyuP4yHixkrMder](https://www.google.com/url?sa=t&rct=j&q=&esrc=s&source=web&cd=&ved=2ahUKEwj125jvtrzAhXeSvEDHSACAgQFnoECAQQAQ&url=http%3A%2F%2Fttm-old.tugraz.at%2Ffw%2Fdown%2F1995_cimac.pdf&usg=AOvVaw3SKL1XEyuP4yHixkrMder) (accessed: October 2021).
- [530] K. Wimmer, W. Sanz, *Int. J. Greenhouse Gas Control* **2020**, 99, 103055.



**Guoxing Chen** is currently a senior scientist at Fraunhofer IWKS. He received his Ph.D. in Engineering, Science and Technology from both the Université Libre de Bruxelles and the University of Mons in 2017. He worked as a Postdoctoral Fellow at the University of Stuttgart and the Technical University of Darmstadt from 2017 to 2020 in the group of Prof. Anke Weidenkaff. His current research activities are the utilization of low-temperature plasmas including plasma catalysis for gas conversion and waste materials recycling and development of CO<sub>2</sub>-resistant mixed ionic–electronic conducting materials for plasma-based reaction separation coupling and oxygen permeation membranes.



**Armin Feldhoff** is extraordinary professor at Leibniz University Hannover and holds the *venia legendi* for Physical Chemistry. His research interests are in thermo-iono-electric (TIE) materials for energy conversion. He received his diploma in physics from the University of Münster and his Ph.D. degree from the Martin-Luther University Halle-Wittenberg. He was pre- and post-doctoral researcher at the Max Planck Institute of Microstructure Physics and postdoctoral researcher at Cornell University and at the French National Centre for Scientific Research. He is an associate editor of *Elektronenmikroskopie*, *Energy Harvesting & Systems* and the *Journal of Electronic Materials* and editorial board member of *Entropy*. He is chair of the Energy Materials and Systems Division of the American Ceramic Society.



**Anke Weidenkaff** is a professor at the Technical University of Darmstadt and the director of Fraunhofer IWKS. Her principal areas of research and expertise are materials science and resource strategies, including the development, synthesis and characterization of sustainable materials for energy conversion and storage. Her current work focuses on smart, regenerative materials and the development of next-generation process technologies for fast and efficiently closed material cycles. Anke Weidenkaff is member of the German Advisory Council on Global Change (WBGU) as well as member of the Advisory Council of the Bundesanstalt für Materialforschung und -prüfung BAM (Federal Institute for Materials Research and Testing).



**Claudia Li** is a postdoctoral researcher at Swinburne University of Technology Sarawak Campus. She received her B.Eng. and Ph.D. from Swinburne University of Technology in 2017 and 2021. Her research interests include membranes, carbon capture technologies, and gas separation.



**Shaomin Liu** is a professor in the College of Chemical Engineering, Beijing University of Chemical Technology (BUCT), China. He received his Ph.D. degree from the National University of Singapore (2002), and then worked as a postdoctoral research fellow at the California Institute of Technology for three years. In recent 15 years, he has been working in the University of Queensland, Curtin University and BUCT, consecutively. His research interests include membrane science and technology for gas separation, environmental remediation, and green chemical synthesis.



**Xuefeng Zhu** is a professor of Dalian Institute of Chemical Physics (DICP), Chinese Academy of Science (CAS), China. He received his Ph.D. degree from DICP in 2007, and became a full professor at DICP in 2014. As a postdoctor, he worked in Arizona State University (USA) in 2008. He works on dense ceramic membranes for gas separation, catalytic membrane reactors for process intensification, solid oxide cells and electrocatalysis for energy conversion.



**Jaka Sunarso** is an associate professor and the Director of the Research Centre for Sustainable Technologies at Swinburne University of Technology Sarawak Campus. He received his B.Eng. from Institut Teknologi Sepuluh Nopember in 2004 and then his M.E. and Ph.D. from the University of Queensland in 2006 and 2010. He then won an Alfred Deakin Postdoctoral Research Fellowship and a Banting Fellowship in 2010 and 2013. His main interests are batteries, fuel cells, membranes, and biomass utilization. His works have accumulated total citations of 8993 with an h-index of 45. He has actively supervised 11 Ph.D. and 7 Master students.

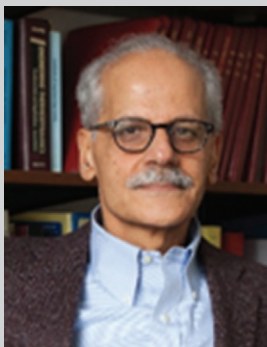


**Kevin Huang** is currently a SmartState endowed chair and director of solid oxide fuel cell center at University of South Carolina. His research interest covers rechargeable batteries, reversible fuel cells, gas separation membranes and multiscale computational modeling. He has published 230+ peer-reviewed journal papers, 2 books, 3 book chapters and been granted 14 US patents. He is the associate editor of *Journal of Electrochemical Energy Conversion and Storage* and past associate editor of *RSC Advances*. He is the recipient of numerous awards, including 2018 Breakthrough Leadership in Research Award, 2017 Educational Foundation Award for Research in Science, Mathematics and Engineering, 2015 College of Engineering and Computing Research Achievement Award, and 2014 University of South Carolina Breakthrough Stars. He currently teaches Advanced Thermodynamics and Energy Storage for graduate student.



**Xiao-Yu Wu** is an assistant professor in the Department of Mechanical and Mechatronics Engineering at the University of Waterloo. He received B.Sc. and M.Sc. degrees from Zhejiang University in 2009 and 2012, and Ph.D. from MIT in 2017. His research group, Greener Production @ Waterloo combines expertise in thermal science, material engineering, and techno-economics to develop sustainable energy conversion and chemical production technologies, e.g., renewable hydrogen/ammonia production, hybrid energy storage, and carbon capture and conversion to value added products.





**Ahmed F. Ghoniem** is the Ronald C. Crane Professor of Mechanical Engineering, Director of the Center for Energy and Propulsion Research and the Reacting Gas Dynamics Laboratory at MIT. He received his B.Sc. and M.Sc. degrees from Cairo University, and Ph.D. at the University of California, Berkeley. He is fellow of the American Society of Mechanical Engineer, the American Physical Society, and the Combustion Institute, and associate fellow of the American Institute of Aeronautics and Astronautics. He received the ASME James Harry Potter Award in Thermodynamics, the AIAA Propellant and Combustion Award and the “Committed to Caring Professor” at MIT.



**Weishen Yang** is a Chair Professor of Dalian Institute of Chemical Physics, Chinese Academy of Sciences (CAS), China. He received his Ph.D. from CAS in 1990. As a visiting scholar, he worked in Birmingham University (UK) in 1989, and University of Southern California (USA) in 2001. He works on the rational design and molecular-level engineering of functional nano-materials for applications in catalysis, and separation (e.g., inorganic membranes).



**Jian Xue** is currently an associate professor at South China University of Technology. He received his B.S. in 2010 and M.S. in 2013 from South China University of Technology. And then he obtained his Ph.D. from Institute of Physical Chemistry and Electrochemistry, Leibniz University Hannover in Germany in 2016. His main research interests are membrane technology and catalytic membrane reactor.



**Haihui Wang** is currently a professor at Tsinghua University, China. He received his Ph.D. from Chinese Academy of Sciences in 2003 and then worked as an Alexander von Humboldt Research Fellow and Postdoc in Leibniz University Hannover in Germany until 2007. He was a professor at South China University of Technology from 2007 to 2020. He joined into Tsinghua University since November 2020. His interests focus on inorganic membranes, membrane reactor and energy materials.



**Zongping Shao** is a John Curtin Distinguished Professor at Curtin University, Australia, and also a professor at Nanjing Tech University, China. He obtained his Ph.D. from Dalian Institute of Chemical Physics, China, in 2000. He worked as a Visiting Scholar at Institut de Recherches Sur La Catalyse, CNRS, France, and then a Postdoctoral Fellow at California Institute of Technology, USA, from 2000 to 2005. His current research interests include fuel cells, lithium-ion batteries, metal-air batteries, solar cells, and oxygen-permeable membranes. He has been recognized as a Highly-Cited Researcher by Clarivate Analytics since 2017.



**Jack H. Duffy** is a graduate research assistant pursuing his Ph.D. in materials science and engineering in Dr. Kyle Brinkman's group at Clemson University in Clemson, SC. He is currently a participant in the Professional Internship Program at the National Energy Technology Laboratory (NETL) through the Oak Ridge Institute for Science and Education (ORISE). He graduated with his B.S. in chemical engineering in 2018 from Northeastern University in Boston, MA. During his undergraduate program, he researched under Dr. Badih Assaf at École Normale Supérieure in Paris, France from January to June 2016.



**Kyle S. Brinkman** is the chair of the Department of Materials Science and Engineering at Clemson University in Clemson, SC. He graduated from the Swiss Federal Institute of Technology in Lausanne, Switzerland with a Ph.D. in materials science and engineering. Brinkman then served as a postdoctoral fellow at the Advanced Industrial Science and Technology Institute in Japan and later worked as a principal engineer in the U.S. Department of Energy's Savannah River National Laboratory. He is a Fellow of ACERS and has authored or co-authored more than 100 peer-reviewed technical publications and government reports, four patents and currently serves as an editor for the Journal of Materials Science, and a DOE-NETL ORISE Faculty Fellow.



**Xiaoyao Tan** is a professor of chemical engineering at Tiangong University, China. He received his Ph.D. degree from Dalian Institute of Chemical Physics, Chinese Academy of Sciences (1995). Prior to his present appointment, he worked as a professor at Shandong University of Technology between 1998 and 2009. His current research interests include preparation and characterization hollow fiber membranes, membrane separation and reaction processes as well as solid oxide fuel cells. He has published over 280 research papers, holds 49 patents and is the author of 10 book or book chapters.



**Yan Zhang** obtained her Ph.D. degree in Industrial Catalysis from Dalian Institute of Chemical Physics in 2014. After that, she joined Membrane Separation & Catalysis Group, Qingdao Institute of Bioenergy and Bioprocess Technology, Chinese Academy of Sciences (QIBEBT, CAS). She is currently an associate professor in QIBEBT, CAS. Her research focuses on membrane separation and catalysis.



**Heqing Jiang** obtained his Ph.D. in Physical Chemistry at Leibniz University of Hannover (Germany). After his postdoctoral stay at Max Planck Institute for Coal Research (Germany), he joined in 2013 as a full professor Qingdao Institute of Bioenergy and Bioprocess Technology, Chinese Academy of Science (QIBEBT, CAS). His main research interest focuses on the multifunctional membranes and their application in separation and catalysis.



**Rémi Costa**, graduated as an engineer in 2005 from Grenoble INP, France. Having completed a Ph.D. at Mines Paristech in 2009, he joined the German Aerospace Center, Department of Electrochemical Energy Technology in Stuttgart as Post-Doctoral researcher. From 2011 he was project leader and coordinated or contributed to several Solid Oxide Cell development projects. Since 2020 he leads the research group on High Temperature Cells and Stacks. His research interests include the elucidation of degradation mechanisms, the development of Solid Oxide Cells and Proton Conducting Ceramic cells – including innovative materials solutions – and their utilization for the energy system.



**Kaspar Andreas Friedrich** is a professor of Mechanical Engineering at University of Stuttgart and the Head of the Electrochemical Energy Technology Department at the German Aerospace Center (DLR) in Stuttgart, Germany. His research areas are electrochemical energy conversion and storage, in particular polymer electrolyte membrane (PEM) and solid oxide (SOC) fuel cells and electrolysis, advanced Li and Mg batteries, and system design. He has authored and coauthored about 250 peer reviewed papers. He received the Fischer medal (Dechema) in 2009 and the Ertl prize 2014 for his scientific work. The activities of the group have received the f-cell Award in Silver 2016 for electrolysis components, the Clean Tech Media Award 2012 (Aviation) and the f-cell Award in Silver 2008 (DLR with Airbus).



**Ralf Kriegel** is leading the department “High-Temperature Separation and Catalysis” at Fraunhofer Institute for Ceramic Technologies and Systems IKTS, Hermsdorf branch of the institute. He got his Ph.D. in inorganic chemistry 1992 in Jena, Germany. Thenceforth he is dealing with complex oxides suited for reversible storage or separation of oxygen from other gases. In the past, he was active in the fundamental research about oxygen stoichiometry of oxides, oxygen transport and chemical expansion. Since appr. 10 years he focuses especially on process development and on the design of membrane plants for industrial applications.